Crystallography Reports, Vol. 50, Suppl. 1, 2005, pp. S1–S9.

STRUCTURE OF INORGANIC COMPOUNDS

Stability of the Modulated Structure of Baĭkal Lazurite and Its Recrystallization at a Temperature of 600°C over a Wide Range of Sulfur Dioxide Fugacities

V. L. Tauson and A. N. Sapozhnikov

Vinogradov Institute of Geochemistry, Siberian Division, Russian Academy of Sciences, ul. Favorskogo 1a, Irkutsk, 664033 Russia

e-mail: vltauson@igc.irk.ru

Received February 8, 2005

Abstract—The stability of three-dimensional incommensurate modulation in cubic lazurite from the Baĭkal region is experimentally investigated at T = 600°C. It is found that the X-ray photoelectron spectra of the annealed samples exhibit a peak corresponding to sulfite and a split peak associated with the (Na,Ca)SO_4 sulfate. It is assumed that the splitting is caused by the ordering of the complexes not involved in the framework. This assumption is confirmed by the presence of a similar split peak in the X-ray photoelectron spectra of triclinic lazurite. It is demonstrated that the initial modulation is retained at the fugacity $f_{SO_2} = 8 \times 10^{-3}$ bar. The decisive factors responsible for the retention of the three-dimensional incommensurate modulation are the temperature and the fugacity of sulfur dioxide. The latter quantity should be close to the stability boundary of the basic lazurite structure. The growth and transformation mechanisms of the modulation formation are considered. © *2005 Pleiades Publishing, Inc.*

INTRODUCTION

It is well known that lazurite is stable to external actions. This mineral has been used to prepare an extremely resistant blue (sky blue) dye since antiquity. According to geothermometric data, lazurite is formed in the range ~600–500°C [1]. A decrease in the temperature is accompanied by a sequential series of phase transformations in lazurite due to the change in its chemical composition. In the Baĭkal region, three structural (cubic, triclinic, monoclinic) modifications of lazurite are formed in the aforementioned temperature range. Cubic lazurite has a three-dimensional incommensurate structure in which the modulation period is not a multiple of the subcell parameter. Triclinic and monoclinic lazurites have commensurately modulated structures, which are responsible for the appearance of additional superstructure (satellite) reflections around the reflections of the cubic subcell in the X-ray diffraction patterns. The high-temperature cubic structure with a three-dimensional incommensurate modulation is formed at temperatures from ~600 to ~500°C. The composition of this modification is characterized by high ratios between sulfate and sulfide sulfur species and virtually does not contain potassium. Afganite, which is a facial analogue of lazurite, is formed at lower temperatures. When forming afganite-bearing metasomatites, triclinic lazurite is predominantly formed in the temperature range ~560–520°C and the monoclinic variety is formed at ~500°C at the front of substitution of phlogopite for lazurite. Compositions with maximum concentrations of sulfide sulfur and potassium are typical of the monoclinic modification. Transformations, in particular, ordering of sulfide and sulfate clusters during lazurite recrystallization, occur as a result of a change in the oxidation state of sulfur, which serves as a center of formation of intraframework clusters and is sensitive to external conditions, primarily, to SO_2 activity (fugacity) f_{SO_2} [2].

The three-dimensional incommensurate modulation of the structure of cubic lazurites from Southern Baĭkal deposits has attracted particular interest of researchers dealing with aperiodic structures [3, 4]. The point is that the sinusoidal three-dimensional modulation is unstable in terms of the continuum theory of elasticity, because the conditions for equilibrium of an elastic medium are not satisfied for this modulation. Note that the sodalite-like structure of lazurite belongs to loose structures with large holes, which are occupied by $[Na_3CaSO_4]^{3+}$ sulfate and $[Na_3CaS]^{3+}$ sulfide clusters [5], whose displacements are weakly affected by the aluminosilicate framework and do not necessarily give rise to considerable internal stresses. In this case, the character of deformation is similar to plastic flow, for which the conditions of mechanical equilibrium are satisfied by itself [2]. The three-dimensional incommensurately modulated crystal structure of cubic lazurite from the Baĭkal region is not determined, even though Bolotina *et al.* [3, 6] attempted to solve this structure within a twin model consisting of three orthorhombic components related by the [111] axis of the cubic cell.

Rastsvetaeva *et al.* [7] determined the average structure of this mineral without regard for satellite reflections. Such a structure corresponds to a superposition of all cells in which the positions of individual atoms are determined. The cation sites in the average structure are split into three subsites, which can be explained by the inadvertent errors arising when the parameters of the modulated structure are calculated within the average approximation. In the commensurately modulated structure of triclinic lazurite, Na and Ca cations occupy different positions and the unit cell involves two $[Na_3CaSO_4]^{3+}$ and four $[Na_{5.5}Ca_{0.5}SO_4]^{4.5+}$ clusters arranged in an ordered manner [8].

The factors responsible for the formation of the three-dimensional incommensurate modulation in cubic lazurite, its frequent occurrence, and retention in metasomatites of lazurite deposits in the Southern Baĭkal region remain unclear. Sapozhnikov *et al.* [9] experimentally revealed that the modulation can be easily released by annealing the mineral in air at moderate temperatures (for 24 h at 600°C). It is not known whether the three-dimensional incommensurate modulation is formed via the growth or transformation mechanism and whether the modulation is reproduced upon growth of lazurite crystals. In our earlier work [2], it was demonstrated that, in lazurites rich with sulfate ions, short-period modulations (involving from four to six unit cells) can arise, whose stability is provided by the balance between the elastic energy of sinusoidal deformations and the energy of cluster ordering in the mineral structure. This corresponds to the conditions of metastable forced equilibrium of type II (according to the classification proposed in [10]). However, a similar equilibrium is possible only over a narrow range of SO_2 fugacities, namely, from ~10^{-2} to ~10^{-5} bar at $T <$ 600°C [2]. Geochemically, it is very difficult to conceive factors responsible for the variation of the fugacity over the aforementioned narrow range taking into account that the fugacity in the stability region of lazurite can vary by ten orders of magnitude and that natural cubic lazurite almost always has a modulated structure. In order to gain an insight into the nature of this unusual phenomenon, it is necessary to analyze more accurately modulation transformations at fixed values of temperatures and activities of volatile components. This paper reports on the first results of such investigations. The release of the modulation in natural three-dimensional incommensurately modulated lazurite was studied over a wide range of SO_2 activities. It was found that, at 600°C (the upper limit of the temperature range of lazurite formation in the Baĭkal region), the modulation is released at all fugacities f_{SO_2} varied within five orders of magnitude in the range where the modulation exists. However, there is a fugacity value at which the modulation is released at a minimum rate.

EXPERIMENTAL TECHNIQUE

The experiments were performed in evacuated sealed silica glass (optical quality) tubes. A gold tube 3 mm in diameter with an oxygen buffer (500 mg) and two platinum tubes 1.5 mm in diameter, one of which contained initial lazurite (as a rule, 25 mg) and the other tube involved a sulfur fugacity indicator (pyrrhotite, 100 mg), were placed in the silica tube with an inner diameter 6 mm and ~80 mm in length. The tubes were placed in pockets of a massive steel holder mounted in a shaft furnace and held for a required time at 600 ± 3°C, followed by cooling in air. The fugacity f of a component in a gaseous phase characterizes its partial pressure in a nonideal gaseous medium. This quantity can be provided by buffer mixtures (for example, a metal–oxide mixture for oxygen and a metal–sulfide mixture for sulfur) or be determined from an indicator phase of variable composition. At a given temperature and total pressure, the composition of such a phase (for example, wüstite $Fe_{1-x}O$ or pyrrhotite $Fe_{1-x}S$) depends only on the fugacity of the corresponding gas component (oxygen, sulfur). In this work, the sulfur fugacity was determined from the pyrrhotite composition and the SO_2 fugacity was calculated from the thermodynamic data on the reaction with the participation of pyrrhotite and S_2 (see below).

When using the Ni–NiO oxygen buffer, the oxygen activity in the system is maintained at a constant level and the SO_2 fugacity is calculated from the reaction

$$O_2 + \frac{1}{2}S_2 = SO_2. \quad (1)$$

Within ~100 h after the beginning of the experiment, the magnetite phase is formed in the pyrrhotite indicator. This allows us to independently calculate the SO_2 fugacity according to the reaction

$$Fe_3O_4 + \left(\frac{3}{2x} + 1\right)S_2 = \frac{3}{x}Fe_xS + 2SO_2. \quad (2)$$

As was shown in our previous work [11], the discrepancy between the results of calculations from two reactions does no exceed $0.2\log f_{SO_2}$. Higher fugacities f_{O_2} were achieved using the metal–oxide buffer of variable composition. This buffer was prepared by annealing Ni + Cu and Cu_2O + NiO mixtures in sealed silica tubes. Then, the metal and oxide components of the buffer were mixed in a ratio of 3 : 2. The heat treatment conditions were as follows: annealing at 800°C for two days and then annealing at 600°C for one day. Since the oxide component of the system is nonideal, the oxygen fugacity cannot be determined from the composition of the buffer mixture and the SO_2 fugacity cannot be calculated from reaction (1). In this respect, the SO_2 fugacity was initially calculated from reaction

(2) according to the relationship

$$\log f_{SO_2} = \frac{1}{2}\log K_{(2)} - \frac{3}{2x}\log a_{FeS} + \left(\frac{3}{4x} + \frac{1}{2}\right)\log f_{S_2}, \quad (3)$$

where $K_{(2)}$ is the equilibrium constant of reaction (2), a_{FeS} is the FeS activity in pyrrhotite, and

$$-2.303RT\log K_{(2)} = \Delta G_{(2)}$$
$$= \frac{3}{x}\Delta G^f_{Fe_xS} + 2\Delta G^f_{SO_2} - \Delta G^f_{Fe_3O_4} - \left(\frac{3}{2x} + 1\right)\Delta G^f_{S_2}. \quad (4)$$

Here, ΔG^f are the Gibbs free energies of formation of the corresponding compounds. When the S_2 and SO_2 fugacities are determined, it is easy calculate the O_2 fugacity from reaction (1).

The experiments were carried out using the three-dimensional incommensurately modulated lazurite taken from the Pokhabinskoe deposit (the Slyudyanka region). The chemical composition of the mineral can be approximately expressed by the formula $Ca_{1.4}Na_{6.6}Si_{6.1}Al_{5.9}(SO_4)_{1.6}S_{0.5}Cl_{0.1}(H_2O)_{1.8}$. Mineral grains were ground in an agate mortar in ethanol. Then, the powder was screened through a sieve with a square-mesh size of 40 μm. The product was elutriated initially in water and then in ethanol. The bottom fraction was rejected. Thereafter, particles ~50 μm or more in size were absent in the sample. The size of the majority of particles falls in the range ~10–20 μm.

TECHNIQUES OF ANALYSIS

The modulation character was determined from the intensity ratio of satellite and subcell reflections [12]. The degree of transformation or the completeness of modulation release was calculated as $\xi = (\xi_{in} - I_s/I_m)/\xi_{in}$, where I_s/I_m is the intensity ratio between the $(4 + n, 4 - n, 1)$ satellite reflection and the (332) reflection [2] and $\xi_{in} = 1.60 \pm 0.02$ is the same ratio for the initial sample of the three-dimensional incommensurately modulated lazurite. The iron content in pyrrhotite was determined accurate to within ±0.1 at % according to the Toulmin–Barton standard technique [13] from the position of the (102) diffraction reflection with the use of NaCl as an internal standard. The phase compositions of the oxide buffers, sulfur fugacity indicator, and lazurite batch were checked by X-ray diffraction analysis on a DRON-3 diffractometer (FeK_α radiation, Mn filter; CuK_α radiation, Ni filter).

The sulfur species in lazurite and products of its annealing were studied by X-ray photoelectron spectroscopy (XPS). This method, as a rule, is used for investigating the surface; however, when a sample is ground immediately prior to measurements, it is possible to obtain nearly true information on the sulfur species in the phase bulk. This is confirmed by the data obtained in our previous work [14], according to which the atomic ratios determined for the sulfate and sulfide sulfur species by X-ray photoelectron spectroscopy and chemical analysis of two lazurite samples are in reasonable agreement. The spectra were recorded on a Riber LAS-3000 spectrometer (equipped with a hemispherical analyzer for electrons with a retarding potential) with the use of nonmonochromatic AlK_α radiation from an aluminum anode (λ = 1486.6 eV; emission current, 20 mA; tube voltage, 10 kV). The binding energy was corrected for the surface charging by using the C 1*s* line (binding energy, 285 eV). The measured S 2*p* lines were represented by the $2p_{3/2}$–$2p_{1/2}$ doublets. In order to determine accurate binding energies, the lines were decomposed according to the special program providing a nonlinear subtraction of the background and a Gauss–Lorentz model of the line shape. The lines were assigned to specific sulfur species in accordance with the $2p_{3/2}$ doublet component on the basis of the data available in the literature [15–19].

EXPERIMENTAL RESULTS

In the course of experiments, the lazurite batch is weakly recrystallized, which can be judged from the appearance of idiomorphic new grains in the form of trigonal plates with a maximum size of ~50 μm (rarely up to 100 μm). These plates bear a resemblance to strongly flattened cubo-octahedra in which two opposite (111) faces are predominantly developed. Neither the sizes nor the number of these crystals are sufficient for their separation from the lazurite batch and analysis.

The calculated fugacities of gases in experiments and the measured degrees of modulation release ξ are listed in Table 1. Analysis of these data demonstrates that the modulation is released under all the studied conditions in the range that was previously treated as the range in which the modulation occurs [2]. Note that, in the time range 100–500 h under investigation, the degree of transformation is minimum at fugacities f_{SO_2} from $10^{-1.96}$ to $10^{-2.41}$ bar (Fig. 1).

Table 2 presents the binding energies of S $2p_{3/2}$ photoelectrons and the corresponding sulfur species in the initial three-dimensional, incommensurately modulated lazurite and the products of its annealing in air and a under closed conditions (Fig. 2). The initial lazurite contains sulfide, polysulfide (S_x^{2-}, $x > 2$), and sulfate sulfur (Fig. 2). This is confirmed by comparison with the spectra of ultramarine [15], which is considered a lazurite form with a disordered distribution of Si and Al atoms in the framework [20]. However, after annealing at a relatively high activity of SO_2, the doublet corresponding to the sulfate is split into two doublets (Fig. 2) and the most intense peak of the $2p_{3/2}$ doublet with a binding energy of 169.0 eV is split into two peaks with lower (167.8 eV) and higher (170.6 eV) binding energies (Table 2). The intensity ratio of these peaks is approximately 3 : 1. These peaks can be attributed only to sodium sulfate and calcium sulfate, respectively [17–19]. Since new phases are not formed in the lazur-

Table 1. Degree of release of the three-dimensional incommensurate modulation upon annealing of crystals of Baikal lazurite at a temperature of 600°C for different fugacities of components in the gaseous phase

Experiment no.	Metal–oxide buffer*	Time, h	Pyrrhotite indicator**		Degree of modulation release ξ	Fugacities of gases, bar		
			phases	FeS content in pyrrhotite, mol %		$-\log f_{O_2}$	$-\log f_{S_2}$	$-\log f_{SO_2}$
1	Ni–NiO	100	*Po* + *Mt*	95.9	0.45	19.14	5.56	4.28
2		500	*Po* + *Mt*	95.9	0.88	19.14	5.56	4.28
3		840	*Po* + *Mt*	95.9	1.00	19.14	5.56	4.28
4	Ni,Cu(21.3)–NiO + Cu_2O	100	*Po* > *Mt*	96.3	0.29	17.23	6.00	2.41
5		500	*Po* > *Mt*	96.4	0.72	17.33	6.12	2.57
6	Ni,Cu(50)–NiO + Cu_2O	100	*Po* > *Mt*	96.0	0.32	16.95	5.65	1.96
7		500	*Po* + *Mt*	96.1	0.66	17.06	5.78	2.13
8	Ni,Cu(65)–NiO + Cu_2O	100	*Po* > *Mt*	95.0	0.68	16.13	4.64	0.63
9		500	*Po* + *Mt*	95.2	0.88	16.30	4.84	0.90
10	Ni,Cu(80)–NiO + Cu_2O	100	*Po* > *Mt*	94.4	0.82	15.63	4.06	−0.16
11		500	*Po* + *Mt*	94.0	0.78	15.30	3.69	−0.67

Note: In experiment no. 8, the amount of lazurite was taken to be larger (60 mg instead of 25 mg) for the subsequent X-ray photoelectron analysis.

* The Cu content (wt %) in the Ni + Cu initial mixture is given in parentheses.

** *Po* is pyrrhotite $Fe_{1-x}S$, and *Mt* is magnetite Fe_3O_4.

ite batch, the case in point is the separation (within crystals) and ordering of sodium and calcium sulfate clusters. This is confirmed by the appearance of superstructure reflections in the X-ray diffraction patterns of the annealed sample. It should be noted that the peak in the range 170–171 eV is observed in the X-ray photoelectron spectra of anisotropic varieties of lazurite. In particular, a similar peak was found for triclinic lazurite (Fig. 3) with an ordered arrangement of clusters in the structure. It can also be seen from Fig. 2 that, depending on the O_2 and SO_2 activities, sulfate is partially transformed into sulfite (SO_3^{2-}), which becomes the dominant sulfur species upon annealing in air. The $SO_4 \longrightarrow SO_3$ transformation is also observed in the system closed to air oxygen (Fig. 2b), even though the degree of transformation is lower and can be determined with a larger uncertainty due to a partial overlapping of the peaks corresponding to the SO_3^{2-} and S_x^{2-} species. However, we can assume that the previously revealed reaction [14]

$$SO_4^{2-} + S_3^{2-} + O_2(\text{gas}) = 2SO_3^{2-} + S_2(\text{gas}) \qquad (5)$$

also proceeds in the system closed to air oxygen at relatively high activities of SO_2.

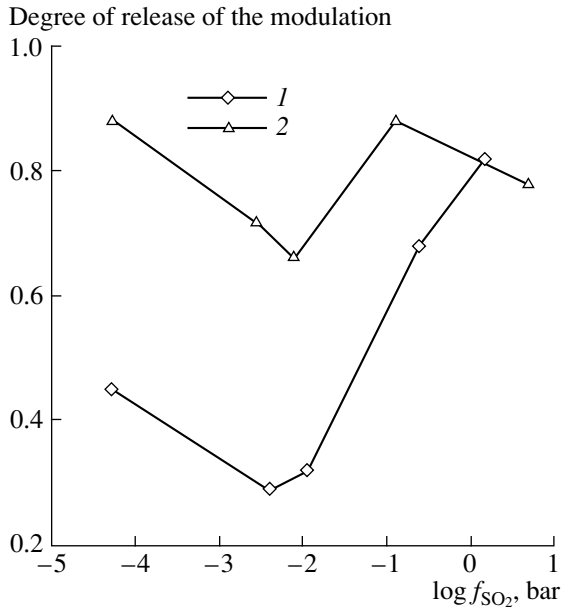

Fig. 1. Degree of release of the three-dimensional incommensurate modulation in cubic lazurite from the Baĭkal region as a function of the SO_2 fugacity in the gaseous phase upon annealing at a temperature of 600°C for (*1*) 100 and (*2*) 500 h.

DISCUSSION OF THE RESULTS

In our earlier work [2], it was experimentally proved that the main factors controlling the phase relations of lazurite (including the stability of the three-dimensional incommensurate modulation) are the temperature and the SO_2 activity in the system. Modulations of the lazurite structure are governed by the presence of

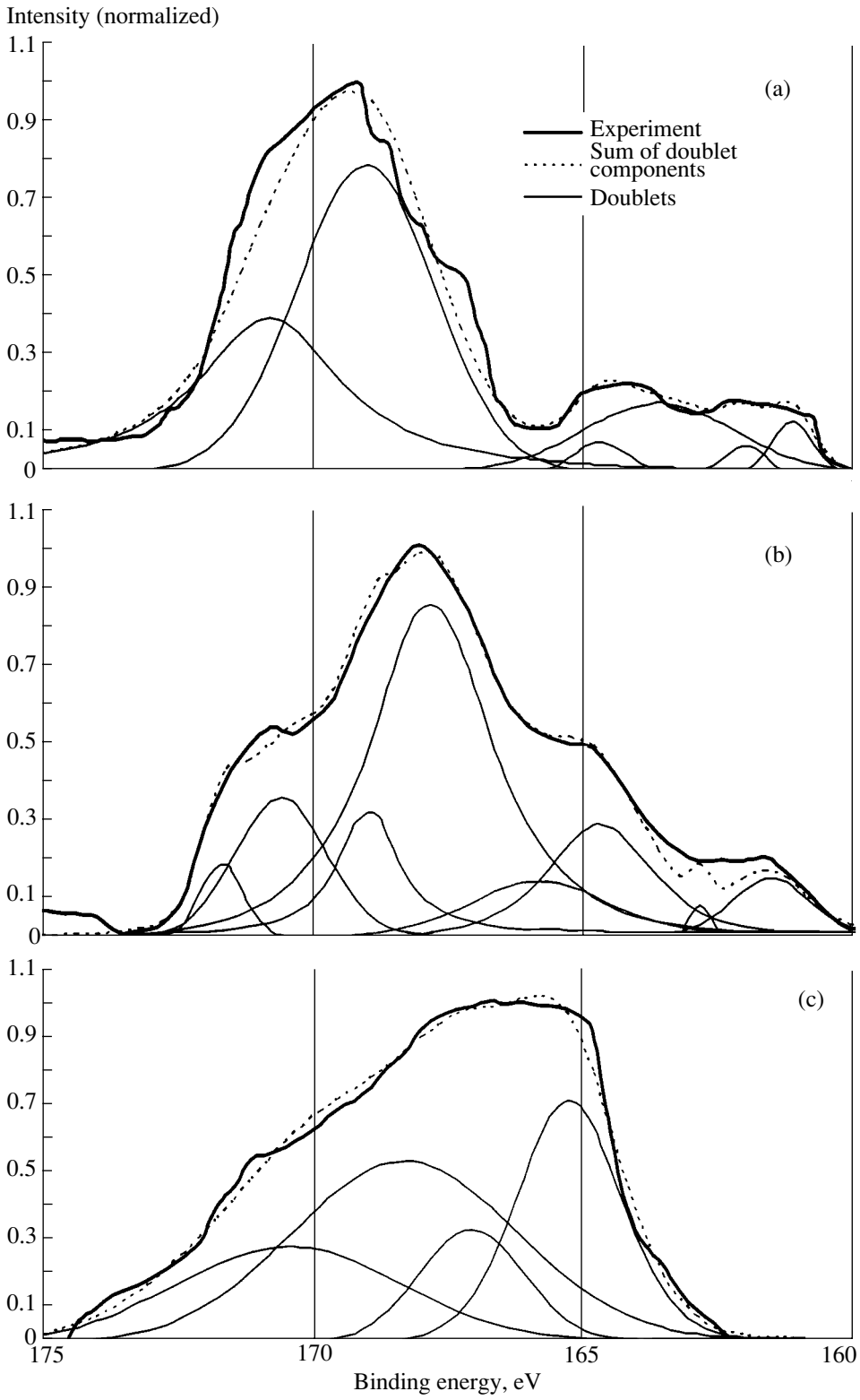

Fig. 2. S 2*p* X-ray photoelectron spectra of (a) the initial lazurite with three-dimensional incommensurate modulation and products of its annealing at temperatures of (b) 600°C (100 h, f_{SO_2} = 0.23 bar) and (c) 800°C (24 h, air). The spectra are decomposed into $2p_{3/2}$–$2p_{1/2}$ doublets. Sulfur species are listed in Table 2.

Table 2. Binding energies of S $2p_{3/2}$ photoelectrons and the sulfur species in lazurite and products of its annealing

Lazurite type	*E*, eV	Hypothetical sulfur species
Cubic lazurite with a three-dimensional incommensurately modulated structure*	161.1	S^{2-}
	163.5	S_x^{2-}
	169.0	SO_4^{2-}
Cubic lazurite after annealing at 600°C for 100 h, f_{SO_2} = 0.23 bar (experiment no. 8, Table 1)	161.5	S^{2-}
	164.7	SO_3^{2-} + S_x^{2-}
	167.8	SO_4^{2-} (Na cluster)
	170.6	SO_4^{2-} (Ca cluster)
Cubic lazurite (small grains) after annealing at 800°C for 24 h in air	165.2	SO_3^{2-}
	168.3	SO_4^{2-}
Triclinic lazurite**	161.5	S^{2-}
	163.8	S_x^{2-}
	167.5	SO_4^{2-} (Na cluster)
	171.0	SO_4^{2-} (Ca cluster)

* Pokhabinskoe deposit (the Southern Baikal region).
** Malo-Bystrinskoe deposit.

sulfate and sulfide complexes (clusters), whose compositions and ratios depend on the external conditions [3]. The data obtained in the present work at T = 600°C indicate that the three-dimensional incommensurate modulation is released over the entire range of fugacities f_{SO_2}, even though the transformation rate is minimum at a fugacity of ~8×10^{-3} bar (Fig. 1). It seems likely that, at 600°C, there are no fugacities f_{SO_2} at which the modulation retains its stability. Early Paleozoic deposits of the Southern Baĭkal region were formed over a very long time (approximately 30 million years [21]), which is quite incomparable to the duration of laboratory experiments. Such a contradiction that resides in the presence and frequent occurrence of three-dimensional incommensurately modulated lazurite in Baĭkal deposits, on the one hand, and the easiness of releasing this structural modulation, on the other hand, can be resolved in two ways. In the first case (growth mechanism), it is assumed that cubic lazurite crystallizes at a lower temperature (<550°C) and over a very narrow range of fugacities f_{SO_2}. In the second case (transformation mechanism), it is suggested that the three-dimensional incommensurate modulation results from a solid-phase transformation (of the spinodal decomposition type). According to this mechanism, as the temperature decreases, the "ideal" (without three-dimensional incommensurate modulation) cubic lazurite formed at 600°C gradually decomposes into domains of different compositions with the formation of structural modulation that reflects the development of sine waves of the composition throughout the structure.

Lazurite can be represented as a solid solution of polysulfide sodalite ($Na_8Al_6Si_6O_{24}S_x$) and haüyne [$Na_6Ca_2Al_6Si_6O_{24}(SO_4)_2$] [11]. Sulfate and sulfide clusters are ordered; however, since the SO_4 sulfate content, as a rule, is higher than the sulfide content, the structure contains excess clusters $[Na_3Ca \cdot SO_4]^{3+}$, i.e., clusters that are not involved in ordering and can be distributed in a random manner [22].

The stability of the three-dimensional incommensurate modulation in cubic lazurite can be provided by different factors. Most likely, the existence region of the modulation consists of two subregions or zones. The first zone is adjacent to the stability boundary of the lazurite phase and corresponds to high fugacities f_{SO_2}. As the fugacity increases, lazurite decomposes into oxide and sulfate phases, including $Na_4Ca(SO_4)_3$ and $CaSO_4$ [2]. The second zone corresponds to lower fugacities f_{SO_2}. In the second zone, cluster ordering is associated with the chemical transformation of sulfate and sulfide (polysulfide) ions into each other. This transformation depends on the SO_2 activity in the gaseous phase. When the condition for forced equilibrium

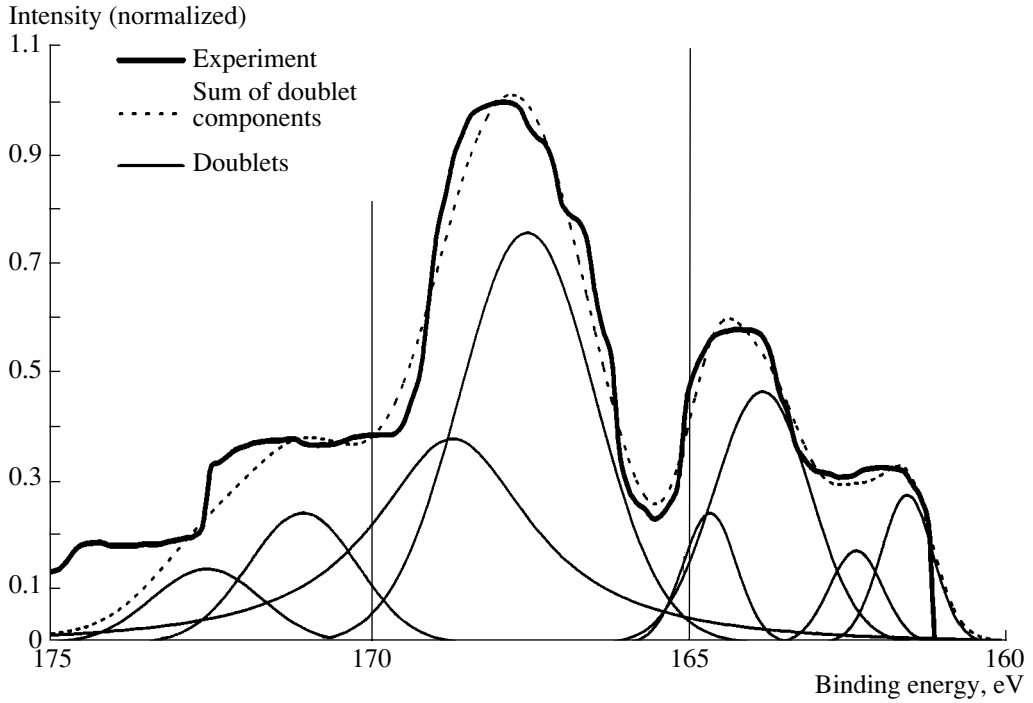

Fig. 3. S 2*p* X-ray photoelectron spectrum of triclinic lazurite from the Baĭkal region (compare the high-energy peak with that in Fig. 2b). Sulfur species are listed in Table 2.

at which the strain energy of the structure is exactly equal to the energy of cluster ordering is violated [2], the modulation is released rapidly. However, if the structure contains excess sulfate clusters ($[SO_4] > [S]$) that are not involved in sulfate–sulfide ordering, the $SO_4 \longrightarrow S$ transformation in a specific range of fugacities f_{SO_2} does not necessarily lead to a change in the degree of cluster ordering. Clusters of disordered domains will be reduced, and newly formed sulfide clusters will be characterized by ordering characteristic of the initial structure. Note that such a "damped" mechanism cannot occur in a system open to air oxygen in which sulfide (polysulfide) ions react with sulfate ions to yield sulfite (SO_3^{2-}) ions [14]. This can be judged from the X-ray photoelectron spectra (Fig. 2c). Under similar conditions, the three-dimensional incommensurate modulation is quite unstable and can be rapidly released, because sulfide clusters disappear.

The above damped mechanism of structure adaptation to changes in the external conditions seems to be improbable for natural systems, in which variations in parameters are usually very pronounced (if for no other reason than long-term nonuniform cooling of the system). In this respect, we consider the first zone of the existence of the three-dimensional incommensurate modulation, in which effects associated with the instability of the sulfide sodalite minal and the "preparation" of the structure to disintegration manifest themselves. In this zone, a decrease in the fraction of sulfide clusters cannot be compensated for and the fraction of sulfate clusters does not increase as a result of the $S \longrightarrow SO_4$ simple transformation. Instead, as can be seen from the X-ray photoelectron data (Fig. 2b), clusters are ordered, which eventually (possibly, under somewhat different conditions, for example, at lower temperatures) leads to the formation of superstructures characteristic of triclinic and other lazurite modifications [23, 24]. It seems likely that the separation of Na (S sodalite) and Ca (haüyne) clusters proceeds via the mechanism similar to spinodal decomposition of a solid solution, in distinction to the above mechanism of sulfide–sulfate disordering with the participation of the gaseous phase. According to the forced equilibrium theory [25], we are dealing here with the state that is controlled by the balance between the chemical energy of composition fluctuations and the energy of cluster ordering. Fluctuation composition waves in developing immiscibility are obstructed by cluster ordering processes that involve not only S and SO_4 clusters with the same ratio of Na and Ca ions (whose distribution is fixed at a constant fugacity f_{SO_2}), but also sulfate clusters with different ratios of Na and Ca ions. A compromise structure should be consistent both with the corresponding modulation of the composition and distortion and also with cluster ordering. It should be emphasized that this equilibrium is attained only in the region very close to the stability boundary of the lazurite phase, above which (along the f_{SO_2} axis) lazurite decomposes into simple and complex oxides and sulfates. The above mecha-

nism can be illustrated by the simple balance formula

$$\Delta \mathbf{E}_{\text{strain}} + \Delta \mathbf{E}_{\text{chem}} = \Delta \mathbf{E}_{\text{ord}}^{\text{S–SO}_4} + \Delta \mathbf{E}_{\text{ord}}^{\text{Na–Ca}}, \qquad (6)$$

where the left-hand side contains the increments of the elastic strain energy and the chemical energy of structural components and the right-hand side includes the energy changes associated with the cluster ordering processes. The adaptability of the given equilibrium (although this equilibrium is assumed to be metastable) is explained by the fact that the terms on the left- and right-hand sides are interdependent and can be "adjusted" to each other in specific ranges. Therefore, such a state can be stable with respect to insignificant variations in the internal thermodynamic parameter.

The proposed model results in interesting geochemical consequences. It follows from this model that an almost constant fugacity f_{SO_2} at a given temperature of crystal formation in the vicinity of the stability boundary of the lazurite system should be a necessary condition for the stability of the three-dimensional incommensurate modulation. However, this leads to the inference that not the SO_2 activity determines the ratio of sulfur species in lazurite but, in contrast, the "internal fugacity" of sulfur dioxide (i.e., the existing distribution of sulfate and sulfide ions in the lazurite structure), maintains a constant partial pressure of sulfur dioxide in the gaseous phase. Such a situation is possible when the mass of the solid phase is considerably larger than that of the gaseous phase in a closed system. In this case, the chemical potential of the mobile SO_2 component cannot be treated as an independent variable that governs the equilibrium state of the system, i.e., as an equilibrium factor. However, we cannot completely rule out the possibility that a constant SO_2 fugacity is maintained by any buffer with a high capacity. Fluctuations that always arise in real systems would lead either to a scenario controlled by the aforementioned damped mechanism (with a decrease in the fugacity f_{SO_2}) or to complete decomposition of lazurite (with an increase in the fugacity f_{SO_2}), whose products were not retained because of their high solubility in a hydrothermal fluid.

CONCLUSIONS

Thus, it was demonstrated that, although a three-dimensional incommensurate modulation of cubic lazurite is easily released even upon short-term annealing at moderate temperatures, such a modulation frequently occurs in the structure of minerals in lazurite deposits of the Southern Baĭkal region and is retained for hundreds of millions of years of their rather complex geologic history. There are at least three mechanisms of release of the three-dimensional incommensurate modulation. The first two mechanisms are heterogeneous. The first mechanism involves rapid release of the modulation in the case of free access for air oxygen due to the reaction between polysulfide and sulfate ions with the formation of sulfite ions. The second mechanism suggests slower sulfide–sulfate disordering (also governed by the gaseous phase) when the system comes out of metastable forced equilibrium that allows for a structural adaptation to a variation in the SO_2 fugacity over a narrow range. The modulation release at relatively high activities of sulfur dioxide in the vicinity of the stability boundary of the lazurite structure, when the instability of the S sodalite minal of lazurite begins to manifest itself, is accompanied by the separation and ordering of Na and Ca sulfate clusters via the purely solid-phase mechanism similar to spinodal decomposition of solid solutions. The stability of the three-dimensional incommensurate modulation can be explained by the fact that the energy of fluctuation composition waves in developing immiscibility is compensated for by the energy of ordering of clusters, including not only S and SO_4 clusters with the same ratio of Na and Ca ions (whose distribution is fixed at a constant fugacity f_{SO_2}) but also sulfate clusters with different ratios of Na and Ca ions. Further experiments will be performed in order to refine the parameters with which the three-dimensional incommensurate modulation is completely retained and to solve conclusively the problem regarding the nature of its stability.

ACKNOWLEDGMENTS

We would like to thank Yu.V. Shchegol'kov for his assistance in performing the spectroscopic investigation of the lazurite crystals.

This work was supported by the Russian Foundation for Basic Research, project no. 03-05-65108.

REFERENCES

1. V. G. Ivanov and A. N. Sapozhnikov, *Lazurites of USSR* (Nauka, Novosibirsk, 1985) [in Russian].
2. V. L. Tauson, V. V. Akimov, A. N. Sapozhnikov, and K. E. Kuznetsov, Geokhimiya, No. 8, 803 (1998).
3. N. B. Bolotina, R. K. Rastsvetaeva, A. N. Sapozhnikov, *et al.*, Kristallografiya **48** (5), 779 (2003) [Crystallogr. Rep. **48** (5), 721 (2003)].
4. Luo Gu-Fend, Zhao Ming, Xiao-Yue, *et al.*, Gaoxiao Dizhi Xuebao **6**, 132 (2000).
5. I. Hassan and P. R. Buseck, Am. Mineral. **74** (3/4), 394 (1989).
6. N. B. Bolotina, R. K. Rastsvetaeva, A. N. Sapozhnikov, *et al.*, Kristallografiya **48** (1), 14 (2003) [Crystallogr. Rep. **48** (1), 8 (2003)].
7. R. K. Rastsvetaeva, N. B. Bolotina, A. N. Sapozhnikov, *et al.*, Kristallografiya **47** (3), 449 (2002) [Crystallogr. Rep. **47** (3), 404 (2002)].
8. V. G. Evsyunin, A. N. Sapozhnikov, A. A. Kashaev, and R. K. Rastsvetaeva, Kristallografiya **42** (6), 1014 (1997) [Crystallogr. Rep. **42** (6), 938 (1997)].
9. A. N. Sapozhnikov, A. Ya. Medvedev, V. G. Ivanov, *et al.*, Zap. Vseross. Mineral. O–va, No. 2, 82 (1994).

10. V. L. Tauson and V. V. Akimov, Geochim. Cosmochim. Acta **61** (23), 4935 (1997).
11. V. L. Tauson, A. N. Sapozhnikov, and K. E. Kuznetsov, in *Proceedings of the International Conference "Crystals: Growth, Properties, Real Structure, and Application," Aleksandrov, Russia, 1999* (VNIISIMS, Aleksandrov, 1999), Vol. 1, p. 278.
12. A. N. Sapozhnikov, V. L. Tauson, and L. N. Matveeva, Zap. Vseross. Mineral. O–va, No. 2, 121 (2001).
13. P. Toulmin III and P. B. Barton, Jr., Geochim. Cosmochim. Acta **28** (5), 641 (1964).
14. V. L. Tauson and A. N. Sapozhnikov, Zap. Vseross. Mineral. O–va, No. 5, 102 (2003).
15. Heyong He, T. L. Barr, and J. Klinowski, J. Phys. Chem. **98** (33), 8124 (1994).
16. Yu. Mikhlin, V. Varnek, I. Asanov, *et al*., Phys. Chem. Chem. Phys. **2**, 4393 (2000).
17. R. V. Siriwardene and J. M. Cook, J. Colloid Interface Sci. **104**, 250 (1985).
18. J. F. Moulder, W. F. Stickle, P. E. Sobol, and K. D. Bomben, *Handbook of X-ray Photoelectron Spectroscopy* (Perkin-Elmer Corporation, Minnesota, 1992).
19. C. D. Wagner, A. V. Naumkin, A. Kraut-Vass, *et al*., www.nist.gov/srd/online.htm.
20. J. Klinowski, S. W. Carr, P. Tarling, and P. Barnes, Nature (London) **330** (6143), 56 (1987).
21. L. Z. Reznitskiĭ, A. B. Kotov, E. B. Sal'nikova, *et al*., Petrologiya **8** (1), 74 (2000).
22. I. Hassan, Am. Mineral. **85**, 1383 (2000).
23. A. N. Sapozhnikov, Zap. Vseross. Mineral. O–va, No. 1, 110 (1990).
24. A. N. Sapozhnikov, V. G. Ivanov, *et al.*, Zap. Vseross. Mineral. O–va, No. 1, 108 (1993).
25. V. S. Urusov, V. L. Tauson, and V. V. Akimov, *Geochemistry of the Solid State* (GEOS, Moscow, 1997) [in Russian].

Translated by O. Borovik-Romanova

Crystallography Reports, Vol. 50, Suppl. 1, 2005, pp. S10–S15.

STRUCTURE OF INORGANIC COMPOUNDS

Structure of Lanthanum Prepared by Quenching from a Liquid State

A. B. Lysenko, O. L. Kravets, and A. A. Lysenko

Dneprodzerzhinsk State Technical University,
Dneprostroevskaya ul. 2, Dneprodzerzhinsk, 51918 Ukraine
e-mail: lysenkoab@bigmir.ru

Received February 3, 2005

Abstract—The structure of lanthanum quenched from a liquid state at cooling rates of 2.5×10^5–10^7 K/s is investigated. It is shown that a mixture of the face-centered cubic β-La phase stable above 583 K and the metastable lanthanum modification with a seven-layer hexagonal lattice consisting of alternating atomic layers *ABCABAC*… is formed in rapidly cooled foils. A mechanism is proposed for the formation of the metastable polytype, according to which the polytype is formed as a result of saturation of the main β-phase with well-ordered stacking faults. © *2005 Pleiades Publishing, Inc.*

INTRODUCTION

Lanthanum, like other light rare-earth elements (Ce, Pr, Nd, etc.), belongs to polymorphic metals [1–3]. Under near-equilibrium conditions, lanthanum crystallizes in the body-centered cubic γ-modification stable in a relatively narrow (59 K) temperature range (Table 1). At a temperature of 1134 K, the γ modification of the metal transforms into the β modification with a face-centered cubic (fcc) lattice. Upon cooling to 583 K, lanthanum undergoes one more polymorphic transformation (β ⟶ α). In this case, the face-centered cubic lattice transforms into a four-layer hexagonal lattice of the *A*3' type. In Table 1, this lattice is designated as the double hexagonal close-packed lattice. According to the data obtained by McHargue *et al.* [4], the last transformation occurs through a gradual change in the sequence of alternating close-packed layers (*ABC*… ⟶ *ABAC*…) and is characterized by a low rate, incompleteness, and a large temperature gradient.

Therefore, lanthanum has two close-packed modifications, namely, the face-centered cubic and double hexagonal close-packed modifications, which differ only in the packing sequence of atomic layers (Fig. 1). The face-centered cubic lattice consists of three closest packed layers *ABC*…, which are represented by the (111) atomic planes. The double hexagonal close-packed lattice is composed of four layers *ABAC*…. This lattice is formed by the (0001) basal planes of the hexagonal prism.

Similar structural varieties of crystalline compounds are referred to as polytypes. The specific atomic volume of each compound does not depend on the number of layers in a unit cell, and the free energies of the compounds only slightly differ from each other. This explains the coexistence of different polytypes and the low rate of polytypic transformations [5].

Reasoning from the concept of polytypism and the data available in the literature on the temperature ranges of stability of different allotropic varieties of lanthanum, it can be expected that, upon slow cooling to room temperature, the lanthanum structure should most likely represented by a mixture of β and α close-packed modifications. In the course of quenching from a liquid state, the formation of the primary structure and subsequent solid-phase transformations occur under conditions of the competitive formation of the polytypic modifications. This can lead to both quantitative and qualitative changes in the crystal structure of the metal. In order to verify the last assumption, we undertook an X-ray diffraction investigation into the structure of the lanthanum samples subjected to different treatments, including rapid quenching at cooling rates up to ~10^7 K/s.

Table 1. Structure and ranges of stability of the allotropic lanthanum modifications [3]

Modification	Lattice type	Stability range, K	Lattice parameter, nm	
			a	*c*
γ	Body-centered cubic (*A*2)	1134–1193	0.426	
β	Face-centered cubic (*A*1)	583–1134	0.5305	
α	Double hexagonal close-packed (*A*3')	<583	0.3722	1.2144

1063-7745/05/5001-S0010$26.00

SAMPLE PREPARATION AND EXPERIMENTAL TECHNIQUE

The experiments were performed with samples of two series (Table 2). Samples of the first series were cut in the form of plates ($15 \times 15 \times 3$ mm in size) from a massive ingot. These samples were annealed in an SShVÉ-12.5/25-43 vacuum electric furnace at temperatures both above and below the temperature of the $\beta \longrightarrow \alpha$ polymorphic transformation. After the high-temperature treatment, the samples were cooled either at a low rate of $\sim 3.3 \times 10^{-2}$ K/s or at a relatively high rate of ~0.7 K/s. In the latter case, after the isothermal treatment, the samples were rapidly transferred from the working zone to the cold part of the vacuum chamber.

Samples of the second series were prepared by quenching a small portion (~50–100 mg) of the liquid metal on the inner surface of a rapidly spinning (3000–8000 rpm) bronze drum. In order to prevent interaction between the melt and air, the quenching from the liquid state was carried out in a purified argon. By varying the pressure of a carrier gas (Ar) and the rate of rotation of the crystallizer drum, we prepared 20- to 100-μm-thick lanthanum foils and individual plates whose thickness did not exceed 10 μm.

The cooling rate v of the products obtained by rapid quenching was determined from their thickness l with the use of the relationships derived by numerically solving the problem of heat transfer between a thin layer of the liquid metal and a massive heat absorber with the subsequent fitting of the results of the numerical simulation to the known experimental values v [6]. These relationships are as follows:

$$\log v = 10.53 - 2.93 \log l \quad \text{at} \quad 20\ \mu\text{m} \le l \le 100\ \mu\text{m}, \quad (1)$$

$$\log v = 8.43 - 1.3 \log l \quad \text{at} \quad l < 20\ \mu\text{m}. \quad (2)$$

The cooling rates calculated from relationships (1) and (2) for the aforementioned thicknesses of the rapidly quenched samples vary from $\sim 5 \times 10^4$ to $\sim 10^7$ K/s.

The structure of the samples was investigated using X-ray diffraction. The X-ray diffraction patterns were recorded on a DRON-3 diffractometer (monochromated Cu_{K_α} radiation). The phase composition of the samples studied was determined by comparing the results of the X-ray diffraction analysis with the ASTM diffraction data file, as well as with the theoretically calculated sets of interplanar distances and relative intensities of the diffraction lines for the hypothetical equilibrium and metastable phases.

RESULTS AND DISCUSSION

Figure 2 shows the most informative portions of the X-ray diffraction patterns obtained for samples of both series. It can be seen from Fig. 2 that the lanthanum sample treated under conditions providing the highest degree of similarity to the equilibrium state (Table 2, regime *1*) contains the α modification stable at room temperature and a small amount of the β-La modification (Figs. 2a, 2b). An increase in the rate of heat treatment at the final stage (regime *2*) leads to an insignificant change (by 5–10%) in the quantitative ratio between the α and β phases due to the increase in the β phase. Therefore, during relatively slow cooling of the lanthanum sample from temperatures corresponding to the stability range of the β modification, the $\beta \longrightarrow \alpha$ transformation is not completed and the amount of the initial β phase increases with an increase in the cooling rate.

Table 2. Treatment conditions of the samples under investigation

Regime	Sample type	Rate of rapid quenching, K/s	Annealing conditions		
			T, K	τ, h	*v*, K/s
1	P		773	1.0	3.3×10^{-2}
2	P		773	1.0	0.7
3	F	10^7			
4	F	2×10^5			
5	F	10^7	673	1.0	1.2

Note: F is the foil prepared by quenching from the melt, and P is the plate cut out from the ingot.

Upon quenching from the liquid state at the highest rate (regime *3*), the structure of the lanthanum sample changes qualitatively. The X-ray diffraction patterns of the rapidly quenched foils (Fig. 2b) involve reflections of the high-temperature β modification and a number of diffraction lines that can be assigned to none of the

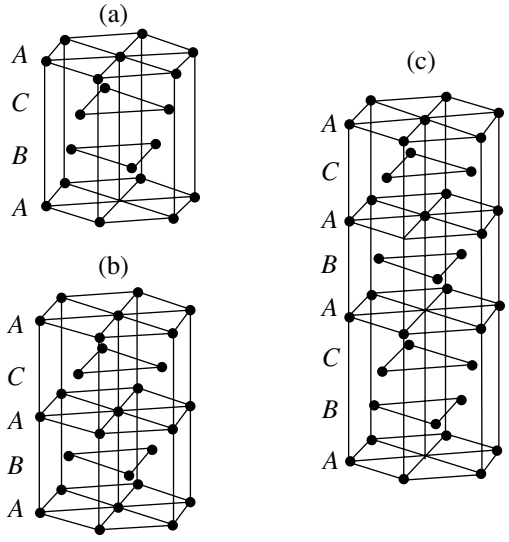

Fig. 1. Crystal lattices of the close-packed polymorphic modifications of lanthanum: (a) face-centered cubic β-La, (b) double hexagonal closed-packed α-La, and (c) the seven-layer lattice (7*R*) formed upon quenching from the liquid state.

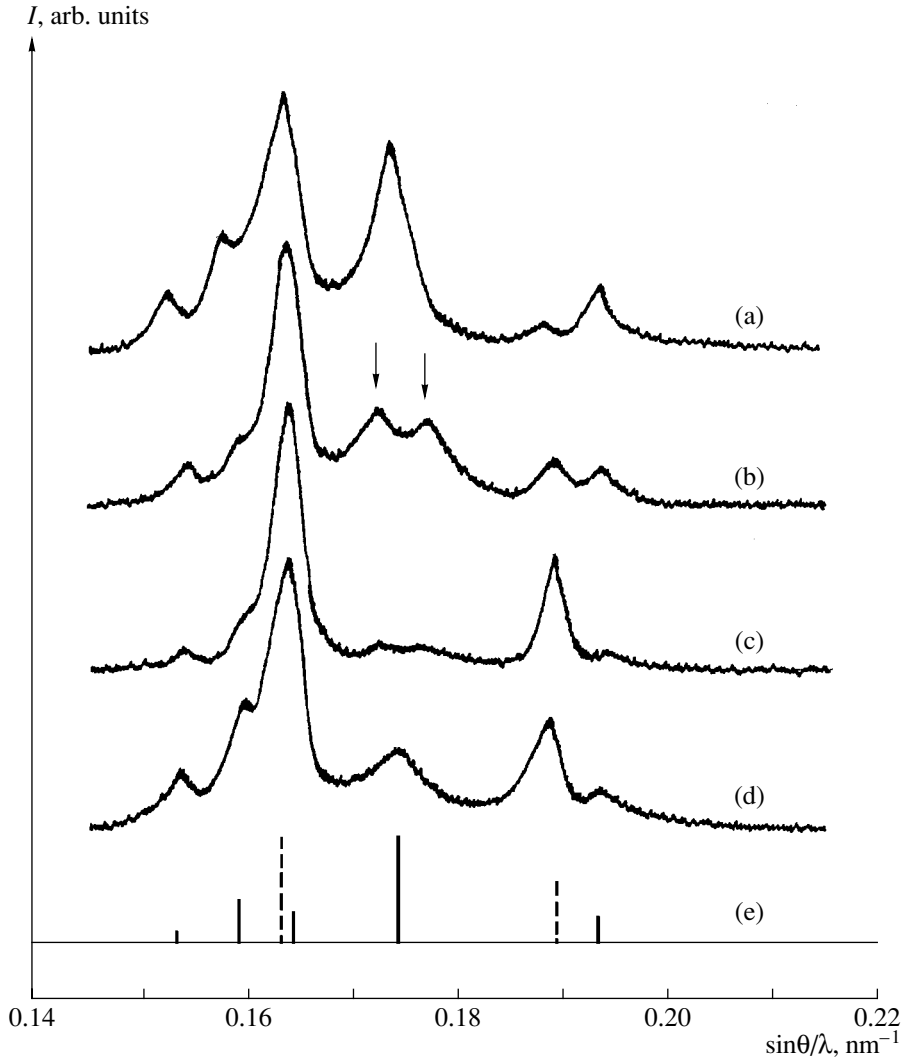

Fig. 2. (a–d) X-ray diffraction patterns of the lanthanum samples treated according to the regimes given in Table 2: (a) the bulk sample (regime *1*) and (b–d) rapidly quenched foils treated according to regimes (b) *3*, (c) *4*, and (d) *5*. (e) X-ray diffraction diagrams of the α-La (solid lines) and β-La (dashed lines) modifications.

equilibrium structural varieties of the metal. It is characteristic that the location and relative intensities of the majority of the unidentified lines correlate reasonably with those observed in the X-ray diffraction diagram of the α-La modification (Fig. 2e). However, this correlation is not complete. The fundamental difference between these diffraction patterns lies in the fact that, instead of the most intense (102) line of the α modification, the X-ray diffraction patterns of the rapidly quenched foils exhibit two lines of moderate intensity (in Fig. 2b, these lines are indicated by arrows). A decrease in the cooling rate to 2×10^5 K/s (regime *4*) brings about a considerable decrease in the intensity of the lines under consideration (Fig. 2c). The subsequent annealing of the rapidly quenched samples (regime *5*) results in the complete disappearance of these lines. As can be seen from Fig. 2d, the X-ray diffraction patterns of the annealed foils are similar to those observed for a mixture of the equilibrium close-packed modifications, with the face-centered cubic β-La phase being predominant.

The experimental data obtained allow us to make the inference that, upon quenching from the liquid state at cooling rates higher than ~10^5 K/s, the lanthanum structure contains the high-temperature β-modification and a metastable modification (hereafter, this modification will be designated as μ-La). The formation of the μ-La phase can be associated with the change in the sequence of the phase transformations occurring during rapid cooling of lanthanum. In this respect, we consider the possible mechanism of the formation and the specific features of the crystal structure of the μ-La phase.

As is known, quenching from a liquid state leads to strong supercoolings, which, for different metals, can reach several hundreds of degrees [7]. Taking into account this circumstance and the narrow temperature

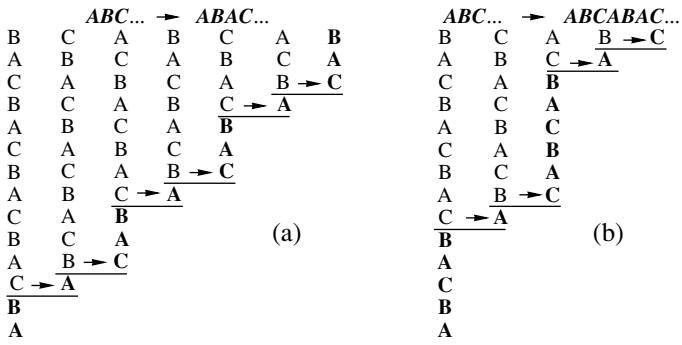

Fig. 3. Schematic diagrams illustrating the transformations of the face-centered cubic lattice into (a) a double hexagonal close-packed lattice of the α-La type and (b) a 7*R* seven-layer lattice typical of the metastable μ modification of lanthanum.

range of stability of the body-centered cubic γ-La phase (Table 1), it is reasonable to assume that crystals of the β modification with a face-centered cubic lattice nucleate first in the supercooled melt during rapid quenching of lanthanum. The nucleated β-La crystals grow at a high rate, which, in turn, encourages the appearance of stacking faults in their structure. The high probability of these processes during crystallization of light rare-earth metals can be judged from the lowest energies of stacking faults among those known for face-centered cubic metals [8].

The development of the crystallization is accompanied by an increase in the number of stacking faults in the main phase, followed by their partial or complete ordering, which results in a decrease in the free energy of the metal. When the number of stacking faults in the metal reaches a critical level and the degree of ordering becomes sufficiently high, the atomic packing changes qualitatively; i.e., there arises a new type of crystal lattice.

The proposed mechanism makes it possible to obtain different types of close-packed structures from the face-centered cubic lattice. As an example of similar transformations, Fig. 3a depicts the schematic diagram illustrating the transformation of a face-centered cubic lattice into a four-layer hexagonal lattice of the α-La type (*A*3'). The left column in Fig. 3a represents the initial sequence of closed-packed atomic layers *ABC*…, which is characteristic of the face-centered cubic structure. The horizontal segments show the positions of relative displacements of the adjacent planes. The arrows indicate the coordinates of the atoms in the displaced layer before and after the displacement. The final configuration of the close-packed layers is marked with bold type.

It can be seen from Fig. 3a that the relative displacements of the two adjacent atomic planes of the face-centered cubic lattice in the crystal lead to the formation of extrinsic stacking faults. In the case of an ordered arrangement of these faults with a period of three atomic layers, the packing sequence of atomic layers transforms into the sequence *ABAC*…, which is characteristic of the α-La lattice. By using a similar procedure, i.e., by introducing periodically arranged stacking faults into the face-centered cubic lattice, it is possible to construct different hypothetical metastable polytypes of the metal that are formed under nonequilibrium cooling conditions.

In order to solve this problem, we performed the computer simulation of the structures whose packings involve different numbers of closed-packed atomic layers alternating in different manners. We considered models in which the number of layers *N* was varied from five to twelve. These models were conventionally denoted as *NR*. When calculating the structure factor of the intensity, the coordinates of the basis atoms (expressed in terms of the hexagonal unit cell parameter) for layers *A*, *B*, and *C* were specified in the following form [9]:

$$\begin{aligned}&(0, 0, n_A/N),\\ &(1/3, 2/3, n_B/N),\\ &(2/3, 1/3, n_C/N),\end{aligned} \qquad (3)$$

where n_A, n_B, and n_C are the integer numbers (0, 1, 2, …, $N - 1$) corresponding to the numbers of close-packed layers *A*, *B*, and *C*.

The unit cell parameters (a^{NR}, c^{NR}) of the multilayer structures were determined under the assumption that, upon the transformation of the face-centered cubic lattice into an *N*-layer lattice *NR*, the atomic packing density and the shortest interatomic distances remain unchanged. In this case, the following relationships are satisfied: $d_{111}^{\text{fcc}} = d_{00N}^{NR}$ and $d_{220}^{\text{fcc}} = d_{110}^{NR}$. These relationships can be rewritten as

$$c^{NR} = Na^{\text{fcc}}/\sqrt{3}, \qquad (4)$$

$$a^{NR} = 2a^{\text{fcc}}/\sqrt{8}. \qquad (5)$$

It should be noted that the lattice spacing of the main face-centered cubic phase is affected by the impurities and excess vacancies frozen upon rapid quenching. For this reason, the unit cell parameters c^{NR} and a^{NR}, which

Table 3. Identification of the X-ray diffraction patterns of the lanthanum samples quenched from the liquid state at a rate of ~10^7 K/s

Experimental data			Identified phases					
			β-La (face-centered cubic), a = 0.5305 nm [3]			μ-La (7*R*), a = 0.3751 nm, c = 2.1441 nm		
sample	I	d_{HKL}, nm	$H\,K\,L$	I	d_{HKL}, nm	$H\,K\,L$	I	d_{HKL}, nm
1	16	0.3251				1 0 0		0.3248
2	25	0.3139				1 0 2		0.3109
3	100	0.3042	1 1 1	100	0.3063	0 0 7		0.3063
4	38	0.2914				1 0 3		0.2957
5	33	0.2814				1 0 4		0.2778
6	18	0.2644	2 0 0	56	0.2653			
7	13	0.2577				1 0 5		0.2589
8	6	0.1874	2 2 0	40	0.1876	1 1 0		0.1876
9	1	0.1697				1 0 11		0.1671
10	3	0.1633				2 0 0		0.1622
						2 0 1		
11	9	0.1606	3 1 1	43	0.1600	1 1 7		0.1599
12	4	0.1561				1 0 12		0.1560
						2 0 4		
13	11	0.1523	2 2 2	13	0.1531	2 0 5		0.1519

were calculated from relationships (4) and (5) with the use of the references values $a^{\beta\text{-La}}$, were corrected at the stage of analyzing the results of the simulation by the best fitting of the interplanar distances calculated for the hypothetical phases to the experimental set of parameters d_{HKL}.

The results of the simulation performed demonstrate that, among all the obtained structural models of the lanthanum quenched from the liquid state at a cooling rate of ~10^7 K/s, the most probable model corresponds to a mixture of the metastable μ-La modification and a residual amount of the main β-phase. In this case, the metastable μ-La modification has a seven-layer lattice with alternating close-packed layers *ABCABAC*… (Fig. 1c). The lattice spacings of these phases, as well as the experimental and calculated sets of interplanar distances and relative intensities I of the diffraction lines, are presented in Table 3. As can be seen, the X-ray diffraction data are in good agreement with the results obtained within the hypothetical structural model of rapidly quenched lanthanum foils.

In order to give a deeper insight into the interrelation between the structure and the mechanism of the formation of the metastable μ-La modification, we emphasize that the crystal lattice 7*R* can be easily constructed from the face-centered cubic lattice by saturating the latter lattice with extrinsic stacking faults that are regularly repeated at intervals of five atomic layers (Fig. 3b). It is also significant that the packing sequence *ABCABAC*… formed in the 7*R*-type structure involves three-layer (*ABC*) and four-layer (*ABAC*) related fragments, which are characteristic of the *A*1-type and *A*3'-type lattices. Consequently, the X-ray diffraction patterns of the rapidly quenched samples are similar in a number of traits to the diffraction patterns of the face-centered cubic and double hexagonal close-packed modifications; as well, they exhibit the aforementioned specific features that indicate a radically new structure of the metastable μ-La phase.

CONCLUSIONS

The metastable structural modification of lanthanum (μ-La) was prepared by quenching from a liquid state at cooling rates of higher than 10^5 K/s. This modification, together with the high-temperature face-centered cubic modification of lanthanum, is identified in rapidly cooled foils.

The crystal lattice of the μ-La modification is adequately described as a seven-layer hexagonal lattice (a = 0.3751 nm, c = 2.1441 nm) composed of closed-packed layers with the packing sequence *ABCABAC*….

Most likely, the metastable modification is formed as a result of the accumulation of stacking faults and their ordered arrangement in the lattice of β-lanthanum, which crystallizes during rapid cooling of the melt.

REFERENCES

1. K. A. Gschneidner, *Rare-Earth Alloys* (Van Nostrand, Princeton, 1961; Mir, Moscow, 1965).
2. Carl J. Altstetter, Metall. Trans. **4**, 2723 (1973).
3. E. M. Savitskiĭ and V. F. Terekhova, *Physical Metallurgy of Rare-Earth Metals* (Nauka, Moscow, 1975) [in Russian].
4. C. J. McHargue, H. L. Yakel, Jr., and L. K. Jetter, Acta Crystallogr. **10**, 832 (1957).
5. L. I. Lysak and B. I. Nikolin, *Physical Principles of Thermal Treatment of Steels* (Tekhnika, Kiev, 1975) [in Russian].
6. A. B. Lysenko, G. V. Borisova, and O. L. Kravets, Fiz. Tekh. Vys. Davlenii (Donetsk) **14** (1), 44 (2004).
7. I. S. Miroshnichenko, *Quenching from a Liquid State* (Metallurgiya, Moscow, 1982) [in Russian].
8. I. I. Novikov, *Defects in the Crystal Structure of Metals* (Metallurgiya, Moscow, 1975) [in Russian].
9. L. I. Lysak, B. I. Nikolin, and A. I. Ustinov, Fiz. Met. Metalloved. **42** (3), 601 (1976).

Translated by O. Borovik-Romanova

Crystallography Reports, Vol. 50, Suppl. 1, 2005, pp. S100–S105.

CRYSTAL GROWTH

Comparative Analysis of the Heat Transfer Processes during Growth of $Bi_{12}GeO_{20}$ and $Bi_4Ge_3O_{12}$ Crystals by the Low-Thermal-Gradient Czochralski Technique

O. N. Budenkova*, M. G. Vasiliev*, V. N. Shlegel, N. V. Ivannikova**, R. I. Bragin**, and V. V. Kalaev*****

** Ioffe Physicotechnical Institute, Russian Academy of Sciences, Politekhnicheskaya ul. 26, St. Petersburg, 194021 Russia*

e-mail: olganb@mail.ioffe.ru

*** Institute of Inorganic Chemistry, Siberian Division, Russian Academy of Sciences, pr. Akademika Lavrent'eva 3, Novosibirsk, 630090 Russia*

**** OOO Soft Impact, St. Petersburg, 194156 Russia*

Received February 7, 2005

Abstract—The heat transfer processes occurring in the solid and liquid phases during growth of $Bi_{12}GeO_{20}$ and $Bi_4Ge_3O_{12}$ crystals by the low-thermal gradient Czochralski method are analyzed and compared. It is experimentally found that, under similar growth conditions, the deflection of the crystallization front for the $Bi_{12}GeO_{20}$ crystal is considerably smaller than the deflection of the crystallization front for the $Bi_4Ge_3O_{12}$ crystal and the faceting of the former front is observed at the earlier stage of pulling. The results of the numerical simulation demonstrate that the different behavior of the crystallization fronts is associated with the difference between the coefficients of thermal absorption in the crystals. *© 2005 Pleiades Publishing, Inc.*

INTRODUCTION

In the Bi_2O_3–SiO_2 and Bi_2O_3–GeO_2 systems, two isostructural compounds, namely, $Bi_{12}GeO_{20}$ and $Bi_{12}SiO_{20}$, crystallize in a sillenite-type structure, and two isostructural compounds, namely, $Bi_4Ge_3O_{12}$ and $Bi_4Si_3O_{12}$, have an eulytine-type structure. Single crystals of these compounds are grown by the Czochralski method and exhibit a strong tendency to faceting. As a rule, the faceting is considered a factor that hinders the growth of high-quality crystals. The formation of facets at the crystallization front has been explained by the deviation from the optimum growth conditions, because additional stresses and a nonuniform distribution of impurities arise in the vicinity of faceted regions [1]. Therefore, it is common practice to suppress the formation of facets by appropriately choosing the growth conditions with large temperature gradients. However, the deterioration of the crystal quality is caused not by the facets themselves but by the processes of crystal growth occurring through different mechanisms on faceted and rough (rounded) regions of the crystallization front. By contrast, the use of small temperature gradients in the Czochralski method leads to the rapid formation of facets already at early stages of crystal pulling, after which the crystal growth occurs only through the layer (facet) mechanism over the entire front of crystallization and it becomes possible to prepare large-sized crystals of very high quality [2].

However, it turns out that, when growing $Bi_{12}GeO_{20}$ and $Bi_4Ge_3O_{12}$ crystals by the low-gradient Czochralski method under similar conditions (i.e., in the same apparatus, under similar temperature conditions, and in identical pulling directions), the behavior of their interfaces after the shouldering stage differs significantly. The facets of the former crystal are formed almost immediately after the required (stationary) diameter is reached, whereas the crystallization front for germanoeulytine appears to be deeply convex toward the melt and becomes fully faceted only in the course of crystal pulling. Without recourse to numerical analysis of this process, it is difficult to determine the factor primarily responsible for the formation of the crystallization front in the crystals under consideration. On the one hand, the thermal parameters of the melts differ significantly (see table). Under similar growth conditions, the Grashof and Reynolds numbers for the $Bi_{12}GeO_{20}$ melt are larger than those for the $Bi_4Ge_3O_{12}$ melt by a factor of approximately 11 and 3, respectively. Hence, we can assume that different convection regimes should be responsible for the different shapes of the crystallization fronts of these crystals [3–5]. On the other hand, both crystals are characterized by the semitransparent bands in the IR spectral range. This implies that heat transfer from the interface through the crystal is provided by heat conduction and radiation, which, in turn, also substantially affects the shape of the crystallization front in the course of crystal pulling [6]. It should be noted that, in [3, 4], the growth of sillenite crystals was

1063-7745/05/5001-S0100$26.00 © 2005 Pleiades Publishing, Inc.

studied without regard for the effect of heat transfer through the crystal on the shape of the crystallization front. Rojo *et al.* [5] assumed that heat transfer in crystals occurs only through thermal conduction. In our earlier work [7], we numerically investigated the effect of heat transfer on the shape of the crystallization front for $Bi_4Ge_3O_{12}$ crystals with a diameter of 7.7 cm. It was demonstrated that, for a diffusely reflective surface of the crystal, the inclusion of radiative heat transfer leads to a moderate deflection of the crystallization front toward the melt and this defection remains virtually unchanged with an increase in the crystal length. Such a situation contradicts the available experimental data. However, when it was assumed that the shouldering cone surface is specularly reflective (Fresnel) and the cylindrical crystal surface is diffuse, the results of calculations were in good agreement with the experimental results. In this case, the crystallization front at small crystal lengths is deflected by more than one radius and the deflection decreases with an increase in the crystal length. Similar results were obtained in simulating the growth of $Bi_{12}GeO_{20}$ crystals with a diameter of 2.8 cm, for which the deflection of the crystallization front toward the melt also turned out to be comparable to the crystal diameter [8]. However, the absorption coefficient of the germanosillenite crystal in the most transparent spectral band is one order of magnitude larger than that of the germanoeulytine crystal (see table). Therefore, at identical sizes of growing crystals, the effect exerted by radiative heat transfer through the solid phase on the interface shape during growth of the $Bi_4Ge_3O_{12}$ crystal should be considerably stronger than that during growth of the $Bi_{12}GeO_{20}$ crystal. It should be noted that the influence of the absorption coefficient of the crystal and the melt on the shape of the crystallization front (all other factors being the same) was considered by Kobayashi *et al.* [9] in the case of growth of $LiNbO_3$ crystals under the assumption that the crystal surface is diffusely reflective and that the temperature conditions correspond to the Czochralski method with large temperature gradients.

In this work, we carried out a comparative analysis of the global heat transfer during growth of crystals of the $Bi_4Ge_3O_{12}$ germanoeulytine and the $Bi_{12}GeO_{20}$ germanosillenite for specular (Fresnel) reflection of radiation from the crystal surface. The results of the numerical simulation were compared with the experimental data.

EXPERIMENTAL TECHNIQUE

The schematic diagram of the apparatus is depicted in Fig. 1. The platinum crucible was immovable, and the crystal was rotated at the rate $\Omega = 15$ rpm. The stationary diameters of the grown crystals were identical and equal to 50 mm. The diameter of the crucible was 70 mm. The pulling rate was 3.5 mm/h. The crystals were pulled along the [111] direction. During growth of the $Bi_4Ge_3O_{12}$ crystals, only the {112} facets were observed at the crystallization front. For the $Bi_{12}GeO_{20}$ crystals, the crystallization front was formed by facets of three types, namely, the {112}, {001}, and {110} facets, depending on the growth conditions. In order to compare the magnitude and shape of the front deflection, we used the $Bi_4Ge_3O_{12}$ and $Bi_{12}GeO_{20}$ crystals in which the central {112} facets occupy the larger part of the crystallization front. Figure 2 displays the micrographs of the $Bi_4Ge_3O_{12}$ (Fig. 2a) and $Bi_{12}GeO_{20}$ (Fig. 2b) crystals with typical shapes of the crystallization fronts.

Thermal and physical properties of the $Bi_4Ge_3O_{12}$ and $Bi_{12}GeO_{20}$ crystals

Parameter	$Bi_4Ge_3O_{12}$	$Bi_{12}GeO_{20}$
Melt		
Melting temperature T_m, K	1323	1203
Density, kg/m^3	6710	8130
Dynamic viscosity	0.044	0.017
Bulk thermal expansion coefficient, 10^{-4} 1/K	0.76	1.2
Thermal conductivity, W/(m K)	0.7832	0.345
Heat capacity, J/(kg K)	356.0	390.0
Thermal diffusivity, m^2/s	2.99×10^{-7}	1.19×10^{-7}
Prandtl number	21.9	17.54
Reynolds number	149	469
Grashof number	7425	84564
Crystal		
Refractive index	2.15	2.35
Absorption coefficient for the most transparent band of the crystal, 1/m	3.0	45.5
Thermal conductivity, W/(m K)	1.2	0.18

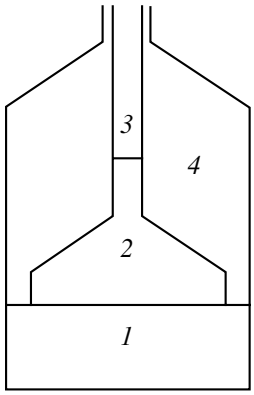

Fig. 1. Schematic diagram of the growth apparatus: (*1*) melt, (*2*) crystal, (*3*) seed holder, and (*4*) gas gap between the crystal and the crucible.

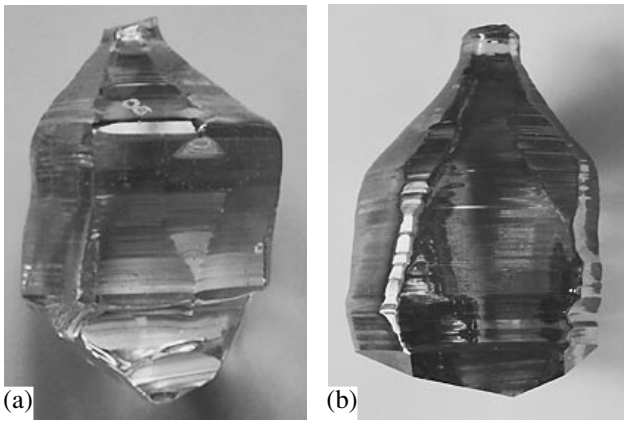

Fig. 2. Typical shapes of the crystallization fronts for (a) $Bi_4Ge_3O_{12}$ and (b) $Bi_{12}GeO_{20}$ crystals.

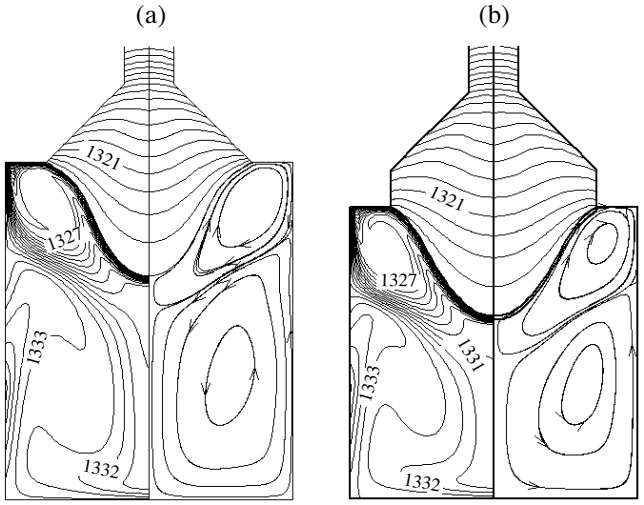

Fig. 3. (a) Temperature fields in the melt and the crystal (at the left) and (b) flow patterns of the melt and the crystal (at the right) for the interface shape calculated for $Bi_4Ge_3O_{12}$ crystals with a specularly reflective surface. The temperatures are given in degrees Kelvin. The isotherms are drawn at 0.5-K intervals.

NUMERICAL SIMULATION

The problem of global heat transfer with the numerical simulation of the shape of the crystallization front was solved in the framework of the quasi-stationary approach described in our previous studies [7, 8]. Within this approach, it was assumed that the crucible contains a crystal whose size above the melt, like the height of the melt, is fixed; i.e., the velocity of movement of the crystal with respect to the crucible can be ignored. At the beginning of each simulation stage, the shape of the crystallization front $h(r)$, as a rule, was assumed to be flat or identical to that obtained in the preceding simulation stage. For a fixed shape of the crystallization front, the simulation consisted in simultaneously solving two stationary problems: the problem of convection and heat transfer in the melt (region *1* in Fig. 1) and the problem associated with the conductive and radiative heat transfer in the crystal and in the gap between the crystal and the crucible (regions *2*, *3*, *4* in Fig. 1). Solving the above problems involved the exchange of the data. As a result of this exchange, we determined the condition under which the conductive heat flux from the liquid phase and the net radiative flux in the region above this phase are equal to each other on the free surface of the melt. The boundary conditions for both problems were specified in the form of the stationary temperature distribution $T_{ext}(z)$ on the inside of the crucible. This distribution was determined by measuring the temperature with thermocouples at several points with the subsequent interpolation of the data obtained to the ranges between these points. In the course of calculations, the temperature distribution $T_{ext}(z)$ was corrected for the temperature $\Delta T(z)$ in order to obtain the necessary pulling rate. The temperature at the crystallization front was assumed to be equal to the melting temperature T_m and remained constant during the simulation. The convective problem was solved with the CGSim program package [10] in the two-dimensional axisymmetric approximation. The radiative heat transfer in the media characterized by different refractive indices and separated by transparent boundaries was calculated with the program which we developed on the basis of the algorithm described by Mamedov and Rucolaine [11]. By solving the two stationary problems, we determined the following fluxes at the crystal–melt interface: the conductive fluxes from the melt $q_L^{cond}(r, h)$, the conductive flux from the crystal $q_S^{cond}(r, h)$, and the net radiative flux from the crystal $q_S^{rad}(r, h)$. With knowledge of all the fluxes involved, it is possible to calculate the rate of crystal growth $V_{GR}^i(r)$ at each point of the crystallization front in the axial direction from the expression

$$V_{GR}^i(r) = [-q_L^{cond,\,i}(r, h) + q_S^{rad,\,i}(r, h) + q_S^{cond,\,i}(r, h)]/Q(\mathbf{n}(r, h)\mathbf{e}_z). \quad (1)$$

Here, Q is the heat of melting, $\mathbf{n}(r, h)$ is the normal to the crystallization front in the direction of the crystal bulk, and $\mathbf{e}_z$ is the unit vector directed along the z axis inward the crystal. The shape of the crystallization front was corrected so that the triple point remained fixed; that is,

$$h^{i+1}(r) = h^i(r) + \tau(V_{GR}^i(r) - V_{GR}^i(R)).$$

Here, τ is the iteration parameter with the dimension of time. In the case when the crystal growth rate calculated from relationship (1) became identical over the entire interface, the calculations were terminated and the shape of the crystallization front was considered to be determined. Otherwise, all the aforementioned stages of the calculation were repeated for a new position of

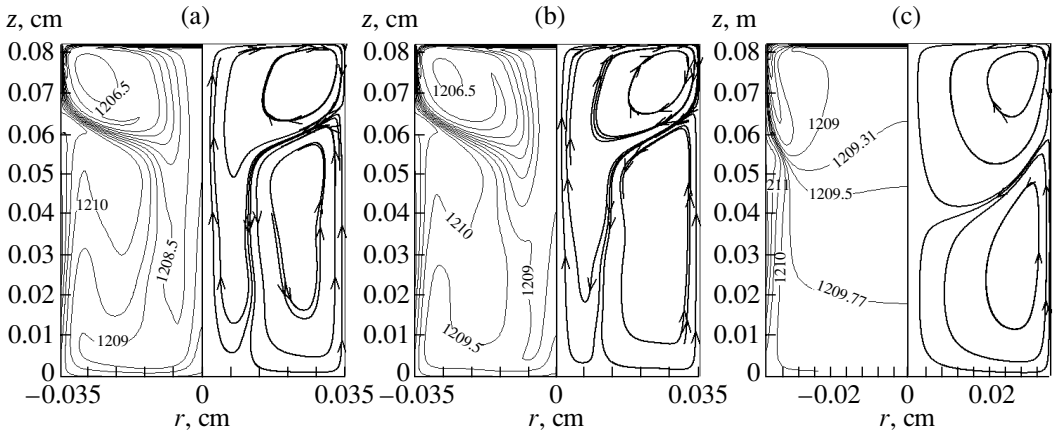

Fig. 4. Temperature fields (at the left) and flow patterns (at the right) of the $Bi_{12}GeO_{20}$ melt according to the calculations for different convection regimes: (a, b) instantaneous diagrams calculated for the nonstationary oscillatory regime under the assumption of the laminar flow and (c) diagrams calculated with due regard for the turbulent flow. The temperatures are given in degrees Kelvin.

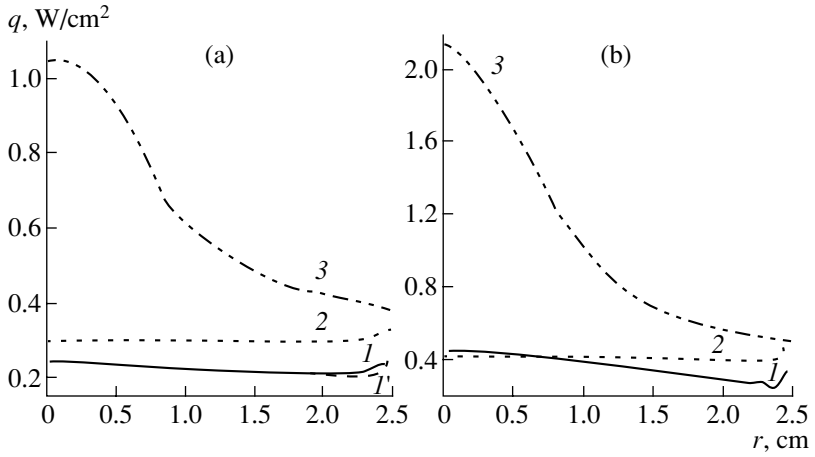

Fig. 5. Distributions of heat fluxes arrived at the crystallization front from the melt in different regimes of heat convection and the total heat fluxes removed through (a) the germanosillenite crystal and (b) the germanoeulytine crystal: (*1*, *1*') the oscillatory regime under the assumption of the laminar flow for the two instantaneous diagrams shown in Figs. 4a and 4b, respectively; (*2*) the regime including the turbulent flow in the melt; and (*3*) the total heat flux removed through the crystal.

the crystallization front. In the numerical simulation, the presence of facets at the crystallization front was disregarded.

RESULTS OF NUMERICAL SIMULATION

The thermal parameters of the studied compounds in the solid and liquid phases are listed in the table. The results of the simulation for the germanoeulytine crystals with a specularly reflective surface are presented in Fig. 3 (hereafter, the numbers in the figures will indicate the temperature T in degrees Kelvin). It should be noted that, as in [7], the deflection of the crystallization front is approximately equal to the crystal radius. The flow pattern in the melt is also similar to that observed in [7]. The forced convection due to the rotation of the crystal is dominant in the region located immediately under the crystal. Below, there exists a vortex of free convection associated with the nonuniform temperature distribution in the melt. In order to ensure the required pooling rate (3.5 mm/h), the experimental temperatures were increased by a temperature ΔT identical along the entire wall of the crucible. For the convective problem to be solved in the two-dimensional axisymmetric approximation, the stationary solution can be obtained over a rather wide range of correcting temperatures ΔT.

However, the situation changes for the germanosillenite melt. As was noted above, the forced and free convection rates in the liquid phase of the $Bi_{12}GeO_{20}$ compound appear to be higher several times. The flow pattern in the melt changes from the pattern predominantly determined by the forced convection to the pattern corresponding to a nonstationary oscillatory regime (Figs. 4a, 4b) when the temperature assigned to the crucible wall increases by only 1.5 K. The nonsta-

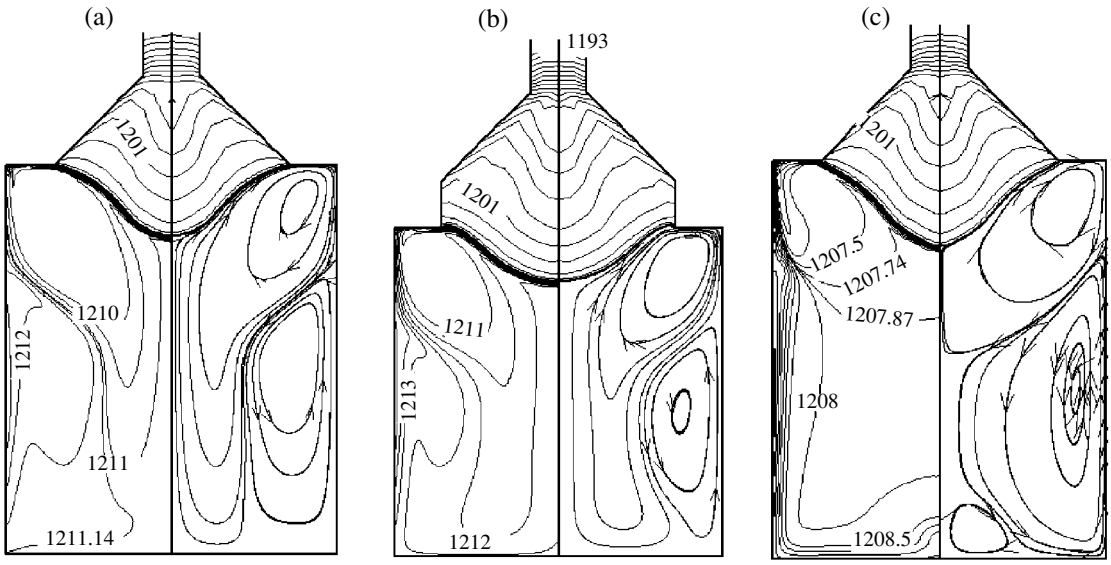

Fig. 6. Temperature fields in the melt and the crystal (at the left) and flow patterns of the melt and the crystal (at the right) with the crystallization front shape calculated for the $Bi_{12}GeO_{20}$ crystal in different regimes of convection in the melt: (a, b) laminar flow and (c) weak turbulent flow. The temperatures are given in degrees Kelvin.

tionary regime manifests itself in a small mutual change in the intensities of the two vertices shown at the right of Figs. 4a and 4b. The corresponding changes in the temperature distributions in the melts are illustrated at the left of these figures.

If the calculations in the latter case are performed under the assumption of the turbulent regime in the melt, we obtain the stationary solution (Fig. 4c). However, it should be noted that this change in the flow regimes affects only slightly the distribution of heat fluxes arrived at the flat crystallization front from the melt (Fig. 5a). For comparison, Fig. 5b shows the distributions of heat fluxes over the flat crystallization front according to the analogous calculations for the $Bi_4Ge_3O_{12}$ crystal. The fluxes that arrive at the interface from the liquid phase are approximately equal for both compounds, whereas the quantity of the heat removed through the germanoeulytine crystal considerably exceeds the quantity of the heat removed by radiation through the germanosillenite crystal.

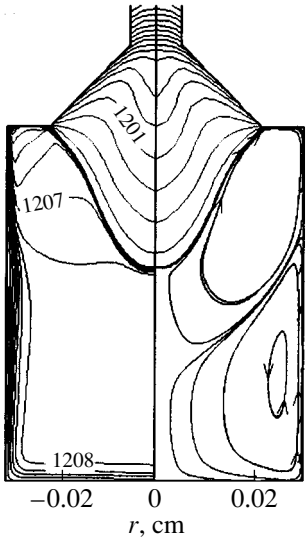

Fig. 7. Temperature fields in the melt and the crystal (at the left) and flow patterns of the melt and the crystal (at the right) with the crystallization front shape calculated for the $Bi_{12}GeO_{20}$ crystal at the absorption coefficient equal to that of the $Bi_4Ge_3O_{12}$ crystal. The temperatures are given in degrees Kelvin.

The interface shape for the $Bi_{12}GeO_{20}$ crystal was calculated for several flow regimes in the melt. In all cases, the deflection of the crystallization front for the $Bi_{12}GeO_{20}$ crystal appears to be smaller than that for the $Bi_4Ge_3O_{12}$ crystal by approximately 1 cm (Fig. 6). In order to prove explicitly that the lower transparency of the germanosillenite crystal leads to a smaller deflection of the crystallization front, the front shape for this crystal was calculated using the same thermal parameters of the $Bi_{12}GeO_{20}$ crystal, except for the absorption coefficient, which was taken equal to the absorption coefficient of the $Bi_4Ge_3O_{12}$ crystal. It turned out that, in this case, the deflection of the crystallization front for the germanosillenite crystal even exceeds the deflection of the crystallization front for the germanoeulytine crystal by approximately 1.5 cm. The results of these calculations are presented in Fig. 7.

CONCLUSIONS

Thus, the results obtained in this study have demonstrated that the decisive factor responsible for the dif-

ferent deflections of the crystallization fronts during growth of germanoeulytine and germanosillenite crystals is the difference between the absorption coefficients of these crystals. For the $Bi_{12}GeO_{20}$ crystal with a lower transparency, the rate of radiative heat transfer is considerably lower and, therefore, the deflection of the crystallization front is substantially smaller. In turn, the smaller deflection of the crystallization front leads to a smaller bend of the isotherms in the vicinity of the interface, thus providing more favorable conditions of the facet formation at the interface.

REFERENCES

1. B. Cockayne, J. Cryst. Growth **3**, 60 (1968).
2. V. N. Shlegel, Yu. V. Shubin, and N. V. Ivannikova, J. Korean Cryst. Growth Cryst. Technol. **13** (1), 1 (2003).
3. M. T. Santos, J. C. Rojo, A. Cintas, *et al*., J. Cryst. Growth **156**, 413 (1995).
4. J. P. Fontaine, G. P. Extrémet, V. Chevrier, and J. C. Launay, J. Cryst. Growth **139**, 67 (1994).
5. J. C. Rojo, C. Marín, J. J. Derby, and E. Diéguez, J. Cryst. Growth **183**, 604 (1998).
6. Qiang Xiao and J. J. Derby, J. Cryst. Growth **128**, 188 (1993).
7. V. S. Yuferev, O. N. Budenkova, M. G. Vasiliev, *et al*., J. Cryst. Growth **253**, 383 (2003).
8. O. N. Budenkova, M. G. Vasiliev, V. S. Yuferev, *et al*., J. Cryst. Growth **266**, 92 (2004).
9. M. Kobayashi, T. Hagino, T. Tsukada, and M. Hozawa, J. Cryst. Growth **235**, 258 (2002).
10. V. V. Kalaev, I. Yu. Evstratov, and Yu. N. Makarov, J. Cryst. Growth **249** (1–2), 87 (2003).
11. M. V. Mamedov and S. A. Rukolaine, in *Proceedings of the 5th International Symposium on Radiation Transfer, Istanbul, Turkey, 2004* (Istanbul, 2004), p. 69.

Translated by O. Borovik-Romanova

Crystallography Reports, Vol. 50, Suppl. 1, 2005, pp. S106–S110.

CRYSTAL GROWTH

Crystallization of $Ba_3Fe_2Ge_4O_{14}$ and $Ba_2Fe_2GeO_7$ in Oxide–Fluoride Fluxes

I. A. Gudim, L. N. Bezmaternykh, and A. F. Bovina

Kirensky Institute of Physics, Siberian Division, Russian Academy of Sciences, Akademgorodok, Krasnoyarsk, 660036 Russia

e-mail: bezm@iph.krasn.ru

Received February 3, 2005

Abstract—Crystallization of trigonal $Ba_3Fe_2Ge_4O_{14}$ and tetragonal $Ba_2Fe_2GeO_7$ barium ferrogermanates is investigated in their own fluxes diluted by B_2O_3–BaF_2 and B_2O_3–PbF_2 mixtures, respectively. The ratios of the components at which the properties of the fluxes satisfy the requirements for controlled crystallization of these incongruently melting compounds are determined. Single crystals of $Ba_2Fe_2GeO_7$ barium ferrogermanate are grown for the first time. © *2005 Pleiades Publishing, Inc.*

INTRODUCTION

In the langasite family, lead gallogermanate $Pb_3Ga_2Ge_4O_{14}$ and barium gallogermanate $Ba_3Ga_2Ge_4O_{14}$ (**I**) are distinguished by the greatest sizes of the large cations [1]. Single crystals of the former compound with sizes suitable for complex investigations into the physical properties were synthesized by the flux method in our previous work [2].

Optical spectroscopic investigations [3] allowed us to make the inference that single crystals $Pb_3Ga_2Ge_4O_{14}$: Nd^{3+} (Si^{4+}) with a disordered structure are very promising for use as active materials in lasers with selective diode pumping. However, contrary to the extrapolation estimates, the piezoelectric activity of $Pb_3Ga_2Ge_4O_{14}$ appeared to be considerably less than that of the compound $Sr_3Ga_2Ge_4O_{14}$ with a smaller radius of the large cation. There arises an important question as to which role is played by the electronic configuration of the large cation in the origin of this deviation. The answer requires additional experimental investigations into the elastic and piezoelectric characteristics of barium gallogermanates and barium ferrogermanates, namely, trigonal $Ba_3Ga_2Ge_4O_{14}$ and tetragonal $Ba_2Ga_2GeO_7$ and $Ba_2Fe_2GeO_7$ (**II**).

Investigation into the properties of barium gallogermanate single crystals as laser matrices with a disordered structure is an important problem. The considerable interest expressed by researchers in the synthesis of barium ferrogermanate single crystals is associated with the problems of low-temperature magnetism.

Belokoneva *et al.* [4] and Lyubutin *et al.* [5] were the first to synthesize compounds **I** and **II** by the solid-phase method. The prepared polycrystalline samples were studied using X-ray diffraction. Compound **II** was additionally investigated by Mössbauer spectroscopy. Structural investigations of single crystals were carried out only for compound **I**. However, the problem concerning the growth of large high-quality single crystals of these compounds suitable for complex studies of their physical properties remains unsolved. In order to solve this problem, in the present work, we investigated crystallization in two families of fluxes:

$$BaO + pFe_2O_3 + qGeO_2 + rB_2O_3 + sBaF_2, \quad (1)$$

$$BaO + pFe_2O_3 + qGeO_2 + rB_2O_3 + sPbF_2. \quad (2)$$

PHASE-PROBING TECHNIQUE

At the first stage of phase probing of solution–melt families (1) and (2), it was necessary to reveal the fluxes in which trigonal compound **I** and tetragonal compound **II** are high-temperature phases crystallizing over a sufficiently wide range of temperatures. The upper limit of this range, reasoning from the necessity of ensuring the stability of the solution–melt composition in the course of long-term operations with an open crucible in air, was chosen as 950–960°C for the first family of fluoride-containing fluxes and 920–930°C for the second family. At the homogenization stages, these ranges were limited by temperatures of 980–1000 and 970–980°C, respectively. At higher operating temperatures, an uncontrollable change in the solution–melt composition becomes considerable due to the selective evaporation of barium and lead fluorides.

Then, crystallization characteristics, such as the concentration dependence of the saturation temperature and the metastability range, and the thermal and hydrodynamic conditions providing the stable growth of single crystals were determined for the chosen fluxes.

In family (1), we sought fluxes in which trigonal compound **I** is characterized by two sequences of crystallizing phases in one of the fluxes with the stoichiometric ratio of oxides of this compound (p = 1/3, q = 4/3). This satisfies the aforementioned limitations on

1063-7745/05/5001-S0106$26.00

the saturation temperature. A similar procedure was performed for tetragonal compound **II** in family (2).

A flux (weight, 30–40 g) was prepared in a platinum cylindrical crucible (D = 15 mm, H = 50 mm) by sequential melting of reactants B_2O_3 (special-purity grade), BaO (analytical grade), Fe_2O_3 (special-purity grade), GeO_2 (reagent grade), BaF_2 (special-purity grade), and PbF_2 (special-purity grade). We used a furnace with silicon carbide heaters and easy access to the operating chamber. The first three oxides were melted at a temperature of 1200°C. After melting the calculated amount of B_2O_3, the crucible was weighed and the losses of B_2O_3 (approximately 10% of the calculated amount) were replenished. The losses were predominantly associated with moisture removal. Oxide BaO was introduced into the melt in small portions, and the weight of the crucible with the melt was again checked after melting the calculated amount. The weight losses (up to 10–15%) were compensated for by adding BaO. The losses upon melting of this reactant were due to the decomposition of barium carbonate, barium peroxide, and barium hydrate impurities contained in this oxide. As a result, the total content of B_2O_3 and BaO oxides and their ratio in the flux were obtained with the necessary accuracy. After melting the calculated amount of Fe_2O_3 oxide, the temperature was decreased to the limiting homogenization temperatures and the GeO_2 and BaF_2 (PbF_2) compounds were added to the melt. The weight of the flux thus prepared differed from the calculated weight by no more than 2–3%.

After homogenization, the temperature was decreased to the predicted saturation temperature. A platinum wire probe was introduced into the flux, and, within 2 h after the introduction, crystallization on this probe was examined under a microscope. This direct probing was continued at a step of 15–20 K to temperatures close to the solidification point of the flux. The crystals formed on the probe were subsequently used for refining the saturation temperature and the equilibrium temperature boundaries of crystallizing phases.

For X-ray powder diffraction analysis, the necessary amount of crystals of the high-temperature phase was grown on the probe. The identified phase composition was compared with the composition of compound **I** under investigation. Then, portions of "deficient" oxides were added to the flux, and the high-temperature phase was again identified. Once the high-temperature phase corresponded to trigonal compound **I**, the composition was varied so that a combination of properties of the flux satisfied the requirements for controlled crystallization.

FLUX COMPOSITIONS AND CRYSTALLIZATION PARAMETERS

Trigonal compound **I** is not a high-temperature phase in fluxes proper, i.e., fluxes that do no contain oxides in addition to crystal-forming oxides (r = 0, s = 0) when they have a ratio close to the stoichiometric ratio ($p \sim 1/3$, $q \sim 4/3$). However, compound **I** becomes the high-temperature phase in fluxes proper that have a high superstoichiometric content of BaO oxide ($p < 1/3$, $q < 4/3$) and are strongly diluted with B_2O_3 oxide ($r \neq 0$, $s = 0$). Table 1 (row *1*) presents an example of the corresponding composition in the group of fluxes (at n = 60):

$$(100 - n)_{wt\,\%}(BaO + 0.62Ba_2O_3) + n_{wt\,\%}Ba_3Fe_2Ge_4O_{14}.$$

The saturation temperature of this flux is T_{sat} = 1000°C, and the trigonal phase crystallizes at least within the temperature range ΔT_{cryst} = 100 K. The measured lattice parameters of the trigonal phase are as follows: a = 8.441 Å and c = 5.352 Å. The faceted form of spontaneously nucleated crystals is represented by

Table 1. Barium ferrogermanate $Ba_3Fe_2Ge_4O_{14}$ in the BaO + pFe_2O_3 + $qGeO_2$ + rB_2O_3 + $sPbF_2$ fluxes

Flux	Composition of the flux					High-temperature phase	T_{sat}, °C	Note
	moles				quasi-binary form			
	p	q	r	s				
1	0.28	0.56	0.36	0	40 wt % ($BaO + 0.62B_2O_3$) + 60 wt % $Ba_3Fe_2Ge_4O_{14}$	$Ba_3Fe_2Ge_4O_{14}$	1000	$\rho_{flux} < \rho_{cryst}$
2	0.77	1.63	1.2	1.94	60.17 wt % ($BaF_2 + 0.62B_2O_3 + 0.225Fe_2O_3 + 0.15GeO_2$) + 39.83 wt % $Ba_3Fe_2Ge_4O_{14}$	$Ba_3Fe_2Ge_4O_{14}$	960	$\rho_{flux} > \rho_{cryst}$
3	0.77	1.81	1.53	1.92	60 wt % ($BaF_2 + 0.8B_2O_3 + 0.225Fe_2O_3 + 0.25GeO_2$) + 40 wt % $Ba_3Fe_2Ge_4O_{14}$	$Ba_3Fe_2Ge_4O_{14}$	850	$\rho_{flux} \approx \rho_{cryst}$
4	0.78	1.64	1.98	1.98	62.88 wt % ($BaF_2 + B_2O_3 + 0.225Fe_2O_3 + 0.2GeO_2$) + 37.12 wt % $Ba_3Fe_2Ge_4O_{14}$	$Ba_3Fe_2Ge_4O_{14}$	870	$\rho_{flux} < \rho_{cryst}$
5	0.83	1.77	1.76	2.2	64.66 wt % ($BaF_2 + 0.8B_2O_3 + 0.225Fe_2O_3 + 0.2GeO_2$) + 35.34 wt % $Ba_3Fe_2Ge_4O_{14}$	$BaFe_{12}O_{19}$	845	$\rho_{flux} \approx \rho_{cryst}$

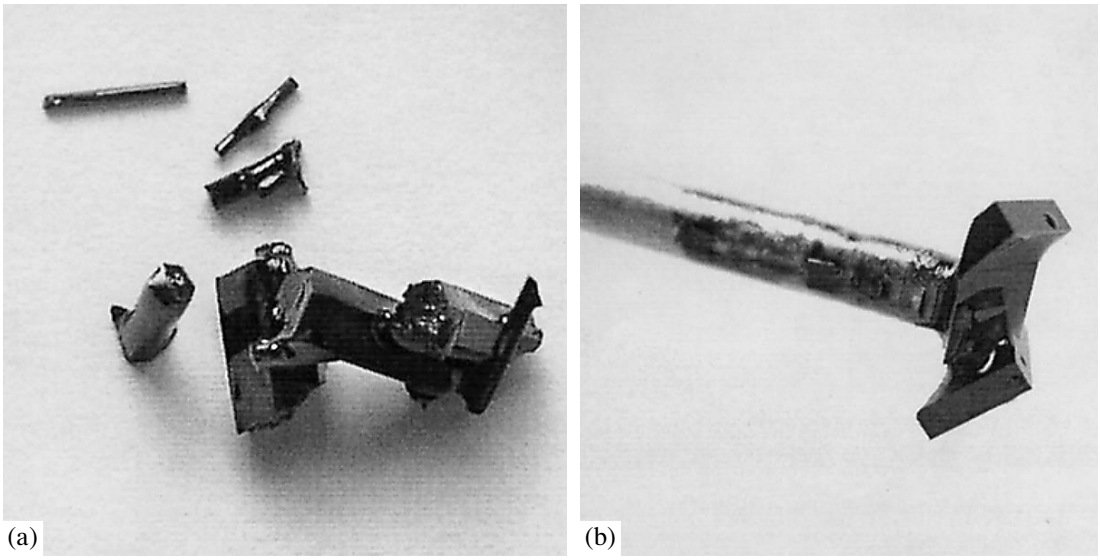

Fig. 1. Ferrogermanate single crystals grown upon spontaneous nucleation: (a) the trigonal barium ferrogermanate $Ba_3Fe_2Ge_4O_{14}$ and (b) the tetragonal barium ferrogermanate $Ba_2Fe_2GeO_7$.

straight-line hexagonal prisms elongated along the threefold axis (Fig. 1a). The concentration dependence of the saturation temperature is depicted in Fig. 2. The dependence has the slope dT_{sat}/dn = 10 K/wt %. At this slope, the crystal yield in the temperature range ΔT_{cryst} = 100 K is equal to 10% of the initial weight of the flux. The metastability range of this flux is ΔT_{met} = 20 K. The metastability range was determined in the following way. After due homogenization of the flux with the platinum probe, the temperature was decreased to a temperature below the saturation temperature. Within 14–16 h, we removed the probe and evaluated the crystal formation. The largest supercooling $\Delta T_{met} = T_{sat} - T$ at which crystals do not nucleate at the probe was taken equal to the metastability range. Note that the density of flux *1* is lower than the density of crystal **I** (ρ_{cryst} = 5.257 g/cm^3). Therefore, this composition can be used for growing single crystals in the surface region of the flux. In operation with the open crucible, the solution–melt composition is stable up to temperatures of 1050–1070°C.

The main disadvantage of this flux as a medium for the growth of single crystals **I** is its high viscosity. Therefore, the limiting rates at which high-quality crystals can be grown are relatively low. Controlled crystallization is substantially complicated by the possible suppression of the metastable state (collapse of the metastable range), which can be represented as follows. At a solution–melt density somewhat lower than the density of crystals grown, the temperature field with $dT/dh < 0$ is produced in the surface region in order to localize the growth process. If crystals spontaneously nucleate on the supercooled open surface of the flux in the course of long-term holding, these crystals are held by the surface tension forces on the surface and grow to a certain critical mass. Then, the crystals sink to the bottom region and begin to dissolve. Upon vigorous stirring, the locally inhomogeneous flux from this region is transferred to the growth zone and brings about multiple nucleation on a crystal holder with seeds and new crystals floating on the surface of the flux.

Own fluxes diluted by a mixture of B_2O_3 with BaF_2 have a lower viscosity. The viscosities of fluxes were qualitatively compared with each other in scale and dynamics of the convective flow pattern observed on the surface of the flux rapidly cooled outside the furnace. A decrease in the viscosity leads to a decrease in the size of cells and an increase in the velocity of their motion. Table 1 presents the compositions of the fluxes based on B_2O_3–BaF_2 mixtures with a nonstoichiometric content of crystal-forming oxides in which compound **I** is the high temperature phase crystallizing in the temperature range ΔT_{cryst} = 50–100 K (compositions *2*, *3*, *4*).

These fluxes, according to the concentration dependences of the saturation temperatures and the metastability ranges, are comparable to the fluxes containing no BaF_2. Note that the density of flux *2* is higher than the density of crystal **I**. This permits us to consider the possibility of growing single crystals with diffusion transfer of the crystallized material to the bottom region of the flux. A comparison of fluxes *3* and *5* demonstrates that, as the superstoichiometric content of GeO_2 decreases, barium hexaferrite $BaFe_{12}O_{19}$ becomes the high-temperature phase.

In family (2), the most attention was concentrated on the study of crystallization in the subfamily satisfying the conditions: $0.2 < p \le 0.5$, $0.4 < q \le 0.5$, r/s = 0.62, and $0.4 < s < 0.6$. The upper limits of the parameters p and q correspond to the stoichiometric ratio of oxides of compound **II** ($BaO : Fe_2O_3 : GeO_2 = 1 : 0.5 :$

Table 2. Barium ferrogermanate $Ba_2Fe_2GeO_7$ in the BaO + pFe_2O_3 + $qGeO_2$ + rB_2O_3 + $sPbF_2$ fluxes

Flux	Composition of the flux					High-temperature phase	T_{sat}, °C	Note
	moles				quasi-binary form			
	p	*q*	*r*	*s*				
1	0.22	0.46	0.32	0.52	68.23 wt % (PbF_2 + 0.62B_2O_3 + 1.09BaO + 0.45GeO_2) + 31.77 wt % $Ba_2Fe_2GeO_7$	Ba_2GeO_4	850	
2	0.27	0.46	0.32	0.52	61.4 wt % (PbF_2 + 0.62B_2O_3 + 0.89BaO + 0.35GeO_2) + 38.6 wt % $Ba_2Fe_2GeO_7$	$BaFe_{12}O_{19}$	875	
3	0.25	0.43	0.3	0.49	62.14 wt % (PbF_2 + 0.62B_2O_3 + BaO + 0.35GeO_2) + 37.86 wt % $Ba_2Fe_2GeO_7$	$Ba_2Fe_2GeO_7$	825	
4	0.31	0.41	0.29	0.47	53.44 wt % (PbF_2 + 0.62B_2O_3 + 0.8BaO + 0.2GeO_2) + 46.56 wt % $Ba_2Fe_2GeO_7$	$Ba_2Fe_2GeO_7$	920	dT_{sat}/dn = 6.5 K/wt %

0.5). At $p > q$, the BaO and Fe_2O_3 contents are superstoichiometric. At $p < q$, the BaO and GeO_2 contents are superstoichiometric. The third condition implies that the fluxes proper are diluted with a PbF_2 + 0.62B_2O_3 mixture in amounts determined by the parameter *s*. The melting temperature of this mixture and the melt viscosity are lower than those of the BaF_2 + 0.62B_2O_3 mixture.

According to the identification of the high-temperature phases, the fluxes under investigation with saturation temperatures $T_{sat} \le 920$°C are separated into three groups (Table 2). These high-temperature phases are represented by the Ba_2GeO_4 orthorhombic compound [a = 7.5805(26) Å, b = 9.9558(29) Å, c = 10.4481(41) Å], the $BaFe_{12}O_{19}$ hexagonal compound, and tetragonal compound **II** (a = 8.323 Å, c = 5.588 Å). Our experimental lattice parameters of tetragonal compound **II** are close (but somewhat smaller) than those of samples **II** prepared by solid-phase reactions in stoichiometric mixtures of the Ba_2CO_3, Fe_2O_3, and GeO_2 compounds [5].

Analysis of solution–melt compositions *1–3* (Table 2) clearly demonstrates the tendency toward transformation of the high-temperature phases with a change in the solution–melt composition. These compositions can serve as reference compositions when optimizing the solution–melt composition. As a result, we determined the composition of the flux in which tetragonal compound **II** is the high-temperature phase and begins to crystallize at the temperature T_{sat} = 920°C (Table 2, composition *4*). The concentration dependence of the saturation temperature for this flux is plotted in Fig. 2. The metastability range is ΔT_{met} = 10 K. The density of the flux is close to that of crystal **II** (ρ_{cryst} = 4.866 g/cm^3). It is this flux that was used for investigating the stability of crystal growth.

STABILITY OF THE GROWTH OF CRYSTALS **II**

Let us consider one of the compromising sets of thermal and hydrodynamic conditions that provide the stable growth of crystals **II** in the surface region of flux *4*. The flux (weight, 90 g) was prepared in the platinum cylindrical crucible (D = 15 mm, H = 50 mm) by sequential melting of reactants B_2O_3 (4.8 g), BaO (36.2 g), Fe_2O_3 (11.7 g), PbF_2 (27.2 g) and GeO_2 (10.1 g). The depth of the flux was 14 mm.

In a crystallization furnace with a nonuniform temperature field, the crucible was located so that the vertical component of the temperature gradient was dT/dh = –(2–3) K/cm. The minus sign means that the temperature decreases away from the crucible bottom. At the stage of primary homogenization, the flux was

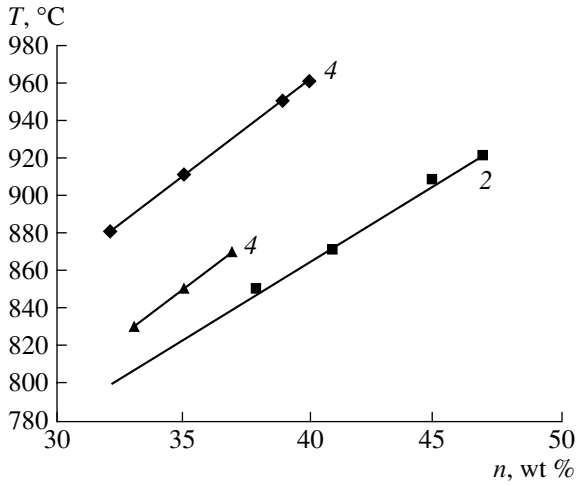

Fig. 2. Concentration dependences of the saturation temperature for the $Ba_3Fe_2Ge_4O_{14}$ ferrogermanate in fluxes *2* (closed rhombuses) and *4* (closed triangles) (Table 1) and the $Ba_2Fe_2GeO_7$ ferrogermanate in flux *4* (closed squares) (Table 2).

held at $T = 980°C$ for 8 h. The saturation temperature $T_{sat} = 920 \pm 2°C$ was determined using test crystals.

Upon secondary homogenization, a crystal holder in the form of platinum rod was dipped in the surface layer of the flux. The crystal holder was either fixed or rotated at a rate $\omega = 30–40$ rpm. After homogenization was completed, the temperature was decreased to $T = T_{sat} – (12–13)$ K; i.e., the flux was supercooled by 2–3 K below the metastability range. At this supercooling, no more than six or eight crystals were formed for 14–16 h on the rod part dipped in the flux. An increase in the holding time did not lead to the collapse of the metastable range with multiple nucleation of crystals on the rod and the surface of the flux in both static ($\omega = 0$) and dynamic regimes ($\omega = 30–40$ rpm). Faces of initially nucleated crystals were developed without formation of macrosteps. The crystals grown for 48 h in the dynamic regime are shown in Fig. 1b. Among four crystals **II** grown in the form of rectangular plates, the largest crystal has sizes of $5 \times 7 \times 2$ mm. The face regions free of the flux are specular.

In one of the experiments on spontaneous nucleation, we grew three crystals 1–1.5 mm in size on the rod end. Then, we investigated the seeded growth. After homogenization, the temperature in the furnace was decreased to $T = T_{sat} + 5$ K and the rod with the crystals was inserted into the furnace. The rod was dipped in the surface layer so that all the crystals were in contact with the flux. The rod was rotated at a rate of 30 rpm. Within 10 min, the temperature was decreased to $T = T_{sat} – 3$ K. Thereafter, the temperature was progressively decreased at a rate of 1 K/day. The crystal sizes increased to $8 \times 5 \times 2.5$ mm^3 for four days. The growth rate appeared to be lower by a factor of approximately 2 due to a considerably smaller supercooling. No instability of the faceted front in the form of macrosteps was observed. The seeded growth with discrete pooling of the growing single crystal was also stable. The described conditions were used for growing single-crystal samples.

CONCLUSIONS

The compositions of oxide–fluoride fluxes for controlled crystallization of trigonal compound **I** and tetragonal compound **II** were determined and their characteristics were investigated. The thermal and hydrodynamic conditions that provide the stable growth of tetragonal single crystals **II** both upon spontaneous nucleation and with the use of seeds were revealed. The results made it possible to prepare single-crystal samples for investigations of elastic, piezoelectric, magnetic, and magnetoelastic properties and also the magnetic structure by neutron diffraction methods.

ACKNOWLEDGMENTS

This work was supported in part by the Division of Physical Sciences of the Russian Academy of Sciences (project no. 2.6) and the Academician K.S. Aleksandrov School.

REFERENCES

1. B. V. Mill and Yu. V. Pisarevsky, in *Proceedings of the 2000 IEEE/EIA International Frequency Control Symposium and Exhibition, Kansas City, MO, United States, 2000* (IEEE, Danvers, 2000), p. 133.
2. L. N. Bezmaternykh, A. D. Vasil'ev, I. A. Gudim, and V. L. Teremov, Kristallografiya **49** (2), 354 (2004) [Crystallogr. Rep. **49** (2), 271 (2004)].
3. A. V. Butashin, L. E. Li, A. F. Konstantinova, and I. A. Gudim, Kristallografiya **49** (3), 514 (2004) [Crystallogr. Rep. **49** (3), 459 (2004)].
4. E. L. Belokoneva, M. A. Simonov, A. V. Butashin, *et al.*, Dokl. Akad. Nauk SSSR **255** (5), 1099 (1980) [Sov. Phys. Dokl. **25** (12), 954 (1980)].
5. I. S. Lyubutin, B. V. Mill', V. G. Terziev, and A. V. Butashin, Kristallografiya **33** (1), 136 (1988) [Sov. Phys. Crystallogr. **33** (1), 78 (1988)].

Translated by O. Borovik-Romanova

Crystallography Reports, Vol. 50, Suppl. 1, 2005, pp. S111–S115.

CRYSTAL GROWTH

Development of the Technology for Large-Scale Production of Lead Tungstate Single Crystals for Physical Experiments

S. F. Burachas[1, 2], S. Ya. Beloglovsky[1], N. A. Vassilieva[1], M. K. Ziomko[1], E. A. Kuznetsova[1], I. V. Makov[1], R. M. Nikitin[1], Yu. A. Saveliev[1], A. A. Vasiliev[2], M. S. Ippolitov[2], V. A. Lebedev[2], V. I. Manko[2], S. A. Nikulin[2], A. S. Nyanin[2], A. A. Tsvetkov[2], and G. Tamulaĭtis[3]

[1] *North Crystals Company, Apatity, Murmansk oblast, Russia*
e-mail: sburachas@mail.ru
[2] *Kurchatov Institute, Russian Research Center, pl. Akademika Kurchatova 1, Moscow, 123182 Russia*
[3] *Vilnius University, Vilnius, Lithuania*
Received February 8, 2004

Abstract—The scientific principles underlying the technology for growing crystals of lead tungstate $PbWO_4$ (PWO) with controlled properties are discussed. The developed technology is implemented at the North Crystals Company in mass production of PWO crystals with 100% reproducibility of operating parameters. This made it possible to solve the problem associated with the preparation of PWO crystals for the ALICE experiment at CERN and to produce the pilot batch of large-sized PWO crystals (diameter, 46 mm; length, 250 mm) with required characteristics for the CMS experiment at CERN. More than 10000 PWO scintillators of high optical quality for the ALICE experiment were fabricated over a short time according to the proposed technique.

INTRODUCTION

An advanced technology for mass production of crystals of lead tungstate $PbWO_4$ (PWO) with reproducible characteristics cannot be developed without recourse to the physical principles underlying the growth of optically homogeneous crystals or without understanding of the nature of the influence exerted by technological factors on the properties of PWO crystals important for their applications in high-energy physics experiments.

The choice of PWO crystals as the basic scintillation material for the CMS and ALICE projects (CERN) in 1994 gave impetus to extensive investigations into the main radiation-optical and luminescence properties of these crystals.

At present, it has been established that ionizing radiation does not affect the scintillation spectrum of PWO crystals. Under irradiation, the scintillation mechanism remains unchanged and the decrease in the specific light yield is predominantly associated with the induced absorption [1, 2]. Moreover, the bleaching of PWO crystals under irradiation was observed by Baccaro *et al.* [3]. Auffray *et al.* [4] revealed the relation between the absorption of a nominally pure crystal in the UV range (350 nm) and the induced absorption. According to [5], the luminescence times in the blue spectral range (420–440 nm) are short and the green emission component is caused by the presence of impurities in crystals. The nature of the green emission component was discussed in [6]. The conditions used for growing optically homogeneous PWO crystals by the Czochralski method in the case of large-scale production were described in our earlier works [6, 7].

It has been found that, irrespective of the growth and heat treatment technology, all nominally pure PWO crystals contain defects responsible for the UV absorption identical for all crystals and their intense radiation coloration. Only doping with trivalent lanthanum-group elements (which hypothetically replace Pb^{2+} ions) leads to an increase in the transparency in the UV range and an improvement of the radiation resistance of PWO crystals [8].

Different substitution mechanisms have been proposed under the assumption on substitution of trivalent lanthanum-group elements for Pb^{2+} ions [8–13]. Lin *et al.* [13] theoretically showed that the absorption band intensity is related to the difference ΔN between the numbers of lead and oxygen vacancies: the larger the difference ΔN, the higher the absorption band intensity. Doping with trivalent ions results hypothetically in the formation of clusters $[2M_{Pb}^{3+} - V_{Pb}]$, which bound a number of lead vacancies so that the number of active lead vacancies decreases. This leads to a decrease in the difference ΔN, suppression of the absorption band at 350 nm, and, hence, an increase in the radiation resistance of PWO crystals.

However, the proposed substitution mechanisms are not conclusive, because the experimental data obtained in [14] demonstrate that the amount of lead ions that evaporated during the growth of PWO crystals is more

than one order of magnitude larger than the amount of dopants introduced upon optimum doping of melts [14].

Nikl *et al.* [15] put forward the concept according to which Pb^{3+} and O^- centers are predominantly responsible for the weak radiation resistance of PWO crystals (in the range 350–370 nm) and the optical absorption at 420 nm. Subsequently, it was revealed that the formation of defects in crystals is affected by the impurity batch composition [16]. The influence of impurity defects on the properties of PWO crystals has been studied in detail [6, 8, 16–19].

Analysis of the data available in the literature shows that the concepts of Pb^{3+} and O^- centers and the substitution of trivalent lanthanum-group elements for Pb^{2+} ions cannot explain all the experimental results obtained in the study of PWO crystals [18].

More recently, on the basis of the experimental data obtained in our previous works [14, 20, 21], we assumed that PWO crystals contain defects associated with the deficit of oxygen in tungsten oxide WO_3 used as the main component of the initial batch. The formula of tungsten oxide WO_{3-x} reflects the presence of tungsten ions W^{5+} and W^{4+} with a lowered valence. The electroneutrality of the crystal as a whole is provided by the appearance of oxygen charged vacancies. In the PWO crystal lattice, a tungsten ion with a lowered valence and an oxygen vacancy bonded to it can be represented as a $[W^{5+}–V_0^+]$ or $[W^{4+}–V_0^{2+}]$ cluster.

The basic regularities of the effect of defects on the properties of PWO crystals depending on the technological conditions were discussed and revealed in [6, 22].

DISCUSSION OF THE RESULTS

Experience suggests that the successful development of mass production of PWO crystals is based on the solutions of the following two main problems:

(i) the optimization of heat treatment conditions necessary for the Czochralski growth of optically homogeneous PWO crystals with a constant diameter;

(ii) a controlled improvement of crystal quality with the use of structural and impurity defects.

The optically homogeneous PWO crystals were prepared [6, 7] with the use of crystal raw materials produced from a high-quality batch [16], a crystallizer with an optimum design, optimum growth conditions chosen on the basis of the physicochemical regularities of Czochralski growth of oxide crystals with a constant diameter [23, 24], and the optimum parameters of the automatic control for the crystal growth process [25].

Our approach is based on the results obtained in our earlier works [14, 20, 21], in which it was demonstrated that the optical properties and the radiation resistance of PWO crystals grown from raw materials are primarily determined by the defects of tungsten oxides of general formula WO_{3-x} ($0 < x < 1$). This formula, with due regard for the valence states of tungsten (6, 5, 4), can be represented in the form $(1 - 2a - b)WO_3 + aW_2O_5 + bWO_2$, where $x = a + b$.

Upon doping of PWO crystals with L_2O_3 oxides (where L = Y, La, Gd), the optical properties of the crystal are governed by the clusters that are formed in the crystal lattice upon replacement of lead or tungsten ions by lanthanum ions with the formation of the corresponding vacancies and displacement of atoms from their positions.

The green component in the X-ray luminescence spectrum of nominally pure PWO crystals under specific annealing conditions can be emitted only from the surface and in the X-ray luminescence spectrum of doped crystals only upon doping with impurities of the molybdenum type [6, 22]. The aforementioned inferences regarding the role played by defects of PWO crystals in an emission are based on the experimental evidence given below.

EXPERIMENTAL EVIDENCE

It has been established that there is a clear correlation between the properties of the PWO crystals and their color and that this correlation depends on the annealing conditions (table, Fig. 1). The annealing conditions, specific light yields, and colors of the PWO samples prepared from the same crystal are presented in the table. The optical transmission spectra of these samples are shown in Fig. 1.

The crystal color is determined by the color complementary to the color of radiation absorbed by charged clusters and depends on the valence of tungsten ions forming these clusters.

Figure 2 shows the X-ray luminescence spectra of polished PWO samples (grown in an inert medium) measured before (spectrum *1*) and after (spectrum *2*) their annealing in air at a temperature of 600°C. It can be seen from Fig. 2 that annealing leads to an increase in the intensity of the green emission component. However, structural defects responsible for the green emission component are formed only in the surface layer of the crystal upon annealing in air. After removal of this layer (0.1–0.2 mm thick), the green emission component disappears and the luminescence spectrum of the annealed crystal becomes identical to that of the unannealed sample. These structural defects in the surface layer play a dominant role only upon X-ray excitation of luminescence, because X rays (up to 200 kV) penetrate into PWO crystals to a depth of ~0.1 mm; i.e., they are almost completely absorbed by the surface layer [6].

Influence of the annealing conditions of the PWO samples ($22 \times 22 \times 10$ mm^3 in size) on their specific light yield and color

Sample	Annealing conditions of the samples			Specific light yield	Color of the sample
	regime **I** annealing in air, °C/h	regime **II** annealing in the reducing atmosphere, °C/h	regime **III** annealing in air, °C/h	photoelectrons/MeV	
O-1	1000/40	950/10	500/5	16.5	Colorless
O-4	1000/40			5.7	Yellow
O-5	1000/40	950/10		4.8	Violet bluish
O-9	1000/40	950/10	1000/10	8.0	Dark yellow

GENERALIZATION OF EXPERIMENTAL RESULTS

The analysis of the main experimental data on the defect formation in PWO crystals allows us to make the following inference. The properties of nominally pure PWO crystals are modified upon heat treatment due to the presence of impurity and structural defects. This modification of defects in PWO crystals can be conventionally considered a solid-phase reaction in a solid with the formation of new chemical compounds and foreign phases in crystals.

We performed a series of experiments on the growth and annealing of undoped and doped PWO crystals under different conditions. In [20], it was revealed that a melt during the crystal growth is enriched in tungsten due to the evaporation of lead in the form of different compounds (predominantly, in the form of the Pb_2WO_5 phase). The formed excess tungsten ions occupy both the tungsten and lead positions; in the latter case, the valence of tungsten ions changes. The electrical neutrality is provided by the formation of oxygen vacancies. Electrons of tungsten ions and vacancies interact with each other. Similar associates can be treated as clusters. These clusters transform an electromagnetic wave incident on the crystal into a scattered wave that is responsible for the crystal color. The change in the color of the PWO crystal upon heat treatment is associated with the change in the valence state of tungsten ions and their oxygen environment. It should be noted that the coloration of crystals upon heat treatment in different media is not clearly understood and the mechanism of color evolution has not been completely revealed. However, when the technological parameters are carefully maintained, the crystal color can serve as an indicator of the crystal quality. As was noted above, the formula WO_{3-x} reflects the averaged valence of tungsten ions over the crystal volume. The formula $(3 - x)$O indicates the averaged number of oxygen ions in the environment of tungsten ions. The quantity x characterizing the oxygen deficit correlates with the crystal color. According to [14], the crystal color is yellow for

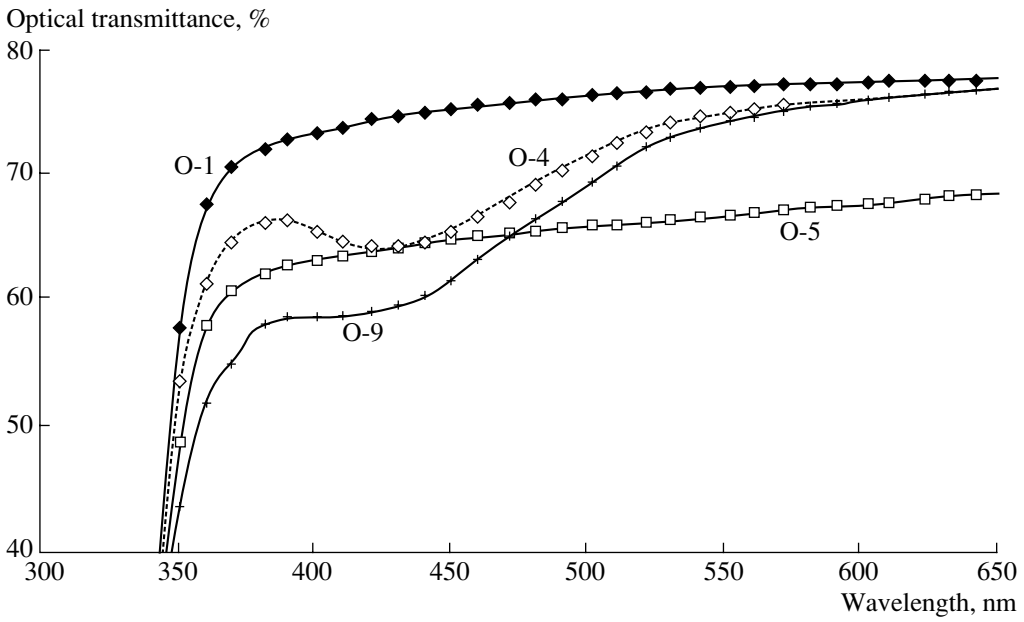

Fig. 1. Optical transmission spectra of the samples presented in the table.

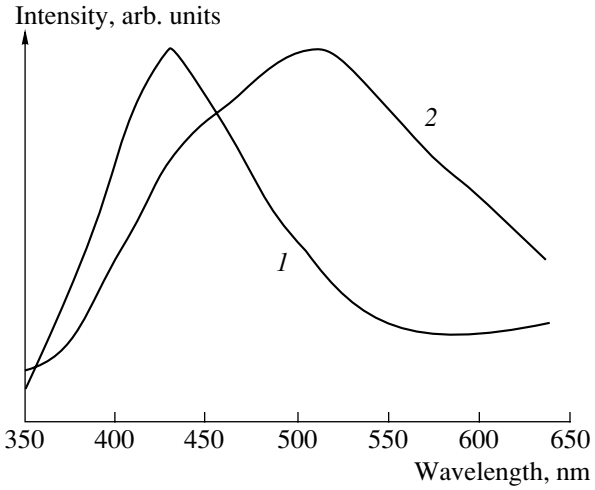

Fig. 2. X-ray luminescence spectra of polished PWO samples (grown in an inert medium): (*1*) before and (*2*) after annealing at 600°C in air.

WO_3, green for $WO_{2.96}$, blue for $WO_{2.8–2.88}$, violet for $WO_{2.7–2.75}$, and brown for WO_2. During long-term reducing annealing, the crystal color changes in the following order: yellow, green, colorless, blue, violet, and brown. A similar change in the color of PWO crystals occurs in the course of long-term exposure to ionizing radiation [21]. The annealing of crystals under oxidizing conditions when the partial oxygen pressure is lower than the equilibrium pressure leads to the reverse sequence of transformations. Upon deep reducing annealing or at a high dose of ionizing radiation, doped crystals become black and undoped crystals acquire a violet color [14].

Therefore, the color and its change under external actions are predominantly governed by the defect clusters. The reduction state of tungsten ions depends on the conditions of growth and annealing of crystals. The oxygen deficit in tungsten oxide WO_{3-x} leads to the formation of defects that are characteristic of PWO crystals and responsible for the optical absorption in the UV range and the crystal color. The valence of tungsten ions in a cluster easily changes in the course of growth, annealing, and exposure to ionizing radiation. This is accompanied by the change in the crystal color.

Doping of PWO melts with oxides of the L_2O_3 type (L = Y, La, Gd, etc.) inhibits the formation of oxygen vacancies and clusters. The content of the L_2O_3 dopant should be chosen so that the optical transparency of crystals would not be reduced. Upon optimum doping, the transparency of crystals in the UV range is maximum.

The influence of the exposure of nominally pure PWO crystals to radiation is similar in many respects to that of reducing–oxidizing annealing. In both cases, the treatment leads to a change in the oxidation state of tungsten ions in clusters and, hence, to a change in the crystal color. The induced absorption is due to the equilibrium of oxidation and reduction of tungsten ions in crystals.

The green component in the luminescence spectrum of PWO crystals can be observed only upon doping of melts with impurities of the Mo type. These impurities form inclusions of the $PbMoO_4$ phase in the crystal matrix. The green component is absent in the luminescence spectrum of pure PWO crystals. This component can appear if structural defects are formed in the vicinity of the crystal surface.

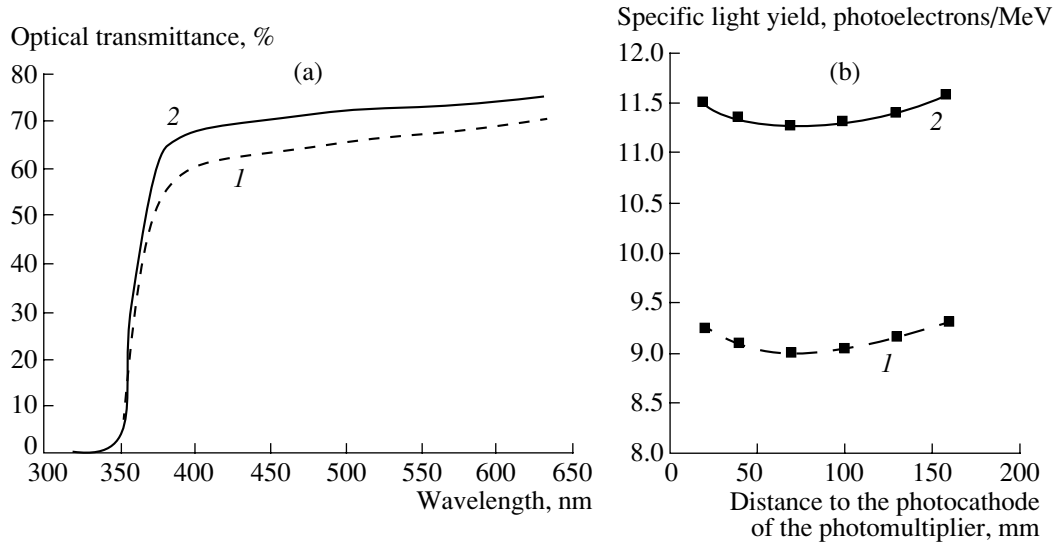

Fig. 3. (a) Average optical transmittance and (b) average quantum yield for 2000 PWO scintillators fabricated (*1*) before and (*2*) after the application of the model under consideration.

It can be seen from Fig. 3 that the use of heat treatment of structural defects and clusters for preparing optically homogeneous crystals permits one to improve substantially the properties of PWO crystals in their mass production.

CONCLUSIONS

Thus, the technology for growing PWO crystals with controlled properties has been designed. The technology was implemented at the North Crystals Company in large-scale production of PWO crystals with 100% reproducibility of operating characteristics. This made it possible to solve the problem associated with the PWO crystals for the ALICE experiment at CERN and to fabricate a pilot batch of large-sized PWO crystals (46 mm in diameter, 250 mm in length) with required parameters for the CMS experiment at CERN. More than 10000 PWO scintillation crystals with a high optical and scintillation quality for the ALICE experiment have been produced to date. The parameters of the crystals are as follows: the quantum yield is higher than 10 photoelectrons/MeV; the variation in the quantum yield along the crystal is less than 5%; and the optical transmittances are higher than 30, 65, and 70% at wavelengths of 360, 420, and 600 nm, respectively.

ACKNOWLEDGMENTS

We would like to thank A.F. Konstantinova (Shubnikov Institute of Crystallography, Russian Academy of Sciences, Moscow) and Yu.S. Kuz'minov (Institute of General Physics, Russian Academy of Sciences, Moscow) for their participation in the discussion of the results obtained in this study and helpful remarks.

This work was supported by the Federal Atomic Energy Agency of the Russian Federation.

REFERENCES

1. E. A. Auffray, P. Lecoq, A. Annenkov, *et al.*, CMS Note No. 97/54 (CERN, Geneva, Switzerland, 1997).
2. Ren-Yuan Zhu, IEEE Trans. Nucl. Sci. **44** (3), 468 (1997).
3. S. Baccaro, P. Bohacek, B. Borgia, *et al.*, Phys. Status Solidi A **164**, R9 (1997).
4. E. Auffray, M. Lebeau, P. Lecoq, and M. Schneegans, CMS Note No. 98/038 (CERN, Geneva, Switzerland, 1998).
5. G. Tamulaitis, S. Burachas, V. Martinov, *et al.*, Phys. Status Solidi A **157**, 187 (1996).
6. S. Burachas, S. Beloglovsky, D. Elizarov, *et al.*, Radiat. Meas. **38** (4–6), 367 (2004).
7. S. Burachas, S. Beloglovsky, A. Vasiliev, *et al.*, Poverkhnost, No. 2, 5 (2002).
8. M. Kobayashi, Y. Usuki, M. Nikl, and K. Nitsch, Nucl. Instrum. Methods Phys. Res. A **399**, 261 (1997).
9. Q. Lin and X. Feng, J. Phys.: Condens. Matter **15**, 1963 (2003).
10. M. Nikl, K. Nitsch, J. Hybler, *et al.*, Phys. Status Solidi B **196**, K7 (1996).
11. M. Nikl, J. Rose, K. Nitsch, and J. H. Asaryan, Mater. Sci. Forum **239–241**, 271 (1997).
12. A. Annenkov, E. Auffray, M. Korzhik, *et al.*, Phys. Status Solidi A **170**, 47 (1998).
13. Q. Lin, X. Feng, Z. Man, *et al.*, Phys. Status Solidi A **181**, R1 (2000).
14. S. Burachas, S. Beloglovski, I. Makov, *et al.*, Nucl. Instrum. Methods Phys. Res. A **486** (1–2), 83 (2002).
15. M. Nikl, K. Nitsch, S. Baccaro, *et al.*, J. Appl. Phys. **82**, 5758 (1997).
16. A. Annenkov, M. Korzhik, and P. Lecoq, Nucl. Instrum. Methods Phys. Res. A **490**, 30 (2002).
17. M. Kobayashi, Y. Usuki, M. Ishii, *et al.*, Nucl. Instrum. Methods Phys. Res. A **465**, 428 (2001).
18. M. Nikl, Phys. Status Solidi A **178**, 595 (2000).
19. S. Burachas, A. Apanasenko, B. Grinyov, *et al.*, Int. J. Inorg. Mater. **3** (8), 1101 (2001).
20. S. Burachas, S. Beloglovski, I. Makov, *et al.*, J. Cryst. Growth **242**, 367 (2002).
21. S. Burachas, S. Beloglovski, I. Makov, *et al.*, Nucl. Instrum. Methods Phys. Res. A **505** (3), 656 (2003).
22. S. Burachas, S. Beloglovsky, D. Elizarov, *et al.*, Nucl. Instrum. Methods Phys. Res. A **537** (1–2), 185 (2005).
23. S. Burachas, O. Kolotii, and B. Timan, Funct. Mater. **3**, 29 (1996).
24. S. F. Burachas, O. D. Kolotii, and B. L. Timan, Kristallografiya **43** (5), 949 (1998) [Crystallogr. Rep. **43** (5), 894 (1998)].
25. S. Burachas, P. Stadnik, and B. Timan, *Automation of Crystal Growth Processes* (NIITÉKhIM, Moscow, 1984) [in Russian].

Translated by O. Borovik-Romanova

Crystallography Reports, Vol. 50, Suppl. 1, 2005, pp. S116–S121.

CRYSTAL GROWTH

Specific Features of the Technology for Large-Scale Processing of Lead Tungstate Crystals for Research in the Field of High-Energy Physics

S. Ya. Beloglovsky, S. F. Burachas, N. A. Vassilieva, M. K. Ziomko, S. V. Lysov, R. M. Nikitin, Yu. A. Saveliev, I. V. Makov, E. A. Kuznetsova, A. A. Chernousov, and Yu. V. Yakovlev

North Crystals Company, Apatity, Murmansk oblast, Russia

e-mail: sburachas@mail.ru

Received February 8, 2005

Abstract—The technology for large-scale processing of lead tungstate crystals intended for investigations in the field of high-energy physics is implemented with the use of the processing equipment at the North Crystals Company. The quality of the PWO scintillators manufactured by the company satisfies the requirements of the ALICE and CMS experiments at CERN. More than 8000 scintillators for the ALICE project and the pilot batch of scintillators for the CMS project have been fabricated. © *2005 Pleiades Publishing, Inc.*

INTRODUCTION

The use of crystals of lead tungstate $PbWO_3$ (PWO) in experiments performed in the field of high-energy physics requires production of scintillators with stable radiation-optical, scintillation, and geometrical characteristics. The choice of PWO crystals as the basic scintillation material for the CMS and ALICE projects (CERN) in 1994 spurred intensive investigations concerned with the development of industrial technology for manufacturing scintillators that must satisfy different requirements, including requirements on the geometrical dimensions and the surface finish [1]. The technology developed by CERN for processing the PWO crystals intended for the CMS project [2] was used at the Bogoroditsk Electrochemical Plant as the basis for the industrial technology of PWO scintillators for the CMS experiment [3].

The development of the technology for producing PWO crystals with controlled properties at the North Crystals Company for the ALICE project [4–6] required simultaneous design of the technology for their processing.

In [7], it was established that PWO crystals grown with the [100] orientation of the growth axis are least prone to damage under mechanical actions. The conditions and optimum oxygen percentage in the medium during annealing of the crystal boule, which reduce the probability of fracture of the crystal during its processing, were determined in [8].

In this work, we considered the implementation of the main stages of the technology for large-scale processing of PWO crystals with the use of the processing equipment existing at the North Crystals Company.

PROPERTIES OF PWO CRYSTALS AFFECTING THE CHOICE OF THE TECHNIQUES FOR THEIR PROCESSING

The basic physicochemical properties of PWO crystals are listed in Table 1. The general view of the PWO crystal grown along the [100] direction is depicted in Fig. 1. The requirements on the physical parameters of PWO scintillators for the ALICE project are given in Table 2. The specification for the geometrical dimensions and surface finish of scintillators are presented in Fig. 2.

Lead tungstate crystallizes in the tetragonal crystal system, has a scheelite-type structure, and belongs to the space group $I4_1/a$. The parameters of the PWO unit cell containing four formula units are as follows: a = 5.462 Å and b = 12.046 Å. The Bragg angles calculated for the crystallographic planes that are most important from the standpoint of the processing technology are listed in Table 3. The PWO samples were investigated on a DRON-4M diffractometer with a standard radiation source ^{29}Cu.

Table 1. Basic physicochemical properties of PWO crystals [9]

Property	Numerical values
Chemical formula	$PbWO_4$
Density, g/cm^3	8.23 ± 0.05
Molecular mass, amu	391
Mohs hardness	4
Melting temperature, °C	1123 ± 3
Refractive index n	1.3–1.9

1063-7745/05/5001-S0116$26.00

In choosing the orientation of seed crystals, the attraction was toward the [100] direction, because the PWO growth in different crystallographic directions determines dominant cleavage planes, namely, the (104) cleavage plane for the (001) plane and the (101) and (112) cleavage planes for the (100) plane. The destructive action of these cleavage planes substantially complicates the problem associated with the preservation of crystal integrity in the course of processing [7]. The basal crystallographic planes (004) and (200) were used to prepare the seeds.

This approach provided reproducibility of the crystals grown in a habit and made it possible to predict the location of the scintillation element in the crystal boule.

The processing techniques were developed to solve the problem associated with the crystal fracture along the cleavage planes due to the thermoelastic stresses, which depend on the physical properties and growth conditions of PWO crystals.

In the study of crystal defects affecting the quality of their processing, cracking of crystals that have pronounced variations in the diameter along the boule height (so-called "skirts" and "necks") is of special importance. During the growth, the crystal structure tends to the energetically most favorable state, in which the internal energy is predominantly represented by the kinetic energy component of the molecular interaction.

If the crystal surface during the crystal growth deviates from a specified shape due to particular factors, the components of the internal energy of the crystal are redistributed in surface regions. In these crystal surface regions, there arise forces of an additional pressure Δp that tend to restore an optimum energy state of the crystal surface. This situation is illustrated in Fig. 3.

Similar defects lead to the formation of crystal regions with different internal energies. Under external actions (for example, incorporation of abrasive grains, sharp temperature drops, etc.), the crystal responds to these actions and tends to minimize its internal energy; i.e., there occurs a so-called crystal discharge that manifests itself as crack formation and even complete fracture of crystal boule macroregions.

SPECIFIC FEATURES OF THE TECHNOLOGY FOR LARGE-SCALE PROCESSING OF PWO CRYSTALS FOR RESEARCH IN THE FIELD OF HIGH-ENERGY PHYSICS

The technology for mechanical processing of PWO crystals involves two stages: the operations associated with the workpiece shaping and the operations ensuring the fulfillment of the requirements for the surface finish of elements.

The technological operations associated with the workpiece shaping were performed on a 3D711VF11 precision surface grinding machine. The machine was modified in order to regulate and control precisely the longitudinal movement of an operating table that feeds

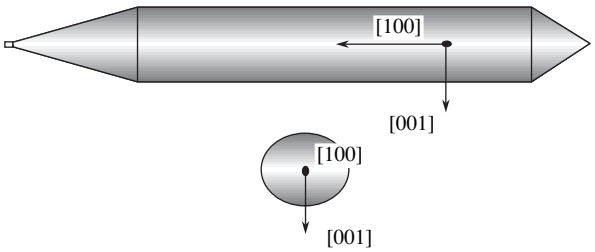

Fig. 1. Schematic drawing of the PWO crystal grown along the [100] direction.

the crystal to the cutting zone. The hydraulic drive of the table was used only for adjustment and setting of the crystal. The cutting was performed with an electromechanical drive. The design provided a wide range of cutting speeds from 30 to 100 mm/min. Triefus D-76-MH3 250/50/1.95 saws were used as a cutting tool. Special holders were designed for the saw fixation. As a result, the runout of the base plane of a spindle under a saw housing was ≤0.02 mm and the saw holder runout was ≤0.005 mm.

In order to provide in-line processing, we rejected the techniques based on the crystal fixation in a gypsum mold [9]. For all cutting stages, we designed special tools that made it possible to firmly fix the crystal in the course of operations, to reduce concentrated loads capable of resulting in a crystal fracture, and to mount securely and precisely the crystal on the operating table of the machine. The tools were produced from a steel with graphite and textolite inserts that play the role of dampers at points of concentrated loads on the workpiece surface. The tools are fastened to a magnetic plate of the operating table equipped with positioning tools.

The first stage of crystal cutting consists in cutting the upper and lower ends (Fig. 4).

Special tools for the operation with the use of two saws were developed for the cutting of crystal sides. As a result, the parallelism of the opposite faces was no worse than 0.02 mm over the entire length (180 mm) of the workpiece (Fig. 5).

It was found that the quality of cutting PWO crystals is affected by the sequence of cutting lateral faces with

Table 2. Requirements imposed on the physical parameters of the PWO scintillator for the ALICE project [6]

Parameter	Numerical values
Color of the scintillator	Colorless
Specific light yield, photoelectrons/MeV	>10
Change in the specific light yield along the scintillator axis, %	<5
Transmittance along the scintillator axis, ≥ %	30, 65, and 70 at wavelengths of 360, 420, and 630 μm, respectively

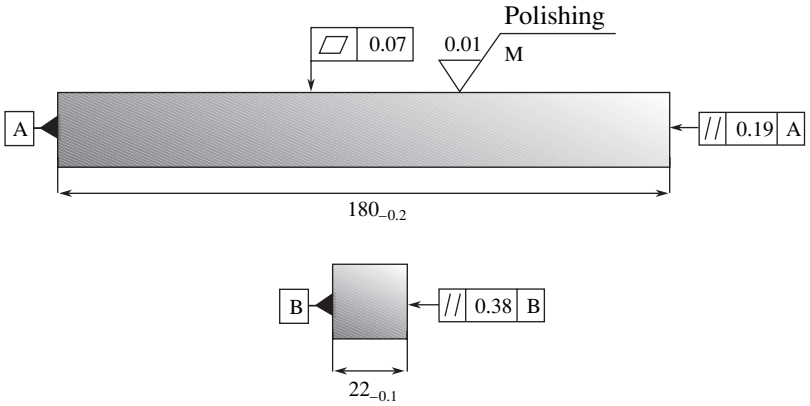

Fig. 2. Specification for the geometrical dimensions and surface finish of scintillators.

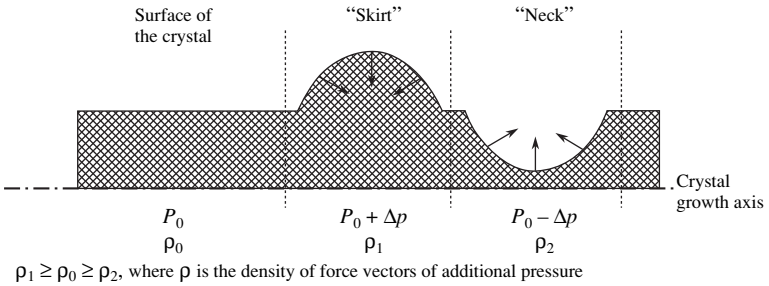

Fig. 3. Illustration of "skirt" and "neck" defects.

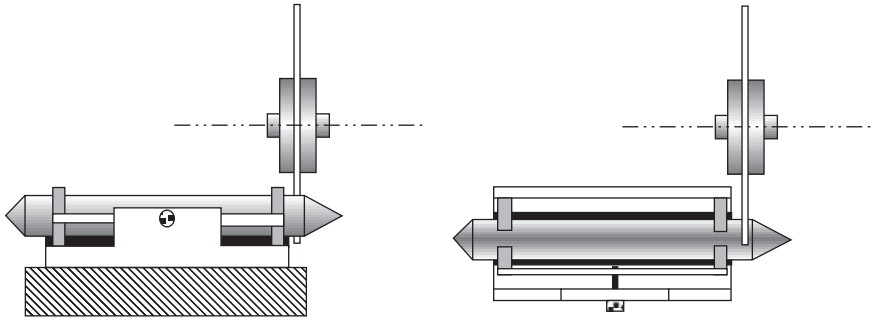

(a) Direction of cutting (b) Plan view

Fig. 4. Schematic diagram of the cutting of cone-shaped crystal ends: (a) the direction of cutting and (b) the plan view.

respect to the cleavage planes of the crystal. In particular, when the faces perpendicular to the cleavage planes are cut first, the subsequent operations lead to cleavage and cracking of the workpiece. The performed investigations enabled us to reveal the cutting sequence for the preparation of the workpiece from the crystal (Fig. 6). This is very important with due regard for structural features of the PWO crystal grown along the [100] direction and growth conditions in a high-gradient zone of a crystallizer. First, the upper part of the boule that contains the largest number of regions with thermoelastic stresses is removed. Second, it becomes possible to avoid the effect of surface crystal structures on the final result of cutting.

The cutting conditions were chosen so that the crystal fracture was excluded. The next stage of processing is the technological operation of fine grinding.

Special tools were designed and produced for in-line grinding of end and lateral faces on the 3D711VF11 machine with the use of a 14V1 250*21*23*3*76 ACM 20/14 4/586 B3.16 grinding diamond disk. The chosen grinding conditions ensured the preservation of workpieces and the reproducibility of the geometrical dimensions in each batch of workpieces (Figs. 7a, 7b).

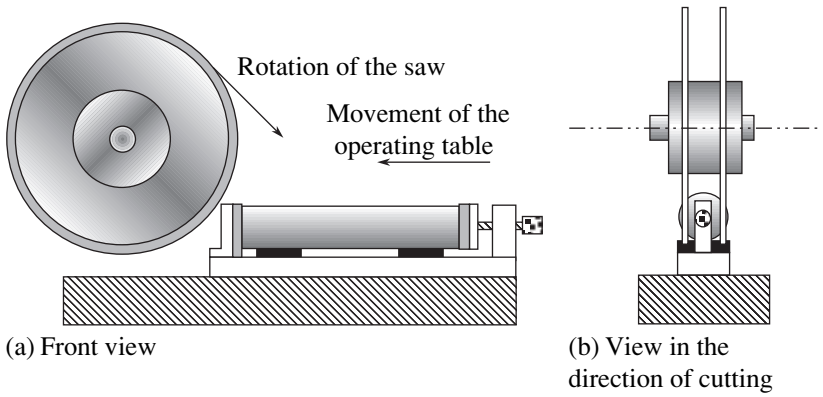

Fig. 5. Schematic diagram of the cutting of lateral crystal sides: (a) the front view and (b) the view in the direction of cutting.

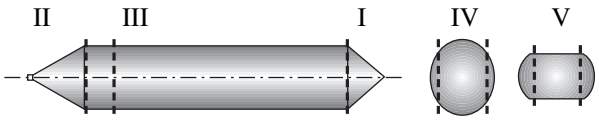

Fig. 6. Sequence of the cutting of the PWO crystal.

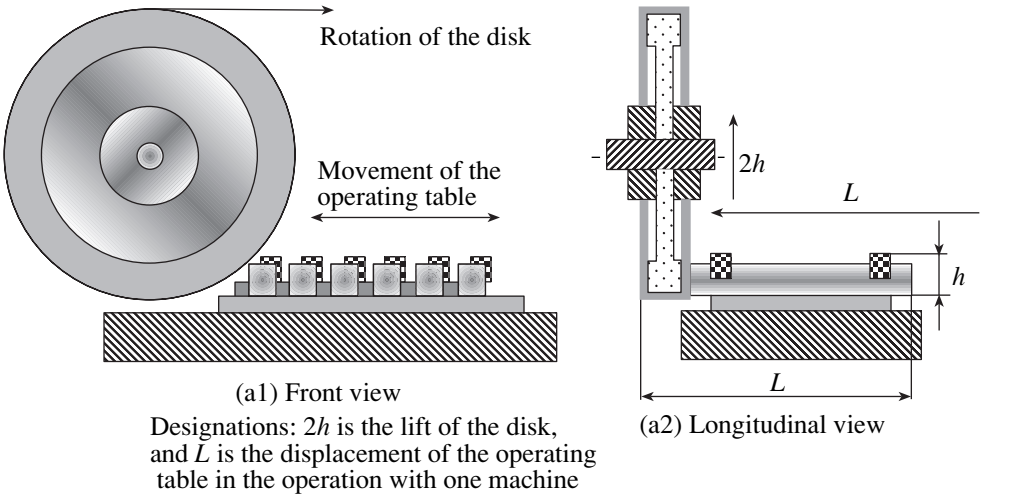

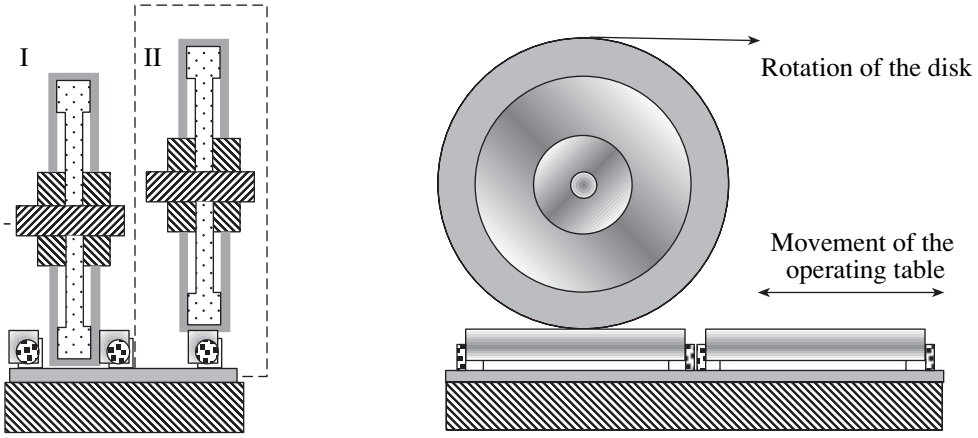

Fig. 7. Schematic diagram of the grinding of (a) end faces and (b) lateral faces of the crystal.

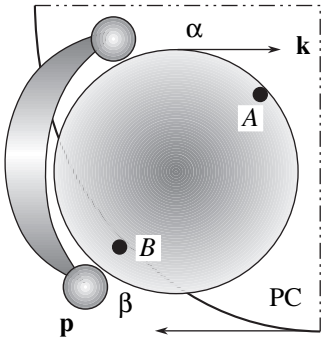

Fig. 8. Schematic diagram of the control over the operation of the compass with a holder.

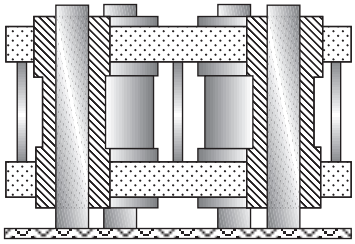

Fig. 9. Holder for polishing end faces of scintillators.

The workpieces were polished on Yu1.M1 machines. In order to provide the smoothness of the start and stop of the polishing operation, the machines were equipped with Mitsubishi FR-E540-7.5K frequency converters.

Special tools were designed for in-line polishing. The masses of the tools and additional weights were chosen so that the resultant vector of the gravity force and the torque of the polishing table could not lead to distortions of the element shape.

A suspension prepared on the basis of distilled water and a diamond submicropowder served as an abrasive. The end and lateral faces were polished using ACM 1/0 and ACM 2/1 submicropowders, respectively.

Holders for polishing ensured the secure fixation of workpieces in a polishing zone but were not fastened mechanically to parts and units of the machine. The polishing tables were equipped with positioning tools ("compasses"), which provide a way of moving workpieces in two degrees of freedom. This ensured a uniform polishing of all workpiece faces in the course of polishing.

The holder was rotated as a result of the difference between the centrifugal moments at the points *A* and *B* (Fig. 8). Bearing hinges α and β played the role of fasteners of the holder and allowed the holder to rotate in the direction of rotation of polishing table. In this case, the instantaneous linear velocities of the holder and the polishing table are characterized by the vectors *k* and *p*, respectively.

The holders with a rigid composite design were used for polishing end faces. Holder flanges were made from textolite, and parts ensuring the rigidity and security of the structure were produced from aluminum. Each workpiece was placed in an aluminum barrel and fixed along the guiding planes. The force pressing the end face to the surface of the polishing table was determined by the total weight of the barrel and the workpiece and was identical for all workpieces. This simplified the control over the removal of the crystalline material.

Composite holders whose parts were prepared from textolite were used to polish lateral faces. On the polishing table, workpieces were freely placed in a textolite holder located inside a guiding ring. A casing for composite weights was placed on workpiece faces opposite those to be processed.

The schematic diagrams of tools for polishing end and lateral faces of scintillators as a unit are depicted in Figs. 9 and 10.

All the operations associated with the processing of PWO crystals were metrologically supported. This per-

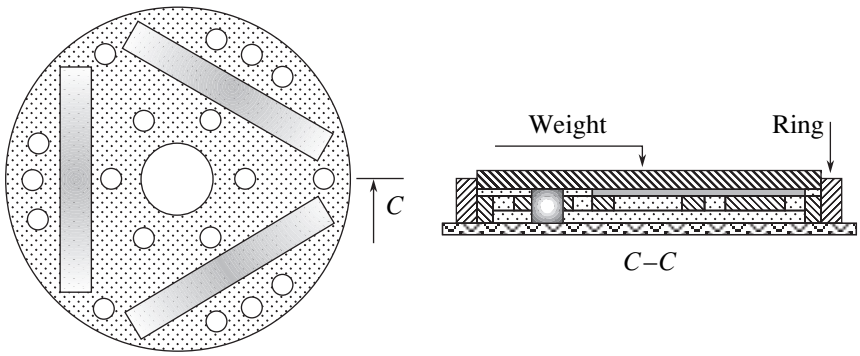

(a) Schematic arrangement of workpieces in the holder

(b) Holder with the weight as a unit

Fig. 10. Holder for polishing lateral faces of scintillators.

Table 3. Bragg angles for crystallographic planes of PWO crystals

(*hkl*)	*D* (*A*)	*I*, %	*Q*, deg
112	3.2512	100	13°42′17″
004	3.0115	20	14°49′10″
200	2.7310	30	16°22′56″
105	2.2043	2	20°27′11″

mitted us to opportunely reveal and correct possible deviations of the shape and dimensions from the specified values. In the technology used, the attraction is toward optical methods (laser stands) and also comparative testing methods based on the use of reference samples.

CONCLUSIONS

An advanced technology for large-scale processing of PWO crystals for investigations in the field of high-energy physics was developed and implemented using the processing equipment available at the North Crystals Company. More than 8000 scintillators satisfying the technical requirements of the ALICE project at CERN were fabricated according to this technology to date. A pilot batch of PWO scintillators Barrel and End Cup was produced for the CMS project at CERN. The good-to-bad ratio at the stage of mechanical processing of PWO crystals is more than 90%.

REFERENCES

1. E. Auffray, M. Lebeau, P. Lecoq, and M. Scheegans, CMS Note No. 1998/038 (CERN, Geneva, Switzerland, 1998).
2. M. Lebeau, CMS Note No. 1997/024 (CERN, Geneva, Switzerland, 1997).
3. A. Annenkov, M. Korzhik, and P. Lecoq, Nucl. Instrum. Methods Phys. Res. A **490**, 30 (2002).
4. S. Burachas, S. Beloglovsky, D. Elizarov, *et al*., Poverkhnost, No. 2, 5 (2002).
5. S. Burachas, S. Beloglovski, I. Makov, *et al*., J. Cryst. Growth **243**, 367 (2002).
6. S. Burachas, S. Beloglovsky, D. Elizarov, *et al*., Mater. Elektron. Tekh., No. 2, 35 (2004).
7. G. Tamulaitis and S. Burachas, Phys. Status Solidi A **157**, 187 (1996).
8. S. F. Burachas, in *Proceedings of the X National Conference on Crystal Growth, NKRK-2002, Moscow, Russia, 2002* (Moscow, 2002), p. 145.
9. CMS Technical Proposal, CERN ILH CC 94-98 (1994); TT ALICE (1999).

Translated by O. Borovik-Romanova

Crystallography Reports, Vol. 50, Suppl. 1, 2005, pp. S122–S123.

CRYSTAL GROWTH

Synthesis, Growth, and Properties of $TlGa_{1-x}Yb_xS_2$ Crystals

É. M. Kerimova, S. N. Mustafaeva, Yu. G. Asadov, and R. N. Kerimov

Institute of Physics, National Academy of Sciences, pr. Dzhavida 33, Baku, 370143 Azerbaidzhan

e-mail: ekerimova@physics.ab.az

Received February 8, 2005

Abstract—The synthesis of $TlGa_{1-x}Yb_xS_2$ single crystals with the partial substitution of ytterbium for gallium is described. Variations in the electric conductivity of grown crystals irradiated with X-rays of various intensities are measured. © *2005 Pleiades Publishing, Inc.*

The study of physical properties of the $TlB^{III}C_2^{VI}$ compounds (B = In, Ga and C = S, Se, Te) and solid solutions on their basis is very important for establishing the relations between their compositions and properties. Recently, we reported the influence of the intercalation of $TlGaS_2$ single crystals with lithium on the dielectric properties [1] and doping with iron on the photoelectric characteristics [2] of these crystals. The present study was undertaken to study the effect of the partial substitution of ytterbium for gallium in $TlGaS_2$ single crystals on their physical properties.

Homogeneous $TlYbS_2$, $TlGaS_2$, $TlGa_{0.999}Yb_{0.001}S_2$, and $TlGa_{0.995}Yb_{0.005}S_2$ samples were obtained by the method of direct synthesis, i.e., by the reaction between the starting components. Homogeneous $TlGa_{1-x}Yb_xS_2$ (x = 0; 0.001; 0.005, 1.0) single crystals were grown by the Bridgman method.

The samples synthesized were ground and placed into 10 cm-long quartz ampules with the internal diameter r = 1 cm evacuated to a pressure of 10^{-3} Pa and then were placed into a furnace having two temperature zones. In the upper furnace zone, the temperature was maintained above the melting points of the components by about 100 K. The temperature in the second zone was lower by 50 K than T_{melt}. The velocity of the ampule motion in the furnace was 0.3 cm/h. The location of the sharp ampoule end in the zone with the temperature T_{melt} resulted in the formation of a crystallization nucleus, whereas the velocity of the ampule motion in the furnace was sufficient for its further growth.

To identify the samples obtained, we obtained X-ray diffraction patterns from the samples synthesized and from the corresponding single crystals. These diffraction patterns turned out to be identical, which indicated the presence of only one phase irrespective of the sample composition. The crystallographic data obtained from the diffraction patterns are listed in the table.

We also studied electrical, photoelectrical, and X-ray dosimetric characteristics of the $TlGa_{1-x}Yb_xS_2$ single crystals. It was established that the partial substitution of ytterbium for gallium resulted in an increase in sample resistivity, displacement of the intrinsic-photocurrent maximum to the long-wavelength range of the spectrum, considerable broadening of the region of spectral sensitivity, and an increase in the amplitude of the extrinsic photocurrent.

Figure 1 shows the dependence of the coefficient of X-ray-induced conductivity of $TlGa_{0.999}Yb_{0.001}S_2$ single crystals at various accelerating potentials of the X-ray tube ranging from 25 to 50 keV. The coefficients of X-ray-induced conductivity, which characterize the sensitivity of single crystals to X-ray radiation, were

Crystallographic data for $TlGa_{1-x}Yb_xS_2$ single crystals

Composition	System	Lattice parameters					Sp. gr.	ρ_x, g/cm^3
		a, Å	b, Å	c, Å	β, deg	z		
$TlYbS_2$	Monoclinic	6.95	15.80	4.01	110	4	$C2_1/n$	7.086
$TlGaS_2$	Monoclinic	10.772	10.772	15.638	100.06	16	$C2/c$	5.560
$TlGa_{0.999}Yb_{0.001}S_2$	Monoclinic	10.776	10.776	15.646	100.06	16	$C2/c$	5.022
$TlGa_{0.995}Yb_{0.005}S_2$	Monoclinic	10.820	10.820	15.723	100.06	16	$C2/c$	4.962

1063-7745/05/5001-S0122$26.00

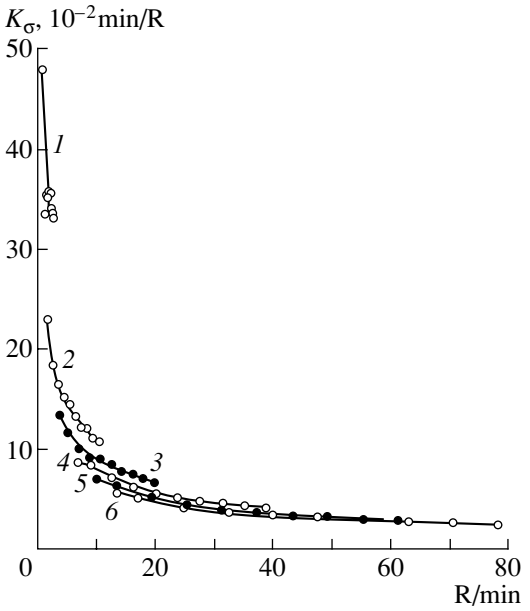

Fig. 1. Coefficient of X-ray sensitivity K_σ of the $TlGa_{0.999}Yb_{0.001}S_2$ single crystal as a function of the irradiation dose at various energies of the X-ray radiation: (*1*) 25, (*2*) 30, (*3*) 35, (*4*) 40, (*5*) 45, and (*6*) 50 keV (T = 300 K).

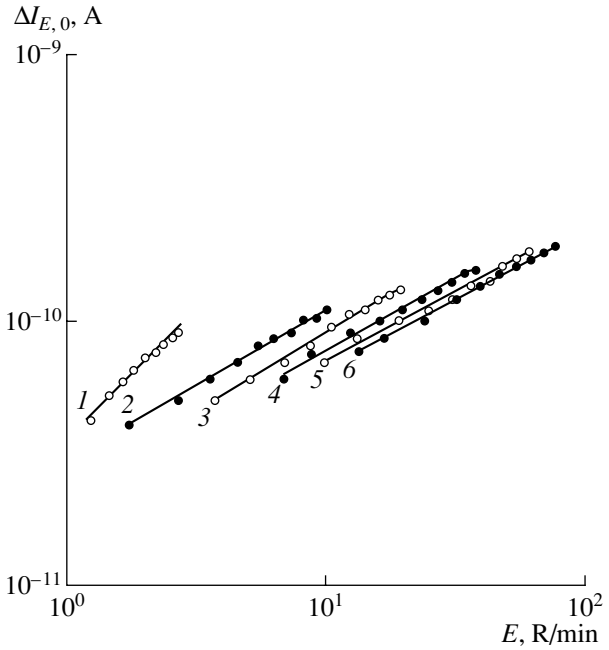

Fig. 2. X-ray-induced current in $TlGa_{0.999}Yb_{0.001}S_2$ single crystal at various accelerating potentials V, keV at the tube cathode: (*1*) 25, (*2*) 30, (*3*) 35, (*4*) 40, (*5*) 45, and (*6*) 50. T = 300 K.

determined from the equation

$$K_\sigma = \frac{\sigma_E - \sigma_0}{\sigma_0 E},$$

where σ_0 and σ_E are the sample conductivities before and after sample irradiation with X-rays, and E is the irradiation dose. The coefficient K_σ of $TlGa_{0.999}Yb_{0.001}S_2$ single crystals turned out to be thrice higher than the K_σ coefficient of $TlGaS_2$ single crystals. Analysis of the experimental data obtained showed that the coefficient K_σ of $TlGaS_2\langle Yb\rangle$ regularly decreases with an increase in the irradiation dose and accelerating voltage V. The characteristic behavior of $K_\sigma(E, V)$ may be explained as follows. At relatively low accelerating voltages, X-ray-induced conductivity is explained mainly by radiation absorption in the subsurface layer. In this case, an increase in the radiation intensity results in a prevalence of the mechanism of surface recombination described by a quadratic law, which, in turn, results in a decrease in the X-ray-induced conductivity. With an increase in the accelerating potential, the efficient harness of the X-ray radiation increases and the depth of radiation penetration into the crystal also increases. In other words, we observe the prevalent absorption-generation of free X-ray carriers in the volume. The fraction of the transmitted X-ray radiation increases. Thus, an increase in the accelerating potential results in a decrease in the coefficient of X-ray-induced conductivity and its more pronounced dependence on the radiation dose.

We also studied the dependence of X-ray induced current in $TlGa_{1-x}Yb_xS_2$ single crystals on the irradiation dose. Figure 2 shows the dependence of X-ray-induced current $\Delta I_{E,0}$ on the irradiation dose for $TlGa_{0.999}Yb_{0.001}S_2$ single crystals. It is seen that irrespective of the energy of X-ray radiation at an accelerating voltage ranging from 25 to 50 keV, these dependences are described by power laws.

Thus, the experimental results show that the partial Ga $\longrightarrow$ Yb substitution in $TlGaS_2$ resulted in an increase of the sensitivity coefficient to X-ray radiation, whereas the $\Delta I_{E,0} \sim E^\alpha$ characteristics tend to be linear, ($\alpha \longrightarrow 1$) tends to be linear in the region of low intensities (of the soft X-ray radiation E, R/min). In the region of high intensities of hard X-ray radiation, α tends to 0.5 (Fig. 2).

REFERENCES

1. S. N. Mustafaeva, Problemy Énergetiki, No. 3, 70 (2004).
2. É. M. Kerimova, S. N. Mustafaeva, and S. I. Mekhtieva, Prikl. Fiz., No. 4, 81 (2004).

Translated by L. Man

Crystallography Reports, Vol. 50, Suppl. 1, 2005, pp. S124–S129.

CRYSTAL GROWTH

Growth of Nonstoichiometric PbTe Crystals by the Vertical Bridgman Method Using the Axial-Vibration Control Technique

I. Kh. Avetisov, A. Yu. Mel'kov, A. Yu. Zinov'ev, and E. V. Zharikov

Mendeleev University of Chemical Technology, Miusskaya pl. 9, Moscow, 125190 Russia

e-mail: aich@rctu.ru

Received December 28, 2004

Abstract—A modification of the vertical Bridgman method with the excitation of low-frequency axial vibrations in the melt (axial-vibration control technique) is developed to grow crystals of volatile chemical compounds. It is shown that the use of the axial-vibration control technique in the growth of PbTe crystals makes it possible to obtain a more uniform distribution of the excess (nonstoichiometric) component over the crystal length. As a result of the intense melt mixing, equilibrium between the vapor phase, the melt, and the growing crystal is fixed so rapidly that it becomes possible to change the nonstoichiometry of a growing crystal by changing the vapor pressure. The composition of the congruently melting lead telluride, determined by comparing the nonstoichiometries of the initial charge and the crystal grown, was found to correspond to $(2.8 \pm 0.3) \times 10^{-4}$ mol excess Te/mol PbTe. © *2005 Pleiades Publishing, Inc.*

INTRODUCTION

The problem of the effective control of heat and mass transfer during the growth of crystals from melt is a subject of intense study. This problem is especially urgent for the Bridgman method, which is characterized by a low efficiency of heat and mass transfer in the liquid phase. In recent years, many attempts have been made to develop effective techniques of growth from melt with the application of a rotating magnetic field, precessing ampoule (CVS technology), ultrasound irradiation of melts, shaking of crystals, and many other methods [1–4].

Methods based on the use of the axial-vibration control (AVC) technique have proven to be the most developed ones, both theoretically and practically. In particular, as shown by numerous model experiments, excitation of axial low-frequency vibrations in a melt, either by introducing an inert vibrating body into the melt in the classical vertical Bridgman method or by applying vibrations directly to the growing crystal in the contactless modification of the Bridgman method [5–10], makes it possible to change significantly the hydrodynamics of fluxes in the melt. The result is changes in the characteristics of the diffusion layer, the curvature of the crystallization front, and some other factors, which significantly affect the characteristics of the crystals grown [5–7]. For example, the use of the AVC technique in [8] made it possible to reduce the density of growth dislocations from 10^3 to 1 cm^{-2} during the growth of sodium nitrate crystals.

The main difficulty in the implementation of a particular technique of melt activation is the absence of a differential approach to melts differing in viscosity, temperature, volatility, and chemical reactivity.

Experiments with the introduction of axial vibrations into a melt were carried out in an open system [11]. In the configuration of the vertical Bridgman method, low-frequency vibrations were introduced into the melt using a disk mounted on a rod, which, in turn, was subjected to mechanical vibrations using a low-frequency loudspeaker.

In this study, we attempted to extend the possibility of using the AVC technique for the crystal growth with controlling both the gas and vapor atmospheres at high (up to 10^6 Pa) and low (down to 10^{-1} Pa) pressures. We chose lead telluride as a model material to check the setup operation. Lead telluride is a narrow-gap semiconductor. There are many data in the literature on the growth of lead telluride crystals from both melt and vapor phase; thus, this compound can be considered a well-studied one [12, 13]. In contrast to $NaNO_3$, which can be grown in an open system in air, PbTe is grown in closed or quasi-closed systems. Taking into account the necessity of controlling the nonstoichiometry of crystals grown, the process should be performed at a controlled vapor pressure of one of the components, determined from the p_i–T projection of the phase diagram of the Pb–Te system.

EXPERIMENTAL

Construction of the Growth Setup

The schematic of the setup for crystal growth by the AVC technique is shown in Fig. 1. The setup is controlled by a personal computer and an LTC crate (ZAO L-Card [14]).

The heating unit of the system is a resistance furnace with seven energy-independent zones. The maxi-

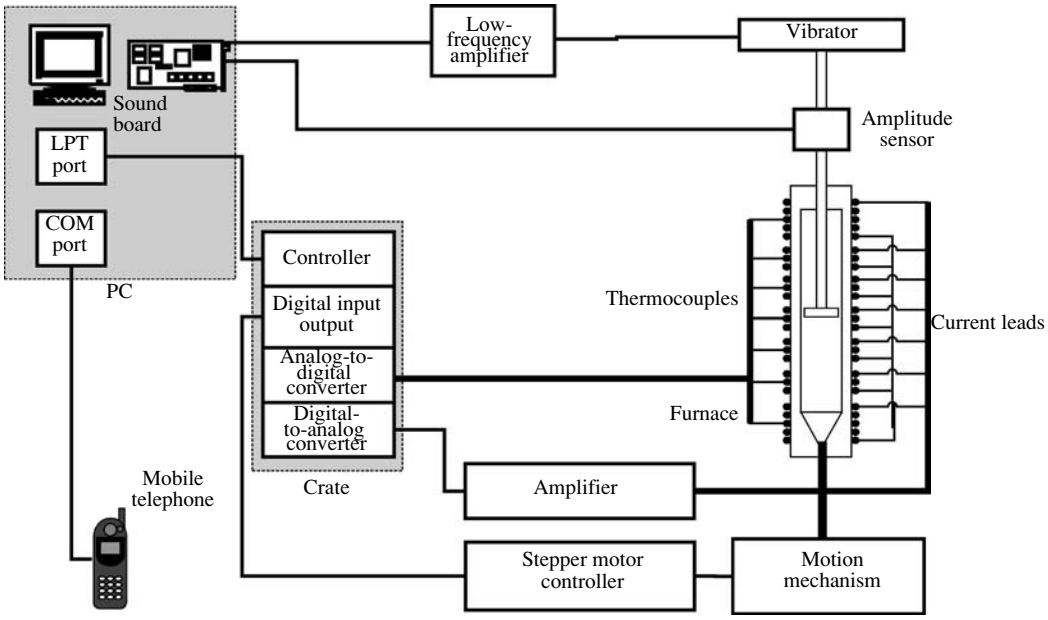

Fig. 1. Schematic of the setup for crystal growth by the vertical Bridgman method with the introduction of low-frequency vibrations into the melt.

mum operating temperature of the furnace is 1300 K; the error in maintaining temperature is ±0.1 K. The mechanism of motion of the growth ampoule, located in the bottom part of the heating unit, is controlled by a stepper motor. A unit step of the motor corresponds to a displacement of the ampoule by 0.2 μm.

Estimation showed that, at a velocity of ampoule motion of 2 mm/h, the maximum deviation of the growth rate from the average value does not exceed 2%.

The unit for the excitation of low-frequency vibrations (Fig. 2) is a system of external permanent magnets *4*, providing a free suspension of the internal permanent magnet *12* and the electromagnet *15*. The internal permanent magnet *12* is placed in a hermetic Teflon housing. The electromagnet *15* provides vibrations of the magnet *12* with a specified frequency and amplitude. A rod *6* with a disk *8* on the end is attached to the Teflon housing of the magnet *12*. During the crystal growth, the disk *8* is immersed in the melt *9*. The rod with the disk is positioned axially with respect to the growth ampoule *7*. The ampoule *7*, the rod *6*, and the disk *8* are removable and can be made of different materials (corundum, boron nitride, platinum, and so on). For the growth of lead telluride, we used elements made of quartz glass.

The electromagnetic vibrator can be shifted vertically to position the disk *8* with respect to the crystallization front. The frequency and amplitude of vibrations is controlled using a specially developed software. An output signal is generated by a sound board with a sampling rate of 40 kHz and amplified by a low-frequency amplifier. The vibration-amplitude feedback is performed using an electromagnetic sensor mounted on the vibrator rod. The computer software can give information about the current operating parameters of the setup and about an emergency situation by sending an SMS message. To this end, a Nokia 6110 mobile telephone was used with a standard Nokia Data Suite 3 interface.

The gas atmosphere in the growth ampoule should be inert to avoid oxidation of lead telluride. Evacuation of the ampoule makes it impossible to control the vapor phase during the crystal growth. The saturation vapor pressure of PbTe molecules at the melting temperature is about 7×10^3 Pa. Hence, when the growth ampoule is evacuated, the material rapidly evaporates and crystallizes in the cold part of the ampoule. Evaporation is enhanced significantly when the vibrating rod is introduced into the melt. Since the rod is colder than the ampoule walls because of the radial gradient, a significant fraction of resublimating lead telluride is condensed on the rod and, finally, jams it. During the experiments, we found that the introduction of argon with a partial pressure of about 8×10^4 Pa into the growth ampoule makes it possible to reduce significantly the evaporation rate of PbTe, as a result of which no more than 5% of PbTe is transferred to the cold part of the ampoule during the growth.

In the preliminary experiments, carried out without applying vibrations, the optimal velocity of vertical ampoule motion was determined to be 2 mm/h at a diameter of the growing crystal of 13 mm. The external temperature gradient in the crystallization zone was 50 K/cm. To compare the results obtained in the conventional and AVC processes, the same conditions were used to grow crystals using the AVC technique.

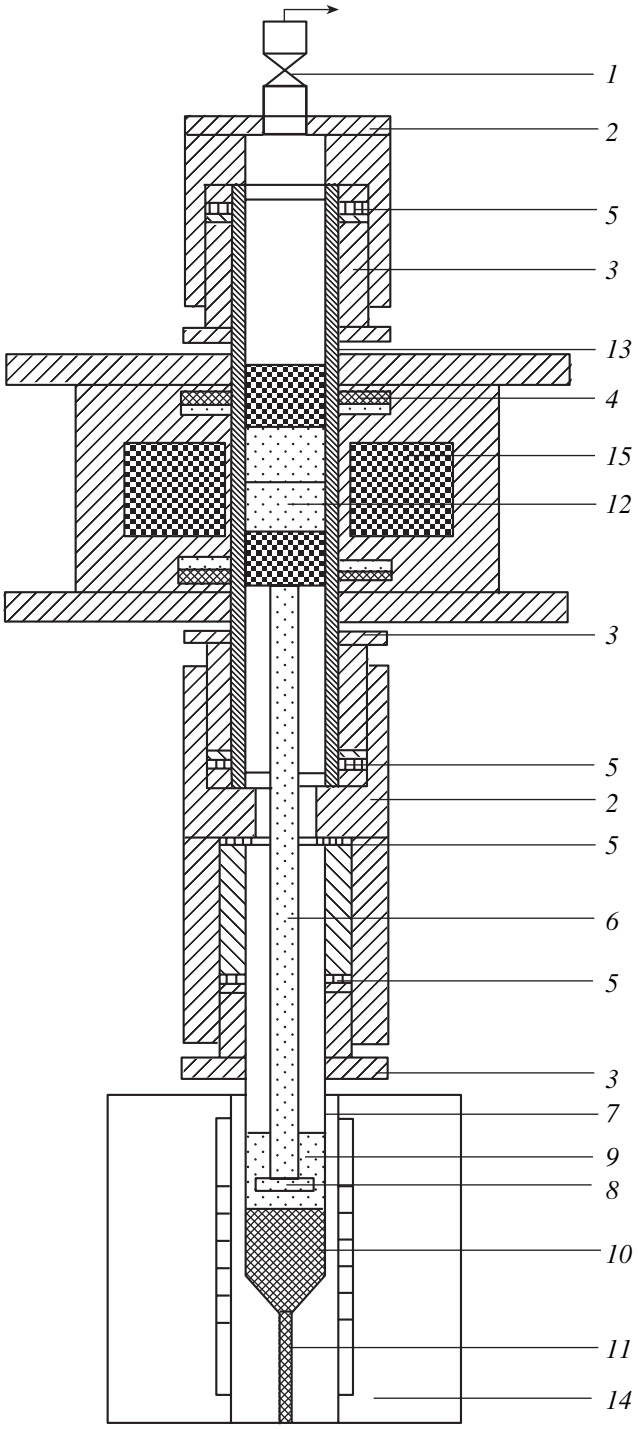

Fig. 2. Schematic of the growth system with the introduction of axial low-frequency vibrations into the melt in an evacuated ampoule: (*1*) vacuum valve; (*2*) tooth-seal housing; (*3*) tooth-seal nut; (*4*) external permanent magnet; (*5*) rubber ring; (*6*) vibrator rod; (*7*) growth ampoule; (*8*) vibrator disk; (*9*) melt; (*10*) crystal; (*11*) ampoule-displacement rod; (*12*) internal permanent magnet; (*13*) glass tube; (*14*) resistance furnace; and (*15*) electromagnet.

Charge Synthesis

The synthesis of nonstoichiometric lead telluride charge was performed in two stages. In the first stage, elementary tellurium (Extra grade, 99.999) and lead (high-purity C-000 grade) were melted in an evacuated graphitized quartz ampoule. The melt was homogenized at 1230 K for 6 h. To achieve completeness of the reaction, tellurium was taken in excess of 0.1 mol % with respect to the stoichiometric composition. After the synthesis, the polycrystalline ingot was ground to powder with an average grain size of 20 μm and the excess tellurium was removed by low-temperature distillation in a vacuum.

In the second stage, the polycrystalline compound obtained was subjected to annealing under controlled partial Te vapor pressure. The Te vapor pressure was chosen on the basis of the known p_{Te_2}–T–X diagram for lead telluride [15]. After the annealing, the ampoule with the compound was quenched and the nonstoichiometry of the compound was determined by the technique described below.

Measurement of the Characteristics of the Crystals

To determine the concentration of the excess component (the nonstoichiometry) in lead telluride, the method of extraction was used [16]. The essence of this method is as follows: upon annealing in an evacuated ampoule in a two-zone furnace, on the basis of the detailed analysis of the p_i–T–x_i phase diagram of the corresponding chemical compound, the conditions are determined at which the excess component is resublimated to the colder part of the ampoule. The temperature of the PbTe compound is 700 ± 10 K and the vapor pressure of Te_2 molecules is 10^{-7} Pa, which corresponds to a temperature of the colder part of the ampoule of 520 K. In this case, by the end of the annealing, the residual concentration of excess tellurium in the compound (whose temperature is higher) coincides with the stoichiometric composition within the measurement error (10^{-7} mol of excess component per PbTe mol) [17]. The amounts of tellurium and lead in the condensate were determined photocolorimetrically [18]. The detection limit of this method is 1 μg of Te(Pb) in a test sample. With allowance for this limit and the real weights of nonstoichiometric lead telluride (from 0.5 to 2 g), the detection limit of excess Te was 2×10^{-6} mol of excess component per PbTe mol.

The type, concentration, and mobility of free charge carriers were determined by measuring the dc-current Hall effect in a dc magnetic field [19].

The dislocation density in the crystals grown was determined in the (100) plane by the etch-pit method, using an etchant of the following composition: KOH : H_2O_2 : $C_3H_5(OH)_3$ (glycerin) : H_2O = 10 : 0.5 : 1 : 10 [20].

Fig. 3. Lead telluride crystal grown by the vertical Bridgman method with the introduction of axial low-frequency vibrations into the melt.

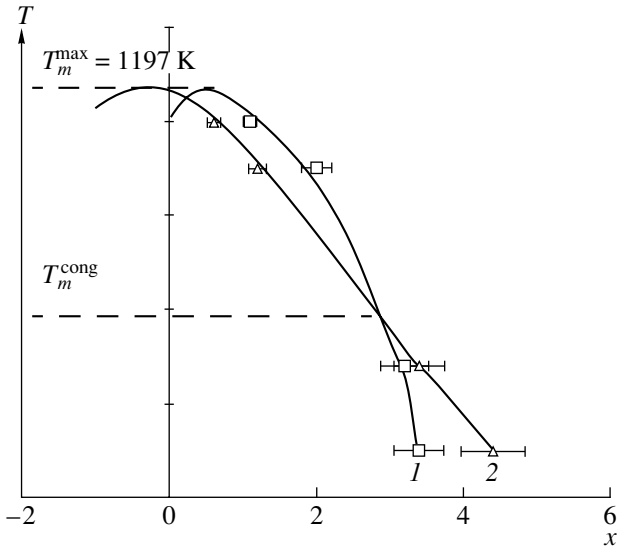

Fig. 4. (*1*) Solidus and (*2*) liquidus lines in the *T*–*x* projection of the phase diagram of the Pb–Te system near the maximum melting temperature of the PbTe compound (*x* is the excess-component concentration: 10^{-4} mol excess Te(Pb)/mol PbTe).

RESULTS AND DISCUSSION

The PbTe crystals grown were boules 40-mm-long in the cylindrical part (Fig. 3). The bottom (conical) part of the crystals was ~10-mm-long. To carry out measurements, the crystals were cleaved in the cleavage planes into three parts: bottom (conical), middle, and top. Table 1 contains the electrical parameters of the crystals, calculated from the Hall measurements.

Analysis of the data obtained showed that the top part of all crystals has a tendency towards a decrease in the concentration of holes, which are majority carriers in the case of the incorporation of excess tellurium into lead telluride [21, 22]. At the same time, the mobility of majority carriers is the highest in the middle part for all crystals.

The difference between the total concentration of excess Te (determined by the direct physicochemical method) and the concentration of free charge carriers was used to calculate the concentration of neutral defects (Table 2). When lead telluride is used as an IR-photosensitive material, the concentration of electrically neutral defects, which can be recombination or attachment centers, determines the kinetic characteristics of the photoconductivity.

Comparison of the total defect concentration with the concentration of ionized defects (Table 2) shows that, as a result of an increase in the vibration amplitude, the difference in these concentrations decreases in all parts of the crystals. This fact indicates that ionized defects become dominant and make the largest contribution to the total defect concentration. Specifically, this situation is characteristic of the high-temperature equilibrium at the boundary of the homogeneity range of PbTe from the side of excess Te [15, 21]. Therefore, an increase in the vibration amplitude makes the chemical potentials of the components in different (solid, melt, vapor) phases closer to their equilibrium values. Thus, the results obtained can be analyzed on the basis of the equilibrium *T*–*x* projection of the phase diagram of the Pb–Te system.

At a vibration amplitude of 100 μm, when the nonstoichiometric Te concentration is almost constant along the entire crystal length, crystals were grown from charges with different excess Te concentrations. Suggesting that the mass transfer through the vapor phase during the crystal growth is suppressed by the inert-gas pressure ($P_{Ar} = 10^5$ Pa), we assumed that, in the initial stage of crystallization, the melt composition

Table 1. Electrical characteristics of the PbTe crystals

Part of the crystal	*A*, μm	X_{Te} in the charge	$p(n)$, cm^{-3}	*m*, $V\ cm^{-1}\ s^{-1}$
Top	0	1.2×10^{-4}	-1.7×10^{18}*	550
Middle			1.5×10^{18}	820
Bottom			1.1×10^{18}	740
Top	36	1.2×10^{-4}	2.9×10^{18}	530
Middle			1.5×10^{18}	750
Bottom			1.8×10^{18}	730
Top	50	1.2×10^{-4}	4.3×10^{18}	440
Middle			1.7×10^{18}	950
Bottom			1.1×10^{18}	900
Top	100	1.2×10^{-4}	3.4×10^{18}	350
Middle			2.2×10^{18}	620
Bottom			2.9×10^{18}	590

* *n*-type conductivity.

Table 2. Concentrations of charged and neutral point defects in PbTe crystals grown at a vibration frequency of 50 Hz and different vibration amplitudes

A, μm	Part of the crystal	X_{Te} in the charge	X_{Te}	X_{ion}	X_{neutr}	$\lvert X_{neutr}/X_{ion}\rvert$
		10^{-4} mol excess Te/mol PbTe				rel. units
0	Top	1.2		–0.57*		
	Middle		0.40	0.51	–0.11	0.21
	Bottom		2.00	0.37	1.63	4.40
36	Top	1.2	0.94	0.98	–0.04	0.04
	Middle		2.00	0.51	1.49	2.96
	Bottom		2.30	0.61	1.69	2.79
50	Top	1.2	0.40	1.45	–1.05	0.72
	Middle		1.47	0.57	0.90	1.57
	Bottom		1.97	0.37	1.60	4.31
100	Top	1.2	1.29	1.15	0.14	0.13
	Middle		1.34	0.74	0.60	0.81
	Bottom		1.78	0.98	0.80	0.82
50	Top	4.4		0.35		
	Middle			0.44		
	Bottom		3.36	0.49	2.87	5.86
50	Middle	3.4	3.2	0.91	2.29	2.52

* *n*-type conductivity.

corresponds to that of the initial nonstoichiometric charge. In Fig. 4, these points correspond to the liquidus composition. The solidus composition was determined from the analysis of the nonstoichiometry of the crystals grown. Since we could not exactly determine the temperatures at which the crystallization occurred, relative values of temperature are plotted on the ordinate axis.

Analysis of the results showed that the congruent melting point of lead telluride corresponds to an excess of Te of about $(2.8 \pm 0.3) \times 10^{-4}$ mol excess Te/mol PbTe. The use of a charge of such composition allowed us to grow crystals with a much lower dislocation density (Table 3).

It was shown previously [23] that, at a fixed vibration frequency, a change in the vibration amplitude in the AVC technique makes it possible to change the crystallization-front shape from convex to concave, with an almost planar front at the optimal point. In this case, the density of growth dislocations in sodium nitrate crystals decreased by several orders of magnitude. As can be seen from Table 3, for the PbTe crystals grown from a charge with an excess Te concentration of 1.2×10^{-4} mol Te/mol PbTe, with an increase in the vibration amplitude to 100 μm, the dislocation density significantly increases. At the same time, the nonstoichiometry distribution becomes uniform over the crystal length. This behavior can be explained by the change in the curvature of the crystallization front from convex to concave with an increase in the vibration amplitude.

The excess Te concentration in the initial charge affects the dislocation density much stronger (Table 3). A decrease in the excess Te concentration, i.e., the use of a charge with a composition close to stoichiometric, leads to a significant increase in the dislocation density. Vice versa, the use of a charge with nonstoichiometry close to the congruent-melting point makes it possible to grow crystals with a very low dislocation density.

Table 3. Dislocation density in PbTe crystals grown from charges with different nonstoichiometry at a vibration frequency of 50 Hz and different vibration amplitudes

A, μm	X_{Te}, mol excess Te/mol PbTe	Dislocation density, cm^{-2}		
		top	middle	bottom
0	1.2×10^{-4}	3×10^5	1.5×10^5	2×10^5
36	1.2×10^{-4}	3×10^5	3×10^5	2.5×10^5
50	1.2×10^{-4}	3×10^5	2.5×10^5	3×10^5
100	1.2×10^{-4}	1×10^6	1.5×10^6	1×10^6
50	6.2×10^{-5}	2×10^6	2×10^6	2×10^6
50	3.4×10^{-4}	7×10^4	7×10^4	7×10^4

CONCLUSIONS

The use of axial vibrations of the solid immersed into a melt as a tool for controlling the heat and mass transfer in the melt during the crystal growth by the Bridgman method gives grounds to suggest that, under certain conditions, the physicochemical parameters of the crystallization process approach the equilibrium values. This circumstance allowed us to determine for the first time the composition of congruently melting lead telluride: $(2.8 \pm 0.3) \times 10^{-4}$ mol excess Te/mol PbTe.

The introduction of axial vibrations into a melt makes it possible to obtain a uniform nonstoichiometry over the length of a growing crystal.

The structural quality of the lead telluride crystals obtained by the Bridgman method depends much more strongly on the nonstoichiometry of the initial charge than on the processes of heat and mass transfer in the melt.

REFERENCES

1. A. S. Senchenkov, I. V. Barmin, A. S. Tomson, and V. V. Krapukhin, J. Cryst. Growth **197**, 552 (1999).
2. G. N. Kozhemyakin, Ultrasonics **35**, 559 (1998).
3. P. Dold and K. W. Benz, Cryst. Res. Technol. **32**, 51 (1997).
4. Y. C. Lu, J. J. Shiau, R. S. Feigelson, and R. K. Route, J. Cryst. Growth **102**, 807 (1990).
5. D. V. Lubimov, T. P. Lubimova, S. Meradji, and B. Roux, J. Cryst. Growth **180**, 648 (1997).
6. A. I. Fedoseyev and J. I. D. Alexander, J. Cryst. Growth **211**, 34 (2000).
7. A. I. Fedyushkin, T. G. Burago, E. V. Zharikov, and V. I. Polezhaev, in *Proceedings of the 7th All-Russia Symposium "Mechanics of Zero Gravity," Moscow, Russia, 2000* (Moscow, 2000), p. 365.
8. A. Yu. Zinov'ev, A. Yu. Mel'kov, A. Kh. Avetisov, and E. V. Zharikov, in *Proceedings of the 10th National Conference on Crystals Growth "NKRK-2002," Moscow, Russia, 2000* (Moscow, 2000), p. 376.
9. I. Kh. Avetisov, E. V. Zharikov, A. Yu. Zinov'ev, and A. Yu. Mel'kov, Prib. Tekh. Éksp. **4**, 146 (2004).
10. Y. Wang, L. L. Regel, and W. R. Wilcox, J. Cryst. Growth **260**, 590 (2004).
11. R. S. Feigelson and E. V. Zhrikov, Techn. Report No. NAG-1457-06 (2001).
12. A. V. Novoselova and V. P. Zlomanov, Curr. Top. Mater. Sci. **7**, 643 (1981).
13. V. Fano, Prog. Cryst. Growth Charact. **3**, 287 (1981).
14. www.lcard.ru.
15. I. Kh. Avetisov, Ya. L. Kharif, and P. V. Kovtunenko, Izv. Akad. Nauk SSSR, Neorg. Mater., No. 22, 410 (1986).
16. Ya. L. Kharif, in *Metods for Study of Deviations from Stoichiometry in Chemical Compounds*, Ed. by P. V. Kovtunenko (Mosk. Khim. Tekh. Inst. Mendeleeva, Moscow, 1988), p. 64 [in Russian].
17. I. Kh. Avetisov, Ya. L. Kharif, and P. V. Kovtunenko, Élektron. Tekh., Ser. Mater. **2**, 72 (1984).
18. Z. Holtzbecher, L. Divis, M. Kral, L. Sucha, and F. Vlacil, *Organic Reagents in Inorganic Analysis* (SNTL-Nakladatelstvi Technicke, Prague, 1975; Mir, Moscow, 1979).
19. E. V. Kuchis, *Methods for Studying the Hall Effect* (Sov. Radio, Moscow, 1974) [in Russian].
20. D. G. Coats and W. D. Lawson, Sr., J. Electrochem. Soc. **108**, 1038 (1961).
21. V. P. Zlomanov and A. V. Novoselova, *P–T–x Phase Diagrams of Metal–Chalkogen Systems* (Nauka, Moscow, 1987) [in Russian].
22. I. Kh. Avetisov, T. V. Zaĭchuk, and Ya. L. Kharif, Izv. Akad. Nauk SSSR, Neorg. Mater., No. 25, 567 (1989).
23. I. Kh. Avetisov, A. A. Chigrai, A. Z. Myaldun, *et al.*, in *Proceedings of the 3rd International Conference "Single Crystal Growth, Strength Problem, and Heat Mass Transfer," Obninsk, Russia, 1999* (Obninsk, 1999), p. 246.

Translated by Yu. Sin'kov

Crystallography Reports, Vol. 50, Suppl. 1, 2005, pp. S130–S135.

CRYSTAL GROWTH

Morphological Transition in the Cellular Structure of Single Crystals of Nickel–Tungsten Alloys near the Congruent Melting Point

V. M. Azhazha*, A. N. Ladygin*, V. Ja. Sverdlov*, P. D. Zhemanyuk, and V. V. Klochikhin****

** Kharkov Institute of Physics and Technology, National Scientific Center, ul. Akademicheskaya 1, Kharkov, 61108 Ukraine*

e-mail: sverdlov@kipt.kharkov.ua

*** PJSC Motor-Sich, ul. Vos'mogo Marta 15, Zaporozhye, 69068 Ukraine*

Received February 3, 2005

Abstract—The structure and microhardness of single crystals of nickel–tungsten alloys containing 25–36 wt % W are investigated. The temperature gradient at the crystallization front and the velocity of the crystallization front are the variable parameters of directional crystallization. It is found that, when the velocity of the crystallization front is 4 mm/min, the morphology of the cellular structure of the single crystals grown from nickel–tungsten alloys changes from square cells to hexagonal cells at a tungsten content of greater than or equal to 31 wt %. As the velocity of the crystallization front increases to 10 mm/min, no morphological transition occurs. It is shown that impurities play an important role in the formation of a cellular structure with cells of different types. © *2005 Pleiades Publishing, Inc.*

INTRODUCTION

Alloys in the nickel–tungsten system possess a number of specific features [1] that are important from both scientific and practical standpoints. Vekilov *et al.* [2] revealed that the thermodynamic properties of nickel–tungsten alloys containing approximately 35 wt % W exhibit an anomalous behavior due to the electronic topological transition occurring in a narrow concentration range. Nickel–tungsten alloys of the above composition are of great practical importance, because it is these alloys that can be successfully used as seeds for the growth of single-crystal blades of gas-turbine engines.

In this respect, it is of interest to investigate the growth of single crystals of nickel–tungsten alloys with a tungsten concentration in the vicinity of the congruent melting point [3].

It is known that the effect exerted by the chemical composition on the morphological stability of the crystallization front during growth of a single crystal is enhanced in the vicinity of the congruent melting point [4]. Moreover, soluble impurities also substantially affect the growth of the single crystal [5]. The quantitative conditions under which the planar crystallization front loses morphological stability and the crystal undergoes a transition to a cellular structure can be described by the Tiller–Jackson–Rutter–Chalmers criterion based on the theory of constitutional supercooling. According to Zasimchuk [5], the impurity concentration at which the planar crystallization front loses of stability lies over a rather wide range from several thousandths of an atomic percent to several atomic percent depending on the temperature and kinetic conditions of crystallization and on the impurity type.

There exists a principle of optimum doping of metal single crystals according to which the optimum content of soluble dopants or the optimum temperature and kinetic conditions of directional crystallization can be chosen in such a way as to provide the formation of a well-developed structure composed of regularly shaped large-amplitude equiaxial cells (usually, hexagonal in the cross section of the crystal) with a high degree of structural perfection. Therefore, it is particularly important to control the content of impurities in alloys used for growing single crystals.

The purpose of this work was to investigate the specific features of the growth and the cellular substructure of single crystals of nickel–tungsten alloys containing 25–36 wt % W.

SAMPLE PREPARATION AND EXPERIMENTAL TECHNIQUE

Single crystals were grown from nickel–tungsten alloys NV-4 (TU 1-92-112-87) of two different batches (hereafter, these alloys will be referred to as alloy *1* and alloy *2*). The compositions of these alloys are given in Table 1. In order to prepare alloys with a decreased tungsten content, the initial material (alloy *2*) was melted with electrolytic nickel via vacuum-induction melting under vacuum at a residual pressure of ~10^{-4} mmHg, followed by crystallization in a steel

Table 1. Results of the chemical analysis of nickel–tungsten alloys at different tungsten contents

Alloy	Nickel	Tungsten, wt %	Impurities, wt % (no higher)			
			Fe	Si	S	P
1	Basis metal	33.6	0.1	0.2	0.002	0.005
2	Basis metal	35.7	0.4	0.2	0.004	0.01
3	Basis metal	32.2	0.1	0.13	0.002	0.002
4	Basis metal	31.0	0.15	0.08	0.002	0.003
5	Basis metal	27.8	0.15	0.07	0.002	0.003
6	Basis metal	25.7	0.15	0.07	0.002	0.004
NV-4 (TU 1-92-112-87)	Basis metal	32–36	≤1.0	≤0.4	≤0.015	≤0.015

mold. The compositions of the alloys thus prepared were controlled using chemical analysis (Table 1).

The elemental composition of the alloys was determined by laser mass spectrometry with photographic recording. The measurements were performed on an ÉMAL-2 high-resolution laser mass spectrometer with Mattauch–Herzog double focusing and an IFO-451 recording microphotometer. The results of analyzing the elemental compositions of the alloys are presented in Table 2.

The single crystals were grown in a molding box fabricated from synthetic corundum. The molding box was preliminarily filled with a liquid melt and was then moved in a temperature field of the heater from the hot zone to the crystallizer. The velocity R of the crystallization front was changed stepwise from 0.4 to 10.0 mm/min. The temperature gradient G at the crystallization front was approximately 20 K/mm. After the directional crystallization, the ceramic box was broken and the samples were withdrawn for further investigations.

The single-crystal samples were prepared in the form of cylindrical rods 9 mm in diameter and ~150 mm long. The transverse and longitudinal microsections for investigations were prepared by cutting the cylindrical rods with a vulcanite wheel. In order to reveal the microstructure, the surface of the microsections was treated in a mixture of water with hydrofluoric and nitric acids (in a ratio of 2 : 1 : 1) for ~30–40 min at room temperature. The microstructure of the samples was examined under a Neophot-32 optical microscope. The crystallographic orientation and the degree of perfection of the single crystals were determined using X-ray diffraction analysis on a DRON-4 diffractometer (Cu_{K_α} radiation). The microhardness of the samples was measured on transverse microsections with a PMT-3 instrument at a load of 50 g.

RESULTS AND DISCUSSION

Earlier [3], we investigated the formation of a cellular structure of the nickel–tungsten alloy under different crystallization conditions as a function of the temperature gradient G and the velocity of the front of directional crystallization R. Alloy *1* was used as the initial material for growing single crystals. The optimum structure of the single crystals was observed at a velocity of crystallization front R = 4 mm/min. In this case, the single crystals have a cellular structure with square cells in the plane perpendicular to the growth direction (Fig. 1a). Under these crystallization conditions, the cells formed in the axial region enriched with tungsten exhibit dendritic features in the form of a Maltese cross. According to [5], the optimum cellular structure of the single crystal corresponds to a maximum amplitude of cellular asperities H/λ, where H is the height of cellular asperities and λ is the cell parameter. To put it differently, the optimum cellular structure is formed at the cell parameters corresponding to the changeover from the cellular growth to the dendritic growth.

Further investigations were carried out with nickel–tungsten single crystals grown from alloy *2*. It was revealed that the cellular structures of the single crystals with different chemical compositions (Tables 1, 2) differ significantly. At the same temperature and kinetic conditions, the cellular structure of the single crystals grown from alloy *2* contains hexagonal rather than square cells (Fig. 1b). Furthermore, the single crystals grown from alloy *2* exhibit a number of specific features, which, for convenience of comparison, are summarized in Table 3.

The difference in the morphology of the cells in alloys *1* and *2* is associated with the difference in their chemical compositions. As can be seen from Table 1, the content of the second main component (tungsten) is 33.6 wt % in alloy *1* and 35.7 wt % in alloy *2*. At these tungsten contents, the compositions of the alloys correspond to the ascending liquidus curve, because, according to the refined data [6], the congruent melting point is observed at a tungsten content of 36.8 wt %. Hence, the specific features that were previously revealed in the properties of disordered nickel–tungsten alloys at a tungsten content in the range 36.2–36.8 wt % and which were explained by the electronic topological transition [2] could not be exhibited in the case of alloys

Table 2. Elemental compositions of the NV-4 alloys

Element	Alloys						Remelted alloy *2*	Distribution coefficient of impurities in nickel k_0^{Ni} [11]
	1	*2*	*3*	*4*	*5*	*6*		
C	0.046	0.049	0.02	0.02	0.02	0.022	0.044	0.20
N	0.00067	0.00045	0.00024	0.00016	0.00012	0.00024	0.00047	
O	0.0031	0.00094	0.002	0.0012	0.00086	0.00052	0.0023	
Al	0.022	0.0001	0.025	0.00004	0.000095	0.00011	0.0003	0.87
Si	0.021	0.02	0.0002	0.0009	0.00038	0.00036	0.029	0.61
P	0.00018	0.00023	0.000095	0.00011	0.000082	0.000095	0.0012	0.02
S	0.0013	0.0014	0.0012	0.0016	0.0013	0.0013	0.0013	<0.01
K	0.00005	<0.00001	0.00011	0.00012	0.000075	0.000075	<0.00001	
Ca	<0.00001	<0.00001	0.00028	0.00028	0.00025	0.00023	<0.00001	<0.1
Ti	0.044	0.0003	0.0001	0.032	0.0012	0.00095	0.0001	0.65
V	0.0028	0.00018	0.00018	0.019	0.000125	0.000095	0.00015	0.84
Cr	0.26	0.017	0.015	0.1	0.012	0.015	0.02	0.86
Mn	0.0005	0.00072	0.00045	0.00041	0.00042	0.00043	0.00032	<1
Fe	0.075	0.062	0.038	0.038	0.038	0.045	0.064	0.93
Ni	Basis metal	Basis metal	Basis metal	Basis metal	Basis metal	Basis metal	Basis metal	<1
Co	0.104	0.02	0.031	0.37	0.023	0.017	0.02	<1
Cu	0.0048	0.0034	0.0048	0.0034	0.0029	0.0029	0.0027	0.81
Mo	0.059	0.0057	0.017	0.085	0.0091	0.0067	0.023	0.89
Nb	0.011	0.0045	0.005	0.085	0.0091	0.00022	0.005	0.86
W	~32.0	~38.0	~32.5	~31.0	~27.8	~25.7	~38.0	1.66
F			0.00002	0.000027	0.000018	0.0002		
Cl			<0.00001	<0.00001	<0.00001	<0.00001		
Br			<0.00008	<0.00008	<0.00008	<0.00008		

1 and *2*. Therefore, the difference in the shape of the cells is caused by the different concentrations of the impurities.

The cell parameters λ for the single crystals grown from alloy *2* are considerably smaller than those determined for alloy *1* in our earlier work [3]. According to the Brody–Flemings model of growth of cells [7], the parameter λ and the growth conditions at the crystallization front are related by the expression

$$\Delta T = m_L \Delta c_{\max} = \frac{GR\lambda^2}{2D_L}. \quad (1)$$

Here, ΔT is the difference between the liquidus temperatures for a particular difference between the concentrations of the dopant, m_L is the slope of the liquidus curve, $\Delta c_{\max}$ is the maximum difference between the dopant concentrations in the melt within the cell, G is the temperature gradient in the melt at the crystallization front, and D_L is the diffusion coefficient of the dopant in the melt. It can be seen from relationship (1) that the presence of dopants (especially, with a high diffusion mobility) in the melt leads to an increase in the size of the cells. In our case, as follows from the analysis of the elemental composition (Table 2), the content of impurities in alloy *1* is considerably higher than that in alloy *2* (in particular, the content of Cu, Nb, O, K, Co, Mo, Ti, V, Cr, or Al in alloy *1* can be higher than that in alloy *2* by a factor of 1.5 to 200). Most likely, this is the main reason why the size of the cells in alloy *1* is approximately 1.5 times greater than the size of the cells in alloy *2* over the entire range of crystallization front velocities (Table 3).

In order to confirm the inference that the impurities have a decisive effect on the morphology of the cellular structure, we grew single crystals from alloy *2* remelted in a ceramic molding box. After the remelting, the contents of O, Al, Si, P, and Mo impurities increased by a factor of approximately 3, 3, 1.5, 5, and 4, respectively (Table 2). As a result, the single crystal grown from this alloy at the velocity of crystallization front R = 4 mm/min had a cellular structure with square cells and the cell parameter λ = 214 μm.

The effect exerted by dissolved impurities on the morphology of the cells in nickel–tungsten single crys-

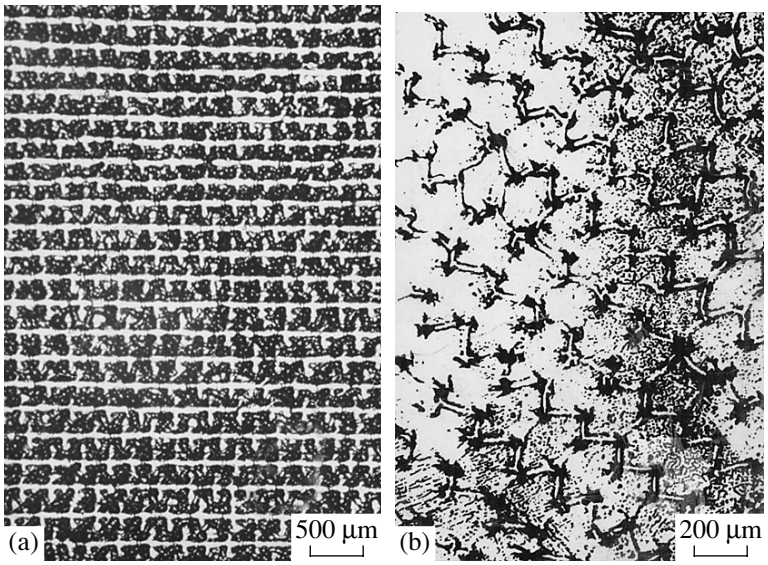

Fig. 1. Transverse microsections of the NV-4 alloy single crystals with different chemical compositions (a) Ni–33.6 wt % W and (b) Ni–35.7 wt % W at the velocity of the crystallization front $R = 4$ mm/min.

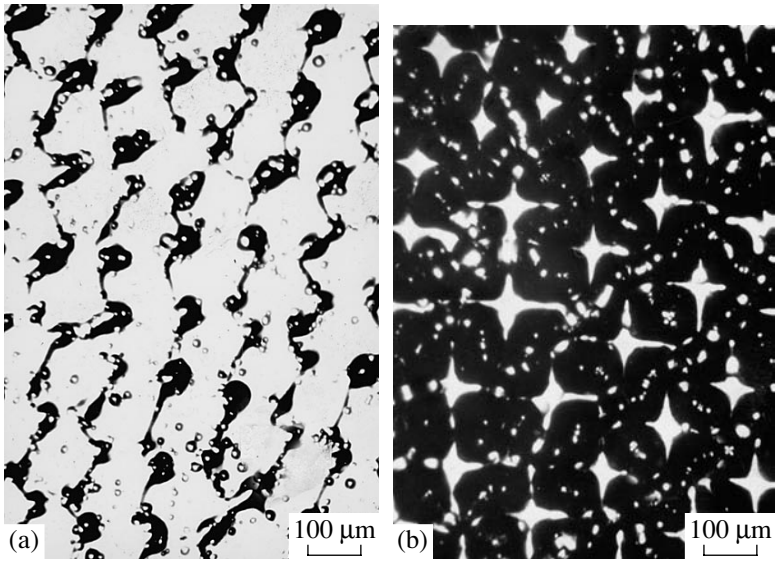

Fig. 2. Transverse microsections of the NV-4 alloy single crystals with decreased tungsten concentrations (a) Ni–32.2 wt % W and (b) Ni–27.8 wt % W at the velocity of the crystallization front $R = 4$ mm/min.

tals can be adequately described within the model of constitutional supercooling [8, 9]. According to this model, the planar front of directional crystallization at a constant temperature gradient G can lose its stability due to an increase both in the velocity of the crystallization front R and in the concentration of dissolved impurities. The evolution in the morphology of the cellular structure of the nickel–tungsten single crystals of alloys *1* and *2* with increasing velocity of crystallization front R is schematically illustrated in Table 4.

Thus, the results obtained indicate that the chemical composition of alloy *2* is inconsistent with the principle of optimum doping. This leads to unstable growth of single crystals and to the formation of a large number of structural defects. The problem can be solved by increasing the velocity of the front of directional crystallization [10]. However, such an increase gives rise to new problems associated with the ratio between the axial and radial components of the temperature gradient. In particular, this can result in a distortion of the shape of the macroscopic crystallization front.

The quality of the nickel–tungsten alloy single crystals can also be improved by decreasing the tungsten content. As follows from [11], the Ni–28 wt % W alloy

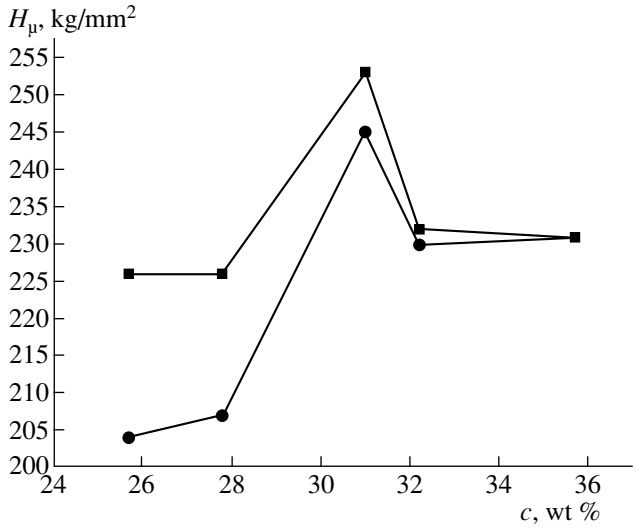

Fig. 3. Dependences of the microhardness on the tungsten concentration *c* in the nickel–tungsten single crystals in the upper (■) and lower (●) regions of the sample.

is technologically optimum for both the growth of single crystals and their subsequent use as seed crystals. For this reason, we prepared alloys with a decreased tungsten content (32.2–25.7 wt %). Alloy *2* was used as the initial material. Metallographic analysis of the microstructure of the single crystals grown at the velocity of crystallization front $R = 4$ mm/min revealed that a decrease in the tungsten content to 31.0 wt % leads to a morphological transition in the cellular structure from hexagonal cells to square cells. Figure 2 shows typical cellular structures of the single crystals at tungsten contents of 32.2 wt % (alloy *3*) and 27.8 wt % (alloy *5*), which were grown at the velocity of crystallization front $R = 4$ mm/min.

The measured dependence of the microhardness H_μ of the single crystals on the tungsten concentration correlates with the morphological transition in the cellular structure (Fig. 3). The microhardness measured in the upper regions of the single crystals containing 31 wt % W is higher than that observed in the lower regions. Most likely, this difference is associated with the phase separation caused by the increase in the temperature range of crystallization.

In conclusion, it should be noted that the degree of structural perfection of the single crystals with a decreased tungsten content (25.7–31.0 wt %) is higher than the degree of structural perfection of the single crystals grown from alloy *2* (with a tungsten content of 35.7 wt %) but lower than that of the single crystals grown from alloy *1*. This indicates that impurities play an important role in the stabilization of the cellular growth of nickel–tungsten alloy single crystals. In our opinion, the special role in this case is played by chromium impurities, because tungsten and chromium belong to the same group of the periodic table and their chemical interaction with nickel should exhibit similar features. Since the atomic weight of chromium is considerably lower and the diffusion mobility of chromium atoms is higher than those of tungsten atoms, the

Table 3. Specific features of the cellular microstructures of single crystals grown from alloys *1* and *2* at velocities of crystallization front $R = 1.2$–10 mm/min

Characteristic of the cellular microstructure	Alloy *1*	Alloy *2*
Cell shape	Square	Hexagonal
Cell parameter λ, μm	294–186	204–140
Cell boundaries	Not revealed	Clearly pronounced cell boundaries in the form of continuous stripes
Ordering of the cell arrangement in the plane perpendicular to the growth direction	Cells are arranged in ribbons aligned parallel to the [100] direction	Cells, as a rule, are arranged in a random manner
Stability of crystal growth	High	Low
Structural perfection	High degree of structural perfection	Large number of blocks with a misorientation angle of 1°–2°

Table 4. Morphology of cells in Ni–W alloys of different chemical compositions as a function of the velocity of the front of directional crystallization

Initial material	Velocity of the front of directional crystallization *R*, mm/min					
Alloy *1*	0.4	0.8	1.2	2.6	4.0	10
Alloy *2*	1.2	4	8	10	15	
Morphology of cells			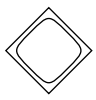			

former atoms can favor stable growth of nickel–tungsten alloy single crystals with a high degree of structural perfection.

REFERENCES

1. I. K. Zasimchuk, Metallofiz. Noveĭshie Tekhnol. **3**, 103 (2000).
2. Yu. Kh. Vekilov, A. V. Ruban, and S. I. Simak, Fiz. Tverd. Tela (St. Petersburg) **35** (10), 2750 (1993) [Phys. Solid State **35** (10), 1361 (1993)].
3. V. M. Azhazha, Yu. V. Gorbenko, G. P. Kovtun, *et al*., Kristallografiya **49** (2), 382 (2004) [Crystallogr. Rep. **49** (2), 307 (2004)].
4. R. A. Swalin, *Thermodynamics of Solids* (Wiley, New York, 1962; Metallurgiya, Moscow, 1968).
5. I. K. Zasimchuk, Metallofiz. Noveĭshie Tekhnol. **23** (3), 293 (2001).
6. O. M. Barabash and V. Z. Voĭnash, Metallofiz. Noveĭshie Tekhnol. **22** (2), 94 (2000).
7. R. E. Shalin, I. L. Svetlov, E. B. Kachanov, *et al*., *Single Crystals of Nickel Heat-Resistant Alloys* (Mashinostroenie, Moscow, 1997) [in Russian].
8. M. Flemings, *Solidification Processing* (McGraw-Hill, New York, 1974; Mir, Moscow, 1977).
9. I. K. Zasimchuk, Vysokochist. Veshchestva, No. 3, 159 (1991).
10. V. N. Toloraiya, N. G. Orekhov, E. N. Kablov, *et al*., Metalloved. Term. Obrab. Met., No. 7, 11 (2002).
11. *Crystallization from Melt: A Handbook*, Ed. by K. Khaĭn and É. Burig (Metallurgiya, Moscow, 1987) [in Russian].

Translated by O. Borovik-Romanova

Crystallography Reports, Vol. 50, Suppl. 1, 2005, pp. S136–S140.

CRYSTAL GROWTH

Synthesis and Physical Properties of $Ag_5Pb_2O_6$ Compound

A. I. Akimov and G. K. Savchuk

Institute of Solid State Physics and Semiconductors, National Academy of Sciences of Belarus, ul. Brovki 17, Minsk, 22072 Belarus

e-mail: akimov@ifttp.bas-net.by

Received February 8, 2005

Abstract—A simple method for the synthesis of the $Ag_5Pb_2O_6$ compound in argon atmosphere is suggested. The optimum conditions for the synthesis of the stoichiometric $Ag_5Pb_2O_6$ compound are determined on the basis of thermogravimetric and DTA data. It is shown that the introduction of strontium ions during synthesis does not considerably change the lattice parameters, crystal structure, electrophysical properties, or thermal stability of the compound. © *2005 Pleiades Publishing, Inc.*

INTRODUCTION

The $Ag_5Pb_2O_6$ phase has usually been achieved by two methods: (4–7)-day synthesis under high oxygen pressure (up to 10 MPa) at temperatures ranging within 350–550°C and (3–12)-day hydrothermal synthesis at 250–350°C [1–3]. The use of highly pressured oxygen and hydrothermal synthesis requires the use of expensive equipment and considerable energy consumption because of the long duration of the experiment. A new method for the synthesis of pure $Ag_5Pb_2O_6$ phase in vacuum with the use of carbon, which play the part of a reducing agent during synthesis was reported in [4]. The crystal structure of $Ag_5Pb_2O_6$ was studied elsewhere [2]. It was shown that the phase is described by the sp. gr. $P31m$ and has the unit-cell parameters a = 5.939(3) Å and c = 6.428 Å. Somewhat different data were indicated in [3, 5]: sp. gr. $P\bar{3}1m$, but the unit-cell parameters were slightly different: a = 5.9324(3) Å and c = 6.4105(3) Å. The physical properties of the compound were studied in [1, 5]. As far as we know, $Ag_5Pb_2O_6$ has never been synthesized in air atmosphere. The present study describes the synthesis conditions of this compound in air atmosphere and measurements of its physical properties.

EXPERIMENTAL

We suggest, for the first time, a cheap method for the synthesis of the $Ag_5Pb_2O_6$ phase in air atmosphere without the use of any specialized equipment. The $Ag_5Pb_2O_6$ compound was synthesized at the Laboratory of Electronic Ceramics at the Institute of Solid State Physics and Semiconductors of the National Academy of Sciences of Belarus by the method of solid-phase reactions. The (22–48)-h synthesis was performed with the use of SrO or $SrCO_3$ (0.02–0.50 wt %) at temperatures ranging from 310 to 400°C. Prior to synthesis, the starting powders were thoroughly mixed in isopropyl alcohol and were pressed into disklike tablets 18 mm in diameter and 3 mm in height.

The evaluation of the average grain size, the study of the microstructure of the sample fracture, and the determination of the elemental composition (EDX analysis) of the experimental samples were performed with the aid of a LEO electron microscope (Germany). Differential thermal analysis (DTA) of the experimental samples was performed with the use of a Setaram TGA92 thermal analyzer (France). The temperature dependence of electrical conductivity was measured by a four-probe method using ac current on the samples in the shape of parallelepipeds.

The lattice parameters of the $Ag_5Pb_2O_6$ phase synthesized with the use of SrO microadditions were refined by the Rietveld method [6].

RESULTS AND DISCUSSION

It is well known [7] that strontium ions change the character of atomic interactions in the PbO–CO_2 system. Therefore, it was reasonable to expect that the same process would also be possible in the PbO_2–Ag_2O and $PbCO_3$–Ag_2O systems.

We prepared the compounds with the compositions containing superstoichiometric amounts of SrO or $SrCO_3$ (0.02–0.50 wt %). The starting components for the synthesis of $Ag_5Pb_2O_6$ were $PbCO_3$ and Ag_2O and also PbO_2 and Ag_2O. The synthesis conditions and the experimental results are indicated in Table 1.

Analysis of the experimental data listed in Table 1 shows that the $PbCO_3$, Ag_2O, and SrO starting materials in the proportion 2 : 2.5 : 0.02 allowed us to synthesize the $Ag_5Pb_2O_{6-x}$ phase for 48 h at 380°C. The use of the PbO_2, Ag_2O, and SrO in the same proportion resulted in a 22-h synthesis of the $Ag_5Pb_2O_6$ compounds at the temperature 310°C. In the first case, the synthesis of the $Ag_5Pb_2O_{6-x}$ phase proceeded by the scheme

$$2PbCO_3 + 2.5Ag_2O + 0.02SrO$$

1063-7745/05/5001-S0136$26.00 © 2005 Pleiades Publishing, Inc.

Table 1. Conditions of $Ag_5Pb_2O_6$ synthesis in air with the use of SrO and $SrCO_3$ microadditives

Starting materials	Synthesis temperature, °C	Synthesis duration, h	Composition of phases synthesized
$PbCO_3$, Ag_2O, $SrCO_3$	380	24	90% $Ag_5Pb_2O_{6-x}$, Pb_2CO_4, $Pb_7C_4O_{15}$, $Pb_{0.57}O$
$PbCO_3$, Ag_2O, $SrCO_3$	400	24	10% $Ag_5Pb_2O_{6-x}$, Ag, Pb_3O_4, PbO
$PbCO_3$, Ag_2O, SrO	380	24	90% $Ag_5Pb_2O_{6-x}$, Pb_2CO_4, $Pb_7C_4O_{15}$
$PbCO_3$, Ag_2O, SrO	380	48	$Ag_5Pb_2O_{6-x}$
$PbCO_3$, Ag_2O, SrO	360	48	80% $Ag_5Pb_2O_{6-x}$, Pb_3O_4, Ag_2O
PbO_2, Ag_2O, $SrCO_3$	350	48	70% $Ag_5Pb_2O_{6-x}$, Pb_2CO_4, $Pb_7C_4O_{15}$
PbO_2, Ag_2O, $SrCO_3$	330	24	80% $Ag_5Pb_2O_{6-x}$, Pb_2CO_4, $Pb_7C_4O_{15}$
PbO_2, Ag_2O, SrO	350	48	50% $Ag_5Pb_2O_{6-x}$, Pb_2O_3, Ag
PbO_2, Ag_2O, SrO	320	48	90% $Ag_5Pb_2O_{6-x}$, Pb_2O_3, Ag
PbO_2, Ag_2O, SrO	310	22	$Ag_5Pb_2O_6$

$$\longrightarrow Ag_5Pb_2O_{6-x} + 0.02Sr + 2CO_2\uparrow$$

and, therefore, the compound thus synthesized has some "oxygen defects." Elemental analysis showed that the $Ag_5Pb_2O_{6-x}$ compound obeys the ratio Ag : Pb : O = 5 : 2.5 : 4.6, which confirms that the structure of the compound synthesized contains some oxygen defects.

In the second case, synthesis proceeded by the reaction

$$2PbO_2 + 2.5Ag_2O + 0.02SrO$$

$$\longrightarrow Ag_5Pb_2O_6 + 0.02Sr + 0.27O_2\uparrow.$$

The $Ag_5Pb_2O_6$ compound thus synthesized has no oxygen defects.

The experimental samples for studying physical properties and temperature stability of the $Ag_5Pb_2O_6$ compound were synthesized according to the second scheme.

Figure 1 shows the diffraction pattern from the $Ag_5Pb_2O_6$ compound synthesized with microadditions of strontium oxide under the above optimum conditions.

The experimental results indicated in Table 1 show that the introduction into the starting mixture of superstoichiometric strontium ions (0.02–0.50 wt %)

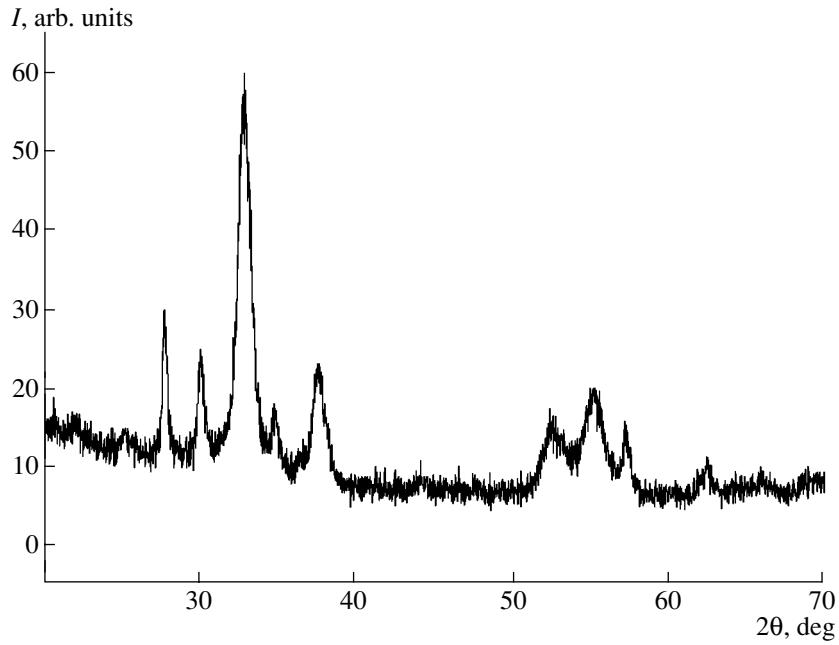

Fig. 1. X-ray pattern from $Ag_5Pb_2O_6$ sample.

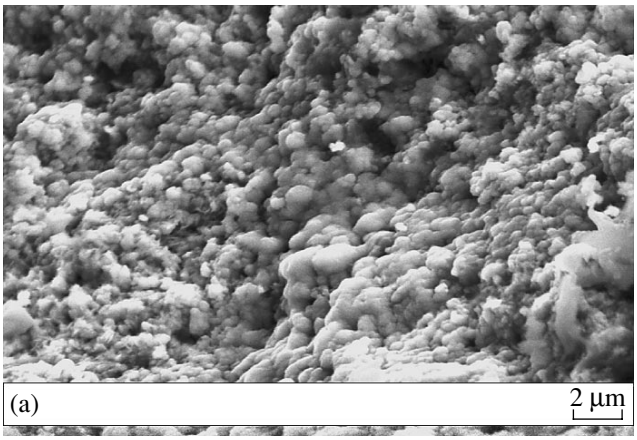

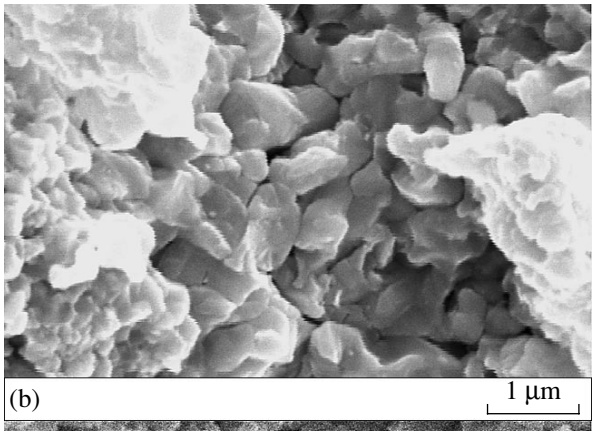

Fig. 2. Microstructure of the fracture of the $Ag_5Pb_2O_6$ sample at two magnifications: (a) 10000 and (b) 50000.

changes the free energy of the system, the rate of the proceeding reactions increases, and the $Ag_5Pb_2O_6$ compound is formed at a lower temperature. An increase in the Sr concentration above 0.5 wt % decelerates the rate of the component interaction and the phase is formed at a higher temperature.

The granulated microstructure of the fracture of the $Ag_5Pb_2O_6$ sample (Fig. 2) consists of fine grains (0.5–1.0 μm). The distributions of Ag, Pb, and O over the grain and the sample are inhomogeneous.

To analyze the effect of strontium ions on the structural parameters of the experimental $Ag_5Pb_2O_6$-based samples, we refined these parameters by the Rietveld method and compared the results obtained with the known data within the sp. gr. $P\bar{3}1m$. The refined parameters of the crystal structure are listed in Tables 2 and 3.

Our studies show that it is most probable that strontium ions in the unit-cell play the role of interstitial defects, since the unit-cell parameters and volume change only slightly. We failed to determine the distribution of strontium ion over the grain by X-ray microanalysis because the amounts of the introduced additions were too small.

Analysis of the results of the structural studies (Tables 2 and 3) shows that SrO microadditions in the synthesis of the $Ag_5Pb_2O_6$ compound slightly increase some interatomic distances (Ag(2)–Ag(2), Pb–O, and Ag(1)–Ag(1)) and slightly decrease some other distances (Pb–Pb, Ag(1)–O, and Ag(2)–O). The introduction of 0.02 wt % of SrO results in a 0.01% increase in the Ag(2)–Ag(2) distances, a 0.04% increase in the Pb–O distances, and a 0.29% increase in the Ag(1)–Ag(1) distances. The introduction of 0.5 wt % of SrO results in a 0.04% increase in the Ag(2)–Ag(2) distances, a 0.11% increase in the Pb–O distances, and a 1.54% increase in the Ag(1)–Ag(1) distances.

Thus, the introduction of a small amount of strontium ions during the synthesis of the $Ag_5Pb_2O_6$ phase does not noticeably change the structural parameters of the experimental samples based on this compound.

Table 2. Refined structural parameters of the $Ag_5Pb_2O_6$ phase synthesized in air with the use of strontium oxide microadditive

$Ag_5Pb_2O_6$ (0.02% SrO)				$Ag_5Pb_2O_6$ (0.5% SrO)			
atom	coordinates			atom	coordinates		
Ag	0	0	0.242	Ag	0	0	0.245
Ag	0.5	0	0	Ag	0.5	0	0
Pb	0.667	0.33	0.5	Pb	0.667	0.33	0.5
O	0.6224	0	0.6890	O	0.6226	0	0.6892
Unit-cell parameters	a = 5.933 Å c = 6.4106 Å			Unit-cell parameters	a = 5.935 Å c = 6.411 Å		
Unit-cell volume	195.424 Å^3			Unit-cell volume	195.568 Å^3		
R	5.5%			R	5.5%		

Table 3. Main interatomic distances in the $Ag_5Pb_2O_6$ structure at different strontium oxide contents

Interatomic distances, Å	SrO additive, wt %		
	0.0 [4]	0.02	0.5
Ag(1)–Ag(1)	3.0937(3)	3.1027(3)	3.1414(2)
Ag(1)–O × 3	2.2855(6)	2.2836(5)	2.2792(6)
Ag(2)–Ag(2) × 4	2.9662(4)	2.9665(3)	2.9675(3)
Ag(2)–O × 3	2.1220(3)	2.1218(0)	2.1212(3)
Pb–Pb × 3	3.4320(4)	3.4220(2)	3.4240(1)
Pb–O × 6	2.2169(9)	2.2178(2)	2.2194(8)

Table 4. Temperatures and enthalpy of $Ag_5Pb_2O_6$ decomposition at different heating rates

Stage of decomposition		Heating rate		
		1 K/min	5 K/min	10 K/min
First stage	Decomposition temperature, °C	448	477	484
	Enthalpy, kJ/mol	–10.367	–7.612	–7.045
Second stage	Decomposition temperature, °C	536	556	566
	Enthalpy, kJ/mol	–13.113	–13.126	–14.145

Therefore, it is reasonable to assume that the presence of strontium ions would not considerably affect the physical properties or the temperature stability of these samples. This assumption is confirmed by the experimental results of the temperature studies of resistivity of the $Ag_5Pb_2O_6$ samples (Fig. 3).

The shape of the curve in Fig. 3 shows that the $Ag_5Pb_2O_6$ samples possess metal-type conductivity. The sample resistivity at room temperature is (0.33–0.37) mΩ cm, which agrees (by the order of magnitude) with the results obtained in [1, 5] and indicates that strontium ions in $Ag_5Pb_2O_6$ do not change the electrophysical properties of the compound.

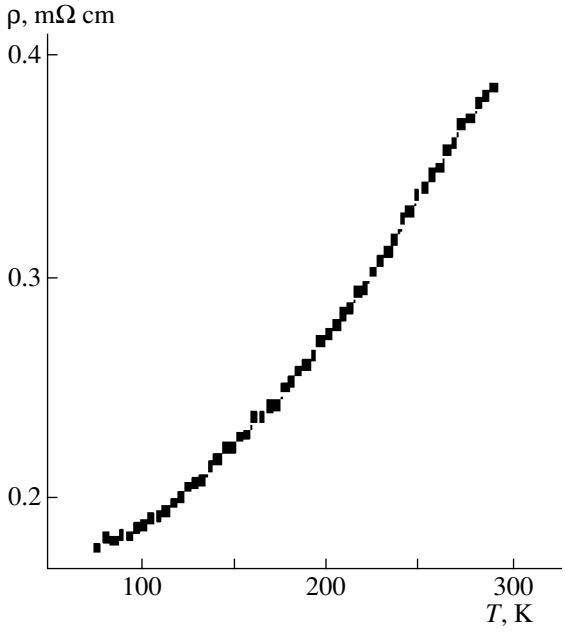

Fig. 3. Temperature dependence of $Ag_5Pb_2O_6$ resistivity.

The decomposition of $Ag_5Pb_2O_6$ synthesized with the addition of strontium oxide was studied by DTA in the temperature range 20–600°C (Fig. 4).

DTA and thermogravimetric studies of the sample decomposition were performed at the heating rate 1, 5, and 10 K/min. Curve *1* in Fig. 4 shows the temperature dependence of the thermal flux and the weight loss at the heating rate 1 K/min. Curve *2* shows the analogous dependence at the heating rate 10 K/min. The weight loss is determined as

$$3Ag_5PbO_6 \longrightarrow 15Ag + 2Pb_3O_4 + 5O_2,$$

$$2Pb_3O_4 \longrightarrow 6PbO + O_2.$$

The decomposition temperature of the compound depends on the heating rate at both the first and second stages of the process (Table 4). The content of strontium oxide in the samples does not influence the decomposition character and temperature. With an increase in the decomposition temperature at the first stage from 1 to 5 K/min, the decomposition temperature shifts by 30 K, whereas at the second stage, this shift is only about 20 K. The change of the heating rate from 5 to 10 K/min makes the shift of the decomposition temperature at both stages practically the same, ~10 K. The thermal effects obtained in DTA allowed us to calculate the enthalpy of the compound decomposition at each stage (Table 4). It is seen that the enthalpy *H* of the decomposition is considerably dependent on the heating rate only at the first stage. At the second stage and at the heating rates used, decomposition proceeds with the evolution of approximately the same amount of heat.

Comparative analysis of the data in [1, 8] shows that the decomposition of the $Ag_5Pb_2O_6$ samples at the heating rate 1 K/min proceeds at temperatures close to those indicated in [1, 8] (452 and 493°C). This indicates that the strontium ions introduced do not change the temperature mode or the character of the $Ag_5Pb_2O_6$ decomposition.

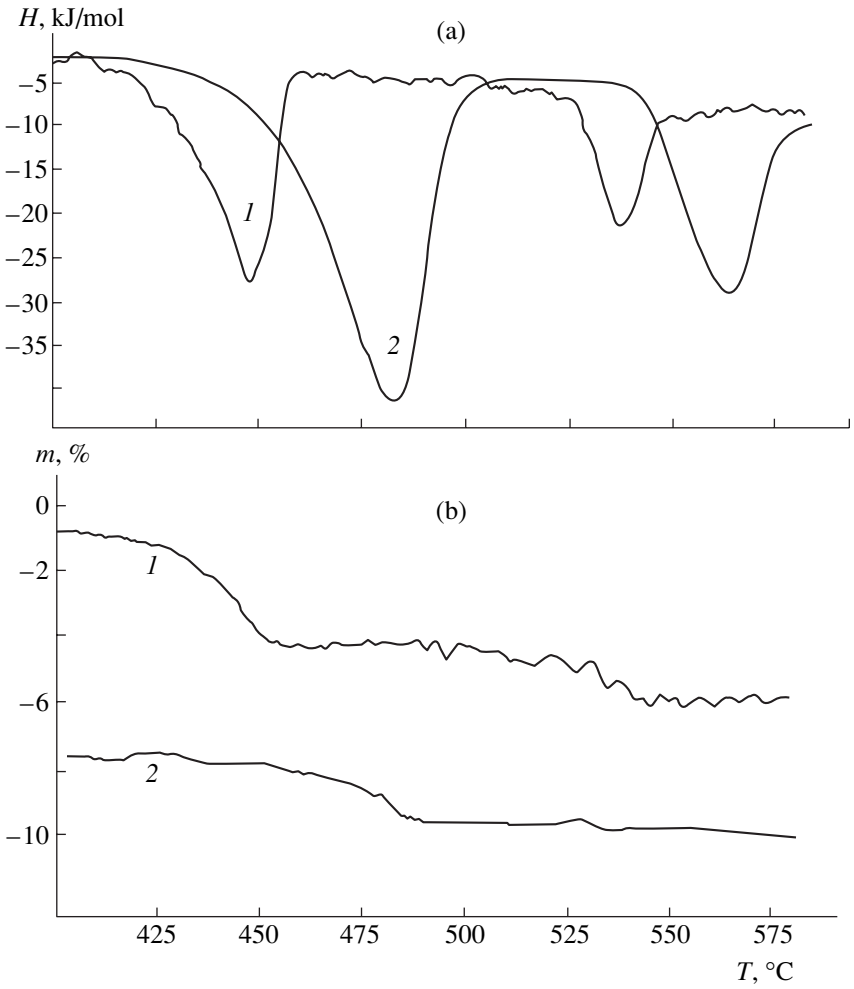

Fig. 4. Temperature dependence of the (a) thermal flux H and (b) weight loss m during heating of the $Ag_5Pb_2O_6$ sample at a rate of (*1*) 1 K/min and (*2*) 5 K/min.

CONCLUSIONS

The studies performed lead to the following conclusions.

A new simple and cheap method for the synthesis of $Ag_5Pb_2O_6$ compounds is suggested and the optimum conditions for the 22-h-synthesis of the compound at 310°C are determined.

It is established that the introduction of strontium ions during $Ag_5Pb_2O_6$ synthesis does not produce any significant effect on its structural parameters or on the conditions of its thermal stability.

It is also shown that the resistivity of $Ag_5Pb_2O_6$ samples at room temperature ranges within 0.35–0.37 mΩ cm. Conductivity of the compound is of the metal type.

ACKNOWLEDGMENTS

This study was supported by the Belorussian Foundation for Basic Research, project no. F01-157.

REFERENCES

1. M. Jansen, M. Borttz, and K. Heidebrecht, J. Less-Common Met. **161**, 17 (1990).
2. A. Bystrom and L. Evers, Acta Chem. Scand. **4**, 613 (1950).
3. M. Jansen and M. Bortz, J. Solid State Chem. **103**, 447 (1993).
4. D. Letian, S. Changjin, Z. Yuheng, and W. Haihu, Physica A **399**, 178 (2003).
5. M. Jansen, M. Bortz, and K. Heidebrecht, J. Cryst. Growth **241**, 347 (2002).
6. H. M. Rietveld, J. Appl. Crystallogr. **2**, 65 (1969).
7. K. Viyasaka and M. Senna, React. Solids **4**, 151 (1987).
8. I. Kouta, Y. Hisanori, K. Shunishi, *et al.*, Physica A **382**, 263 (2002).

Translated by L. Man

Crystallography Reports, Vol. 50, Suppl. 1, 2005, pp. S141–S144.

CRYSTAL GROWTH

Synthesis and Thermally Stimulated Luminescence of Polycrystalline $Sr_{1-x}Eu_xB_4O_7$

M. F. Dubovik, T. I. Korshikova, S. V. Parkhomenko, and A. V. Tolmachev

Institute for Single Crystals, National Academy of Sciences of Ukraine, pr. Lenina 60, Kharkov, 61001 Ukraine

e-mail: parkhomenko@isc.kharkov.ua

Received February 3, 2005

Abstract—Specific features of the solid-phase synthesis of $Sr_{1-x}Eu_xB_4O_7$ (x = 0–0.15) in air are studied. The photo- and thermally stimulated luminescence of $Sr_{1-x}Eu_xB_4O_7$ is investigated in the range of Eu content $0.01 < x < 0.15$. The main energy parameters of traps are determined. It is shown that the peak of thermally stimulated luminescence at T = 380 K can be related to the decomposition and radiative relaxation of the [$Eu^{3+}_{Sr^{2+}}$, F^+ center] pair. © *2005 Pleiades Publishing, Inc.*

INTRODUCTION

Strontium tetraborate SrB_4O_7 (SBO) is known to be a promising nonlinear optical material [1]. The luminescence properties of activated SBO:(Eu, Tm, Cu, Ag, Bi, Yb) crystals were investigated in [2–8] and the migration of the electron excitation energy in SBO:Eu crystals was analyzed in detail in [9]. It was shown in [10] that in the temperature range T = 300–670 K unactivated SBO crystals show thermally stimulated luminescence (TSL), whose intensity is comparable with that of a TLD-700 solid-state dosimeter based on LiF(Mg,Ti). Introduction of rare-earth activators into SBO may lead to the formation of new centers of light sum storage, i.e., to an increase in the TSL yield. This situation was implemented in SBO:Dy and SBO:Eu compounds [11–13]; however, no data on the nature of trapping centers in pure SBO and activated SBO:Eu were reported in the noted studies.

According to [13], the SrB_4O_7 and EuB_4O_7 compounds are isostructural. It is known that in SBO:Eu synthesized in air europium can be stabilized in the divalent state [2, 3, 9]. However, the concentration limit at which single-phase solid solutions $Sr_{1-x}Eu_xB_4O_7$ may exist during synthesis in air has not been determined. In this work we investigated the synthesis conditions for $Sr_{1-x}Eu_xB_4O_7$ solid solutions, determined the concentration incorporation limit for Eu^{2+}, and analyzed the thermoluminescent properties of these solutions.

EXPERIMENTAL

Samples of $Sr_{1-x}Eu_xB_4O_7$ (x = 0–0.15) were synthesized by the solid-phase method at T = 700–900 K in air. Differential thermal analysis (DTA) was performed on a Q-1500D (MOM) derivatograph and X-ray powder analysis (XPA) was carried out on a Siemens D500 diffractometer using Cu_{K_α} radiation. Optical measurements were performed on pelleted samples with a thickness of 3 mm and a diameter of 10 mm prepared by the pressing of synthesized powders under a load of 10^8 Pa. Before pressing, a powder weight was mixed with a 3% aqueous solution of polyvinyl alcohol in a ratio of 20 : 1 and carefully grinded. The pellet density was as high as 3.0 g/cm^3 and the hardness was 4 g/cm^3 at an average grain size of 1–2 μm. The photoluminescence (PL) of $Sr_{1-x}Eu_xB_4O_7$ samples was investigated on an SDL-2 (LOMO) automatic complex using a xenon lamp as an excitation source. TSL curves were recorded using an FÉU-79 photomultiplier on an experimental setup with a controlled heating rate (5 K/min). An X-ray tube with a copper anode (U = 160 kV, I = 9 mA) was used as a radiation source.

RESULTS AND DISCUSSION

The SBO compound is crystallized into an orthorhombic system with the lattice parameters a = 4.237 Å, b = 4.431 Å, and c = 1.0706 Å. A unit cell contains two formula units: Z = 2 [14]. SBO has a specific crystal structure formed by nonplanar six-membered rings of anionic groups $(B_3O_9)^{9-}$ consisting of three-dimensional $(BO_4)^{3-}$ groups (Fig. 1). In $(BO_4)^{3-}$ groups, each B atom is coordinated by four O atoms. The Sr atom in this structure is coordinated by nine O atoms; the Sr–O distance varies from 2.52 to 2.84 Å [14].

SBO was synthesized by the reaction

$$SrCO_3 + 4H_3BO_3 \longrightarrow SrB_4O_7 + 6H_2O + CO_2.$$

Figure 2 shows the DTA curves for the SBO samples obtained in different temperature and time modes. DTA curve *1* of the initial SBO mixture shows endothermic peaks in the range T = 120–140°C, which correspond to the dehydration of orthoboric acid. The diffuse exother-

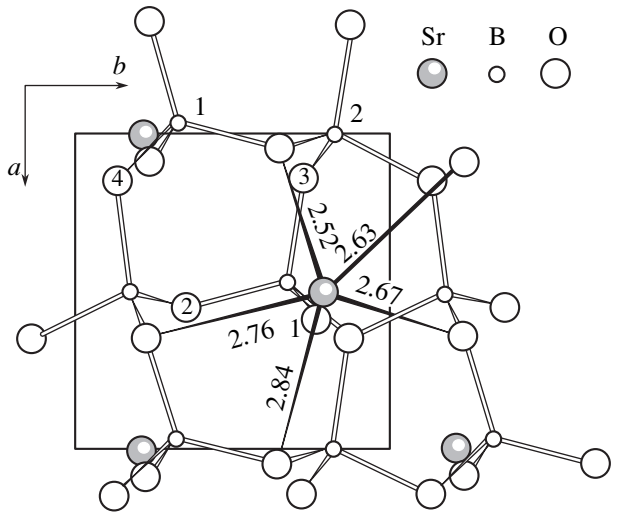

Fig. 1. Fragment of the SrB_4O_7 structure projected onto the (001) plane.

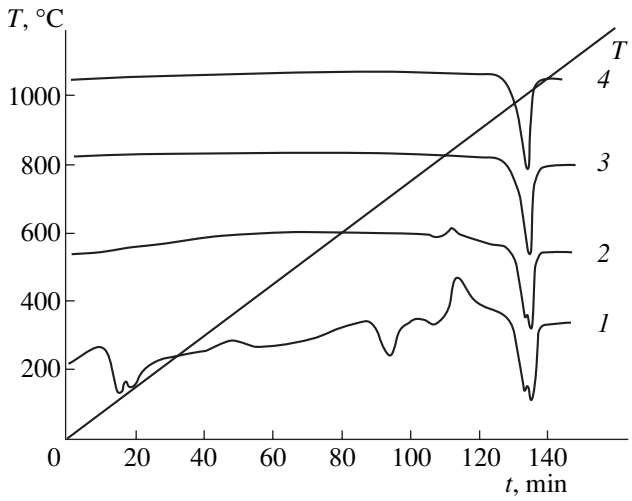

Fig. 2. DTA curves: (*1*) raw mixture of powders, (*2*) SBO after the heat treatment at T = 700°C for 5 h, (*3*) SBO after the heat treatment at T = 700°C for 5 h and T = 900°C for 5 h, and (*4*) $Sr_{1-x}Eu_xB_4O_7$ (x = 0.01–0.05) after the heat treatment at T = 700°C for 5 h and T = 900°C for 5 h.

mic peak in the temperature range 300–400°C is likely to be due to the phase transition in boron oxide. The reaction of solid-phase interaction between the components, accompanied by the mass loss due to the thermal decomposition of strontium carbonate, occurs in the temperature range from 660 to 900°C. The endothermic peak in the range 1005–1015°C corresponds to the melting point of SBO. We failed to fix the melt crystallization temperature of this system by the DTA method owing to the tendency to strong supercooling and glass formation and the high melt viscosity.

The DTA heating curve of the sample subjected to a heat treatment at T = 700°C (Fig. 2, curve *2*) shows a small exothermic peak at 850°C and a dual melting peak, which indicates an incompleteness of the solid-phase interaction in this system. According to the phase diagram data [15], the first peak at T = 1005°C may account for the decomposition of the incongruent phase $Sr_4B_{14}O_{25}$ formed as a second phase during the SBO synthesis, whereas the second peak at T = 1015°C corresponds to the SBO melting. Repeated annealing at T = 900°C with intermediate grinding allowed us to obtain a single-phase compound with the content of the first phase exceeding 95%. The corresponding DTA curve showed one endothermic peak related to the congruent SBO melting (Fig. 2, curve *3*).

In the series of $Sr_{1-x}Eu_xB_4O_7$ solid solutions, the maximum intensity of the Eu^{2+} PL corresponds to x = 0.15 [9]. The DTA curves of polycrystalline $Sr_{1-x}Eu_xB_4O_7$ samples with x = 0.01–0.05 prepared by the above-described technique show one endothermic peak at 1015°C, which is characteristic of congruent melting. The absence of other peaks is indicative of the single-phase composition of the samples. At higher Eu contents, the DTA curve of the $Sr_{0.85}Eu_{0.15}B_4O_7$ polycrystal show an additional endothermic peak at T = 440°C, which is likely to indicate the multiphase composition of these samples. According to the preliminary XPA data, the fraction of the phase of strontium tetraborate SrB_4O_7 in this sample is 85%; the second phases are europium tetraborate EuB_4O_7, europium orthoborate $EuBO_3$, and europium metaborate EuB_3O_6.

Taking into account that the ionic radii of the Eu^{2+} and Sr^{2+} ions have fairly close values (1.31 and 1.32 Å, respectively), we can suggest that the activator is incorporated into the crystallographic position of the Sr^{2+} ion. It is known that a rare-earth activator is in the highest charge state in the matrices in which its electronegativity χ is lower than the electronegativity of the cation it substitutes [16]. In the case under consideration, χ_{Eu} = 1.01 eV > χ_{Sr} = 0.99 eV. Therefore, when SBO is activated with europium, the formation of the activating center $Eu^{2+}_{Sr^{2+}}$ is the most likely process. Stabilization of the Eu ion in the divalent state during the synthesis in air is related to the presence of the rigid boron–oxygen framework composed of BO_4 polyhedra. This framework prevents Eu^{2+} ions from interaction with oxygen [3].

The PL data for the polycrystals confirm the above suggestion. The PL spectra of $Sr_{1-x}Eu_xB_4O_7$ (Fig. 3, curves *1–3*) show a band peaked near λ = 370 nm. This band is due to the $4f^65d - 4f^7$ transitions in Eu^{2+} ions [2]. The luminescence excitation spectrum of Eu^{2+} ions contains lines at λ_1 = 250 nm and λ_2 = 302 nm, which is consistent with the data of [2]. With an increase in the Eu content, additional peaks arise in the PL spectrum of the $Sr_{0.85}Eu_{0.15}B_4O_7$ sample in the wavelength range λ = 585–705 nm (see inset in Fig. 3). The PL in this range may be related to the presence of europium metaborate EuB_3O_6 (the second phase) in the $Sr_{0.85}Eu_{0.15}B_4O_7$ samples since europium orthoborate $EuBO_3$ does not luminesce in this wavelength range [17].

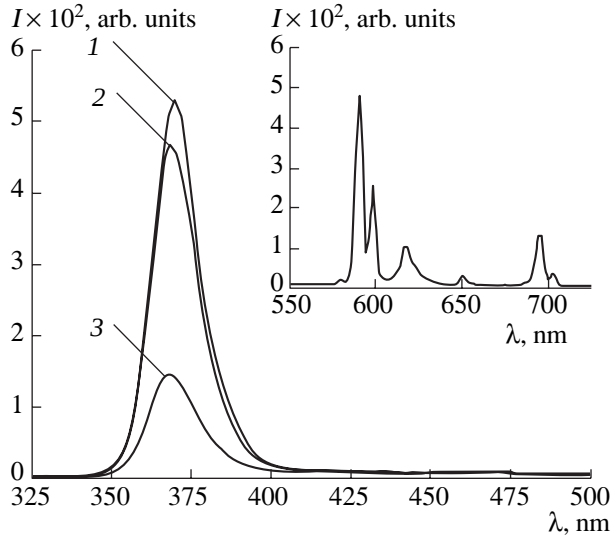

Fig. 3. PL spectra of $Sr_{1-x}Eu_xB_4O_7$ excited by radiation with λ = 270 nm: x = (*1*) 0.15, (*2*) 0.05, and (*3*) 0.01. The inset shows the Eu^{3+} PL spectrum of a $Sr_{0.85}Eu_{0.15}B_4O_7$ sample.

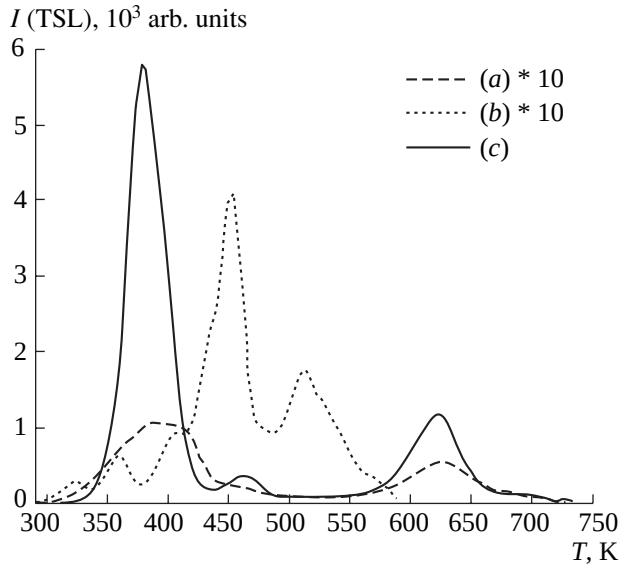

Fig. 4. TSL curves of (*a*) SBO, (*b*) TLD-100, and (*c*) $Sr_{1-x}Eu_xB_4O_7$ (x = 0.01).

All irradiated samples demonstrated a decrease in the PL intensity of Eu^{2+} ions. This can be due to the fact that some ions undergo the radiation-induced transition $Eu^{2+} \longrightarrow Eu^{3+}$. The TSL curve of pure SBO shows three peaks at T = 380, 460, and 625 K (Fig. 4a). Activation of SBO by europium does not lead to the occurrence of new TSL peaks but increases the intensity of the existing peaks (Fig. 4c). Note that the activation by europium most significantly affects the intensity of the low-temperature peak at T = 380 K. The parameters of traps were calculated, according to [18], by constructing a TSL curve in the coordinates $\ln(I/n)$–$1/T$ and $\ln(I/n^2)$–$1/T$. The recorded TSL peaks of the $Sr_{1-x}Eu_xB_4O_7$ samples (x = 0.01–0.15) are described by the first-order kinetics; their activation energies are 0.73, 1.21, and 1.95 eV, respectively. The TSL efficiency of $Sr_{1-x}Eu_xB_4O_7$ (x = 0.01) is higher by an order of magnitude than that of LiF(Mg,Ti) (TLD-100). At larger values of x (>0.05), the light sum stored by the crystals also increases (Fig. 5).

On the basis of the data obtained, we suggest that at the europium content x = 0.01–0.05 activating centers of one type ($Eu^{2+}_{Sr^{2+}}$) are formed in the positions of the substituted strontium. By the instant when the ionizing radiation is switched off, some part of Eu^{2+} ions have captured holes [19]. The Eu^{3+} ion has a smaller ionic radius in comparison with the Eu^{2+} ion (0.109 and 0.131 nm, respectively). Therefore, the capture of a hole by a Eu^{2+} ion should lead to the local distortion of the EuO_9 polyhedron and the excess charge should be compensated due to the polarization effect. During the irradiation, trapping centers (for example, F^+ centers) are formed in the oxide crystal $Sr_{1-x}Eu_xB_4O_7$. In the real structure, these centers can be located in the immediate vicinity of recharged Eu^{3+} ions and initiate the generation of Coulomb pairs [$Eu^{2+}_{Sr^{2+}}$, F^+ center]. Such a pair, stable at the instant of the irradiation termination, will lead to the light sum storage and contribute to the TSL. During the thermal decomposition, an F^+ center decays and an electron is captured by the Eu^{3+} ion with subsequent relaxation via radiative recombination: $Eu^{3+} + e^- \longrightarrow (Eu^{2+})^* \longrightarrow Eu^{2+} + h\nu$. After annealing

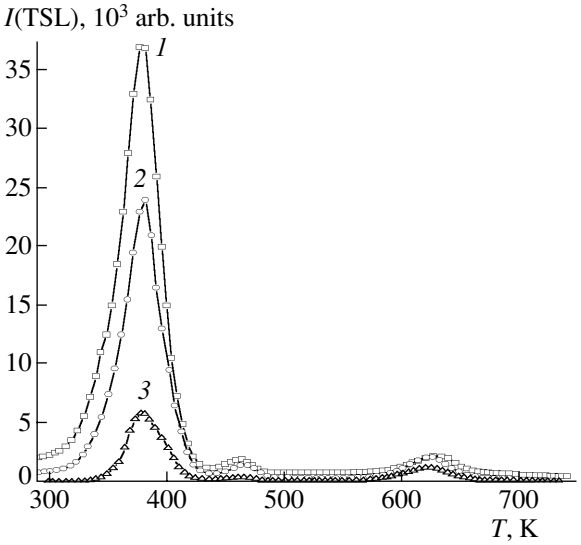

Fig. 5. TSL curve of the $Sr_{1-x}Eu_xB_4O_7$ samples with x = (*1*) 0.15, (*2*) 0.05, and (*3*) 0.01 subjected to X-ray irradiation with a dose of 9000 R.

at 700 K, the PL intensity of $Sr_{1-x}Eu_xB_4O_7$ returns to the initial value. Thus, the mechanism of the formation of the TSL peak at $T = 380$ K with the activation energy $E = 0.73$ eV is related to the thermal decomposition of electronic traps.

CONCLUSIONS

It is established that during the synthesis of $Sr_{1-x}Eu_xB_4O_7$ solid solutions ($x \le 0.15$) in air the second phases are europium tetraborate EuB_4O_7, europium orthoborate $EuBO_3$, and europium metaborate EuB_3O_6. It is shown that the activation of SBO by europium does not lead to the occurrence of new TSL peaks but only redistributes the intensity of the existing ones. The TSL peak at $T = 380$ K with the activation energy $E_T = 0.73$ eV can be due to the thermal decomposition of the F^+ center with subsequent radiative relaxation of the Eu^{2+} ion. The light sum stored in SBO:Eu^{2+} is larger by more than an order of magnitude than that stored in TLD-100, which gives grounds to consider SBO:Eu^{2+} as a promising material for thermoluminescent dosimetry of thermal neutrons.

REFERENCES

1. Yu. S. Oseledchik, A. L. Prosvirin, V. V. Starshenko, *et al.*, J. Cryst. Growth **135**, 373 (1994).
2. K. Machida, G. Adachi, and J. Shiokawa, J. Lumin. **21**, 101 (1979).
3. H. Liang, H. He, Q. Zeng, *et al.*, J. Electron Spectrosc. Relat. Phenom. **124**, 67 (2002).
4. W. J. Schipper, A. Meijerink, and G. Blasse, J. Lumin. **64**, 55 (1994).
5. J. W. M. Verwev, J. M. Coronado, and G. Blasse, J. Solid State Chem. **92**, 531 (1991).
6. A. Meijerink, M. M. E. van Heek, and G. Blasse, J. Phys. Chem. Solids **54** (8), 901 (1993).
7. G. Blasse, A. Meijerink, M. Nomes, *et al.*, J. Phys. Chem. Solids **55** (2), 171 (1994).
8. G. Blasse, G. J. Dirksen, and A. Meijerink, Chem. Phys. Lett. **167** (1–2), 41 (1990).
9. A. Meijering, J. Nuyten, and G. Blasse, J. Lumin. **44**, 19 (1989).
10. M. Santiago, A. Lavat, E. Caselli, *et al.*, Phys. Status Solids A **167**, 233 (1998).
11. M. Santiago, C. Grassely, E. Caselli, *et al.*, Phys. Status Solids A **185** (2), 285 (2001).
12. A. Lavat, E. Caselli, M. Santiago, *et al.*, Cryst. Res. Technol. **39** (10), 840 (2004).
13. K. S. Mishra, J. K. Berkovitz, B. G. DeBoer, and A. E. Dale, Phys. Rev. B **37** (13), 7230 (1988).
14. A. Perloff and S. Block, Acta Crystallogr. **20** (2), 274 (1966).
15. D. P. Kudrjavtcev, Yu. S. Oseledchik, A. L. Prosvirnin, *et al.*, J. Cryst. Growth **254**, 456 (2003).
16. M. F. Dubovik, A. I. Promoskal', and B. S. Skorobogatov, Opt. Spektrosk. **20** (3), 371 (1966).
17. Yu. V. Fenisov, B. F. Dzhurinskiĭ, and V. A. Kizel', Neorg. Mater **5** (7), 1240 (1969).
18. V. V. Antonov-Romanovskiĭ, *The Kinetics of the Photoluminescence of Crystal Phosphors* (Nauka, Moscow, 1966) [in Russian].
19. A. J. Wojtowicz, in *Proceedings of the Conference on Inorganic Scintillators and Their Applications, Delft, SCINT-95, Netherlands, 1995* (Delft Univ. Press, Delft, 1995), p. 95.

Translated by Yu. Sin'kov

Crystallography Reports, Vol. 50, Suppl. 1, 2005, pp. S145–S148.

CRYSTAL GROWTH

Mechanism of Formation of GaN Buffer Layers on Sapphire by Chemical-vapor Epitaxy

E. N. Vigdorovich

Moscow State Academy of Instrumentation Engineering and Informatics, ul. Stromynka 20, Moscow, 107876 Russia

e-mail: info@emal.zelcom.ru

Received December 28, 2004

Abstract—Conditions of nucleation during epitaxy are determined by the properties of the substrate surface and the process parameters. On the basis of the Gibbs representations, the nucleation energy and rate are calculated as functions of supersaturation for the process of metal–organic chemical-vapor epitaxy: heteroepitaxy (on Al_2O_3) and homoepitaxy of GaN (0001). The conditions for GaN crystallization and the possibilities of transition from three- to two-dimensional nucleation are determined. © *2005 Pleiades Publishing, Inc.*

INTRODUCTION

Nitrides of elements of the III group (GaN, InN, and AlN) and their alloys have some properties that make it possible to significantly improve the functional characteristics of optoelectronic elements, transistors, and other devices. A larger band gap, in comparison with conventional semiconductors (Si, GaAs, InP, and so on), a high carrier mobility, and better limitation of carriers in these nitrides make it possible to develop on their basis high-efficiency emitters of green, blue, and white luminescence and super-power transistors. Chemical-vapor epitaxy is the main method of fabrication of GaN-based heterostructures. Therefore, it is of great interest to investigate the processes of nucleation of epitaxial layers during the formation of multilayer structures [1–3].

INCUBATION PERIOD IN HETEROEPITAXY

In the study of the processes of epitaxy of semiconductors, one phenomenon that has attracted the attention of researchers has been referred to as the delay in the beginning of growth or the incubation period. During this period in the initial stage of the process, no epitaxial layer arises on the substrate. As far back as 1969, it was found [4] that, for the molecular-beam epitaxy of Si, the delay in the beginning of growth is 20 min. In the 1980s [5], an incubation period was observed for the homoepitaxy of Ge (180 s) and GaAs (10 s). Recently, this phenomenon has attracted the attention of researches studying the heteroepitaxy of GaN on sapphire (GaN/Al_2O_3) [6]. In the general case, the incubation period may include the characteristic times of different transient processes, which accompany the settling of an operation regime of the vapor-transport system, the period of time-dependent layer nucleation, supersaturation accumulation, kinetic factors, and so on. However, we believe the physicochemical aspects related to heteroepitaxial nucleation to be decisive factors.

According to the thermodynamic theory of crystallization, the total energy of a cluster of three-dimensional (3D) nuclei can be expressed as [7, 8]

$$\Delta G = \Delta G_V + \Delta G_S, \quad (1)$$

where ΔG_V and ΔG_S are the volume and surface components of the energy, respectively.

In a more detailed form,

$$\Delta G = a_3 r^3 \Delta F_V + a_1 r^2 \sigma_1 + a_2 r^2 \sigma_2 - a_3 r^2 \sigma_3, \quad (2)$$

where r is the cluster size; $\sigma_{1,2,3}$ are the free surface energies of the cluster, interface, and substrate, respectively ($\sigma_2 = \sigma_1 + \sigma_{ad}$, where $\sigma_{ad} < 0$); ΔF_V is the volume free energy of the material condensation; and a_i are the cluster-shape constants.

For a hemispherical boundary between the cluster and the gas phase, $a_1 = 2\pi$, $a_2 = \pi$, and $a_3 = (2/3)\pi$. The dependence (2) has a maximum corresponding to the values of the critical free energy (ΔG^{cr}) and the critical cluster size (r^{cr}), at which clusters begin to grow. At $\delta\Delta G/\delta r = 0$,

$$r^{cr} = -(2\sigma_1 + \sigma_2 - \sigma_3)/\Delta F_V, \quad (3)$$

$$\Delta G^{cr} = (r^{cr})^3 \Delta F_V. \quad (4)$$

For chemical-vapor epitaxy, ΔF_V is the thermodynamic supersaturation, which can be written as

$$\Delta F_V = (RT/V)\ln(K_p^* - K_p^0), \quad (5)$$

where V is the molar volume of a cluster; R is the universal gas constant; T is temperature; and K_p^* and K_p^0 are the constants of the corresponding chemical reac-

Parameters of the basal lattice plane (0001) and the free surface energy

Parameter	Al_2O_3	AlN	GaN	InN
a, nm	0.475	0.311	0.319	0.353
σ, (10^{-4}), J cm^{-2}	3.9	1.7	1.6	1.2

tions for the initial (*) and equilibrium (0) states, respectively (at the reactor input and in the growth zone).

Thus, calculating the critical size of a cluster for the real conditions of heteroepitaxy (temperature, supersaturation, and growth rate), we can determine the time τ of the formation of stable 3D films. In essence, this time is the incubation period:

$$\tau = r^{cr}/v^{hom}, \quad (6)$$

where v^{hom} is the rate of homoepitaxial nucleus growth.

In view of the absence of reliable data on the free surface energy of the materials under study, we estimated this parameter using the equation for the potential of Coulomb interaction between unlikely atoms in the crystallographic plane (0001) [4] (see table).

The estimated value of the surface free energy is $\sigma_2 = 2.6 \times 10^{-4}$ J/cm^2.

For typical conditions of the chemical-vapor heteroepitaxy of GaN on sapphire (temperature 1050°C, thermodynamic supersaturation $\Delta F_V = 9 \times 10^2$ J/cm^3), we find the critical cluster size $r^{cr} = 84$ Å and the incubation time $\tau = 21$ s. An increase in the growth rate leads to a decrease in τ and vice versa. A similar dependence should be observed with an increase in the supersaturation in the system.

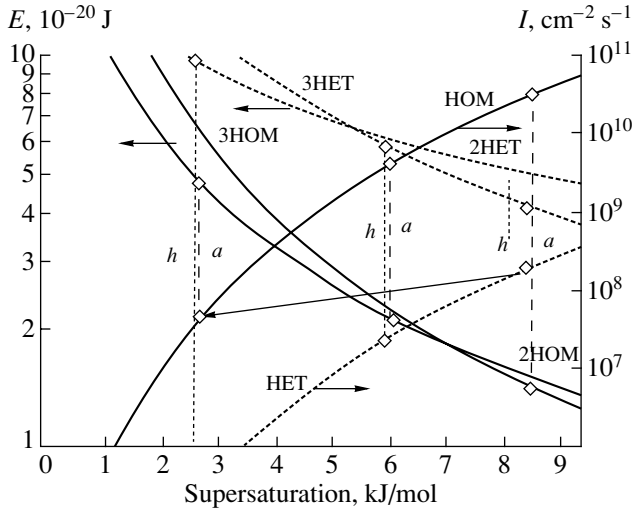

Fig. 1. Dependences of the energy E and nucleation rate I on supersaturation for the 2D (2HOM, 2HET) and 3D (3HOM, 3HET) nucleation during homo- and heteroepitaxy (HOM and HET, respectively).

FORMATION OF A BUFFER LAYER

The conditions for the layer nucleation during epitaxy are determined, on the one hand, by the physical and crystallographic properties of the substrate surface and, on the other hand, by the process parameters. The difference between the physical and crystallographic characteristics of the substrate and the layer determines the energy barrier during the nucleation, while the process conditions make it possible to control the nucleation mechanism, i.e., the formation of two-dimensional (2D) or 3D nuclei.

On the basis of the Gibbs representations [9], the equations for the work of the formation of 2D and 3D nuclei during epitaxy can be written as

$$E_2 = [\pi c V(2\sigma_1 + \sigma_2 - \sigma_3)^2/8\Delta F_V],$$
$$E_3 = [\pi V^2(2\sigma_1 + \sigma_2 - \sigma_3)^2/3\Delta F_V], \quad (7)$$

where V is the molar volume of a material, c is the thickness of a monolayer, and ΔF_V is the supersaturation.

For the chemical-vapor epitaxy of GaN using a metal–organic compound containing Ga (MOCGa) and NH_3 (hydride metal–organic vapor-phase epitaxy, MOVPE), which is performed at a large excess of ammonia, the MOCGa concentration in the vapor phase is the decisive factor in the crystallization and, accordingly, the supersaturation can be written as

$$\Delta F_V = RT\ln(P^*_{MOC}/P^0_{MOC}),$$

where P^*_{MOC} is the partial pressure of MOC Ga at the input of the reactor and P^0_{MOC} is the equilibrium pressure of MOC Ga at the substrate.

The nucleation rate can be written as $I_i = I_i^0 \exp(-E_i/kT)$. The kinetic coefficient I_i^0 is related to the adsorption ability of the crystallization surface. Therefore, this coefficient for heteroepitaxy (physical adsorption) on sapphire, I^0_{HET}, is significantly smaller than the corresponding coefficient for homoepitaxy (chemical adsorption), I^0_{HOM}. Analysis shows that the average value of the ratio I^0_{HOM}/I^0_{HET} is 1×10^4. The value of I^0_{HOM} taken for the analysis is 1×10^{14} cm^{-3} s^{-1}.

In this study, qualitative analysis of the nucleation in the range of real supersaturations is performed for GaN hydride MOVPE (Fig. 1). It can be seen that the nucleation can be implemented, for example, at small supersaturations, when the formation of 2D nuclei at hetero- (*het*) and homoepitaxy (*hom*) is energetically more favorable. However, the rate of heteroepitaxial nucleation is extremely small in this case and the incubation period may be fairly long. Heteroepitaxial at high rates is energetically favorable at large supersaturations and 3D nucleation. It can also be seen that, at high supersat-

urations, after the formation of a continuous 3D nucleation layer (and, therefore, at the transition from heteroepitaxy to homoepitaxy), the nucleation rate at the 3D growth sharply increases as a result of the decrease in the energy barrier, which leads to the formation of structurally disordered layers. In the range of intermediate supersaturations, we can implement 3D heterophase nucleation and 2D homoepitaxial growth, but it is technologically difficult to stabilize the growth conditions.

To obtain high-quality nucleation layers, it is expedient to perform heteroepitaxy at high supersaturations under conditions of 3D nucleation. In addition, at the instant of transition to homoepitaxy, the supersaturation in the system should be sharply decreased to change for the conditions of 2D nucleation (*het* $\longrightarrow$ *hom* in Fig. 1), which provides more perfect layers. This procedure is difficult to perform in an actual process.

We can decrease the energy jump when going from heteroepitaxy to homoepitaxy by decreasing the energy of the substrate surface. One of the ways to do this is to form monoatomic AlN layers on a sapphire substrate. Such a layer can be formed by either nitridation of the sapphire surface (i.e., treatment of sapphire in NH_3 vapor at high temperatures) or deposition of a thin Al layer on a sapphire substrate before the GaN epitaxy. In both cases, an AlN layer is formed on the sapphire surface, whose surface energy is close to that of GaN. In this case, the GaN nucleation can be almost immediately implemented through the 2D mechanism, which makes it possible to obtain layers of high crystallographic perfection.

Actually, all the main processes occurring during the two-stage GaN heteroepitaxy can be traced using laser reflectometry. The results are shown in Fig. 2. The reflectogram in Fig. 2 demonstrates all phases of the structure formation during the two-stage hydride MOVPE epitaxy. After the incubation period (Fig. 2; *1*, *2*), the formation of 3D nuclei (*3*) occurs at a low (600°C) temperature (LT), i.e., at high supersaturation. Primary coalescence (*4*), related to the growth of nuclei, occurs during the annealing with an increase in temperature (decrease in supersaturation) and is accompanied by a change in the shape and orientation of the nuclei. In this case, the density of nuclei decreases and diffusion zones are formed. The secondary coalescence (*5*) at a high (1050°C) temperature (HT) is accompanied by the coalescence of neighboring islands during their growth and exposure of large areas on the substrate surface, on which secondary nucleation may occur. Before the homoepitaxial growth (6), a crystallographic network with a large number of pores (channels) is formed, these channels are filled, and the growth surface is smoothed out; i.e., a transition to the 2D growth occurs.

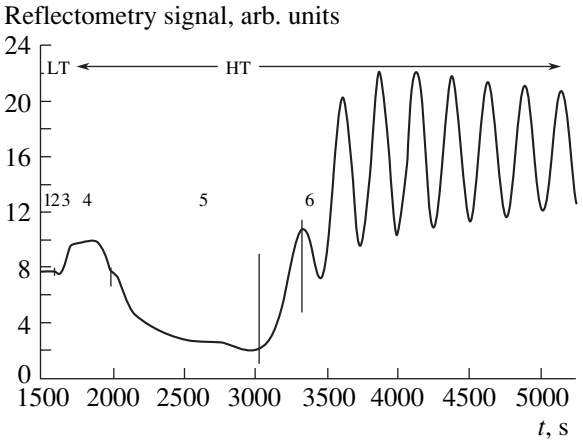

Fig. 2. Reflectogram of the GaN epitaxy (LT: 600°C, HT: 1050°C): (1) incubation period, (2) formation of subcritical nuclei, (3) formation of 3D nuclei, (4) primary coalescence, (5) secondary coalescence, and (6) 2D homoepitaxial growth.

CONCLUSIONS

The model proposed here was confirmed in the investigation of GaN nucleation on the $Al_2O_3(0001)$ surface, using MOVPE in a horizontal reactor with high-frequency heating. When the conditions of GaN nucleation are not optimal, low-resistivity buffer layers of low perfection with carrier concentrations from 5×10^{17} to 5×10^{18} cm^{-3} and carrier mobilities in the range 20–50 cm^2 V^{-1} s^{-1} are generally obtained.

When heterostructures for emitters are obtained, particular attention is given to the initial stages of nucleation during the heteroepitaxy. Optimization of the functional properties of heterostructures made it possible to determine the characteristics of the initial stages of the heterostructure growth. The thickness of the 3D low-temperature (450–650°C) nucleation layer should not exceed 20–25 nm. Annealing of the nucleation layer is carried out by increasing temperature to 1020–1070°C and decreasing the NH_3 consumption in the system, which provides good conditions for the transition from the 3D to the 2D growth of buffer layers with a low concentration of defects. The subsequent (homoepitaxial) layers, which form the active region of the heterostructure, are grown with increased NH_3 consumption at high temperatures (low supersaturation). GaN-based heterostructures obtained under these conditions can be used to design blue, green, and white light-emitting diodes with high efficiency (10–25%) [2].

Transistor technology requires the absence of a high-conductivity layer near the interface between the nucleation and main layers (N_D should not exceed 10^{16} cm^{-3}). These requirements can be satisfied using specially developed processes (formation of nucleation layers). For example, it was shown in [10] that, after the optimization of the growth process, the doped GaN layers with a carrier concentration of 4×10^{17} cm^{-3} had a

mobility up to 250 $cm^2 V^{-1} s^{-1}$. After the optimization (the two-stage growth), the width of the rocking curve (XRD FWHM) was 0.1°–0.08° at sapphire nitridation for 60 s, with the subsequent formation of Al monolayers before the growth of a (25–30)-nm $Al_{0.05}Ga_{0.95}N$ buffer layer. Such structures were used to design a test element of a field transistor with a channel length of 3 μm and a length of contacts of 60 μm with high functional characteristics.

REFERENCES

1. I. Akasaki, J. Cryst. Growth **237–239**, 905 (2002).
2. E. E. Zavarin, A. V. Sakharov, A. I. Besyul'kin, *et al.*, in *Proceedings of 2nd All-Union Conference "Nitrides of Gallium, Indium and Aluminium, Structures and Devices," St. Petersburg, Russia, 2003* (St. Petersburg, 2003), p. 91.
3. O. Ambacher, J. Phys. D: Appl. Phys. **31**, 2653 (1998).
4. B. A. Joyce, R. R. Bradly, B. E. Watts, and G. R. Booker, Philos. Mag. **19** (158), 403 (1969).
5. *Problems of Semiconductor Film Epitaxy*, Ed. by L. N. Aleksandrov (Nauka, Moscow, 1972) [in Russian].
6. V. B. Pushnyi, A. S. Usikov, B. Ya. Berg, *et al.*, in *Proceedings of 3rd Russian Conference on Physics of Semiconductors "Semiconductors-97," Moscow, Russia, 1997* (Moscow, 1997), p. 359.
7. O. G. Kozlova, *Growth of Crystals* (Mosk. Gos. Univ., Moscow, 1967) [in Russian].
8. *Physics of Fine Films*, Ed. by M. I. Elinson (Mir, Moscow, 1967), Vol. 2, p. 14 [in Russian].
9. K. Meyer, *Physicochemical Crystallography* (Metallurgiya, Moscow, 1972) [in Russian].
10. A. A. Arendarenko, E. N. Vigdorovich, Yu. N. Sveshnikov, *et al.*, in *Proceedings of 3rd All-Russian Conference "Nitrides of Gallium, Indium, and Aluminium: Structures and Devices," St. Petersburg, Russia, 2004* (St. Peterburg Gos. Ped. Univ., St. Petersburg, 2004), p. 26.

Translated by Yu. Sin'kov

Crystallography Reports, Vol. 50, Suppl. 1, 2005, pp. S149–S151.

CRYSTAL GROWTH

Growth of Homogeneous Single Crystals of GeSi Solid Solutions Using a Ge Seed by the Modified Bridgman Method

G. Kh. Azhdarov* and R. Z. Kyazimzade**

** Institute of Physics, Academy of Sciences of Azerbaijan, pr. Dzhavida 33, Baku, 370143 Azerbaijan*

*** Azerbaijani State Academy of Oil, Baku, Azerbaijan*

e-mail: zangi@physics.ab.az

Received February 7, 2005

Abstract—A modified technique for the growth of homogeneous Ge-rich GeSi single crystals is developed on the basis of the vertical Bridgman method using a Ge seed and a Si source rod. Single crystals were grown in two stages. In the first stage, a Si source rod was partially immersed in the Ge melt above the seed. A gradual increase in the Si content in the melt leads to constitutional supercooling at the crystallization front and to the growth of an inhomogeneous GeSi buffer single crystal. The first stage ends when the temperature at the crystallization front becomes equal to the liquidus temperature of the specified composition of the Ge–Si system. In the second stage, a homogeneous GeSi single crystal is grown while maintaining a constant growth temperature. The growth temperature is controlled by an appropriate balance between the pulling and feeding rates. Relations determining the optimal process parameters (the pulling and feeding rates and the temperature gradient at the crystallization front) for growing crystals of specified composition are obtained. © *2005 Pleiades Publishing, Inc.*

The classical semiconductors Si and Ge, which are basic materials of modern microelectronics, are completely dissolved in each other at any ratios in both the liquid and solid states. The potential range of application of GeSi solid solutions includes substrates for epitaxy, photo- and gamma detectors, solar cells, thermoelectric generators, and other optoelectronic devices. Hence, the problem of the fabrication of high-quality massive GeSe single crystals of specified composition is fairly urgent.

Recently, massive crystals of GeSi solid solutions were grown by the Czochralski method [1–7], the Bridgman method [8–12], the zone-melting method [12–14], the floating-zone method [15, 16], and the multicomponent zone-melting method [17]. In almost all these studies, the crystals grown had an inhomogeneous composition along the pulling axis because a limited amount of Si Ge melt was used in the growth process. It was only in a few studies that crystals with homogeneous regions containing from 2 to 15 at % of Si were obtained. These regions followed the initial region characterized by a nonuniform distribution of the components in the matrix

It has been noted that the main difficulties in growing homogeneous GeSi single crystals are related to the following specific features of the system. (i) A significant segregation of the components occurs during the growth, which leads to constitutional supercooling of the melt near the crystallization front and, as a result, to the violation of the single-crystal structure of the matrix. The equilibrium segregation coefficient of the components changes from 5.5 in Ge-rich compositions to 0.33 in Si-rich compositions. (ii) The significant lattice mismatch between germanium and silicon (4%) requires the presence of appropriate GeSi single-crystal seeds for the initiation of single-crystal growth from a melt of the corresponding composition. The absence of such seeds leads to a lattice mismatch at the seed/melt interface. As a result, stresses arising in the contact zone suppress the single-crystal growth. There are different ways to solve this problem (see [5]).

In this study, we propose a new technique for growing homogeneous Ge-rich $Ge_{1-x}Si_x$ single crystals, which is based on the modified vertical Bridgman method. Figure 1 shows the schematic diagram of the growth of GeSi crystals by this method and the temperature profile in the working volume of the heater. Single crystals are grown in two stages. First, after the melting of a Ge charge above the single-crystal seed, a crystallization front is established (starting point *A*). Then, in the first stage (*B*), a Si source rod is partially introduced at a rate ϑ_1 into the Ge melt through its upper surface. In this stage, the crystal grows in a static mode, without switching on the mechanism of crucible pulling. A gradual increase in the Si content in the melt leads to constitutional supercooling at the crystallization front and to the growth of a GeSi single crystal with a composition varying along the pulling axis. The Si content in the crystal and the growth temperature increase to the values determined by the volume of the source rod introduced into the melt, after which a temperature is established at the crystallization front, which is determined by the liquidus temperature of the Ge–Si system of the corresponding composition. In the second stage

1063-7745/05/5001-S0149$26.00

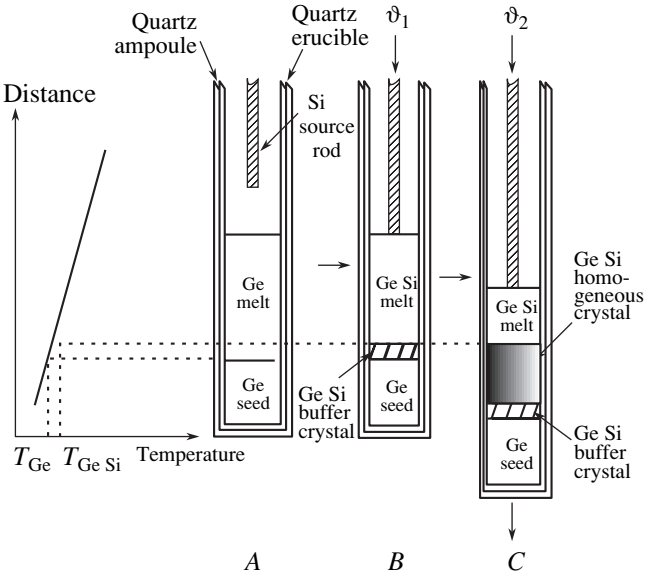

Fig. 1. Temperature distribution in the heater (left) and the schematic diagram of the growth of homogeneous GeSi single crystals (right): (*A*) starting point, (*B*) stage *1* (growth of a buffer crystal of variable composition on a Ge seed), and (*C*) stage *2* (growth of a homogeneous GeSi crystal on the buffer crystal).

(*C*), the mechanism of crucible pulling is switched on and a homogeneous GeSi single crystal is grown while the growth temperature is maintained at a constant. The growth temperature is controlled by balancing the melt composition using a corresponding ratio of the pulling and feeding rates.

We present below the calculated distribution of the components in GeSi crystals grown under the noted conditions, which determines the operating parameters for the growth of crystals with homogeneous composition along the pulling axis.

The problem is solved in the Pfann approximation under the following conventional conditions: the crystallization front is planar, there is an equilibrium between the solid and liquid phases at the crystallization front, the diffusion of the components and the convection in the melt provide for the homogeneity of the liquid phase throughout in the entire volume, the diffusion of Ge and Si atoms in the solid phase is negligible, and the source rod is completely dissolved after its submersion into the melt. Note that, for the Ge–Si system, these conditions are satisfied at growth rates below 10^{-6} m/s [1].

Let us introduce the following designations: V_0 and V_l are the volumes of the melt in the crucible at the initial and current instants of time, respectively; V_c and V_{Si} are the volumes of the crystallizing melt and the dissolving Si rod per time unit, respectively; C_l and C_c are the Si contents in the melt and the crystal, respectively; C is the amount of Si in the melt; K is the equilibrium segregation coefficient of Si; and t is time.

With the above designations, we can write the following relations for the first stage (*B*) of the growth of a buffer crystal of variable composition in the static mode:

$$C_l = \frac{C}{V_l} \text{ and } \frac{dC_l}{dt} = \frac{\dot{C}V_l - \dot{V}_l C}{V_l^2} = \frac{\dot{C} - \dot{V}_l C_l}{V_l}. \quad (1)$$

According to the condition for the problem, we assume that V_c and V_{Si} are time-independent during the time interval under consideration.

Then, taking into account that $C_c = C_l K$, we find that

$$V_l = V_0 - (V_c - V_{Si})t, \quad \dot{V}_l = -V_c + V_{Si} \text{ and}$$
$$\dot{C} = -V_c C_l K + V_{Si}. \quad (2)$$

Substituting relations (2) into (1), separating variables, and integrating, we obtain

$$(V_c - V_{Si}) \int_0^{C_l} \frac{dC_l}{C_l(V_c - V_c K - V_{Si}) + V_{Si}} = \frac{1}{1 - (1 - V_{Si}/V_c)V_c t/V_0}. \quad (3)$$

Here, the lower integration limit is taken to be zero because the starting melt is pure germanium. Denoting V_{Si}/V_c as α and taking into account that $V_c t/V_0 = S_c l/V_0$ (S_c is the cross-sectional area of the crystal, and l is the crystal length counted from the starting point of the crystallization front), we can write Eq. (3) in the form

$$l = \frac{V_0}{S_c}\frac{1}{1-\alpha}\left\{1 - \exp\left[-\int_0^{C_l} \frac{dC_l(1-\alpha)}{C_l(1-K-\alpha)+\alpha}\right]\right\}. \quad (4)$$

Equation (4) makes it possible to determine the value of α for the growth of a buffer crystal of specified length l, with the composition of the end part equal to the composition C_c^* of the homogeneous crystal grown in the second stage. Note that the length of the buffer crystal is determined by the temperature gradient at the crystallization front and the difference between the liquidus temperatures of Ge and GeSi of specified composition. To take the integral in (4), one has to know the analytical dependence of K on C_l. As shown by the phase diagram of the Ge–Si system, the value of K, depending on the melt composition, changes in a complicated way from 5.5 to 1 and cannot be described analytically [18]. Taking into account this circumstance, the integral in (4) was calculated numerically using the values of the equilibrium segregation coefficient of silicon from the Ge–Si phase diagram.

The value of l corresponding to the required composition C_c^* at the final position of the crystallization front of the buffer crystal indicates the beginning of the second stage (*B*) of the growth of the GeSi crystal with a uniform distribution of the components.

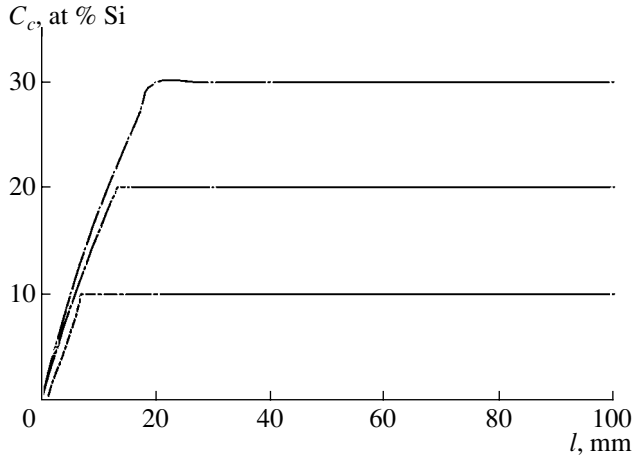

Fig. 2. Calculated distributions of Si along the three GeSi ingots grown in two stages to obtain crystals with a Si content of 10, 20, and 30 at % in the homogeneous part. The calculations assumed that the melt height at the starting point is 100 mm and the temperature gradient in the growth zone of the buffer crystal is 50 K/cm.

Obviously, the condition for the growth of homogeneous crystals of solid solutions is the constancy of the melt composition during the entire technological cycle. For $C_l^*/dt = 0$, we obtain from Eqs. (1) and (2)

$$C_l^* = \frac{\alpha^*}{K - 1 + \alpha^*} \text{ or } C_c^* = \frac{K\alpha^*}{K - 1 + \alpha^*}. \quad (5)$$

Equations (5) demonstrate the possibility of growing homogeneous crystals with a constant value of α^*, which is determined by specified values of C_l^* and K.

Figure 2 shows as an example the calculated distributions of the Si content along the pulling axis for three GeSi ingots grown in two stages to obtain crystals with Si contents in the homogeneous parts of 10, 20, and 30 at %. In the calculations, we assumed that the melt height at the starting point is 100 mm and the temperature gradient in the growth zone of the buffer crystal is 50 K/cm. The initial portions of the curves for the crystals with variable composition in Fig. 1, which correspond to the first stage (*B*) of the crystal growth in the static mode, are calculated from Eq. (4) using a preliminary calculated value of α. The plateau in the curves corresponds to the second stage (*C*), in which a crystal with the composition determined by Eq. (5) grows. The curves in Fig. 2 demonstrate the possibility of obtaining GeSi solid solutions with a required uniform composition by the modified Bridgman method. As follows from the analysis of the above data, the growth rate of a buffer crystal with a variable composition is determined by the temperature gradient at the crystallization front and the rate of feeding of melt with silicon (ϑ_1). The optimal value of this process parameter, at which high-quality single crystals are obtained, can be determined from experiment.

On the basis of the above-said, we can conclude that the modified Bridgman method using a source rod made of the secondary component and a single-crystal seed of the primary component can be successfully applied to grow crystals of solid solutions of specified composition with a uniform distribution of the components.

REFERENCES

1. G. Kh. Azhdarov, T. Kucukomeroglu, A. Varilci, *et al.*, J. Cryst. Growth **226**, 437 (2001).
2. I. Yunenaga, J. Cryst. Growth **198–199**, 404 (1999).
3. I. Yunenaga and M. Nonaka, J. Cryst. Growth **191**, 393 (1998).
4. I. Yunenaga, J. Cryst. Growth **226**, 47 (2001).
5. N. V. Abrosimov, S. N. Rossolenko, W. Thieme, *et al.*, J. Cryst. Growth **174**, 182 (1997).
6. N. V. Abrosimov, S. N. Rossolenko, W. Thieme, *et al.*, J. Cryst. Growth **166**, 657 (1996).
7. P. G. Azhdarov and N. A. Agaev, Inorg. Mater. **35** (8), 763 (1999).
8. C. Marin and A. G. Ostrogorsky, J. Cryst. Growth **211**, 378 (2000).
9. P. Dold, A. Barz, S. Recha, *et al.*, J. Cryst. Growth **192**, 125 (1998).
10. K. Kadakura and Y. Takano, J. Cryst. Growth **171**, 56 (1997).
11. L. Helmers, J. Schilz, and G. Bachr, J. Cryst. Growth **165**, 381 (1996).
12. A. Barz, P. Dold, U. Kerat, *et al.*, J. Vac. Sci. Technol. B **16**, 1627 (1998).
13. D. Bliss, B. Demczuk, B. Anselmo, *et al.*, J. Cryst. Growth **174**, 187 (1997).
14. J. Wollweber, D. Shulz, and W. Shroeder, J. Cryst. Growth **163**, 243 (1996).
15. J. Wollweber, D. Shulz, and W. Shroeder, J. Cryst. Growth **158**, 166 (1996).
16. T. A. Campbell, M. Schweizer, P. Dold, *et al.*, J. Cryst. Growth **226**, 231 (2001).
17. K. Nakajima, S. Kodama, S. Miyashita, *et al.*, J. Cryst. Growth **205**, 270 (1999).
18. R. V. Olesinski and J. C. Abbaschian, Bull. Alloy Phase Diagrams **5**, 180 (1984).

Translated by Yu. Sin'kov

Crystallography Reports, Vol. 50, Suppl. 1, 2005, pp. S152–S158.

CRYSTAL GROWTH

A Phase-Field Model with Two-Component Order Parameter for Spontaneous Crystallization in a Melt of Pure Metal

P. V. Melenev, N. D. Nyashina, and P. V. Trusov

Perm State Technical University, Komsomol'skiĭ pr. 29a, Perm, 614600 Russia

e-mail: aquatoria@mail.ru

Received February 3, 2005

Abstract—A phase-field model with the two-component order parameter is proposed for describing the crystallization of a pure metal. The model is constructed on the basis of the Ginzburg–Landau theory of phase transitions using the principle of the positivity of entropy production in an open weakly nonequilibrium system. This makes it possible to use the proposed model for describing nonisothermal processes. A number of one-dimensional and two-dimensional problems associated with the simulation of a solidified structure under different temperature conditions are solved. © *2005 Pleiades Publishing, Inc.*

INTRODUCTION

According to experimental data, physicomechanical characteristics of a solid metal depend substantially on the parameters of the cast structure formed upon crystallization. This and other factors (including rapid progress in the development of computer science and mathematical methods) have explained the considerable interest expressed by researchers in simulating the cast structure of a solidifying melt over the last two decades.

Structuring processes cannot be described within traditional formulations of heat and mass transfer problems, because these formulations disregard the main factors responsible for the formation of structures. An appropriate basis for the solution of similar problems is provided by the phase-field model, which is based on the apparatus of weakly nonequilibrium thermodynamics and includes the formalism of the Ginzburg–Landau theory of phase transitions [1]. According to this theory, the field of the order parameter characterizing the deviation of the system from thermodynamic equilibrium is introduced and a phase transition is considered a change in this field. A change in the order parameter at each point is accompanied by release of heat, which, in turn, affects the rate of this change. In the framework of such an approach, unlike traditional formulations of the Stefan problem, the interface is defined as an order parameter isoline. This permits one to take into account the surface tension anisotropy and the interface curvature, which are the main structuring factors that render the interface nonisothermal.

MATHEMATICAL FORMULATION OF THE PROBLEM

Crystallization in a melt of a pure metal in some domain is described in terms of the phase-field model. In the works devoted to this model, the free energy functional and the principle of lack of increase in the free energy in irreversible processes (valid for isothermal cases) have been used frequently [2, 3]. However, temperature supercooling is one of the main driving forces of crystallization. Another important factor is the latent heat of crystallization. In order for these two effects to be included, temperature variations in the domain should be described within the phase-field model. Therefore, consideration of the entropy of the system in our problem seems to be more justified, because the evolution of the system according to the second law of thermodynamics should be accompanied by an increase in the entropy (including nonisothermal conditions). The equations of the model will be derived using the formalism proposed by Wang *et al.* [4]. Then, we will analyze a two-dimensional variant of the problem (the Cartesian coordinate system with an orthonormalized basis set $\{i, j\}$).

Let us consider a closed domain Ω filled with a pure metal that can undergo a liquid–crystal phase transition. We assume that the temperature gradient and the rate of temperature change in the domain are not very high and external actions (for example, electromagnetic fields) on a melt are absent. Moreover, we will examine the problem on the mesolevel and disregard the influence of melt motion and stresses arising in the material.

1063-7745/05/5001-S0152$26.00

As in [5], we introduce the characteristic of the phase state, namely, an order parameter consisting of two components $\{\varphi(t, \mathbf{r}), \theta(t, \mathbf{r})\}$. The component φ can be interpreted as the degree of ordering of the material (the fraction of occupied sites in the crystal lattice) at a point (more precisely, in a microvolume) with a radius vector $\mathbf{r}$ at an instant of time t, so that the values of $\varphi = 0$ and 1 correspond to the liquid and crystalline states, respectively. The component θ is the angle between one of the principal crystallographic directions and the heat flux. It is evident that, taking into account the order N_0 of the symmetry axis in the lattice under consideration, we can analyze variations of the component θ in the range from 0 to $2\varphi/N_0$. This approach allows us to describe the simultaneous growth of several arbitrarily oriented crystals, their interaction, and the formation of the polycrystalline structure of the material.

It is assumed that the entropy of an arbitrary subvolume of the domain $V \in \Omega$ can be written in the form

$$S = \int_V \left\{ s(e, \varphi) - \frac{1}{2}(\varepsilon|\nabla\varphi|)^2 - \frac{1}{2}(\eta|\nabla\theta|)^2 \right\} dV, \quad (1)$$

where $s(e, \varphi)$ is the entropy density, e is the internal energy density, and the parameters ε and η can be functions of the order parameter. The gradient terms in the entropy functional are introduced by analogy with the internal energy functional proposed in the works by Landau and Ginzburg and also Cahn and Hilliard, who used the gradient approach, according to which the potential depends not only on the thermodynamic variables but also on their gradients (when the gradients of these variables are sufficiently large). Therefore, the proposed functional includes the order parameter gradients, whereas the temperature gradient is not involved in an explicit form in the expression for the entropy. In this case, the degree of disorder does not change if the gradients are equal to zero.

In order to allow for the surface energy anisotropy of the crystal, we assume that the parameter ε depends on the crystal surface orientation, which is described by the angle $\psi = \bar{\psi} - \theta$, where $\bar{\psi}$ is the angle between the abscissa axis and the vector $-\nabla\varphi$ aligned along the normal to the interface (Fig. 1).

The third term in expression (1) reflects the effect of misorientation of neighboring crystals. It is assumed that this effect depends on the ordering of the material and, hence, it is possible to write $\eta(\varphi)$.

Now, we differentiate expression (1) with respect to time and separate the relationship for the entropy flux through the boundary of the subvolume V. Then, the time dependence of the entropy can be represented in the following form:

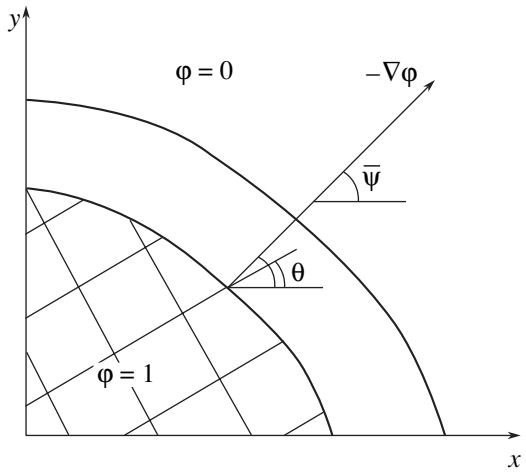

Fig. 1. Schematic drawing of the interface.

$$\dot{S} = \int_V \left\{ \mathbf{q} \cdot \nabla\left(\frac{1}{T}\right) + \left[\frac{1}{T}\left(\frac{\partial e}{\partial \varphi}\right)_S + X_\varphi\right]\dot{\varphi} + X_\theta\dot{\theta} \right\} dV$$

$$- \int_{\delta V} \mathbf{n} \cdot \left\{ \left(\frac{\partial s}{\partial e}\right)_\varphi \mathbf{q} + Y \right\} d(\delta V),$$

where

$$X_\varphi = \nabla \cdot [\varepsilon(\psi)(\varepsilon(\psi)\mathbf{I} + \varepsilon'(\psi)\mathbf{J}) \cdot \nabla\varphi] - \frac{\eta'(\varphi)}{2}|\nabla\theta|^2,$$

$$X_\theta = \varepsilon(\psi)\varepsilon'(\psi)|\nabla\varphi|^2 + \nabla \cdot (\eta(\varphi)\nabla\varphi),$$

$$Y = \dot{\varphi}[\varepsilon(\psi)^2\nabla\varphi + \varepsilon(\psi)\varepsilon'(\psi)\mathbf{J} \cdot \nabla\varphi] + \dot{\theta}\eta(\varphi)\nabla\theta.$$

Here, the tensor $\mathbf{J}$ is represented as $\mathbf{J} = -\mathbf{ij} + \mathbf{ji}$ and $\mathbf{I} = \mathbf{ii} + \mathbf{jj}$ is a unit tensor.

As follows from the second law of thermodynamics, the entropy production in any subvolume $V \in \Omega$ is positive. The entropy production can be found by subtracting the entropy flux through the boundary δV from the quantity $\dot{S}$; that is,

$$\dot{S} + \int_{\delta V} \mathbf{n} \cdot \left\{ \frac{\mathbf{q}}{T} + Y \right\} d(\delta V) \geq 0.$$

In the integrand, $\frac{\mathbf{q}}{T}$ is the entropy flux caused by the temperature gradient and Y is the entropy flux associated with the change in the phase field (the change in the ordering and orientation of the growing crystal) at

the boundary of the subvolume *V*. Consequently, the positivity of entropy production

$$S_{prod} = \int_V \left\{ \mathbf{q} \cdot \nabla\left(\frac{1}{T}\right) + \left[\frac{1}{T}\left(\frac{\partial e}{\partial \varphi}\right)_S + X_\varphi\right]\dot{\varphi} + X_\theta \dot{\theta} \right\} dV \geq 0$$

can be provided by choosing the following relationships for the heat flux and the time derivatives of the variables:

$$\mathbf{q} = M_T \nabla\left(\frac{1}{T}\right), \tag{2}$$

$$\begin{aligned} \tau\dot{\varphi} &= -\frac{1}{T}\left(\frac{\partial e}{\partial \varphi}\right)_S \\ &+ \nabla \cdot [\varepsilon(\psi)(\varepsilon(\psi)\mathbf{I} + \varepsilon'(\psi)\mathbf{J}) \cdot \nabla\varphi] - \frac{\eta'(\varphi)}{2}|\nabla\theta|^2, \end{aligned} \tag{3}$$

$$\tau\dot{\theta} = \varepsilon(\psi)\varepsilon'(\psi)|\nabla\varphi|^2 + \nabla \cdot (\eta(\varphi)\nabla\theta), \tag{4}$$

where τ and M_T are positive parameters and the tensor $\mathbf{I}$ is written as $\mathbf{I} = \mathbf{ii} + \mathbf{jj}$. The equation describing the internal energy density is represented in the form

$$\dot{e} = -\nabla \cdot \left[M_T \nabla\left(\frac{1}{T}\right)\right]. \tag{5}$$

Equations (2)–(4) form the system of the master equations for the order parameter and the internal energy density, respectively.

The derivative of the internal energy density in formula (5), as a rule, is determined using the free Helmholtz energy density [4]

$$f = e - Ts,$$

whose differential is given by the relationship

$$df = \left(\frac{\partial e}{\partial \varphi}\right)_S d\varphi - s dT. \tag{6}$$

Consequently, at a constant temperature *T*, the function $f(T, \varphi)$ at any fixed component φ can be written as follows:

$$f(T, \varphi) = -T\int_{T_M}^{T} \frac{e(z, \varphi)}{z^2} dz + TG(\varphi), \tag{7}$$

where T_M is the melting temperature and $G(\varphi)$ is an arbitrary function.

For the internal energy density, we propose the following relationship:

$$e = e_s(T) + [1 - p(\varphi)]L(T) = e_l(T) - p(\varphi)L(T), \tag{8}$$

where e_s and e_l are the classical internal energy densities of the solid and liquid phases, respectively; $L(T) = e_l(T) - e_s(T)$; $p(0) = 0$; $p(1) = 1$; and $L(T_M) = L_0$ is the latent heat of melting.

With allowance made for relationship (8), function (7) can be rewritten in a more specific form

$$f(T, \varphi) = T\left[-\int_{T_M}^{T} \frac{e_l(z)}{z^2} dz + p(\varphi)Q(T) + G(\varphi)\right], \tag{9}$$

where

$$Q(T) = \int_{T_M}^{T} \frac{L(z)}{z^2} dz \tag{10}$$

is a monotonically increasing function that passes through 0 at the point T_M.

Making allowance for formula (6), Eqs. (3) and (5) can be represented as follows:

$$\tau\dot{\varphi} = X_\varphi - Q(T)p'(\varphi) - G'(\varphi), \tag{11}$$

$$\begin{aligned} &\dot{e}_l(T) - p'(\varphi)L(T)\dot{\varphi} - p(\varphi)L'(T)\dot{T} \\ &= -\bar{\nabla} \cdot \left[M_T \bar{\nabla}\left(\frac{1}{T}\right)\right]. \end{aligned} \tag{12}$$

When the temperature and volume are fixed, the free energy of the system in the equilibrium state is minimum. Since it is assumed that the crystalline and liquid phases are metastable in the temperature range under consideration, the free Helmholtz energy density should have local minima at the points $\varphi = 0$ and 1 at any temperatures in the studied range (this ensures the existence of a supercooled liquid or a superheated crystal); that is,

$$\left.\frac{\partial f}{\partial \varphi}\right|_{\varphi = 0; 1} = 0, \quad \left.\frac{\partial^2 f}{\partial \varphi^2}\right|_{\varphi = 0; 1} > 0. \tag{13}$$

Furthermore, the function *f* of the temperature *T* should be continuous at the melting point:

$$f(T_M, 0) = f(T_M, 1). \tag{14}$$

From expression (9) for the free energy density with due regard for conditions (13) and (14), we find

$$[G'(\varphi) + p'(\varphi)Q(T)]_{\varphi = 0, 1} = 0, \tag{15}$$

$$[G''(\varphi) + p''(\varphi)Q(T)]_{\varphi = 0, 1} > 0, \tag{16}$$

$$G(0) = G(1). \tag{17}$$

In order to obey Eqs. (15)–(17), the function $G(\varphi)$ can be chosen in the form of a *W*-shaped potential with minima at zero and unity. The simplest example of this function is given by the expression

$$G(\varphi) = G_0 g(\varphi) = G_0 \varphi^2 (1 - \varphi)^2, \tag{18}$$

where $G_0 > 0$ [4]. Note that, when using the function $G(\varphi)$ in the form (18), we have $f(T_M, 0) = f(T_M, 1) = 0$. The dependence $p(\varphi)$ should also be chosen so that

Eqs. (15)–(17) must be satisfied. For example, the dependence $p(\varphi)$ can be constructed in the form

$$p(\varphi) = \int_0^\varphi g(z)dz \Big/ \int_0^1 g(z)dz.$$

Then, with the use of function (18), we obtain

$$p(\varphi) = \varphi^3(10 - 15\varphi + 6\varphi^2).$$

In order to simplify the developed model, the internal energy density of the liquid can be approximated by a linear temperature dependence

$$e_l(T) = e_l(T_M) + c(T - T_M),$$

where c is the specific heat capacity (it is assumed that c = const).

The parameter M_T can be specified in the form $M_T = \lambda T^2$, where λ is the thermal conductivity coefficient. In a strict sense, for anisotropic materials (including crystals), it is necessary to consider the tensor λ, which accounts for the possible anisotropy of heat transfer along different directions. However, in the present work, we use only the scalar constant thermal conductivity coefficient. Taking into account these assumptions, the evolution equations (11), (4), and (12) of the model are written in the following final form:

$$\begin{aligned}\tau\dot{\varphi} &= \varepsilon_0^2\nabla\cdot[\hat{\varepsilon}(\psi)(\hat{\varepsilon}(\psi)\mathbf{I} + \hat{\varepsilon}'(\psi)\mathbf{J})\cdot\nabla\varphi] \\ &- \eta_0\frac{\hat{\eta}'(\varphi)}{2}|\nabla\theta|^2 - Q(T)p'(\varphi) - G_0 g'(\varphi),\end{aligned} \quad (19)$$

$$\tau\dot{\theta} = \varepsilon(\psi)\varepsilon'(\psi)|\nabla\varphi|^2 + \nabla\cdot(\eta(\varphi)\nabla\theta), \quad (20)$$

$$(c - p(\varphi)L'(T))\dot{T} - p'(\varphi)L(T)\dot{\varphi} = \lambda\bar{\nabla}^2 T. \quad (21)$$

The derived system of Eqs. (19)–(21) describes the evolution of the components of the order parameter and the temperature field.

SOLUTION OF TEST PROBLEMS

Equations (19)–(21) were used to solve several test problems for one- and two-dimensional domains Ω.

The calculations given below were performed with the parameters for tin [6], because this is one of the metals whose homogeneous crystallization has been experimentally investigated over a few decades [7].

The constants ε_0 and G_0 were estimated from the physical characteristics of the material according to the procedure proposed in [4]. The constants τ and η_0 in the present work served as the model parameters. The results given below were obtained at the following constants: $\varepsilon_0 = 4.0\times10^{-6}$, $G_0 = 3.0\times10^6$, $\tau = 2.0\times10^5$, and $\eta_0 = 5.0\times10^{-10}$.

Let us analyze the one-dimensional variant of the problem. We assume that a constant supercooling $-\Delta u$ is maintained at the boundaries of the domain under consideration; that is, $T(0, x) = T(t, -\infty) = T(t, +\infty) = -\Delta u$.

For the phase field, we chose randomly distributed perturbations with an amplitude of 0.1 (the orientation angle θ is randomly distributed) as the initial conditions and the periodic boundary conditions $\varphi(t, -\infty) = \varphi(t, +\infty)$ and $\theta(t, -\infty) = \theta(t, +\infty)$.

Equations (19) and (20) contain the nonlinear differential operators. Therefore, the explicit scheme with constant steps in time and coordinate was applied to solve the problem. In this case, we used the difference analogues of the derivatives that provided the first-order approximation in time and the second-order approximation in coordinate. In order to ensure stability of the numerical solution, the time integration step was chosen according to the Courant conditions [8]. The coordinate step was determined by the domain size and the number of nodes in the computational grid.

Figure 2 presents the distributions of the degrees of ordering and the orientation angles at several instants of time. These distributions reflect the development of the crystallization process. It can be seen from Fig. 2 that, at the initial stage ($t = 5\times10^{-5}$, 7×10^{-5} s), crystallization begins at several nuclei whose growth is predominantly responsible for the increase in the fraction of the solid phase. In the domain, there are several regions of the crystallized material (the degree of ordering φ is close to unity), which are separated by regions with a lower degree of ordering. At later stages of the process ($t = 10\times10^{-5}$, 35×10^{-5} s), the crystals begin to interact with each other: certain crystals grow at the expense of other crystals, and their orientations become similar to each other. A decrease in the number of crystals is associated with, first, melting of small-sized crystals due to the release of the latent heat of crystallization during the growth of large-sized crystals, and, second, orientational alignment of neighboring crystals with similar orientations. As a consequence, the number of grains decrease and their sizes increase in the domain.

Therefore, the solution of the one-dimensional variant of the problem shows that the system is characterized by a realistic behavior: the formation of ordered identically oriented subregions (grains) separated by narrow regions of the material with a lower degree of ordering. This enables us to apply the developed approach to the two-dimensional problem.

As was noted above, the model equations (19)–(21) were derived on the basis of the entropy functional. This provides a way of describing solidification under nonisothermal conditions and allowing for the influence of the latent heat of the phase transition on the process.

Now, we consider a rectangular domain across which the temperature gradient is specified at the initial instant of time: a constant supercooling occurs at one boundary of the domain (at the left of Fig. 3), and the melting temperature is maintained at the opposite boundary. Moreover, it is assumed that the order

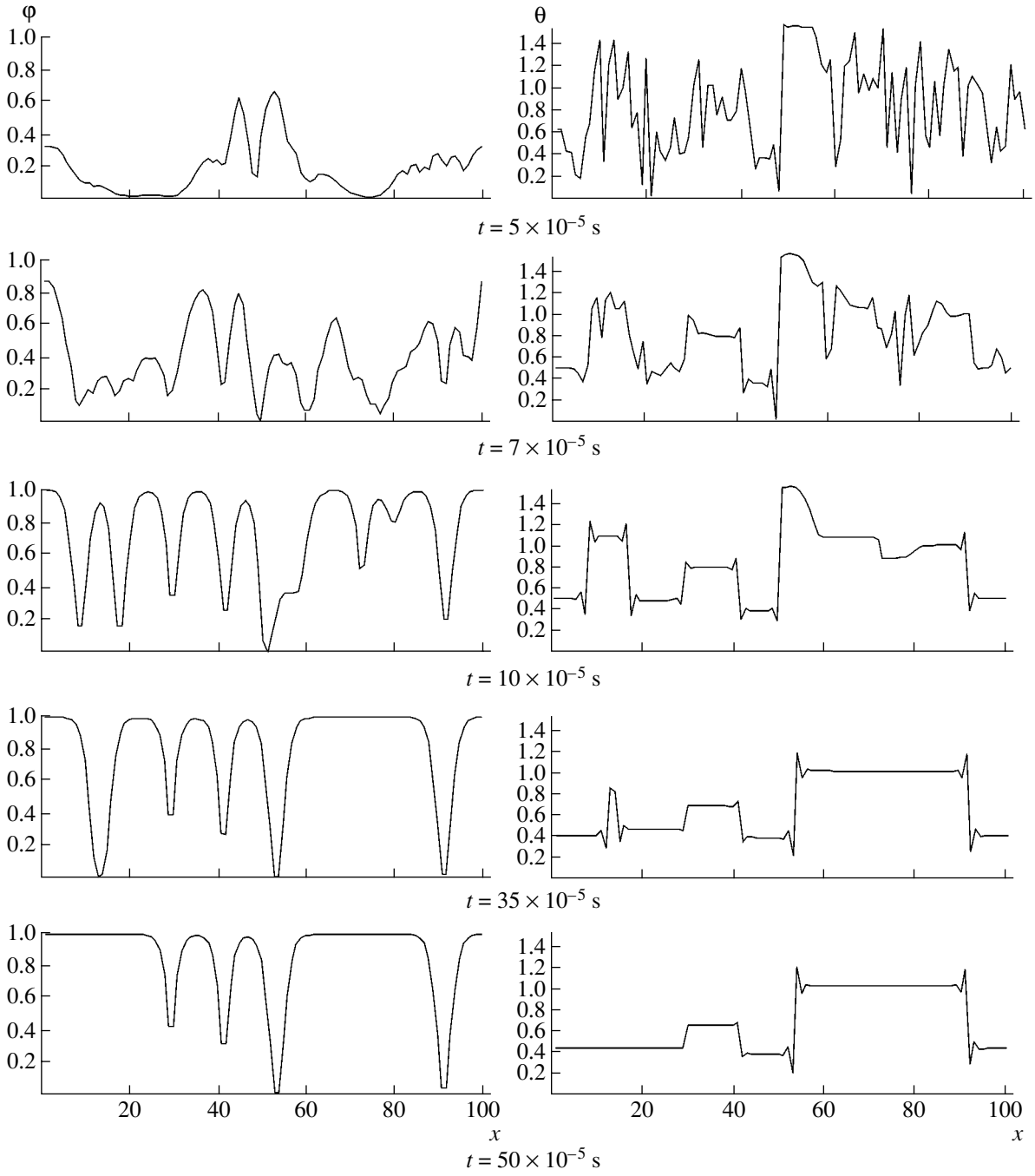

Fig. 2. Solutions of the one-dimensional isotropic problem for several instants of time. Tick marks on the horizontal axis are spaced at 10^{-6} m.

parameter flux through these boundaries is absent and that the periodic boundary conditions are imposed on the other two boundaries. A similar situation can be observed in melt regions in the vicinity of matrix walls (or substrate if the case in point is the experiments with small-sized melt droplets) whose temperature is lower than the temperature in the melt. The crystal lattice of the solid phase has sixfold symmetry.

The development of the crystallization process is illustrated in Fig. 3. Microcrystals nucleate on the cooled boundary, grow, and acquire an elongated shape. Then, crystals at the cold boundary of the domain interact with each other and stick together to produce larger crystals. As a result, there remain only several grains growing in the direction of heat removal. Note that the crystallization front has a small curvature.

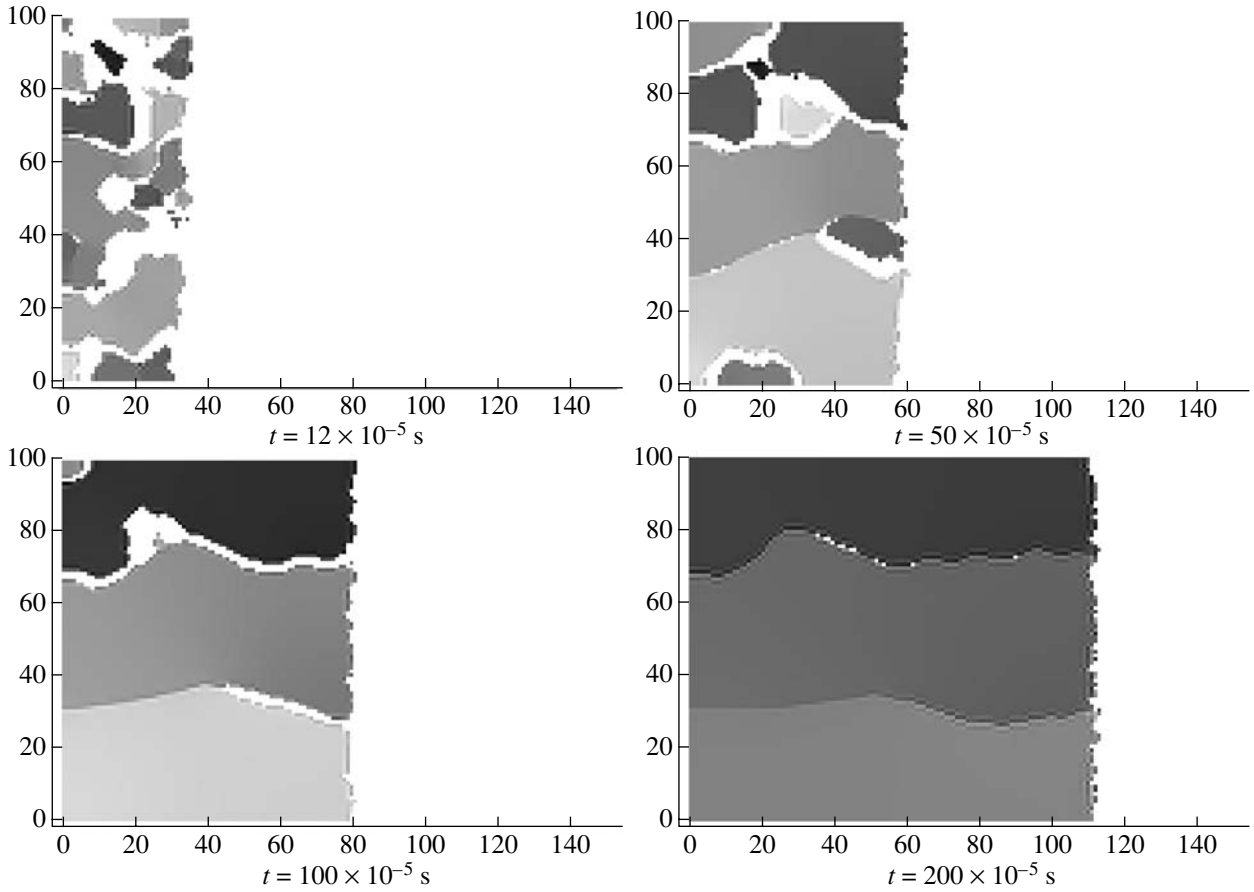

Fig. 3. Phase-field distributions at constant temperatures at the left and at the right boundaries of the domain (different gray tints correspond to growing grains with different crystallographic orientations). Tick marks on the axes are spaced at 10^{-6} m.

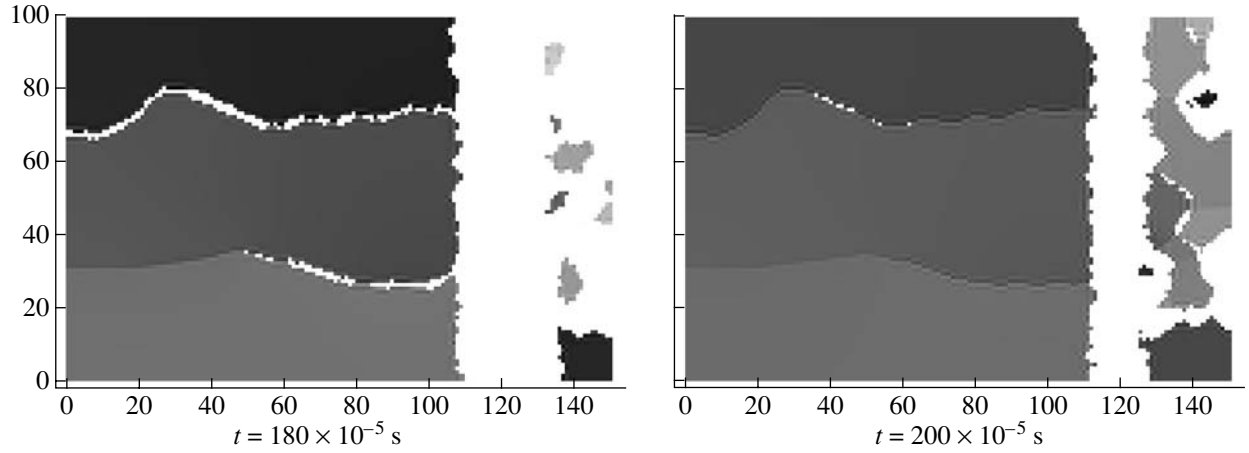

Fig. 4. Phase-field distributions in the case of the cooled right boundary. Tick marks on the axes are spaced at 10^{-6} m.

Furthermore, we examined one more variant of the above problem. It was assumed that, at the initial instant of time, the conditions are identical to those in the preceding problem. However, at an instant of time, the temperature at the right boundary begins to decrease. This problem describes the situation when a sample involving the domain under consideration is cooled with time. The phase field distributions for this problem are shown in Fig. 4. Before cooling the second boundary of the domain, the crystallization process

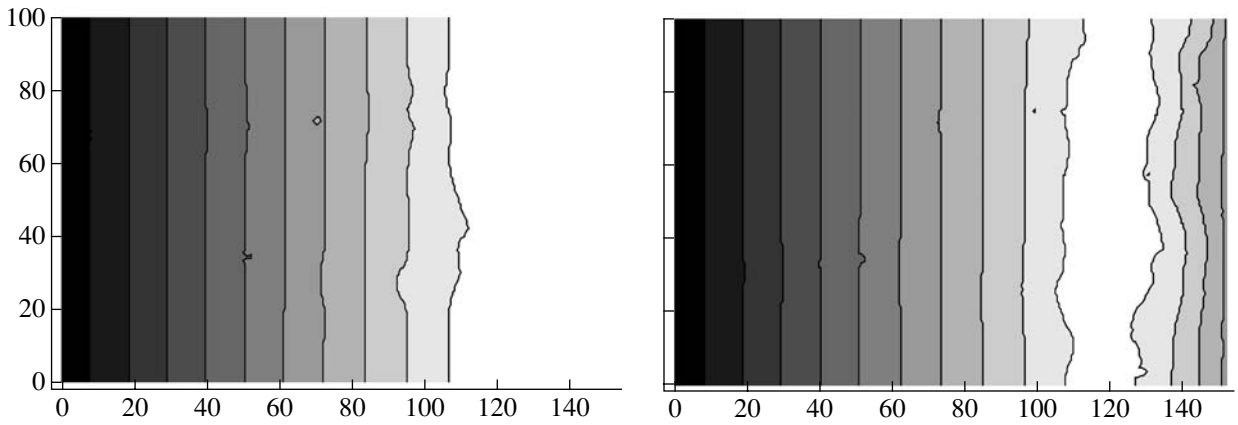

Fig. 5. Temperature distributions at the instant of time $t = 2$ ms for the problems illustrated in Figs. 3 and 4. Tick marks on the axes are spaced at 10^{-6} m.

proceeds identically to that described in the previous problem. Then, solid nuclei suspended in the melt arise in the region adjacent to the cooled boundary and begin to grow. The formation of crystals in the vicinity of the cooled domain boundary can be explained by the fact that the temperature in this region is lower than the temperature ahead of the crystallization front (which is heated by the latent heat released during the growth of the solid phase) (Fig. 5).

CONCLUSIONS

Thus, the two-component order parameter was introduced by analogy with [4]. The master equations for this order parameter were obtained using the principle of the positivity of entropy production. The use of this principle rather than the principle of the minimum free energy (as in the isothermal case) made it possible to derive thermodynamically justified evolution equations for the components of the order parameter and the temperature field and to include nonisothermal conditions of crystallization. The physical meaning of the parameters entering into the evolution equations was revealed by analyzing simplified equations of the system.

The test calculations for the one-dimensional problem demonstrated that the proposed model quantitatively describes physical aspects of crystallization and grain formation. The solved two-dimensional problems with temperature gradients permitted us to reveal that the model describes the formation of grains elongated in the direction of the temperature gradient.

ACKNOWLEDGMENTS

This work was supported by the Russian Foundation for Basic Research, project no. Ural-2004 04-02-96030.

REFERENCES

1. *Collected Papers of L. D. Landau* (Pergamon, Oxford, 1965; Nauka, Moscow, 1969), Vol 1.
2. J. S. Langer, *Models of Pattern Formation in First-Order Phase Transitions* (World Scientific, Singapore, 1986), p. 165.
3. G. Caginalp, Arch. Ration. Mech. Anal. **92**, 205 (1986).
4. S.-L. Wang, R. F. Sekerka, A. A. Wheeler, *et al.*, Physica D (Amsterdam) **69**, 189 (1993).
5. R. Kobayashi, J. A. Warren, and W. C. Carter, Physica D (Amsterdam) **119**, 415 (1998).
6. *Tables of Physical Data: A Handbook*, Ed. by I. K. Kikoin (Atomizdat, Moscow, 1976) [in Russian].
7. V. P. Skripov and V. P. Koverda, *Spontaneous Crystallization of Supercooled Liquids* (Nauka, Moscow, 1984) [in Russian].
8. M. G. Boyarshinov, *Numerical Methods* (Perm. Gos. Tekh. Univ., Perm, 1999), Part 2 [in Russian].

Translated by O. Borovik-Romanova

Crystallography Reports, Vol. 50, Suppl. 1, 2005, pp. S159–S167.

CRYSTAL GROWTH

Theoretical and Experimental Study of the Formation of Grown-in and As-Grown Microdefects in Dislocation-Free Silicon Single Crystals Grown by the Czochralski Method

N. A. Verezub*, A. I. Prostomolotov*, M. V. Mezhennyĭ, M. G. Mil'vidskiĭ**, and V. Ya. Reznik*****

** Institute for Problems of Mechanics, Russian Academy of Sciences, pr. Vernadskogo 101, Moscow, 117526 Russia*

*** State Institute of Rare Metals, Bol'shoĭ Tolmachevskiĭ per. 5, Moscow, 119017 Russia*

e-mail: icpm@mail.girmet.ru

**** Institute of Chemical Problems for Microelectronics, Bol'shoĭ Tolmachevskiĭ per. 5, Moscow, 119017 Russia*

Received February 18, 2005

Abstract—A complex theoretical and experimental investigation is performed, including the following stages. (i) Simulation of the processes of the recombination of intrinsic point defects and the formation of grown-in microdefects in dislocation-free Si single crystals 200 mm in diameter grown in modern commercial heating units. The simulation takes into account the thermal history of the defect growth. Modified designs of heating units are analyzed to compare the results of the simulation of thermal processes during the growth of Si single crystals 200 mm in diameter with a shield in the crucible region. The thermal history of the crystal is simulated, the recombination of intrinsic point defects near the crystallization front is analyzed, and the formation of vacancy microdefects in the temperature range t = 1200–900°C is modeled. This simulation made it possible to determine the effect of a heat shield on the processes of v–i recombination and microdefect formation. (ii) Microdefects in as-grown crystals and in crystals subjected to thermal treatments are investigated by optical and electron microscopy; specific features of the generation and motion of dislocations are analyzed for Si wafers containing microdefects of different types, formed as a result of the decomposition of the supersaturated solid solution of oxygen during multistep heat treatments of Si wafers. (iii) The three-dimensional problem of determining the field of elastic stresses caused by the wafer weight is solved in the isotropic approximation for 200- and 300-mm Si wafers placed on three or symmetrically arranged point supports of different areas. © *2005 Pleiades Publishing, Inc.*

INTRODUCTION

The problems of the production of modern very large scale ultra integrated circuits are related to the use of wafers with an internal getter formed by the controlled decomposition of the supersaturated solid solution of oxygen in silicon during multistep heat treatments. As a result, oxygen-containing precipitates are formed in the wafer bulk, which, depending on their nature and size, can both play the role of centers of the heterogeneous nucleation of dislocations and serve as their stoppers, hindering their generation and motion.

An urgent problem is to monitor and control the sizes and distributions of microdefects throughout the entire process of wafer fabrication: from the initial stages of crystal growth to the final stages of heat treatment of Si wafers.

A complex theoretical and experimental investigation is performed here. This investigation includes (i) simulation of the processes of the recombination of intrinsic point defects and the formation of grown-in microdefects in dislocation-free Si single crystals 200 mm in diameter, grown in modern commercial heating units, taking into account the thermal history of their growth; (ii) optical and electron microscopy study of microdefects in the as-grown state and after heat treatments; and (iii) the calculation and measurement of stresses in 200- and 300-mm Si wafers during high-temperature annealing.

SIMULATION OF HEAT TRANSFER AND DEFECT FORMATION DURING THE GROWTH OF DISLOCATION-FREE Si SINGLE CRYSTALS

We considered a modification of the heating unit design to compare the results of the simulation of thermal processes during the growth of 200-mm Si single crystals in the presence of a heat shield in the crucible region. Using the calculated thermal history of a crystal, we analyzed the recombination of intrinsic point defects near the crystallization front and then simulated the formation of vacancy microdefects in the temperature range t = 1200–900°C. This analysis made it pos-

1063-7745/05/5001-S0159$26.00 © 2005 Pleiades Publishing, Inc.

sible to determine the effect of the heat shield on the processes of *v–i* recombination and the formation of microdefects.

SIMULATION OF TEMPERATURE FIELDS IN A GROWING CRYSTAL

Global numerical approximation and solution of the equations were carried out using the finite-element method. In the axisymmetric approach, the radiation-conductive heat transfer in the volume of the heating unit was modeled in the gray-body approximation taking into account the crystallization of the silicon melt. Specific features of the temperature distributions in a crystal were considered for different growth stages as applied to a typical heating unit. The calculations were performed using the CRYSTMO software [1].

A preliminary stage in the analysis of the defect formation in Si crystals is the calculation of the thermal history of the crystal growth. Since the thermal processes are fairly fast, the entire growth process was represented as a sequence of independent stationary stages (10, 15, …, 100% of the cylindrical part of the ingot) for a specific geometry of the heating unit. Taking into account the data obtained within the global thermal model, we calculated the analytical expressions for the temperature field in the growing crystal $T(\tau, r, z)$ at any instant of time and for any point of the crystal with due regard for the shape of the crystallization front.

Variable geometric parameters of the growth process, which strongly affect the heat exchange in the heating unit and changes in the temperature field in the crystal, are the positions of the crucible and the heater; the melt height; the crystal length; and the pulling rate V_p (varied by a certain program).

The effect of the crucible-related heat shield on the temperature field in the crystal in the growth stage of 100% is shown in Fig. 1: large axial temperature gradients are observed in the crystal part located in the crucible region.

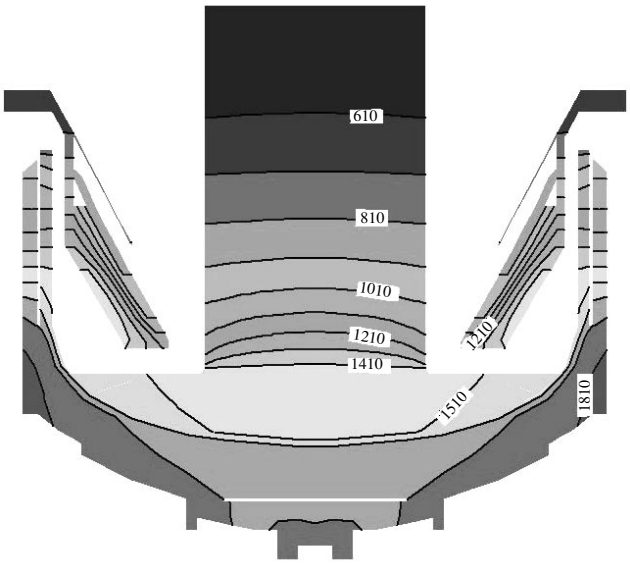

Fig. 1. Distributions of isotherms in the heating unit for the growth stage 100% body. Numbers indicate temperature (°C).

ANALYSIS OF THE DISTRIBUTIONS OF INTRINSIC POINT DEFECTS AND COMPARISON WITH EXPERIMENTAL DATA

The nonstationarity of the growth process is taken into account by changing the temperature field in this region, depending on time or (which is the same) the parameter. These data are taken from the global thermal model in the analytical form. Taking into account the temperature field within the nonstationary model of the *v–i* recombination [2], we calculated the distributions of the residual concentrations of vacancies C_v and interstitials C_i (Fig. 2). The results correspond to the growth stage of 40% in the regime of inverted pulling rate, at V_p = 0.4 mm/min. In this stage, large temperature gradients occur and the crystal grows in the interstitial (*i*) regime, whereas at lower pulling rates the mixed vacancy–interstitial regime is implemented. It is noteworthy that the *i* regime is implemented only at the

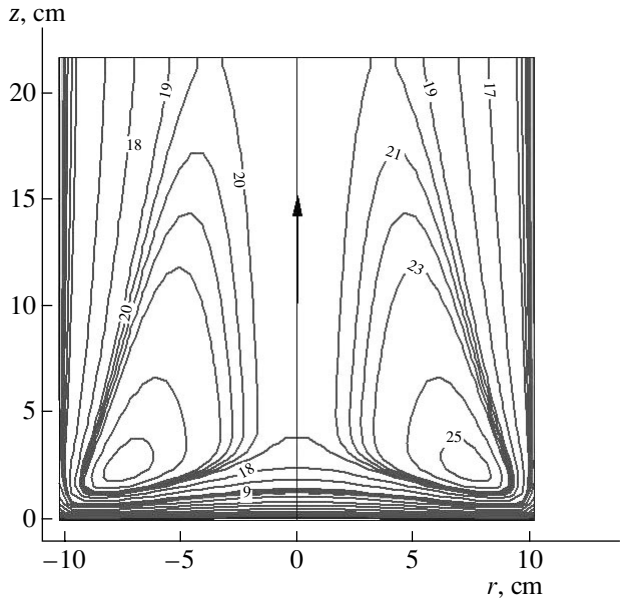

Fig. 2. Distribution of isolines of the residual concentration difference $\Delta C = C_i - C_v$ after the *v–i* recombination for the growth stage 40% body at V_p = 0.4 mm/min. Numbers on the isolines indicate: ΔC = (*1*) -2.2×10^{14}, (*3*) -1.6×10^{14}, (*5*) -1×10^{14}, (*7*) -4.5×10^{13}, (*9*) 0, (*11*) 4.3×10^{12}, (*13*) 6.2×10^{12}, (*15*) 1.3×10^{13}, (*17*) 4.2×10^{13}, (*19*) 7.1×10^{13}, (*21*) 7.6×10^{13}, (*23*) 8.1×10^{13}, and (*25*) 1.0×10^{14} cm^{-3}.

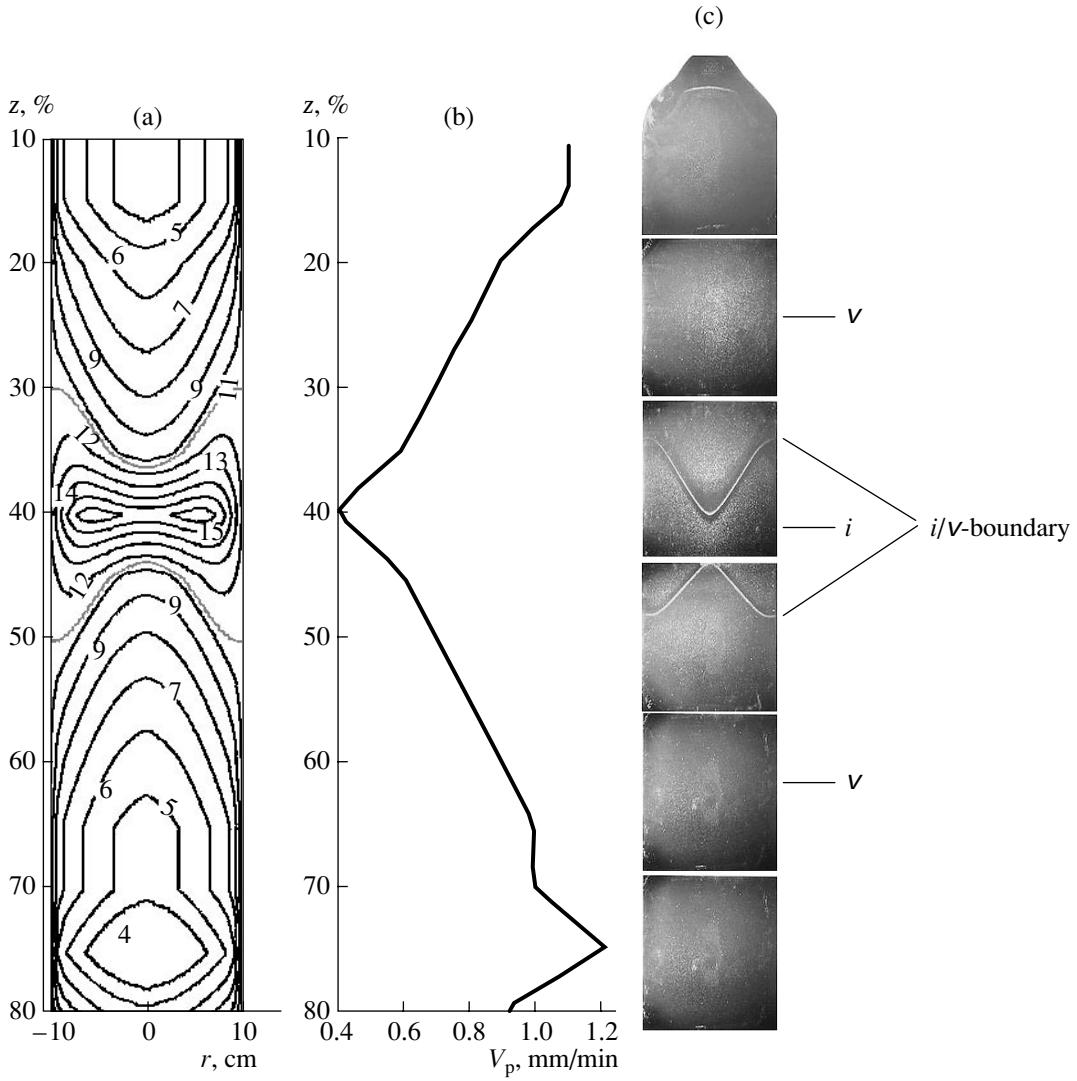

Fig. 3. Calculated and experimental data. (a) Calculated distribution of isolines of the residual concentration difference after the *v*–*i* recombination. Numbers on the isolines indicate: ΔC = (*1*) -1.5×10^{14}, (*3*) -1.3×10^{14}, (*5*) -9.2×10^{13}, (*7*) -5.9×10^{13}, (*9*) -2.6×10^{13}, (*11*) 0, (*13*) 2.4×10^{13}, (*15*) 5.8×10^{13}, (*17*) 9.1×10^{13}, (*19*) 1.2×10^{14}, (*21*) 1.6×10^{14}, (*23*) 1.9×10^{14}, and (*25*) 2.2×10^{14} cm^{-3}. (b) Pulling rate distribution along the ingot axis. (c) Experimental carrier lifetime map for the Si crystal grown in the closed thermal zone (*v* and *i* denote the regions corresponding to the vacancy and interstitial regimes, respectively; *v*/*i* is the boundary separating these regions).

ingot periphery and a vacancy ring with a radius R_{OSF} arises at the crystal center.

To illustrate the nonstationary changes in the two-dimensional (2D) distributions of intrinsic point defects after the *v*–*i* recombination, we performed calculations for all (10–100%) growth stages. At a more detailed variation in the parameter, the values of C_i and C_v were calculated by an interpolation of the temperature and pulling rate to intermediate time intervals. The 2D distribution maps obtained by calculating the distribution of the residual concentration difference over the crystal length are shown in Fig. 3a. The corresponding profile of the pulling rate V_p, averaged per hour of the growth process, is shown in Fig. 3b. Changes in the position of the *v*/*i* boundary corresponding to the calculated data can be clearly seen in the experimental carrier lifetime map (Fig. 3c). Comparison of the position and shape of the *v*/*i* boundary in Figs. 3a and 3b shows their complete coincidence.

ANALYSIS OF THE FORMATION OF VACANCY MICRODEFECTS

We developed the theory of the formation of vacancy microdefects (pores and oxide particles) proposed in [3] to calculate the 2D distributions of these microdefects in single-crystal silicon ingots using the above-mentioned data on the specific thermal history of

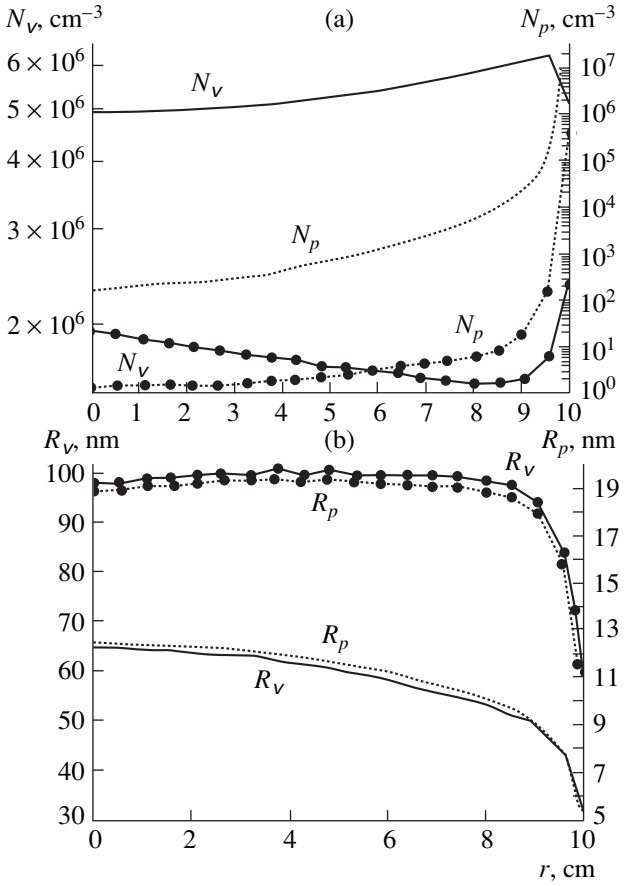

Fig. 4. Radial distributions of the concentrations and sizes of vacancy microdefects: (a) concentrations of pores and oxide particles (N_v and N_p, respectively) and (b) sizes of pores and oxide particles (R_v and R_p, respectively). Lines with and without circles correspond to the heating units without and with a thermal shield, respectively.

the crystal and the calculated distributions of residual intrinsic point defects after the *v*–*i* recombination.

Important parameters determining the perfection of dislocation-free Si single crystals are the density of microdefects and their size. The radial distributions of these parameters for two designs of heating units operating in the conventional fast pulling regime are shown in Figs. 4a and 4b. Note that micropores are dominant among microdefects. The density of oxide particles is high only in a narrow layer near the lateral ingot surface. Micropores are larger in size than oxide particles by a factor of about 5.

EXPERIMENTAL STUDY OF THE SPECIFIC FEATURES OF THE GENERATION AND MOTION OF DISLOCATIONS IN Si WAFERS

We analyzed the specific features of the generation and motion of dislocations in Si wafers containing microdefects of different types that were formed due to the decomposition of the supersaturated solid solution of oxygen occurring during multistep heat treatments of Si wafers (used to form an internal getter) and as a result of the application of external loads.

Experimental samples were cut from 150-mm wafers of dislocation-free single-crystal Si of the vacancy type [4] grown by the Czochralski method along the ⟨100⟩ direction. The concentration of oxygen dissolved in the samples was (7–8) × 10^{17} cm^{-3}. The resistivity of the samples was ~10 Ω cm. The wafers under study were subjected to different multistep heat treatments, including the regime of internal getter formation. The heat treatment regimes used by us are listed in Table 1. Samples for mechanical tests were shaped as parallelepipeds $25 \times 4 \times 0.6$ mm^3 in size with the largest face oriented in the {100} plane; the longest side was oriented along the ⟨110⟩ direction. The samples were chemically polished in an acid mixture HF : HNO_3 = 1 : 6 for 5 min to remove a ~40-μm layer from the surface. After this procedure, the sample under study was placed in a four-point bend test system. Mechanical tests were performed at t = 600°C.

The stresses causing the generation of dislocations from internal sources in the wafer bulk were determined by the start of the intense generation of dislocations in the regions located at a large distance from the supports and the sample edges. Selective chemical etching of such samples revealed pronounced slip lines on their surface and the samples themselves showed macroscopic bending. The structural features of the samples were investigated by the methods of optical microscopy (with selective etching in the Yang etchant [5]) and transmission electron microscopy (TEM).

In the context of the data obtained by us, the scheme of evolution of the defects related to the decomposition of the supersaturated solid solution of oxygen during the formation of the internal getter in Si wafers is as follows.

At low-temperature (nucleation) annealing (450 or 650°C), the decomposition of the supersaturated solid solution of oxygen is accompanied by the formation of atomic conglomerates having donor properties. We showed previously [6] by diffuse X-ray scattering that impurity clouds are formed in this stage of a multistep heat treatment. These clouds are regions with a higher (in comparison with the matrix) content of dissolved oxygen; i.e., they are similar to Guinier–Preston zones. The size of the impurity clouds is 0.2–5 μm. With an increase in the duration or temperature of nucleation annealing, the impurity clouds vanish, leaving large atomic conglomerates (up to several hundred atoms), which serve as nuclei of future oxygen-containing precipitates.

In the initial stages of the growth annealing at 1000°C, small quasi-two-dimensional oxygen-containing precipitates, coherent with the matrix, are formed in

the samples. These precipitates are 20–25 nm in size and shaped as plates (Fig. 5a).

When the size of precipitates becomes as large as 30–40 nm, they acquire a pronounced plate-like shape with a ratio of the linear size to the thickness of about 10 : 1. In this stage of decomposition, plate-like precipitates begin to lose coherence with the environment. Perfect dislocation loops are formed around plate-like precipitates (Fig. 5b).

Plate-like precipitates grow with an increase in the growth annealing time. When they become as large as 50–60 nm in size, the generation of prismatic dislocation loops begins by the mechanism of prismatic extrusion, leading to the formation of linear precipitate–dislocation complexes (Fig. 5c). The average size of such complexes is 2–3 μm.

Further growth of precipitates occurs with the gradual transformation of their shape, which manifests itself primarily in an increase in the precipitate thickness. Precipitates with linear sizes of 250–300 nm are shaped as parallelepipeds with a ratio of the linear sizes to the thickness of about 4 : 1. This transformation is accompanied by the formation of bulk dislocation tangles around precipitates; i.e., globular precipitate–dislocation complexes arise (Fig. 5d). The development of globular precipitate–dislocation complexes is accompanied by secondary oxygen precipitation at climbing dislocation fragments, which sometimes leads to the secondary prismatic extrusion of dislocation loops. The sizes of globular precipitate–dislocation complexes generally do not exceed 1 μm.

In addition to the above-described defects, in the later stages of the decomposition of the supersaturated solid solution of oxygen, the wafers also contain interstitial stacking faults 3–3.5 μm in size (Fig. 5e), dislocation dipoles 3–4 μm in size (Fig. 5f), and perfect dislocation loops (50–200 nm).

The results of the investigation of the structural features of thermally treated samples are listed in Table 2. TEM study revealed no defects in the samples of series 1 and 2. According to the diffuse X-ray scattering data, impurity clouds 0.2–5 μm in size are present in the samples of series 1, and the samples of series 2 contain atomic conglomerates (nuclei of oxygen-containing precipitates). Figure 6 shows the results of the measurement of shear stresses σ_{gen} corresponding to the start of the intense generation of dislocations from internal sources in the samples under consideration. In the thermally treated samples of series 1 and 2, we observed a significant increase in σ_{gen} in comparison with the as-grown state. According to the TEM data, an avalanche-like generation of dislocations occurs in these samples: a large number of sources (apparently, of the same type) generate dislocations almost simultaneously. The nature of these sources has not yet been established. The largest increase in σ_{gen} was observed in the samples of series 3, in which plate-like precipitates play the role of heterogeneous nucleation centers.

Table 1. Regimes of multistep heat treatment of Si wafers

Series no.	Heat treatment regime
1	1000°C/15 min + 450°C/16 h
2	1000°C/15 min + 650°C/16 h
3	1000°C/15 min + 650°C/16 h + 800°C/4 h + 1000°C/0.5 h
4	1000°C/15 min + 650°C/16 h + 800°C/4 h + 1000°C/4 h
5	1000°C/15 min + 650°C/16 h + 800°C/4 h + 1000°C/16 h
6	1000°C/15 min + 450°C/16 h + 650°C/16 h + 1000°C/4 h

Multistep heat treatments used in the conventional technique of the formation of an internal getter in wafers (samples of series 4–6) lead to their significant softening. In these samples, the values of σ_{gen} are much smaller than in the as-grown samples. A characteristic feature of the samples of these series is the presence of relatively large microdefects: linear precipitate–dislocation complexes, globular precipitate–dislocation complexes, stacking faults, and dislocation dipoles (Table 2). An especially significant decrease in σ_{gen} is observed in the samples of series 6, which have fairly high concentrations of stacking faults and dislocation dipoles. According to the TEM data, it is these defects that are the most effective centers of the heterogeneous nucleation of dislocations. In comparison with these defects, globular precipitate–dislocation complexes show much lower activity as centers of the heterogeneous nucleation of dislocations under the action of external loads. Small plate-like precipitates are least effective as centers of the heterogeneous nucleation of dislocations under external loads.

ANALYSIS OF THE GENERATION OF DISLOCATIONS IN Si WAFERS DUE TO STRESSES CAUSED BY THE WAFER WEIGHT AND NONUNIFORM HEATING

To analyze the probability of dislocation generation in Si wafers due to stresses caused by the wafer weight and nonuniform heating, it is necessary to know the level of actual stresses occurring during a heat treatment. The stress threshold, above which heterogeneous sources begin to generate dislocations in Si wafers under certain conditions, was experimentally determined in [7, 8]. During the annealing, a wafer is freely

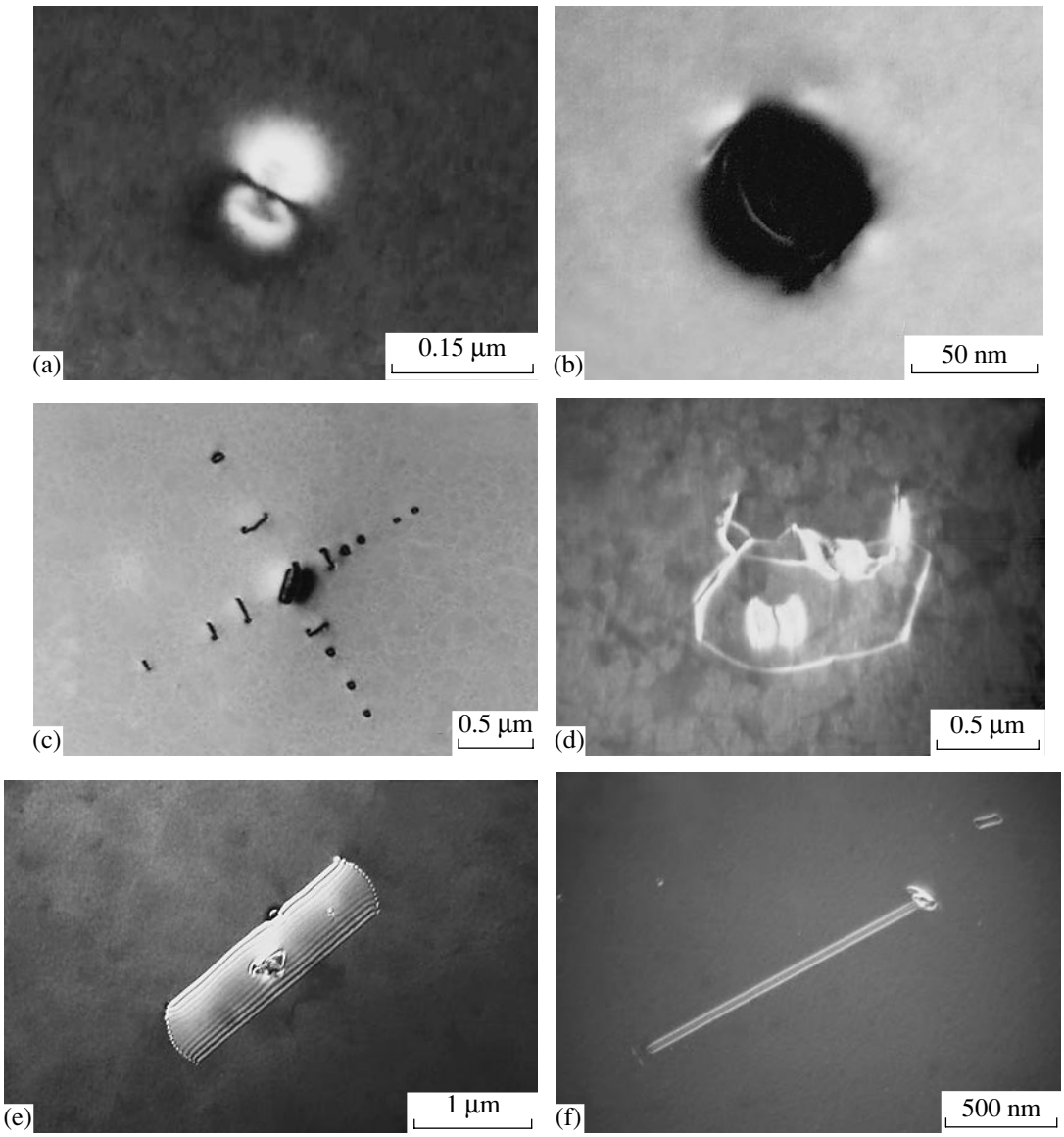

Fig. 5. TEM images of defects in the samples of series *3–6*: (a) planar matrix-coherent precipitates, (b) planar precipitates surrounded by a perfect dislocation loop, (c) linear precipitate–dislocation complexes, (d) globular precipitate–dislocation complexes, (e) stacking faults, and (f) dislocation dipoles.

placed on three or four symmetrically arranged supports.

The mathematical statement of the problem with specified edge conditions was formulated in [9]. The general strain pattern changes only slightly with a change in the number of supports and is rather complicated. On the basis of the bending scheme we used, the strain in the wafer was analyzed at three characteristic points at which maximum changes were observed with a change in the radial position of the supports. Figure 7 shows the dependences of the strain at the characteristic points on the support area for the wafers placed on three or four supports located at a distance of $0.7R$ from the wafer center, where R is the wafer radius. For each scheme of the support location, the strains at the chosen characteristic points depend weakly on the support contact area. The increase in the number of supports from 3 to 4 makes it possible to decrease significantly the wafer bending, especially at point *1* (the peripheral point located at the largest distance from the support).

The maximum values of the von Mises stress σ_M are observed near the support points. It can be clearly seen from the data shown that the stresses are the lowest when the supports are located at a distance of (0.6–0.7R) from the wafer center. Figure 8 shows the dependence of the maximum values of σ_M for a 300-mm wafer at different radial locations of three and four supports. The increase in the wafer diameter from 200 to 300 mm leads to an increase in the maximum strains by a factor of about 4.5 (calculation was performed for

Table 2. TEM data on microdefects in thermally treated Si wafers

Series no.	Type, size, and density of microdefects			
	impurity clouds*	atomic conglomerates	coherent plate-like precipitates	coherent plate-like precipitates with a dislocation loop
1	0.2–5 μm**, 3×10^8 cm^{-3}***	absent	absent	absent
2	absent	present	absent	absent
3	absent	absent	25–30 nm, 4.3×10^9 cm^{-3}	absent
4	absent	absent	absent	300 nm, 3×10^{10} cm^{-3}
5	absent	absent	absent	150 nm
6	absent	absent	25 nm, 5.8×10^{11} cm^{-3}	100 nm, 3×10^{10} cm^{-3}
Series no.	Type, size, and density of microdefects			
	linear precipitate–dislocation complexes	globular precipitate–dislocation complexes	stacking faults	dislocation dipoles
1	absent	absent	absent	
2	absent	absent	absent	
3	absent	absent	absent	absent
4	2 μm, 2.8×10^{10} cm^{-3}	0.8 μm, 7×10^9 cm^{-3}	2 μm, 2.5×10^8 cm^{-3}	absent
5	5 μm, 6×10^{10} cm^{-3}	2 μm, 9×10^{10} cm^{-3}	2 μm, 9×10^9 cm^{-3}	absent
6	absent	absent	1.5–2 μm, 5×10^9 cm^{-3}	3–4 μm, 4.5×10^8 cm^{-3}

* Diffuse X-ray scattering data [6].
** Size of microdefects.
*** Density of microdefects.

wafers of the same thickness: 1000 μm). Figure 9 shows the comparative data on the dependence of the maximum values of σ_M on the support area for a 300-mm Si wafer located on three or four supports. As one would suggest, the region of maximum stresses decreases with a decrease in the support area due to a decrease in the size of the perturbation region at the contact between the wafer and the support. It is noted

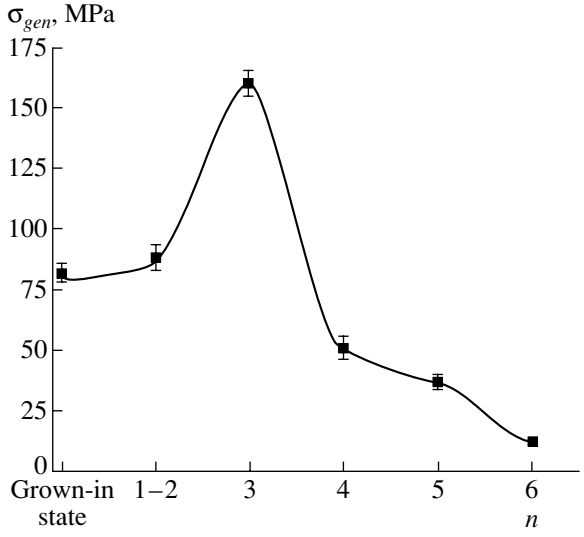

Fig. 6. Measured stresses σ_{gen} corresponding to the start of the intense generation of dislocations from internal sources for the samples from different series (n is the number of a series).

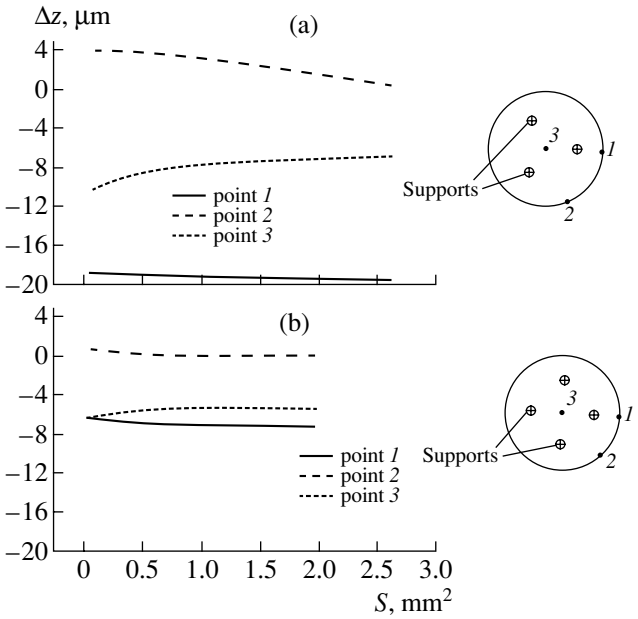

Fig. 7. Dependence of the gravitational strain at characteristic wafer points on the support area S for wafers located on (a) three and (b) four supports.

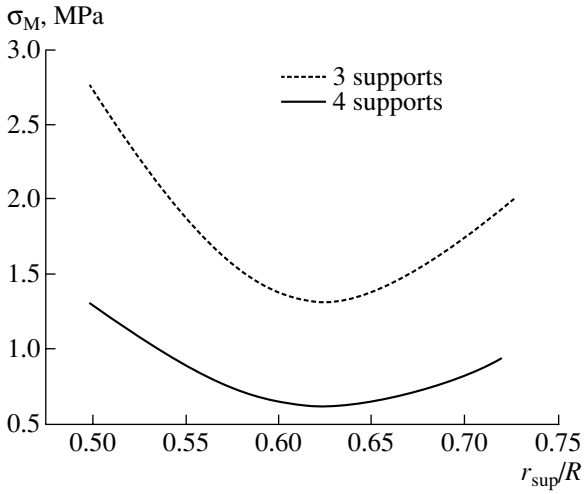

Fig. 8. Dependence of the maximum stress σ_{max} for a 300-mm wafer at different radial arrangements of three and four supports.

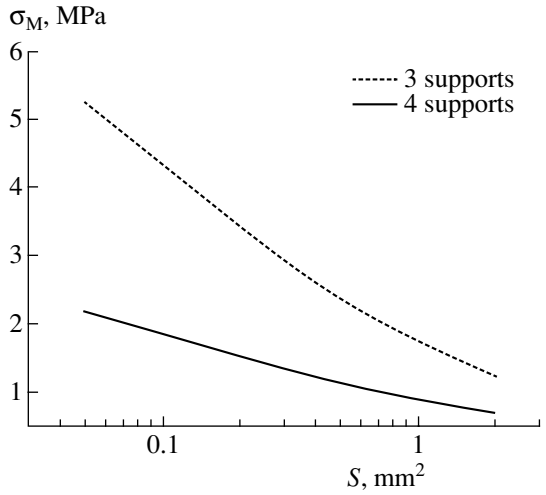

Fig. 9. Dependences of the maximum stress σ_{max} on the support area for a 300-mm Si wafer located on three and four supports ($r_{sup}/R = 0.7$).

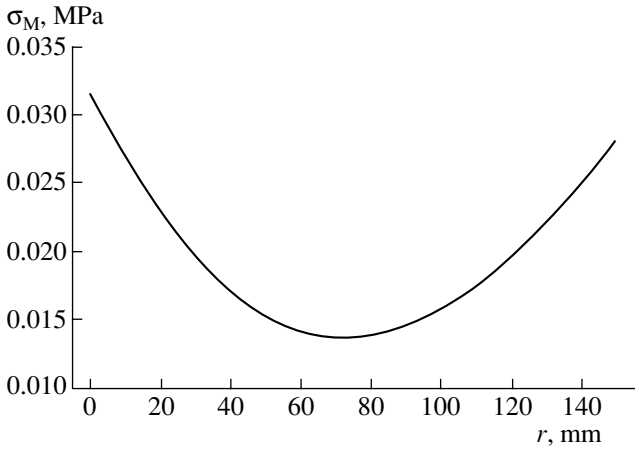

Fig. 10. Radial distribution of the thermal stress σ_{max} for a 300-mm wafer, calculated for a radial temperature drop of 1 K.

worthy that the general level of stresses in the main region of the wafer increases with a decrease in the contact area, still remaining sufficiently low (0.01–0.05 MPa). The dependences in Fig. 9 indicate that in the case of four supports the maximum stresses σ_{max} decrease by a factor of 2 for a contact area of 2 mm^2. This difference increases even more with a decrease in the contact area. Thus, the change from three to four supports makes it possible to decrease significantly both the level of maximum stresses in the contact region (by more than a factor of 2) and the level of stresses in the entire wafer. In this case, the maximum wafer bending also significantly decreases (by a factor of about 3).

Thermoelastic stresses result from the nonuniform temperature distribution in the wafer plane, which is related to the heating conditions. The conventional approach was used in the calculation. As in the case of the action of gravitational forces, we used the von Mises stress σ_M to characterize the strained state

Figure 10 shows as an example the results of the calculation of the radial distribution of the thermal stresses σ_M for a 300-mm wafer. The calculation was performed for a radial temperature drop of 1 K. The temperature at the wafer center was assumed to be 1273 K. At a radial temperature drop of 1 K, the maximum thermal stresses σ_{max} are 0.03 MPa, which is much lower than the gravitational stresses. The regions of maximum thermal shear stresses are at the center and the edge of the wafer. At the same time, these stresses are minimum near the supports, in contrast to the gravitational stresses. The maximum thermal shear stresses for 300-mm wafers at this temperature drop between the center and the edge of the wafer are ~0.01 MPa. An increase in the radial temperature drop causes a proportional increase in the thermoelastic stresses. Calculation shows that the maximum thermal stresses occurring during thermal annealing are comparable in magnitude with maximum gravitational stresses only for 200-mm wafers at radial temperature drops below 10 K. For 300-mm wafers, even at the same radial temperature drops, the gravitational stresses greatly exceed the thermal ones.

Thus, the three-dimensional problem of determining the field of elastic stresses caused by the wafer weight is solved in the isotropic approximation for 200- and 300-mm Si wafers located on three or four symmetrically arranged point supports with different contact areas.

ACKNOWLEDGMENTS

This study was supported by the Russian Foundation for Basic Research, project no. 04-02-17168.

REFERENCES

1. N. A. Verezub, M. G. Mil'vidskiĭ, and A. I. Prostomolotov, Materialovedenie, No. 3, 2 (2004).

2. A. I. Prostomolotov, in *Proceedings of 4th International Conference on Single Crystal Growth and Heat and Mass Transfer, Obninsk, Russia, 2001* (Obninsk, 2001), Vol. 3, p. 689.
3. V. V. Voronkov, Mater. Sci. Eng. B **73**, 69 (2000).
4. V. V. Voronkov and R. Falster, J. Cryst. Growth **204**, 462 (1999).
5. K. H. Yang, J. Electrochem. Soc. **131**, 1140 (1984).
6. V. T. Bublik, S. Yu. Matsnev, K. D. Shcherbachev, *et al.*, Fiz. Tverd. Tela (St. Petersburg) **45** (10), 1825 (2003) [Phys. Solid State **45** (10), 1918 (2003)].
7. M. V. Mezhennyĭ, M. G. Mil'vidskiĭ, V. F. Pavlov, and V. Ya. Reznik, Fiz. Tverd. Tela (St. Petersburg) **43** (1), 47 (2001) [Phys. Solid State **43** (1), 47 (2001)].
8. M. V. Mezhennyĭ, M. G. Mil'vidskiĭ, V. F. Pavlov, and V. Ya. Reznik, Fiz. Tverd. Tela (St. Petersburg) **44** (7), 1230 (2002) [Phys. Solid State **44** (7), 1284 (2002)].
9. M. V. Mezhennyĭ, M. G. Mil'vidskiĭ, and A. I. Prostomolotov, Fiz. Tverd. Tela (St. Petersburg) **45** (10), 1794 (2003) [Phys. Solid State **45** (10), 1884 (2003)].

Translated by Yu. Sin'kov

Crystallography Reports, Vol. 50, Suppl. 1, 2005, pp. S16–S21.

STRUCTURE OF INORGANIC COMPOUNDS

Stabilization of Lattice Period in Quinary Solid Solutions of the A^3B^5 Compounds

V. V. Kuznetsov*, E. R. Rubtsov*, and E. A. Kognovitskaya**

** St. Petersburg State University of Electrical Engineering (LETI), St. Petersburg, Russia*
e-mail: vvkuznetsov@mail.eltech.ru
*** Ioffe Physicotechnical Institute, Russian Academy of Sciences,*
Politekhnicheskaya ul. 26, St. Petersburg, 194021 Russia

Received February 3, 2005

Abstract—The stabilizing effect of elastic strains on the lattice period of a quinary solid solution is considered. The expression for the stabilization factor for quinary solid solutions of the $A_xB_{1-x}C_yD_zE_{1-y-z}$ type is derived. It is shown that the stabilizing influence of the substrate sharply increases in the vicinity of the region of the chemical spinodal. The stabilization factors are calculated for the $Ga_xIn_{1-x}P_yAs_zSb_{1-y-z}$ and $Al_xGa_yIn_{1-x-y}P_zAs_{1-z}$ quinary solid solutions isoperiodic to InAs, GaSb, and GaAs. It is shown that in the region of thermodynamic instability the stabilization factor has negative values. The changes in the composition of the above elastically strained quinary solid solutions are analyzed with respect to the equilibrium composition. It is also shown that stabilization of the lattice period does not signify the stabilization of its composition.

As is well known [1, 2], elastic strains arising at the mismatch of the lattice periods of the epitaxial solid-solution layer and the substrate give rise to changes in the solid-solution composition, which, in turn, changes the period of its crystal lattice. In this case, the lattice period of the layer becomes close to the lattice period of the substrate. In other words, the indicated elastic strains have a stabilizing effect on the lattice period of the solid solution.

Qualitatively, this effect was described with the aid of a specially introduced stabilization factor [3, 4] in the form

$$q = (a_0 - a_s)/(a_1 - a_s), \quad (1)$$

where a_0 is the lattice period of the solid solution crystallized under the conditions of thermodynamic equilibrium; a_1 is the lattice period of the epitaxial layer in the free state, i.e., after the removal of strains; and a_s is the period of the substrate lattice. The technique for calculation of $\ldots A^3B^5$ was reported in [3, 4].

Below, we consider the characteristic features of the calculation of the stabilization factor for quinary systems. This calculation is based on the method of calculation of the contact supersaturation considered in [5]. In essence, the method reduces to the following. Knowing the composition x_0, y_0, and z_0 of the solid solution, one determines the composition of the liquid phase at the given temperature from the equations of the equilibrium phase diagram. Once the composition of the liquid phase is found, one may also determine the composition of the solid solution, x_1, y_1, and z_1, from the equations of the coherent phase diagram. The composition of the equilibrium solid solution, x_0, y_0, z_0, is used to obtain the equilibrium period of the crystal lattice, a_0, and, using the composition of the elastically stressed solid solution, x_1, y_1, z_1, also the deformed lattice period a_1. However, such a sequence of stabilization-factor calculations is too cumbersome and complicated. In order to simplify this procedure, we first derive the formula for the stabilization factor of the lattice period for A^3B^5-based quinary systems. With this aim, we derive the expression relating the stabilization factor q to the solid-solution composition and the process temperature.

The state of the thermodynamic liquid–solid equilibrium is described by the corresponding change in the free energy of the quinary system, which is equal to zero [6],

$$\Delta G_0^s = G^s(x_0, y_0, z_0, T_0) - \sum_{i=1}^{5} n_{0i}\mu_i^l(T_0) = 0, \quad (2)$$

where n_{0i} is the number of moles of the ith component per mole of the solid solution and $\mu_i^l(T_0)$ is the chemical potential of the ith component in the liquid phase at the equilibrium temperature T_0. Under the conditions of phase equilibrium, the following conditions are fulfilled for a quinary system:

$$(\partial\Delta G_0^s/\partial x)_{\substack{x=x_0\\y=y_0\\z=z_0}} = 0;$$
$$(\partial\Delta G_0^s/\partial y)_{\substack{x=x_0\\y=y_0\\z=z_0}} = 0; \quad (\partial\Delta G_0^s/\partial z)_{\substack{x=x_0\\y=y_0\\z=z_0}} = 0. \quad (3)$$

When considering the state of the coherent metastable equilibrium, one has to take into account the energy of elastic strains changing the equilibrium temperature and, thus, also the solid-solution composition:

$$\Delta G_1^s = G^s(x_1, y_1, z_1, T_1) + G^{el} - \sum_{i=1}^{5} n_i \mu_i^l(T_1) = 0, \quad (4)$$

where n_i is the number of moles of the ith component per mole of elastically stressed solid solution and G^{el} is the elastic energy of the strained solid phase. In this case

$$(\partial \Delta G_1^s/\partial x)_{\substack{x=x_0\\y=y_0\\z=z_0}} = 0;$$
$$(\partial \Delta G_1^s/\partial y)_{\substack{x=x_0\\y=y_0\\z=z_0}} = 0; \quad (\partial \Delta G_1^s/\partial z)_{\substack{x=x_0\\y=y_0\\z=z_0}} = 0. \quad (5)$$

Subtracting Eq. (2) from Eq. (4) and assuming that in both cases the liquids of the equivalent compositions correspond to the phase equilibrium, we arrive at the function $g(x_1, y_1, z_1, T_1)$

$$g(x_1, y_1, z_1, T_1) = G^s(x_1, y_1, z_1, T_1) - G^s(x_0, y_0, z_0, T_0) - \sum_{i=1}^{5} [n_i \mu_i^l(T_1) - n_{0i} \mu_i^l(T_0)] = -G^{el}. \quad (6)$$

Expanding the function $g(x_1, y_1, z_1, T_1)$ into a Taylor series in degrees of Δx, Δy, Δz, and ΔT with due regard for Eq. (3) and the linear approximation of its temperature dependence, we obtain

$$g(x_1, y_1, z_1, T_1) \approx \frac{1}{2}\frac{\partial^2 g(x_0, y_0, z_0, T_0)}{\partial x^2}(x_1 - x_0)^2 + \frac{1}{2}\frac{\partial^2 g(x_0, y_0, z_0, T_0)}{\partial y^2}(y_1 - y_0)^2 + \frac{1}{2}\frac{\partial^2 g(x_0, y_0, z_0, T_0)}{\partial z^2}(z_1 - z_0)^2 + \frac{\partial^2 g(x_0, y_0, z_0, T_0)}{\partial x \partial y}(x_1 - x_0)(y_1 - y_0) + \frac{\partial^2 g(x_0, y_0, z_0, T_0)}{\partial x \partial z}(x_1 - x_0)(z_1 - z_0) + \frac{\partial^2 g(x_0, y_0, z_0, T_0)}{\partial y \partial z}(y_1 - y_0)(z_1 - z_0) + \frac{\partial g(x_0, y_0, z_0, T_0)}{\partial T}(T_1 - T_0). \quad (7)$$

Taking into account that the free energy of a mole of quinary solid solution of the type $A_xB_{1-x}C_yD_zE_{1-y-z}$ in the absence of elastic strains is determined, in full accordance with the approximation of a regular solution, by the following expression [7]:

$$G_0^s = xy\mu_{AC}^0 + (1-x)y\mu_{BC} + xz\mu_{AD}^0 + (1-x)z\mu_{BD}^0 + x(1-y-z)\mu_{AE}^0 + (1-x)(1-y-z)\mu_{BE}^0 + RT[x\ln(x) + (1-x)\ln(1-x) + y\ln(y) + z\ln(z) + (1-y-z)\ln(1-y-z)] + \alpha_{AB}^s x(1-x) + \alpha_{CD}^s yz + \alpha_{CE}^s y(1-y-z) + \alpha_{DE}^s z(1-y-z), \quad (8)$$

where μ_{ij}^0 are the chemical potentials of pure binary compounds ij, which are the components of the solid solution under consideration, and α_{kl}^s are the parameters of interatomic interactions in the solid phase that take into account the deviation from the ideal solution. The expressions for the partial derivatives of G_0^s with respect to the composition are

$$\frac{\partial^2 G_0^s}{\partial x^2} = \frac{RT}{x(1-x)} - 2\alpha_{AB}^s = \delta_1;$$
$$\frac{\partial^2 G_0^s}{\partial y^2} = \frac{RT(1-z)}{y(1-y-z)} - 2\alpha_{CE}^s = \delta_2;$$
$$\frac{\partial^2 G_0^s}{\partial z^2} = \frac{RT(1-y)}{z(1-y-z)} - 2\alpha_{DE}^s = \delta_3;$$
$$\frac{\partial^2 G_0^s}{\partial x \partial y} = \alpha_{C1} + (1-2x)(\alpha_{AC-BC}^s - \alpha_{AE-BE}^s) + z(\alpha_{AC-AD}^s - \alpha_{BC-BD}^s) + (1-2y-z)(\alpha_{AC-AE}^s - \alpha_{BC-BE}^s) - z(\alpha_{AD-AE}^s - \alpha_{BD-BE}^s) = \beta_1; \quad (9)$$
$$\frac{\partial^2 G_0^s}{\partial x \partial z} = \alpha_{C2} + (1-2x)(\alpha_{AD-BD}^s - \alpha_{AE-BE}^s) + y(\alpha_{AC-AD}^s - \alpha_{BC-BD}^s) + (1-2z-y)(\alpha_{AD-AE}^s - \alpha_{BD-BE}^s) - y(\alpha_{AC-AE}^s - \alpha_{BC-BE}^s) = \beta_2,$$
$$\frac{\partial^2 G_0^s}{\partial y \partial z} = \frac{RT}{(1-y-z)} + \alpha_{CD}^s - \alpha_{CE}^s - \alpha_{DE}^s = \beta_3,$$

where α_{Ci} is the combination of the energies of pair interactions between the nearest tetrahedrally coordinated atoms from different sublattices. The parameters α_{Ci} characterize the excessive mixing energy in quinary solid solutions determined from the formula given elsewhere [8].

Now, ignoring the temperature dependence of the coefficients of component activity (because of the smallness of ΔT) and taking into account the chemical potentials,

$$\begin{gathered}\mu_{ij}^0 = \mu_i^{0,l} + \mu_j^{0,l} + RT\ln(\gamma_i^{sl}\gamma_j^{sl}/4) - \Delta S_{ij}^F(T_{ij}^F - T);\\ \mu_i^l = \mu_i^{0,l} + RT\ln(\gamma_i^l x_i^l),\end{gathered} \tag{10}$$

we can modify Eq. (7) to the form

$$\begin{aligned}&\frac{1}{2}\delta_1(x_1 - x_0)^2 + \frac{1}{2}\delta_2(y_1 - y_0)^2 + \frac{1}{2}\delta_3(z_1 - z_0)^2\\ &+ \beta_1(x_1 - x_0)(y_1 - y_0) + \beta_2(x_1 - x_0)(z_1 - z_0)\\ &+ \beta_3(y_1 - y_0)(z_1 - z_0) - \frac{\Delta T}{T_0}\Bigg[\sum_{i=1}^{2}\sum_{j=3}^{5} n_{0i}n_{0j}H_{ij}^F\\ &- \alpha_{AB}x(1-x) - \alpha_{CD}yz - \alpha_{CE}y(1-y-z)\\ &- \alpha_{DE}z(1-y-z)\Bigg] = -G^{el}.\end{aligned} \tag{11}$$

In the above equation, T_{ij}^F, H_{ij}^F, and ΔS_{ij}^F are the temperature, enthalpy, and entropy of melting of the binary compound *ij*; γ_i^l and x_i^l are the activity coefficient and concentration of the *i*th component in the liquid phase, respectively; γ_i^{sl} and γ_j^{sl} are the activity coefficients of the *i*th and *j*th components of the binary melt of the stoichiometric composition ($x_i^l = x_j^l = 0.5$); $\Delta T = T_0 - T_1$ is the equilibrium supercooling induced by stresses [9]. Introducing the notation

$$\begin{aligned}H_{\text{eff}} &= \sum_{i=1}^{2}\sum_{j=3}^{5} n_{0i}n_{0j}H_{ij}^F - \alpha_{AB}x(1-x)\\ &- \alpha_{CD}yz - \alpha_{CE}y(1-y-z) - \alpha_{DE}z(1-y-z)\end{aligned} \tag{12}$$

and using the expression for elastic energy obtained in [5], we may represent Eq. (11) in the form

$$\begin{aligned}&\frac{1}{2}\delta_1(x_1 - x_0)^2 + \frac{1}{2}\delta_2(y_1 - y_0)^2 + \frac{1}{2}\delta_3(z_1 - z_0)^2\\ &+ \beta_1(x_1 - x_0)(y_1 - y_0) + \beta_2(x_1 - x_0)(z_1 - z_0)\\ &+ \beta_3(y_1 - y_0)(z_1 - z_0) - \frac{\Delta T}{T_0}H_{\text{eff}} = -\sigma(a_1 - a_s).\end{aligned} \tag{13}$$

Taking into account conditions (5) and assuming that $T_0/T_1 \approx 1$ (because, in practice, ΔT does not exceed several degrees), we may differentiate Eq. (13) with respect to composition to obtain

$$\begin{aligned}&\delta_1(x_1 - x_0) + \beta_1(y_1 - y_0) + \beta_2(z_1 - z_0)\\ &\quad = -2\sigma(a_1 - a_s)k_x,\\ &\delta_2(y_1 - y_0) + \beta_1(x_1 - x_0) + \beta_3(z_1 - z_0)\\ &\quad = -2\sigma(a_1 - a_s)k_y,\\ &\delta_3(z_1 - z_0) + \beta_2(x_1 - x_0) + \beta_3(z_1 - z_0)\\ &\quad = -2\sigma(a_1 - a_s)k_z,\end{aligned} \tag{14}$$

where $k_x = \partial a/\partial x$, $k_y = \partial a/\partial y$, and $k_z = \partial a/\partial z$.

Now, it is easy to modify Eqs. (14) to the form

$$\begin{aligned}x_1 - x_0 &= 2\sigma(a_1 - a_s)\\ &\times \frac{k_x(\beta_3^2 - \delta_2\delta_3) + k_y(\delta_3\beta_1 - \beta_2\beta_3) + k_z(\delta_2\beta_2 - \beta_1\beta_3)}{\delta_3(\delta_1\delta_2 - \beta_1^2) + \beta_3(\beta_1\beta_2 - \delta_1\beta_3) + \beta_2(\beta_1\beta_3 - \delta_2\beta_2)};\\ y_1 - y_0 &= 2\sigma(a_1 - a_s)\\ &\times \frac{k_x(\delta_3\beta_1 - \beta_2\beta_3) + k_y(\beta_2^2 - \delta_1\delta_3) + k_z(\delta_1\beta_3 - \beta_1\beta_2)}{\delta_3(\delta_1\delta_2 - \beta_1^2) + \beta_3(\beta_1\beta_2 - \delta_1\beta_3) + \beta_2(\beta_1\beta_3 - \delta_2\beta_2)};\\ z_1 - z_0 &= 2\sigma(a_1 - a_s)\\ &\times \frac{k_x(\delta_2\beta_2 - \beta_1\beta_3) + k_y(\delta_1\beta_3 - \beta_1\beta_2) + k_z(\beta_1^2 - \delta_1\delta_3)}{\delta_3(\delta_1\delta_2 - \beta_1^2) + \beta_3(\beta_1\beta_2 - \delta_1\beta_3) + \beta_2(\beta_1\beta_3 - \delta_2\beta_2)}.\end{aligned} \tag{15}$$

Now, the dependence of the lattice period on the composition is represented as

$$a_1 - a_0 = k_x(x_1 - x_s) + k_y(y_1 - y_s) + k_z(z_1 - z_s). \tag{16}$$

Substituting Eq. (14) into Eq. (15), we obtain

$$\begin{aligned}q &= 1 + 2\sigma[k_x^2(\delta_2\delta_3 - \beta_3^2) + k_y^2(\delta_1\delta_3 - \beta_2^2)\\ &+ k_z^2(\delta_1\delta_2 - \beta_1^2) + 2k_xk_y(\beta_2\beta_3 - \delta_3\beta_1)\\ &+ 2k_xk_z(\beta_1\beta_3 - \delta_2\beta_2)\\ &+ 2k_yk_z(\beta_1\beta_2 - \delta_1\beta_3)]/[\delta_3(\delta_1\delta_2 - \beta_1^2)\\ &+ \beta_3(\beta_1\beta_2 - \delta_1\beta_3) + \beta_2(\beta_1\beta_3 - \delta_2\beta_2)].\end{aligned}$$

Equation (17) for the stabilization factor corresponds to the left-hand side of the equation of a coherent spinodal [10]. The expression in the fraction denominator corresponds to the equation of chemical spinodal. This fact results in the infinite value of the sta-

Fig. 1. Stabilization factor in (a) $Ga_xIn_{1-x}P_ySb_{1-y-z}/InAs$ ⟨111⟩ and (b) $Ga_xIn_{1-x}P_yAs_zSb_{1-y-z}/GaSb$ ⟨100⟩ at $f = -1\%$ and $T = 773$ K and (c)$Al_xGa_yIn_{1-x-y}P_zAs_{1-z}/GaAs$ ⟨100⟩ at $f = -1\%$ and $T = 1073$ K; (*1*) positive and (*2*) negative values.

(a)

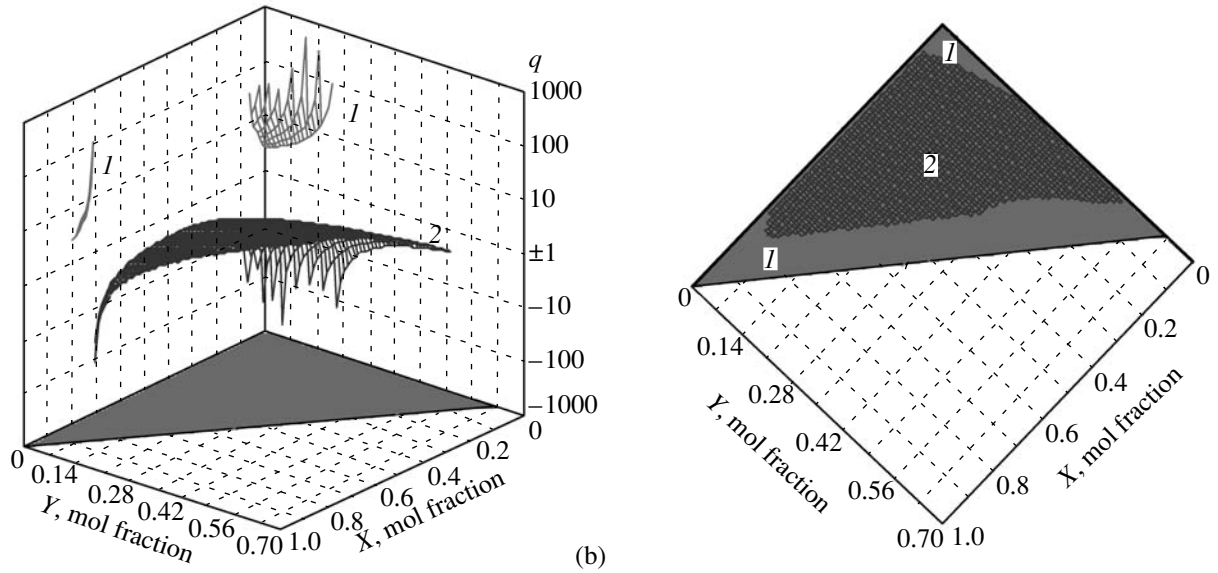
q
1000
100
10
±1
−10
−100
−1000
0
1
2
0
0.14
0.28
0.42
0.56
0.70
Y, mol fraction
0.2
0.4
0.6
0.8
1.0
X, mol fraction

(b)

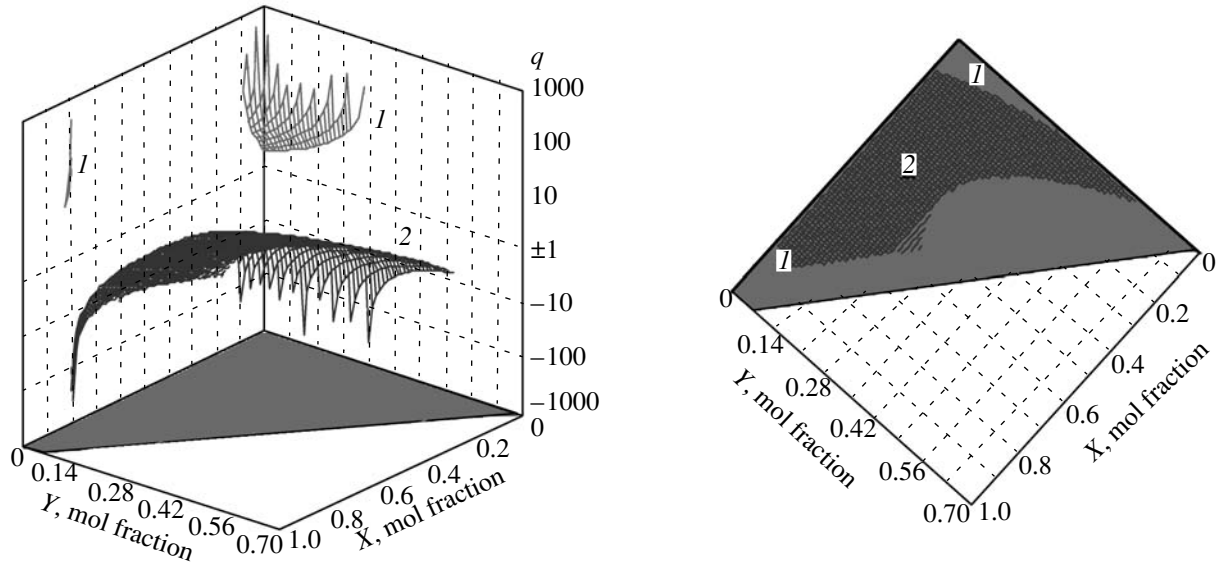
q
1000
100
10
±1
−10
−100
−1000
0
1
2
0
0.14
0.28
0.42
0.56
0.70
Y, mol fraction
0.2
0.4
0.6
0.8
1.0
X, mol fraction

(c)

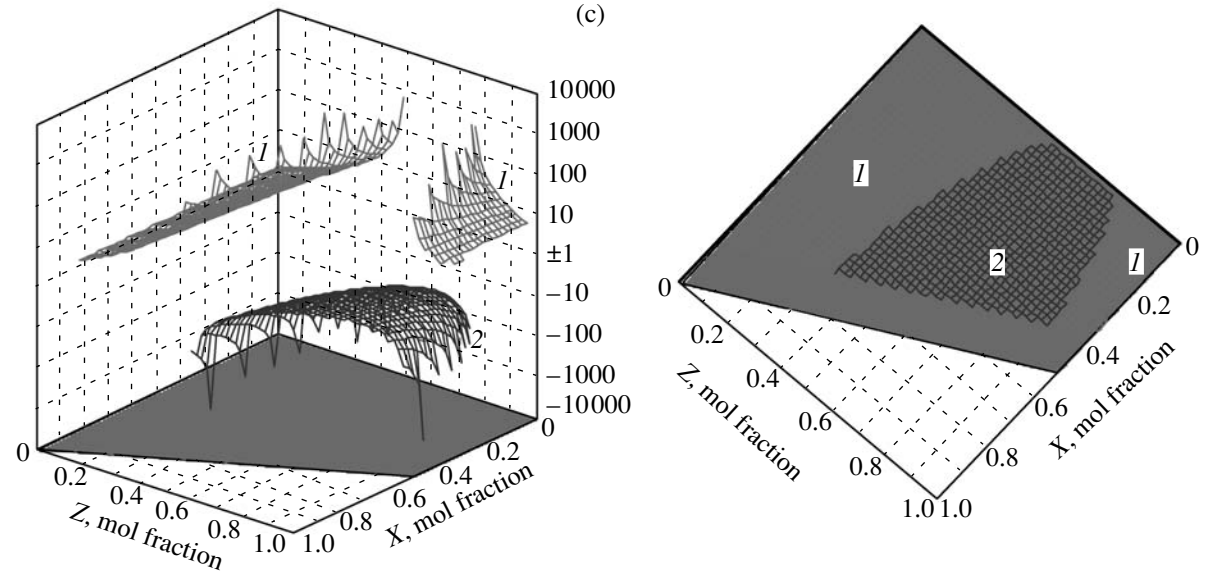
10000
1000
100
10
±1
−10
−100
−1000
−10000
0
1
2
0
0.2
0.4
0.6
0.8
1.0
Z, mol fraction
X, mol fraction

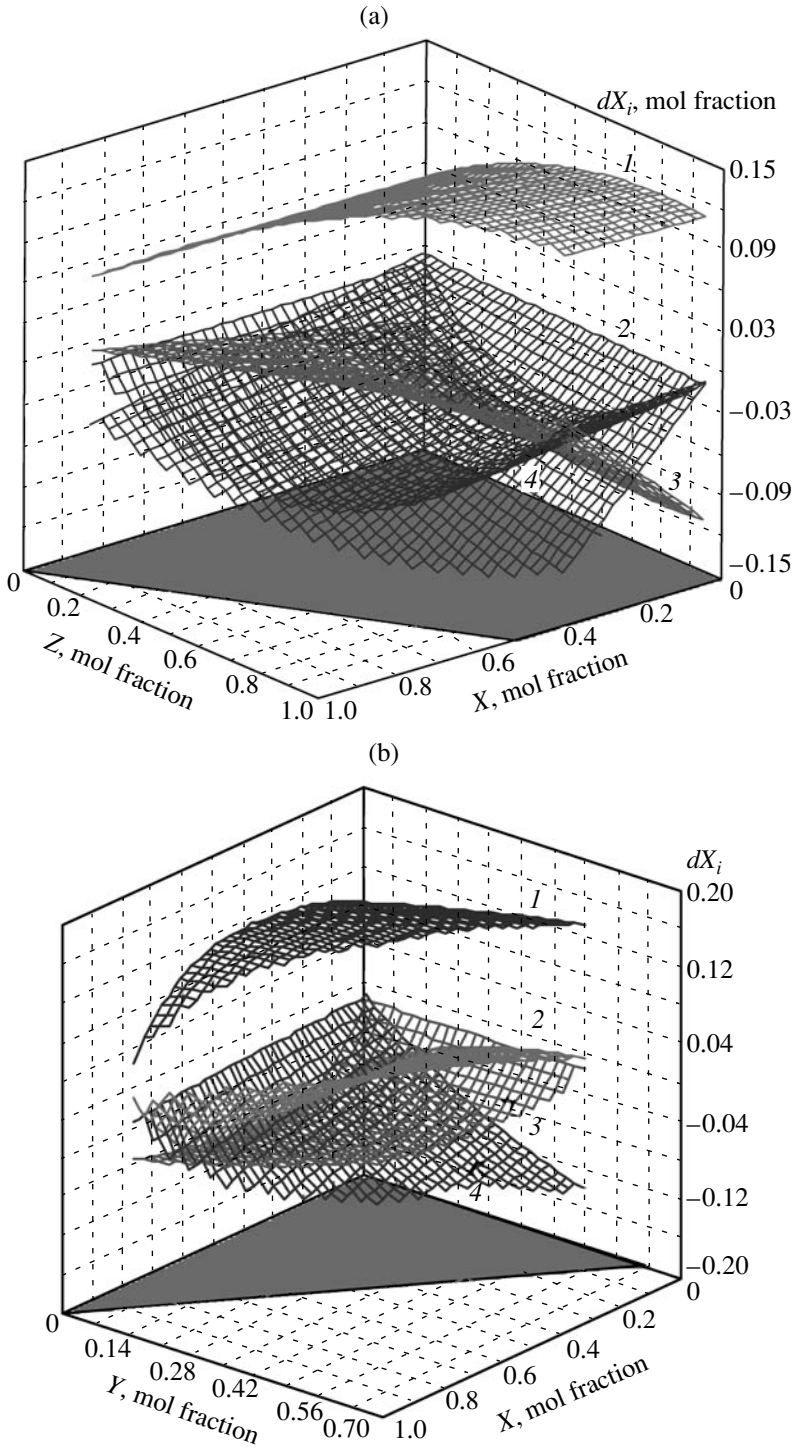

Fig. 2. The change of the composition of elastically stressed solid solution with respect to the equilibrium composition. (a) The $Al_xGa_yIn_{1-x-y}P_zAs_{1-z}$/GaAs ⟨100⟩ at $f = -1\%$ and $T = 1073$ K; (*1*) In, (*2*) Al, (*3*) Ga, (*4*) P; and (b) $Ga_xIn_{1-x}P_yAs_zSb_{1-z}$/GaSb ⟨100⟩ at $f = -1\%$ and $T = 773$ K; (*1*) Sb, (*2*) As, (*3*) Ga, and (*4*) P.

bilization factor at the boundary of the spinodal decomposition region. In practice, this signifies that the stabilizing effect of the substrate dramatically increases in the vicinity of the chemical-spinodal region.

The stabilization factor for quinary solid solutions of the composition $Ga_xIn_{1-x}P_yAs_zSb_{1-y-z}$ isoperiodic to InAs and GaSb at the crystallographic orientations {100} and {111} ($T = 773$ K) and $Al_xGa_yIn_{1-x-y}P_zAs_{1-z}$/GaAs

at the crystallographic orientation {100} (T = 1073 K) was calculated with the use of the thermodynamic parameters from [11]. The data obtained are presented in Fig. 1.

Analysis of the calculated data shows that, in the region of thermodynamic instability, the stabilization factor takes negative values. This is explained by the change in curvature of the curve of the free energy of the solid-solution composition, which results in a reversal of the sign of Δa.

It is for this reason that the values of contact supercooling in the region of spinodal decomposition also have negative values [5]. The negative ΔT_K indicates that in this region the contacting phase is not the supersaturated but undersaturated liquid phase, which gives rise to substrate dissolution in this region. Substituting Eqs. (15) into Eqs. (13), we arrive at a simple formula for evaluating contact supercooling in the form

$$\Delta T = (T_0/H_{\text{eff}})\sigma(a_0 - a_s)^2/q. \quad (17)$$

The above equation is valid for ternary, quaternary, and quinary systems [2, 4]. It is seen that, at negative stabilization factors, the ΔT value also becomes negative.

In quinary and quaternary solid solutions, stabilization of the lattice periods does not signify the stabilization of the solid-solution composition. This is confirmed by the analysis of composition variations in elastically stressed solid solutions with respect to the equilibrium solid solution performed for quinary solid solutions of the compositions $Al_xGa_yIn_{1-x-y}P_zAs_{1-z}$/GaAs and $Ga_xIn_{1-x}P_yAs_zSb_{1-y-z}$/GaSb. Examples of such calculations are illustrated by Fig. 2.

Thus, we derived an expression for the stabilization factor of quinary solid solutions of the $A_xB_{1-x}C_yD_zE_{1-y-z}$ type. We also analyzed the stabilizing effect of elastic strains on the lattice period of quinary solid solution for an example of the Ga–In–P–As–Sb and Al–Ga–In–P–As systems.

REFERENCES

1. V. V. Kuznetsov, P. P. Moskvin, and V. S. Sorokin, J. Cryst. Growth **88**, 241 (1988).
2. V. V. Kuznetsov, P. P. Moskvin, and V. S. Sorokin, *Nonequilibrium Effects in Liquid-phase Heteroepitaxy of Semiconductor Solid Solutions* (Metallurgiya, Moscow, 1991) [in Russian].
3. V. V. Voronkov, L. M. Dolginov, A. N. Lapshin, and M. G. Mil'vidskiĭ, Kristallografiya **22** (2), 375 (1977) [Sov. Phys. Crystallogr. **22** (2), 211 (1977)].
4. V. S. Sorokin, Kristallografiya **31** (5), 844 (1986) [Sov. Phys. Crystallogr. **31** (5), 500 (1986)].
5. É. R. Rubtsov, V. V. Kuznetsov, V. I. Ratushnyĭ, and E. A. Kognovitskaya, Zh. Fiz. Khim. **77** (2), 197 (2003) [J. Phys. Chem. **77** (2), 197 (2003)].
6. A. A. Selin and V. A. Khanin, Zh. Fiz. Khim., No. 11, 2734 (1979).
7. V. S. Sorokin and É. R. Rubtsov, Neorg. Mater. **29** (1), 28 (1993).
8. É. R. Rubtsov, V. V. Kuznetsov, and O. A. Lebedev, Neorg. Mater. **34** (5), 525 (1998).
9. Yu. B. Bolkhovityanov, *Contact Phenomena at the Phase Boundary before Liquid-phase Epitaxy of A^3B^5 Compounds* (Inst. Fiz. Poluprovodn. SO Akad. Nauk SSSR, Novosibirsk, 1982) [in Russian].
10. V. V. Kuznetsov, É. R. Rubtsov, and I. I. Parfenova, Izv. Vyssh. Uchebn. Zaved., Tsvetn. Metall., No. 3, 57 (1997).
11. É. R. Rubtsov, V. S. Sorokin, and V. V. Kuznetsov, Zh. Fiz. Khim. **71** (3), 415 (1997) [J. Phys. Chem. **71** (3), 346 (1997)].

Translated by L. Man

Crystallography Reports, Vol. 50, Suppl. 1, 2005, pp. S168–S172.

CRYSTAL GROWTH

Synthesis of Polymer Magnetic Microspheres and Study of Their Magnetic Properties

É. H. Éfendiyev*, R. A. Ali-zade*, and V. P. Zubov**

** Institute of Physics, Academy of Sciences of Azerbaijan, pr. Dzhavida 33, Baku, Az-1143 Azerbaijan*

*** Shemyakin–Ovchinnikov Institute of Bioorganic Chemistry, Russian Academy of Sciences, ul. Miklukho-Maklaya 16/10, Moscow, 117997 Russia*

e-mail: efendiyeveg@azdata.net

Received February 3, 2005

Abstract—Polymer magnetic microspheres are synthesized on the basis of collagen and polysterene by introducing magnetite nanoparticles into these materials. It is determined by transmission electron microscopy that nanoparticles are separated from each other and cannot aggregate. The magnetization curve of polymer magnetic microspheres is found to be very close to the theoretical curve calculated on the basis of the Langevin equation. It is established that the magnetization occurs by the Néel mechanism. The magnetic moments of nanoparticles are oriented in an external magnetic field by their rotation inside the nanoparticles. The relaxation time of magnetite nanoparticles is estimated to be 7×10^{-12} s. © *2005 Pleiades Publishing, Inc.*

INTRODUCTION

Magnetic nanoparticles are currently being widely investigated in both liquid organic media [1, 2] and polymer matrices [3, 4]. The interest in these systems is due to their new magnetic properties and to the prospects of their application in nanoelectronics [5]. In addition, there are data in the literature on the synthesis and investigation of polymer microspheres containing one magnetic particle from 0.1 to 200 μm in size [6, 7]. Such systems are characterized by large values of the residual magnetization and the coercitive force. Therefore, their application requires preliminary demagnetization. Polymer microspheres containing magnetic nanoparticles—polymer magnetic microspheres (PMMSs)—are of great importance for practical medicine and biology. For example, they are used to transport drugs, select biological materials and cells, and perform enzymatic reactions [8–10]. PMMSs are a convenient object for the study of magnetic nanoparticles because the latter are protected from external effects in microspheres. In contrast to polymer microspheres containing one large magnetic particle, polymer microspheres filled with many small magnetic nanoparticles, up to 100 nm in size, have superparamagnetic properties (zero values of the residual magnetization and the coercitive force). This circumstance makes it possible to use them repeatedly in different manufacturing processes.

The magnetic properties of PMMSs are determined by the magnetic properties of nanoparticles and their concentration in polymer microspheres, because the polymer matrix is diamagnetic and has a high permittivity ε. For example, for polystyrene, ε = 2.5–2.6 at $f = 10^6$ Hz and $t = 20°C$. The composites obtained by introducing nanoparticles into polymer microspheres have specific electrical and magnetic properties in high-frequency electromagnetic fields. The sizes of nanoparticles and PMMSs make it possible to consider them as physically small systems with properties differing from the characteristics of massive objects [11].

We have already investigated magnetite nanoparticles. The size distribution of nanoparticles was obtained in [12]. The synthesis was performed by the method of chemical deposition of divalent and trivalent iron salts with excess alkali. It is shown that the size distribution of nanoparticles can be described with rather high accuracy using an asymmetric histogram that is flat from the side of large nanoparticles. The morphology of magnetite nanoparticles was investigated in [13]; it was shown that the surface chemical composition of nanoparticles differs from the bulk composition, and it was found that the surface magnetic properties of nanoparticles are weaker. The magnetization of chains composed of magnetite nanoparticles was investigated in [14] taking into account the magnetic dipole–dipole interaction. An expression for the magnetization of such systems was also derived in [14]. The structure and some physical properties of PMMSs were investigated in [15]; it was shown that no aggregation of nanoparticles occurs in a polymer matrix.

This study, continuing the series of our investigations into the structure and properties of magnetite nanoparticles incorporated into a polymer matrix, is devoted to the preparation of PMMSs and analysis of their magnetic properties. Specifically, we investigated the magnetization and magnetic susceptibility of PMMSs and attempted to explain the mechanism of PMMS magnetization.

1063-7745/05/5001-S0168$26.00

EXPERIMENTAL

Preparation of PMMSs for Study

PMMSs were prepared on the basis of collagen and polystyrene with the introduction of magnetite nanoparticles into them. PMMSs with three different diameters having a small spread were synthesized: 255 ± 1.5, 179.1 ± 1.5, and 46.9 ± 7.3 μm.

Magnetite nanoparticles were introduced into polymer microspheres by two methods: (i) directly during the synthesis of polymer microspheres and (ii) by treating fabricated porous polymer microspheres with salts of divalent and trivalent iron salts with the subsequent precipitation of magnetite nanoparticles. The precipitation occurs under the action of excess alkali. Magnetite nanoparticles are located in microsphere pores. The complete description of the synthesis conditions for PMMSs with different concentrations of nanoparticles and the analysis of some of their physical properties were reported in [16, 17]. As magnetic fillers for PMMSs, we used magnetite nanoparticles of four types synthesized in different carrier media and having different average diameters: 9.5 ± 0.1, 7.7 ± 0.1, 7.3 ± 0.1, and 5.5 ± 0.1 nm. The methods and conditions of preparation of magnetite nanoparticles were described in [18].

Determination of the PMMS Diameter

The PMMS diameter was measured on an MBI-15 optical microscope using different magnifications: 100, 160, and 256, depending on the carrier (liquid or gaseous) medium. We measured the diameter of 250 PMMSs and performed statistical treatment of the results obtained. The statistical analysis of the diameter values and the construction of histograms of the PMMS diameter distribution showed that the size distribution of synthesized microspheres (mean quadratic deviation $\sigma_{mean} = 22.683$) is flatter from the side of large sizes (the asymmetry coefficient $\varepsilon_{mean} = 0.383$) and is characterized by the polydispersity coefficient $K_{mean} = 1.057$. Figures 1 and 2 show the micrograph and the histogram of the size distribution of collagen PMMSs.

The PMMS diameter depends on the properties of the carrier medium (molecular mass, polarity, viscosity, and so on). In this study, we used aqueous solutions of ethanol and glycerin as carrier media during the synthesis, storage, and investigation of PMMSs. Penetration of molecules of the medium into porous PMMSs leads to an increase in the microsphere size.

Measurement of the dependence of the average diameter of PMMSs on the time of their storage in a mixture of glycerin and water in the ratio 4 : 1 showed that the PMMS diameter increases with time and tends to a constant value at large storage times ($t > 35$ h) (Fig. 3). We measured the time dependence of the average PMMS diameter in glycerin–water mixtures with different glycerin/water ratios: 4 : 0.1, 4 : 0.5, 4 : 1.5, and 4 : 2. The final values of the average PMMS diameter for these media were 305.5 ± 1.6, 307.5 ± 1.7, 308.9 ± 1.7, and 313.4 ± 1.7 μm, respectively. These values were reached during 30–48 h. Therefore, all measurements of the physical characteristics of PMMSs transferred into a viscous medium were per-

Fig. 1. Micrograph of PMMSs (polymer microspheres containing magnetic nanoparticles).

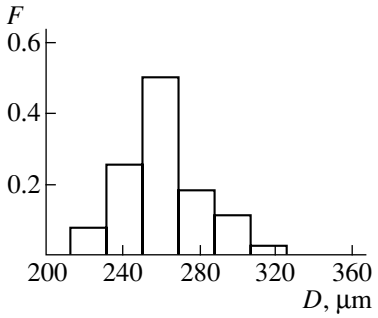

Fig. 2. Histogram of the PMMS diameter distribution.

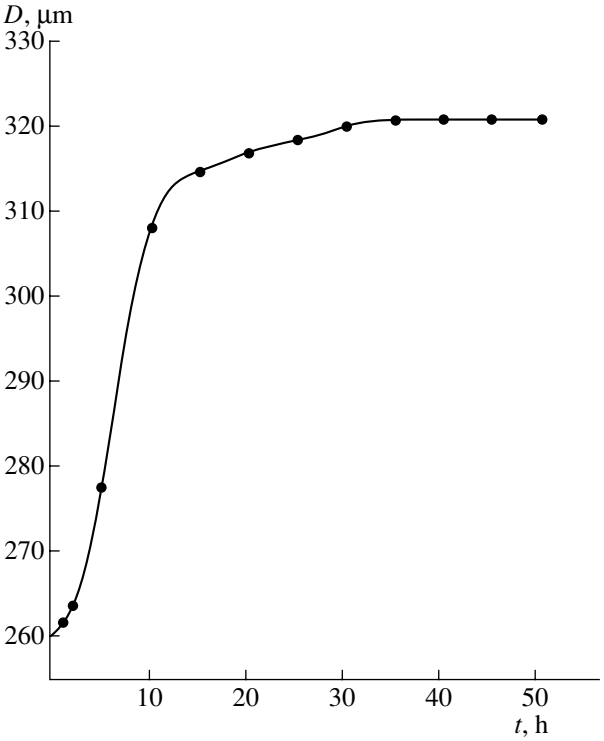

Fig. 3. Dependence of the PMMS diameter on the time of storage in the glycerin–water mixture (4 : 1).

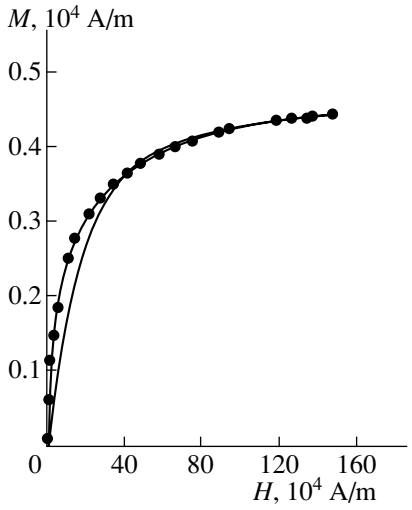

Fig. 4. Experimental (circles) and calculated (solid line) PMMS magnetization curves for the magnetite concentration $\varphi_m = 0.00984$.

formed after 48 h, i.e., after the PMMS size reached the constant value.

Measurement of the Magnetization

To investigate the magnetic properties of nanoparticles incorporated into a polymer matrix and to confirm the fact that nanoparticles do not aggregate in polymers (as was shown by the electron microscopy study of PMMS cuts [15]), we measured the magnetization of nanoparticles. The measurement was performed in a vibrating-coil magnetometer based on an FL-1 electromagnet. The magnetic field varied up to 10^5 A/m. The magnetization was determined by the method described in [19]. The measurement error was less than 3%. Figure 4 shows the PMMS-magnetization curve (circles) measured for the volume concentration of magnetite nanoparticles $\varphi_m = 0.01$ at room temperature.

Measurement of the Magnetic Susceptibility of Individual PMMSs

To measure the magnetic susceptibility of an individual PMMS, we developed a setup similar to that described in [20]. The magnetic susceptibility of individual PMMSs was found by measuring the velocity of PMMSs moving in a viscous medium in the nonuniform field of a ferromagnetic cylinder placed in a uniform magnetic field. The magnetic susceptibility χ was determined by the formulas [20]

$$\chi = \chi_0 + \frac{12\pi\eta R_0 D r^5}{t\mu_0 V M_s a^2 (M_s a^2 + 2H_0 r^2)}$$

at $H_0 > M_s/2$

and

$$\chi = \chi_0 + \frac{3\pi\eta R_0 D r^5}{t\mu_0 V \frac{\mu-1}{\mu+1} H_0^2 a^2 \left(\frac{\mu-1}{\mu+1} a^2 + r^2\right)}$$

at $H_0 < M_s/2$,

where $\chi_0 = 10^{-6}$ is the magnetic susceptibility of the viscous medium; r is the distance from the cylinder axis to the PMMS center; R_0 and V are the radius and the volume of a PMMS, respectively; $a = 1.008$ mm is the radius of the ferromagnetic cylinder; η is the viscosity of the medium; μ_0 is the magnetic constant; $M_s = 0.5 \times 10^5$ A/m is the saturation magnetization of the ferromagnetic cylinder; H_0 is the constant magnetic field; t is the time during which a PMMS passes the distance r; and $D = 86.7$ is the magnification parameter. The magnetic susceptibility of individual PMMSs was measured at room temperature in different magnetic fields: 2.4, 50.0, and 206.84 kA/m. All these values of the magnetic field are within the linear portion of the dependence of the magnetic field strength on the electric field strength in the coils of the FL-1 electromagnet. To satisfy the condition of the uniform slow motion of PMMSs in a gradient magnetic field (the Reynolds number is $\sim 10^{-3}$), we used a glycerin–water mixture with a ratio of the components of 4 : 1 as a viscous medium; the viscosity of this medium is 38.85 mPa s. The viscosity was measured at room temperature using a VPZh-3 viscometer with an inner diameter of the capillary of 0.99 mm. The viscometer constant is 0.774 mm/s.

RESULTS AND DISCUSSION

As can be seen from Fig. 4, the PMMS magnetization curve at the concentration of magnetite nanoparticles $\varphi_m = 0.0098$ is characteristic of superparamagnetic media. The saturation magnetization is $M_s = 4.034$ kA/m and the initial magnetic susceptibility is $\chi_0 = 0.026$. The average, maximum, and minimum magnetic diameters of magnetite nanoparticles, determined by the formulas from [13, 21] on the basis of the magnetization data, are 3.78, 7.80, and 1.86 nm, respectively. The magnetic diameters determined from the magnetization data and those obtained from the electron microscopy data are in agreement with each other.

The theoretical magnetization curve, plotted using the Langevin equation, is shown in Fig. 4 (the solid line). As can be seen from Fig. 4, the experimental and theoretical magnetization curves are very close to each other. This circumstance indicates that the magnetic diameters of nanoparticles are found correctly by the method proposed in [21] and confirms that magnetite nanoparticles in a polymer matrix are separated and located at a certain distance from each other; i.e., they do not aggregate in the matrix.

Periodic measurement of the concentration of magnetite nanoparticles in PMMSs and analysis of their magnetic properties every half year showed that the magnetic properties remain constant during the observation time interval. This fact indicates that the nanoparticles under study are rigidly fixed in the polymer matrix and their concentration is stable. The rigid fixation of nanoparticles in the matrix shows that their magnetization occurs by the Néel mechanism. Orientation of the magnetic moment of a nanoparticle in an external magnetic field occurs through the rotation of the magnetic moment within the nanoparticle. The relaxation time of magnetite nanoparticles was estimated to be 7.028×10^{-12} s. Since the duration of measuring the PMMS magnetization is much longer than the relaxation time of the magnetic moment, each nanoparticle exhibits superparamagnetic behavior.

We measured the magnetic susceptibility of 120 individual PMMSs with an average diameter of 269.9 μm at the magnetite concentration $\varphi_m = 0.0098$ and $H = 206.84$ kA/m. This value of the magnetic field was specially chosen for the given concentration of nanoparticles in the polymer matrix and the viscosity of the carrier medium. The average magnetic susceptibility of one PMMS is 4.79×10^{-3}. The matching between the histograms of the PMMS distributions over the diameter and the logarithmic value of the magnetic susceptibility, calculated by the χ^2-criterion method, turned out to be 95%, which may indicate a correlation between the magnetic susceptibility and the PMMS diameter. In this context, on the basis of measuring the magnetic susceptibility of individual PMMSs with different diameters, we plotted the dependence of the magnetic susceptibility of PMMSs on their diameter (Fig. 5). Previously, random values of the magnetic susceptibility for all PMMS diameters were rejected by the method of 4*D*- and *Q*-criteria [22].

To explain the dependence obtained (Fig. 5), we suggested that PMMSs consist of disks of different diameters. The thickness of the disks is equal to the distance between magnetite nanoparticles; hence, each disk consists of only one layer of nanoparticles. Thus, the total magnetic moment of PMMSs is equal to the sum of the magnetic moments of disks of different diameters. In turn, the magnetic moments of the disks are the sums of the magnetic moments of chains of magnetite nanoparticles, which are aligned along the microsphere diameter.

The magnetic moment of a nanoparticle chain depends on the magnetic moment of each individual nanoparticle and the number of nanoparticles in the chain. These parameters, in turn, depend on the force of interaction between the nanoparticles and the strength of the external magnetic field [23]. For strong magnetic fields and a small number of nanoparticles in a chain (due to either a low concentration of nanoparticles or a small PMMS diameter), the magnetic moment of a chain is determined by the total number of nanoparticles forming the chain; i.e., all nanoparticles are involved in the magnetization process. In weak magnetic fields, the magnetic dipole–dipole interaction plays the key role in the magnetization of the chains [14]. In this case, the energy of the dipole–dipole interaction exceeds the energy of interaction of magnetic dipoles with the external magnetic field. Therefore, for weak magnetic fields and a large number of magnetite nanoparticles in a chain (due to either a high concentration of nanoparticles or a large PMMS diameter), some nanoparticles in neighboring chains form closed subsystems with a zero total magnetic moment. Therefore, the number of nanoparticles contributing to the magnetization decreases, the chain length decreases as well, and all these factors reduce the magnetic moments of each individual chain and each individual cross section. As a result, the total magnetic moment of PMMSs decreases.

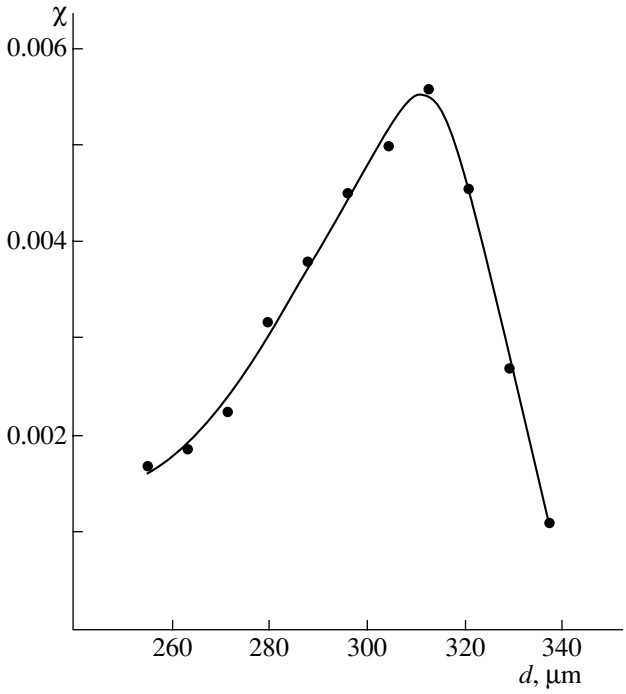

Fig. 5. Dependence of the PMMS magnetic susceptibility on the PMMS diameter.

As was suggested above, the magnetization of PMMS particles with small diameters ($d = 294.22$ μm, see Fig. 5) occurs due to the magnetization of the nanoparticle chains oriented along the external magnetic field. In this case, chains of nanoparticles exhibiting magnetic dipole–dipole interaction are magnetized by parallel magnetization reversal. With an increase in the PMMS diameter up to 294.22 μm, the number of nanoparticles in chains increases, increasing the magnetization and the magnetic susceptibility. The initial magnetic susceptibility of PMMSs calculated by us using the formula from [14] was 1.698×10^{-3}, which is in agreement with the experimental value found by mea-

suring the magnetic susceptibility of individual PMMSs with small diameters (d = 223.2 μm, χ_0 = 1.681×10^{-3}; d = 223.3 μm, $\chi_0 = 1.92 \times 10^{-3}$; the initial portion of the curve in Fig. 5).

The dependence of the magnetic susceptibility of PMMSs on the magnetite concentration was investigated in the low-concentration range (φ_m = 0.0007, 0.001, 0.003, 0.008, and 0.01) for the magnetic field H = 50 kA/m to confirm the above-described mechanism of magnetization. The investigation showed that at low magnetite concentrations the magnetic susceptibility of PMMSs increases with an increase in the concentration of nanoparticles. This dependence can be described by the linear equation $\chi = 0.69\varphi_m - 0.52 \times 10^{-3}$. This circumstance confirms our suggestion that at low magnetite concentrations all nanoparticles forming chains are involved in the magnetization process. An increase in the magnetite concentration leads to an increase in the number of nanoparticles in chains and, therefore, increases the magnetic susceptibility.

For large PMMS diameters ($d \geq 294.22$ μm) and at a constant magnetite concentration, the number of magnetite nanoparticles aligned along the microsphere diameter increases. The numbers of nanoparticles with the average diameter d = 5.48 nm in PMMSs with diameters of 304.36, 314.51, and 324.13 μm, found from the data on the magnetite concentration (φ_m = 0.013) in PMMSs, are 17913, 18510, and 19076, respectively. The numbers of magnetite nanoparticles aligned in chains in the external magnetic field H = 206.84 kA/m, calculated by the formula from [23], are 16310, 14310, and 13096, respectively. As can be seen, the number of nanoparticles in chains decreases at large PMMS diameters, which leads to a decrease in the magnetic moment of the chains and, correspondingly, in the magnetic susceptibility of PMMSs.

Thus, the investigation performed here showed that magnetite nanoparticles are uniformly distributed in PMMSs. The size of nanoparticles does not change during the PMMS synthesis. The magnetic diameters of nanoparticles determined from the PMMS-magnetization curve of and calculated from the corresponding geometric diameters are in agreement with each other. PMMSs have superparamagnetic properties. The magnetic characteristics of PMMSs are determined by the characteristics of magnetic nanoparticles and their concentration. Magnetization of PMMSs occurs through the orientation of the total magnetic moment, which is the sum of the magnetic moments of disks composed of PMMSs. The magnetic moments of the disks are, in turn, sums of the magnetic moments of chains of magnetite nanoparticles aligned along the PMMS diameter. In the case of small PMMS diameters and strong magnetic fields, all nanoparticles forming magnetic chains are involved in the magnetization, whereas for large PMMS diameters and weak magnetic fields, closed dipole subsystems are formed, which leads to a decrease in the PMMS magnetization.

REFERENCES

1. M. Zahn, J. Nanopart. Res. **3** (1), 73 (2001).
2. A. N. Vinogradov, Zh. Fiz. Khim. **74** (7), 1324 (2000) [J. Phys. Chem. **74** (7), 1188 (2000)].
3. G. Yu. Yurkov, S. P. Gubin, D. A. Pankratov, *et al.*, Neorg. Mater. **38** (2), 186 (2002).
4. H. Srikanth, R. Hajndl, C. Chrinos, *et al.*, Appl. Phys. Lett. **79** (21), 3503 (2001).
5. R. W. Siegel, *Executive Summary and Introduction and Overview, Nanostructure Science and Technology: World Technology Evaluation Center (WTEC) Panel Report on R and D Status and Trends in Nanoparticles, Nanostructured Materials, and Nanodevices*, Ed. by R. W. Siegel, R. W. E. Hu, and M. C. Roco (Kluwer, Dordrecht, 1999).
6. U. Schroder and G. Lindia, US Patent No. 4,687,748 (1987).
7. C. Berl, W. Tak, and K. H. Bartholomew, EP Patent No. 0,180,384 (1986).
8. J. T. Kemshead and J. Ugelstad, Mol. Cell. Biochem. **67** (1), 11 (1985).
9. F. P. Wayne, K. Jeongsoon, and S. J. Brunce, Biochem. Biophys. Acta **816** (1), 83 (1985).
10. H. Ovadia, A. M. Carbone, and P. Y. Paterson, J. Immunol. Methods **53** (1), 109 (1982).
11. L. D. Landau and E. M. Lifshitz, *Course of Theoretical Physics* (Nauka, Moscow, 1982; Pergamon Press, New York, 1988).
12. R. A. Ali-zade, Phys. B (Proc. Suppl.) **63** (1), 406 (1998).
13. R. A. Ali-zade, Izv. Akad. Nauk Azerbaijan **20** (2), 88 (2000).
14. R. A. Ali-zade, Fiz. Azerbaijan, No. 1, 37 (1999).
15. É. H. Éfendiyev and R. A. Ali-zade, in *Proceedings of IV National Conference on Application of X-rays, Synchroton Radiation, Neutrons, and Electrons to Material Characterization (RSNÉ-2003), Moscow, Russia, 2003* (Moscow, 2003), p. 215.
16. S. I. Turkin, Yu. V. Lukin, E. A. Markvicheva, *et al.*, SU Patent No. 1 486 515, Byull. Izobret., No. 22, 100 (1989).
17. S. I. Turkin, Yu. V. Lukin, E. A. Markvicheva, *et al.*, SU Patent No. 1 567 623, Byull. Izobret., No. 20, 105 (1990).
18. A. N. Buryakov, I. A. Gritskova, V. P. Zubov, *et al.*, SU Patent No. 1 628 478, Byull. Izobret., No. 6, 194 (1991).
19. V. I. Chechernikov, *Magnetic Measurements* (Mosk. Gos. Univ., Moscow, 1969) [in Russian].
20. Yu. A. Plyavin'sh and É. Ya. Blum, Magn. Gidrodin., No. 4, 3 (1983).
21. E. E. Bibik, B. Ya. Matygullin, Yu. L. Raĭkher, and M. I. Shliomis, Magn. Gidrodin., No. 1, 68 (1973).
22. W. Feller, *An Introduction to Probability Theory and Its Applications* (Wiley, New York, 1971; Mir, Moscow, 1984).
23. M. I. Shliomis, Usp. Fiz. Nauk **112** (3), 427 (1974).

Translated by Yu. Sin'kov

Crystallography Reports, Vol. 50, Suppl. 1, 2005, pp. S22–S27.

REAL STRUCTURE OF CRYSTALS

Block (Mosaic) Structure as an Indicator for Cooling of Crystals Grown from a Melt

B. G. Ivanov* and E. S. Kaeva**

** Federal State Unitary Enterprise "Vavilov State Optical Institute, All-Russia Research Center," Birzhevaya liniya 12, St. Petersburg, 199034 Russia*

e-mail: bimgvfa@hotmail.ru

*** State University of Fine Mechanics and Optics, St. Petersburg, 197101 Russia*

e-mail: optics@mail.ru

Received February 3, 2005

Abstract—The specific features of the formation of the block (mosaic) structure with low-angle misorientation of the block boundaries are investigated using fluorite and germanium crystals as an example. These structural features are considered an indicator of conditions under which plastic deformation and polygonization occur during cooling of the crystals grown from melts. © *2005 Pleiades Publishing, Inc.*

INTRODUCTION

In this paper, we consider a block structure (so-called mosaic structure) that frequently occurs in crystals grown from high-temperature melts [1–4] and is formed at the stage of cooling (annealing) of crystals according to the classical mechanism of plastic deformation and subsequent polygonization. As a rule, the mosaic structure involves a large number of relatively small blocks with low misorientation angles between neighboring blocks. This defect leads to a substantial decrease in the quality of crystalline materials and considerably restricts and even often completely excludes the application of these materials in cases where their homogeneity must necessarily be high (high-resolution power optics, glass–metal seals, X-ray diffraction analysis, photolithography, etc.).

Until recently, the problem associated with control of this defect was considered primarily for anisotropic materials, such as corundum, sellaite, yttrium lithium fluoride, etc. However, at present, there has arisen a need suppressing (up to complete elimination) a mosaic structure (and factors responsible for its formation) in high-symmetry cubic crystals, such as calcium, barium, and lithium fluorides; garnets; germanium; etc. In particular, the use of large-aperture excimer lasers for photolithography in the UV spectral range imposes heavy demands on a correcting material in these optical systems, namely, high-quality single-crystal fluorite (CaF_2). For these purposes, it is necessary to grow large single crystals (up to 300 mm or more in diameter) with a controlled orientation and an anomalous birefringence of the order of $(1–2) \times 10^{-7}$ [1]. The main contribution to the anomalous birefringence of crystals is made by residual stresses that are primarily associated with the low-angle boundaries of the mosaic structure [2–6].

The specific features of the mosaic structure, i.e., a combination of sizes of individual blocks and low-angle misorientation between neighboring blocks in the crystal bulk, are related to plastic deformation and polygonization processes in crystals. It should be remembered that these processes begin immediately after the growth stage in crystal regions before completing the growth of the entire crystal. The plastic deformation and polygonization processes proceed under stresses caused by the temperature gradient in the growth and cooling zones. In a number of cases, the stresses induced by possible mechanical loads, structural defects, growth defects, and other factors can substantially affect the plastic deformation; however, the temperature gradient makes the main contribution.

The plastic deformation is most pronounced at premelting temperatures in the vicinity of the crystallization front and at sufficiently low yield stresses. Therefore, the onset of plastic deformation that is responsible for the future mosaic structure is essentially irreducible in character. For simplicity, this deformation, according to a stronger or weaker bending of the crystal structure (the future block structure with low-angle boundaries), can be represented as a combination of alternating regions of elementary bendings [5, 7] ("corrugated" structure) with a "width defect" of the corresponding crystal volume [5]. It should be emphasized that this structure is formed under compressive "reduced" stresses, which act along possible slip planes and perpendicular to planes of future block boundaries.

In the mosaic structure, a relatively random orientation of individual blocks that predominantly have small sizes as compared to the crystal sizes is characterized by a regular distribution of block misorientations in the crystal bulk. Investigations into specific features of this structure as an indicator of plastic deformation pro-

1063-7745/05/5001-S0022$26.00

cesses at the initial stage of cooling the crystal can provide important information on the temperature–time conditions of these processes [3].

EXPERIMENTAL TECHNIQUE

In order to investigate a block structure, i.e., to reveal quantitative regularities of misorientation of mosaic blocks, we developed a method for determining the block orientation in crystals with the use of measurements of reflection of optical radiation from the surface [8]. This method is based on the determination of the spatial distribution of light rays reflected from crystallographic planes (faceted regions, cleavages, etc.) that are formed (or artificially produced) on the crystal surface.

In essence, the reflection method is as follows (Fig. 1). A parallel light beam *2* is directed normally to the surface of crystal *1* under investigation. Beam *4* reflected from tilted planes (*hkl*) *3* (cleavage fragments, etc.) arrives at screen *5*, which is also located normally to incident light beam *2*. The reflections observed in screen *5* form a light pattern that corresponds to symmetry of the direction in the crystal with the angles φ (the azimuthal angle of the reflected beam) and 2ρ (the angle of deviation of the reflected beam from the normal). The method has a high sensitivity, allows one to determine the misorientation angle between microblocks in polar coordinates with an accuracy of 10′–15′, and is efficient at low misorientation angles, as is the case with mosaic structures.

The experimental setup (Fig. 2) designed on the basis of this method makes it possible to determine the orientation of mosaic blocks by scanning the crystal surface with a laser beam and recording the reflections in the screen [9].

The angle ρ of inclination of the (*hkl*) reflection plane (for example, the plane of a microcleavage formed after rough grinding) to the crystal surface (see Fig. 1) is calculated from the formula

$$\rho = \frac{1}{2}\arctan(a/b). \quad (1)$$

The distance *b* from the crystal surface to the screen is fixed after mounting and adjusting crystals for measurements. The cleavage depth *h* does not affect hardly at all the error in measurements, because it is considerably smaller than the distance *b*. At the known distance *b*, it is possible to calculate the orientation angles ρ from formula (1) and to graticulate the screen according to the angles ρ (rather than 2ρ). In the screen (Fig. 2d), the calculated orientation angles ρ are plotted along the *X* and *Y* axes (concentric circles). The azimuthal angles φ of the deviation of reflected beams are determined at $\rho \neq 0$ (at $\rho = 0$, φ is indeterminate) from the straight lines passed through the center of the *XY* coordinate system. The angle φ_0 for each crystal sample is arbitrarily chosen depending on the geometry of the sample or its other characteristic features. The other azimuthal angles φ for the crystal under investigation are exactly related to the angle φ_0. When scanning the crystal along circles by rotating a table with the crystal (Fig. 2c), the azimuthal angle φ is added to the rotation angle of the table β ($0° \le \beta \le 360°$) on the screen. The angle $\varphi' = \varphi + \beta$ is recorded in the screen. In order to obtain the sought azimuthal angle φ, all the angles φ' should be recalculated to the initial table position, i.e., at $\beta = 0°$ ($\varphi = \varphi' - \beta$).

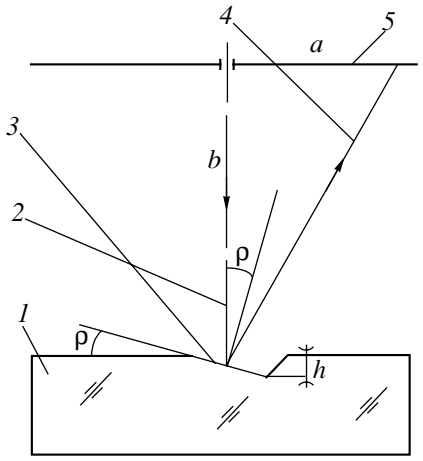

Fig. 1. Illustration of calculating the angle ρ of inclination of the (*hkl*) plane to the crystal surface from the angle of reflection of the light beam: (*1*) crystal, (*2*) incident light beam, (*3*) (*hkl*) crystallographic plane, (*4*) reflected light beam, and (*5*) screen.

The aforementioned technique was used to study mosaic structures of fluorite (CaF_2) and germanium crystals grown by vertical directional crystallization from melts (Bridgman–Stockbarger method) [1, 10–12].[1] The crystals were grown in the form of disks 100–300 mm in diameter and 20–70 mm thick in graphite crucibles. The crucibles with melts were sunk at a rate of 2–10 mm/h from the heating zone through the gradient zone (growth zone) formed by a diaphragm. In this case, the material passed through the stages of nucleation, growth, and cooling of the crystal.

RESULTS AND DISCUSSION

The misorientation of mosaic blocks was measured by scanning roughly ground surfaces of the upper and lower faces of the fluorite crystals and the upper surface of the germanium crystals and recording reflections from {111} cleavages on the screen. Moreover, we also visually observed the development of the mosaic structure on these surfaces and the lateral surfaces of the disks. The results obtained can be summarized as follows.

[1] The germanium crystals were supplied by V.A. Pis'mennyĭ and V.N. Vetrov.

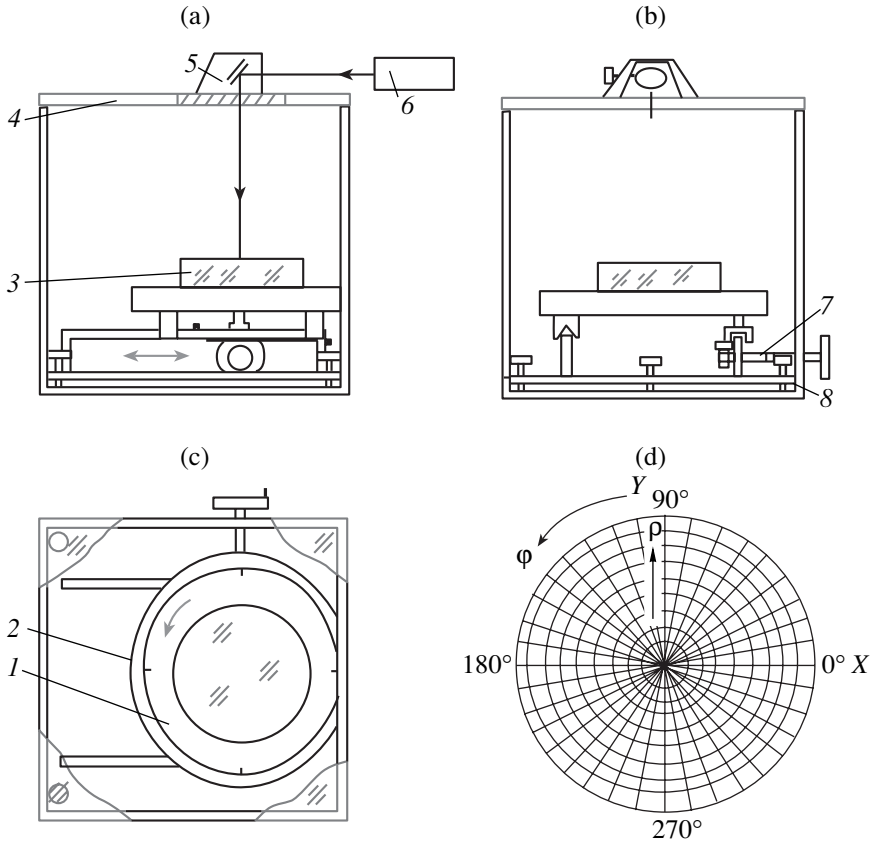

Fig. 2. Schematic diagram of the setup for measuring the misorientation of mosaic blocks [9] in (a–c) three projections: (*1*) movable part of the table, (*2*) immovable part of the table, (*3*) crystal, (*4*) screen, (*5*) unit with a mirror, (*6*) laser, (*7*) gear, and (*8*) adjusting screws. (d) Graticule of the screen.

(1) All the fluorite and germanium crystals under investigation have, to some extent, a mosaic structure over the entire volume. The low-angle boundaries on the upper (Fig. 3a) and lower (Fig. 3b) surfaces of the fluorite crystals, as well as on the upper surface of the germanium crystal (Fig. 4), are rather curved and exhibit a tendency toward radial arrangement with respect to the center of the surfaces. Similar boundaries on the lateral surfaces tend to be located along the generatrix of the cylinder. This indicates that, for the most part, dislocation walls are vertically arranged in the crystal bulk. Therefore, the mosaic structures of both crystals are similar to each other. In turn, this suggests similar specific features of the temperature field at the initial stages of cooling the crystals in the Bridgman–Stockbarger method.

(2) In the fluorite crystals, the mosaic structure of the upper surface closely resembles the mosaic structure of the lower surface. The general regularities of the structure and misorientation of mosaic blocks on these surfaces are similar to each other. There are regions that have virtually identical mosaic structures. This indicates that, under thermal and mechanical stresses, the crystal structure in the bulk is characterized by the same bending. The dependences of the misorientation angle between mosaic blocks in the fluorite crystal 300 mm in diameter and 50 mm thick are depicted in Fig. 5. The measurements were performed along the circles with different radii on the upper and lower surfaces of the disk with the same initial angle φ for all the circles. It can be seen from Fig. 5 that the dependences of the misorientation angle between mosaic blocks for both surfaces exhibit a similar general behavior.

(3) The misorientation angle between mosaic blocks on the upper and lower surfaces and, correspondingly, in the bulk of the crystals (Figs. 5, 6) regularly increases away from the center from less than 1° for central crystal regions to several degrees at the periphery. An increase in the misorientation angle is attended by the formation of a more developed mosaic structure that involves a larger number of mosaic blocks with more pronounced boundaries in between. This regularity suggests that there arise compressive stresses in peripheral regions of the samples at temperatures corresponding to active plastic deformation. Most likely, this is associated with the fact that, at the initial stages of cooling, the cooling rate of containers is higher than the cooling rate of crystals and, hence, containers have a compressive action on the crystals. The graphite container with the grown crystal passes through the dia-

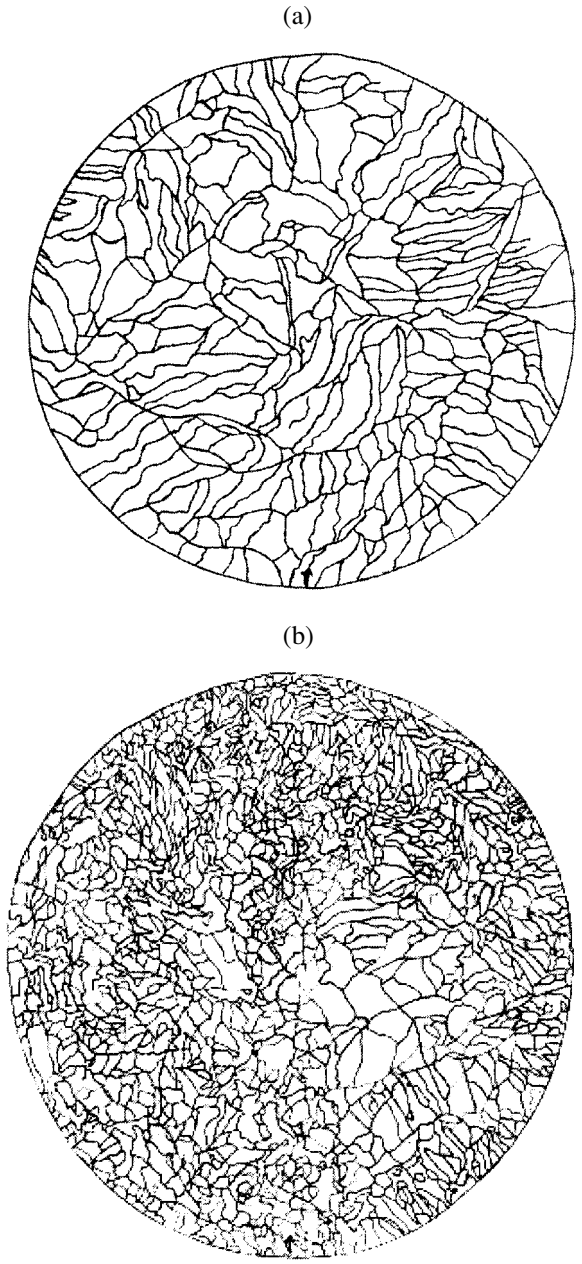

Fig. 3. Low-angle grain boundaries on the (a) upper and (b) lower surfaces of the fluorite crystal (diameter, 300 mm).

phragm and appears to be in a relatively cold zone. Owing to intense radiation and a high thermal conductivity of graphite, the cooling rate of the side walls of the container is considerably higher than that of the grown crystal in the container. At the melting temperatures of fluorite crystals and, especially, germanium, graphite, whose melting (sublimation) temperature exceeds 3900 K, is a very rigid material that virtually does not undergo plastic deformation. However, we can state with assurance that the fluorite and germanium crystals at premelting temperatures undergo plastic

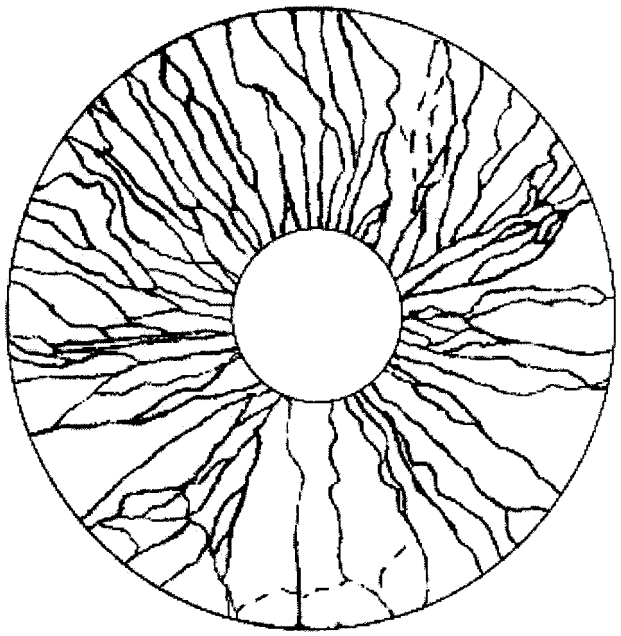

Fig. 4. Low-angle grain boundaries on the upper surface of the germanium crystal (diameter, 130 mm).

deformation even at very low stresses (due to the low yield stress). As a consequence, although the thermal expansion coefficient of graphite is larger, on average, than those of the grown crystals, the total shrinkage of the crucible turns out to be considerably larger. The crucible with a sufficiently strong structure (wall thickness) has a compressive action on the peripheral crystal regions (as a hoop on a barrel) and produces tangential stresses that relax via plastic deformation of the corrugation type [5]. The subsequent polygonization after relaxation of compressive stresses and completion of plastic deformation leads to the formation of low-angle boundaries that are predominantly perpendicular to the disk surfaces.

(4) Although the mosaic structures of the upper and lower surfaces of the fluorite crystals closely resemble each other in the block misorientation [see (1)–(3)], the specific features of these structures differ substantially and indicate different degrees of their polygonization. On the upper surface, mosaic blocks are characterized by larger sizes and misorientation angles and more pronounced boundaries (Fig. 3a). On the lower surface, which was in contact with the crucible during growth and cooling of the crystal, there are a large number of mosaic blocks whose sizes are rather small and equal to ~1–2 mm and less, i.e., at the limit of possible observation (the diameter of the laser beam spot is approximately equal to 3 mm). In some regions, the misorientation angles between blocks are within the sensitivity of the method (10'–15'). As a result, boundaries between blocks are meandering and cannot be clearly revealed in a visual way (Fig. 3b).

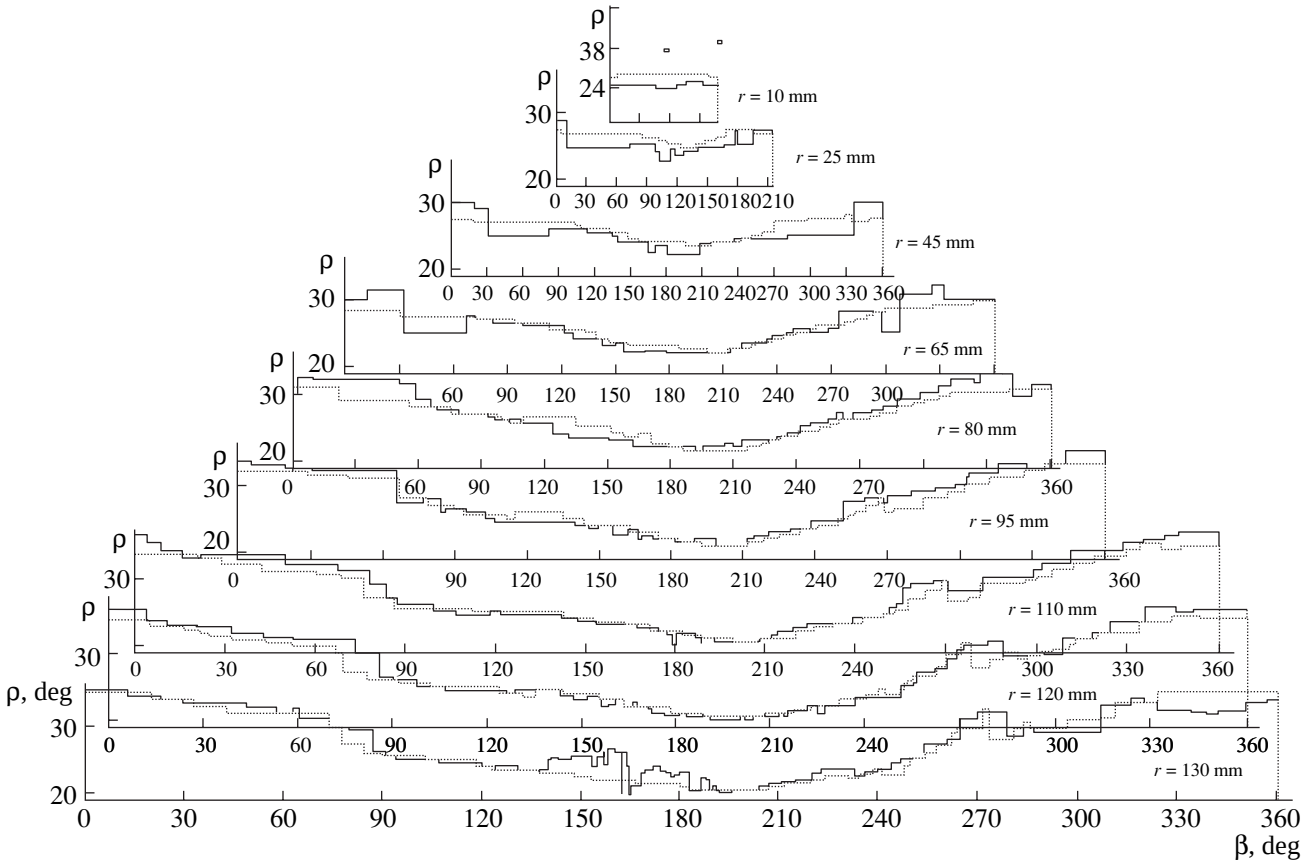

Fig. 5. Dependences ρ(β) obtained by laser beam scanning of the upper (solid lines) and lower (dotted lines) surfaces of the CaF_2 crystal along the circles of different radii.

It seems likely that specific temperature–time conditions differed in the upper and lower crystal regions. The upper crystal region and the upper surface, which in the course of cooling was in incomplete contact with the graphite crucible located above, were at high temperatures for a longer time as compared to the lower crystal region. The polygonization process on the lower surfaces of the disks was terminated at the initial stages and did not lead to such an increase in the sizes of mosaic blocks as in the case of the upper surface.

Thus, the performed quantitative investigations into the low-angle misorientation of neighboring blocks permitted us to reveal specific features of the mosaic structure, such as sizes, shape, and spatial distribution of misorientation angles between neighboring blocks over the crystal volume. These are important characteristics of the mosaic structure and are directly related to the parameters of growth and cooling of the crystals. Undeniably, there exists a quantitative relation between the temperature gradient in the crystal cooling zone, plastic deformation (as a response of the crystal to stresses induced by temperature gradients), and polygonization, which results in the stress relaxation in the deformed crystal and generates secondary stresses determining the anomalous birefringence. Therefore, the obtained specific features are qualitative characteristics of the plastic deformation processes and can be quantitative when revealing the correlation between temperature fields in the plastic deformation zone and the mechanical properties of crystals and make it possible to interpret thoroughly the processes responsible for the formation of the mosaic structure [5].

In order to grow perfect crystals without indications of plastic deformation and mosaic structure, it is necessary to eliminate their origin, namely, thermal and mechanical stresses. It follows from these rather stringent requirements that, at all (especially, initial) stages of active plastic deformation during cooling of crystals, it is necessary to provide small temperature gradients and other technological parameters that do not result in stresses exceeding the yield stress at any point of the crystal [5]. The last condition is associated with the fact that the excess of the yield stress even at one local point leads to the development of plastic deformation at considerably lower stresses induced by the temperature field gradient. This deformation can covers large crystal regions with the corresponding negative consequences [3, 5].

The study of the mosaic structure as an indicator of temperature fields in the zones of growth and cooling

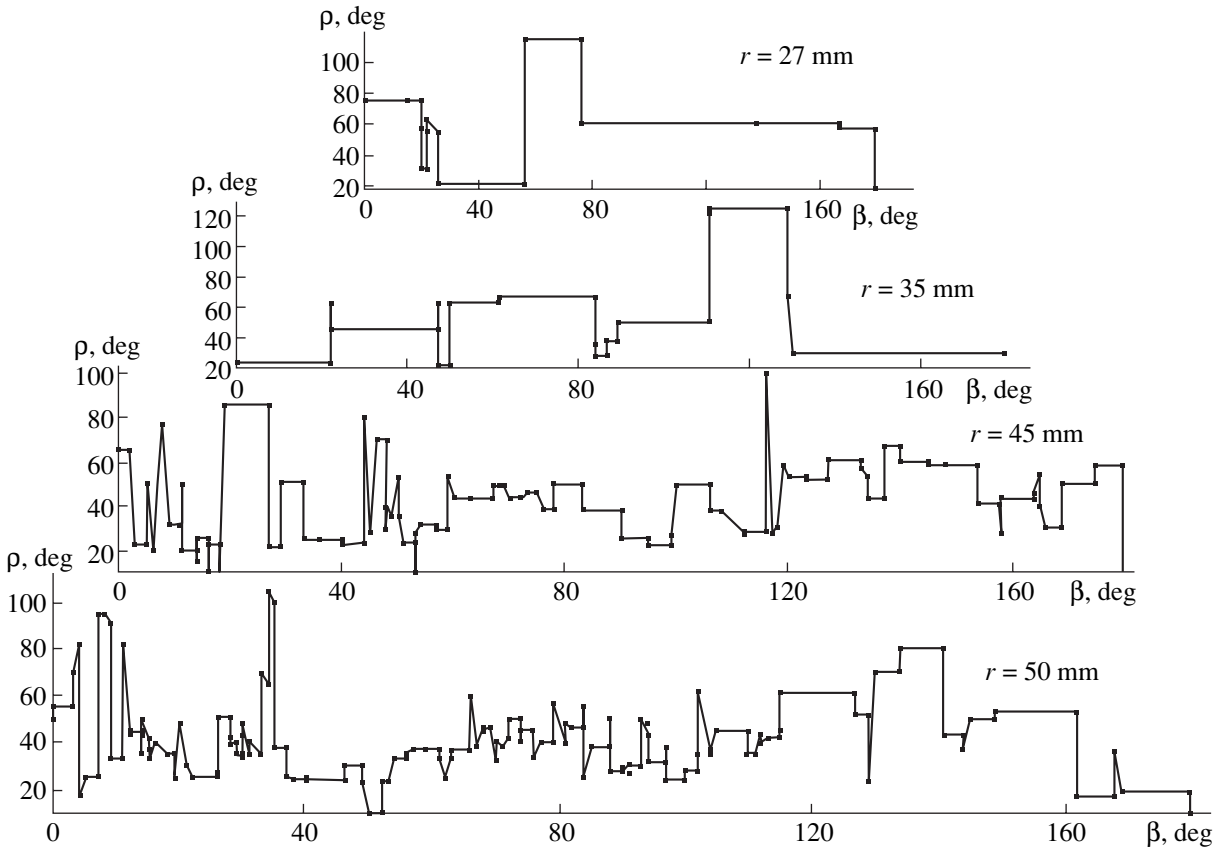

Fig. 6. Dependences ρ(β) obtained by laser beam scanning of the upper surface of the germanium crystal (diameter, 130 mm) along the circles of different radii.

(annealing) of crystals and other technological conditions can provide information important for revealing the factors responsible for the formation of this defect and ways for its elimination. This holds much significance for the use of crystals in science and engineering.

ACKNOWLEDGMENTS

This work was supported by the Council on Grants from the President of the Russian Federation for Support of Leading Scientific Schools (project no. RI-112/001/192).

REFERENCES

1. G. T. Petrovskiĭ, V. M. Reĭterov, I. A. Mironov, *et al.*, in *Proceedings of the 6th International Conference on Applied Optics, St. Petersburg, Russia, 2004* (St. Petersburg, 2004), Vol. 2, p. 39.
2. S. V. Tsivinskiĭ and L. A. Maslova, Izv. Akad. Nauk SSSR, Ser. Fiz. **36** (3), 575 (1972).
3. B. G. Ivanov and M. I. Musatov, Opt.–Mekh. Prom-st., No. 2, 35 (1979).
4. A. N. Belaya, in *Proceedings of the 6th International Conference on Crystal Growth, Moscow, USSR* (Moscow, 1980), Vol. 3, p. 222.
5. B. G. Ivanov, Poverkhnost, No. 6, 52 (2002).
6. A. K. Przhevuskiĭ and E. S. Kaeva, Opt. Zh. **70** (11), 68 (2003).
7. A. A. Urusovskaya, *Some Problems of the Physics and Elasticity of Crystals* (Akad. Nauk SSSR, Moscow, 1960), p. 75 [in Russian].
8. S. Rösch, Sachs., Akad. Wiss. **39** (6), 5 (1926).
9. B. G. Ivanov, E. S. Kaeva, and D. I. Klimenchenko, Izv. Vyssh. Uchebn. Zaved., Mater. Elektron. Tekh., No. 1 (2005) (in press).
10. V. A. Sokolov, Tr. Gos. Opt. Inst. **54** (188), 21 (1983).
11. B. G. Ivanov, V. M. Reĭterov, and A. Turkboev, Opt. Zh. **66** (5), 89 (1999).
12. L. M. Avkhutsky, S. N. Borozdin, and E. G. Chernevskaya, in *Proceedings of the 4th International Conference on Single-Crystal Growth and Heat and Mass Transfer, Obninsk, Russia, 2001* (Obninsk, 2001), p. 334.

Translated by O. Borovik-Romanova

Crystallography Reports, Vol. 50, Suppl. 1, 2005, pp. S28–S31.

PHYSICAL PROPERTIES OF CRYSTALS

Effect of External Forces on the Dielectric and Pyroelectric Properties of Strontium–Barium Niobate Crystals

O. V. Malyshkina, B. B. Ped'ko, A. A. Movchikova, and I. V. Morgushka

Tver State University, Sadovyĭ per. 35, Tver, 170002 Russia

e-mail: Olga.malyyshkina@tversu.ru

Received February 3, 2005

Abstract—It is shown that high-temperature annealing of strontium–barium niobate crystals increases the mobility of domain boundaries in these crystals. This effect manifests itself in a shift of the peak of the effective permittivity of annealed samples to weaker fields. It is ascertained that the polarization of strontium–barium niobate crystals caused by annealing results in their more homogeneous single-domain state. The effect of Ce and Cr impurities on the polarization state of the surface layers in strontium–barium niobate crystals is considered. © *2005 Pleiades Publishing, Inc.*

INTRODUCTION

Strontium–barium niobate (SBN) crystals with the general formula $Sr_xB_{1-x}Nb_2O_6$ have the structure of tetragonal potassium–tungsten bronzes and belong to ferroelectric relaxors with a diffuse phase transition [1]. Currently, SBN crystals are widely used in optoelectronics [1] because they are characterized by a large value of electro-optic coefficient (420×10^{-12} m/V). At the same time, it is known that the degree of formation of the single-domain state in a crystal affects significantly its physical properties [1–4]. Such factors as an external electric field and high-temperature annealing may strongly change the polarization state of SBN crystals. In this context, the dielectric and pyroelectric properties of SBN crystals subjected to the action of these factors are of interest.

Data on the distribution of the polarization and the space charge in the surface regions of ferroelectric crystals can be obtained by analyzing the frequency dependences of the pyroelectric current [5]. When a rectangular modulation of a heat flow is used, the nonuniform polarization distribution affects the shape of the pyroelectric response [6]. In this context, we investigated the state of the surface layers of polar cuts of SBN crystals ($x = 0.61$) by analyzing their pyroelectric response using the dynamic method.

EXPERIMENTAL

When a modulated heat flow is incident on a crystal, the latter is heated only at a certain depth x, which is dependent on the modulation frequency f: $x = (\alpha/\pi f)^{1/2}$, where α is the thermal diffusivity. The pyroelectric current (in the case of a nonuniform polarization distribution in a sample), measured by the dynamic method, is also a function of the modulation frequency of the heat flow. Thus, the pyroelectric current can be interpreted in this case as produced by a layer of depth x. Hence, the pyroelectric coefficient, calculated on the basis of this pyroelectric current, is the effective pyroelectric coefficient of the layer.

The frequency dependences of the pyroelectric current were measured for all samples at room temperature in the frequency range 2–400 Hz, which, for SBN crystals, corresponds to the range of penetration depths of thermal waves from 12 to 180 μm. To investigate the polarization in deeper layers, it is necessary to use low modulation frequencies for the heat flow. Since conventional measurements (using a mean-value voltmeter) are impossible in this case, we used digital methods of signal processing.

In this work, we investigated both pure SBN single crystals and SBN single crystals with Cr (1000 and 2000 ppm) and Ce (1000, 4000, and 8000 ppm) impurities. The impurity concentration corresponded to the composition of the melt used to grow crystals (1 ppm = 10^{-4} at %).

The pyroelectric coefficient was measured on the sample sides onto which both negative and positive ends of the polarization vector emerged ($-P_s$ and $+P_s$, respectively).

We also investigated the effect of annealing (in air) on the polarization state in the SBN crystals. Annealing in air was performed at 200°C for 4 h. Primarily polarized and annealed samples were studied, as well as samples subjected to the action of an ac electric field of ~300 V/mm. The crystals were polarized in an electric field of 500 V/mm in the paraelectric phase (~120°C) with subsequent field cooling down to room temperature.

1063-7745/05/5001-S0028$26.00

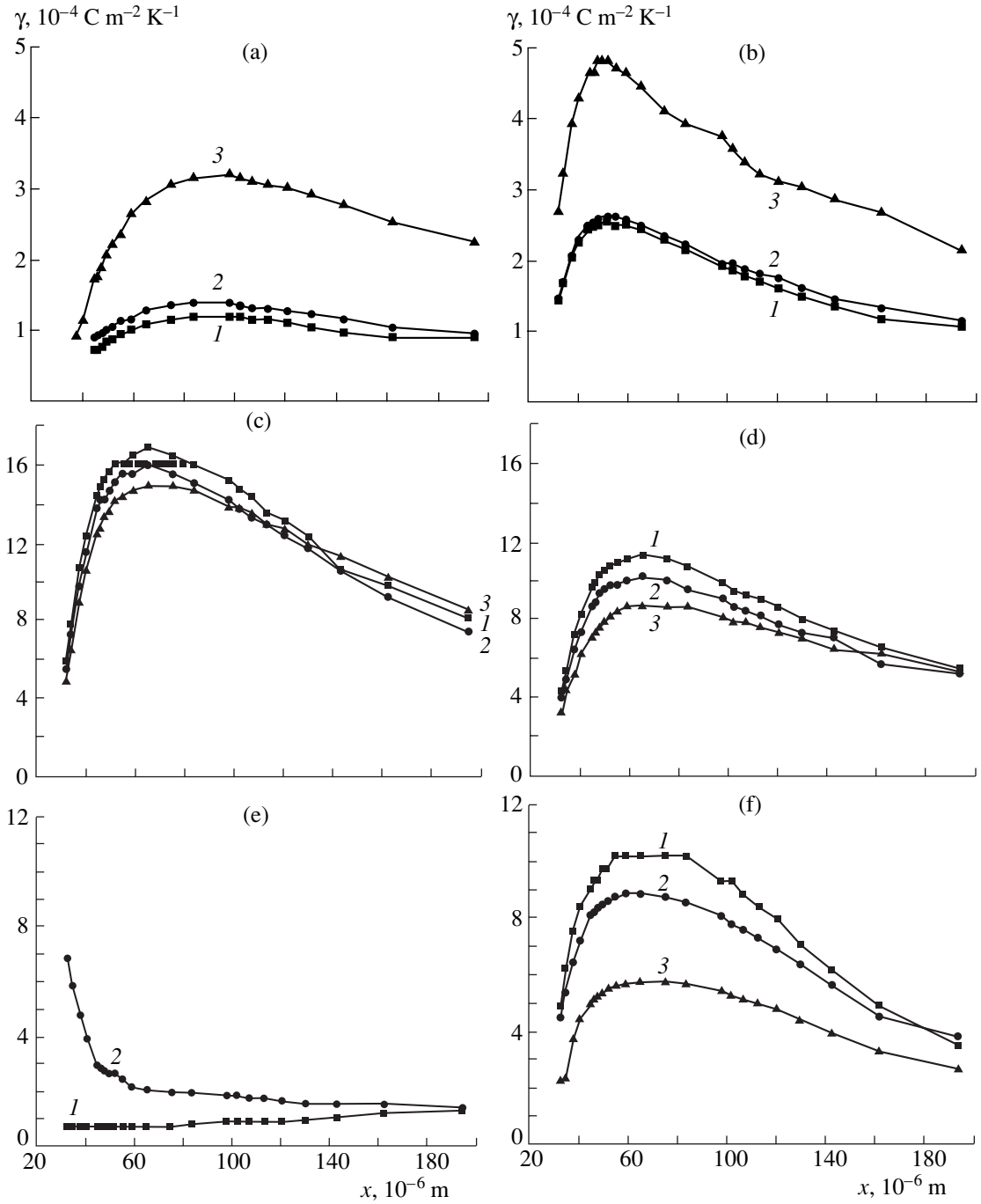

Fig. 1. Distributions of the effective values of the pyroelectric coefficient γ over thickness *x* of SBN crystals doped with Ce to a concentration of 8000 ppm (a, b) and Cr to a concentration of 2000 ppm (c, d) and pure SBN crystals (e, f) on the sides corresponding to the positive (a, c, e) and negative (b, d, f) ends of the polarization vector: (*1*) polarized samples; (*2*) after 100 h after polarization; and (*3*) after the action of an ac electric field.

RESULTS AND DISCUSSION

In all polarized SBN samples with either Ce (Figs. 1a, 1b; curves *1*) or Cr impurity (Figs. 1c, 1d; curves *1*), a nonuniform distribution of the pyroelectric coefficient over the sample thickness was observed. The values of the pyroelectric coefficient in the layer located at a depth from 30 to 80–120 μm (depending on the type and concentration of the impurity) were found to be larger than those in the other volume. At the same time, in a pure SBN crystal (Figs. 1d, 1e; curves *1*), such behavior of the pyroelectric coefficient was observed only on the side corresponding to the $+P_s$

polarization. On the other side, the pyroelectric response near the surface was slightly lower than in the bulk.

This behavior of the pyroelectric coefficient indicates that the polarization in the layer is stronger than near the surface and in the bulk of the crystal. This character of the pyroelectric coefficient distribution gives grounds to suggest that the polarization of an SBN crystal in an external field is incomplete. The region in the bulk of the crystal, located far from the surface, remains partially depolarized. We should not exclude from consideration the fact that the volume charge localized near the surface may affect the polarization in the layer. The data on the crystal etching, performed by us previously [4], show that the surface layer is almost single-domain, whereas deeper etching reveals multidomain regions. Thus, polarization leads to the formation of a single-domain layer in the sample at a depth of about 10 μm. At larger depths, the state becomes less single-domain (i.e., in the terminology of [3], the domain density increases). The decrease in the polarization of the surface layer (thinner than 5 μm) is related to the screening of the spontaneous polarization by the surface charge.

It should be noted that, for the Ce-doped SBN crystals, immediately after the polarization (Figs. 1a, 1b; curves *1*), the pyroelectric response on the side corresponding to $-P_s$ (Fig. 1b) is much higher than that on the side corresponding to $+P_s$ (Fig. 1a). It should also be noted that the pyroelectric response decreases with an increase in the Ce concentration.

For SBN samples with low Cr concentrations (not higher than 1000 ppm), the pyroelectric response is the same at both sides. At the same time, for an SBN crystal with a Cr concentration of 2000 ppm, the pyroelectric coefficient for the side corresponding to $+P_s$ (Fig. 1c) is larger than that for the side corresponding to $-P_s$ by a factor of almost 1.5 (Fig. 1d).

Exposure of crystals for 100 h at room temperature without applying external forces leads to a change in the pyroelectric-coefficient distribution in the samples under study. In a pure SBN sample, on the side corresponding to $+P_s$, a sharp increase in the pyroelectric response is observed near the surface. At the side corresponding to $-P_s$, the pyroelectric coefficient decreases (Figs. 1e, 1f; curves *2*). In the doped SBN crystals, the variation in the pyroelectric coefficient is insignificant (Figs. 1a–1d; curves *2*).

The effect of an ac electric field on SBN:Cr and SBN:Ce crystals does not lead to their depolarization (Figs. 1a–1d; curves *3*). In contrast, in a pure SBN crystal placed in an ac field, the pyroelectric response is observed only on the side corresponding to $-P_s$, and its value is much smaller than that for the polarized sample (Figs. 1e, 1f). Moreover, in SBN crystals with a high Ce concentration (8000 ppm), the pyroelectric response increases after the action of an ac electric field.

Investigation of the annealed SBN samples showed that annealing leads to an almost complete depolarization of the doped crystals. Only a weak pyroelectric response is observed when one of the sample sides is subjected to heating at frequencies exceeding 40 Hz. These conditions correspond to a penetration depth of ~40 μm of thermal waves in the sample. According to the pyroelectric-current direction, the polarization in this layer is directed from the bulk to the sample surface. At the same time, the pyroelectric response of a pure annealed SBN crystal coincides in magnitude with that of a depolarized crystal; however, the polarization for both sample sides is directed from the bulk to the surface.

Investigations of the effective permittivity also indicate that annealing affects the state of the domain structure. According to [7], the effective capacitance should strongly increase in fields corresponding to the maximum reconstruction of the domain structure. Experiments showed a shift of the peak of the effective permittivity of the annealed samples to weaker fields. This behavior of the permittivity may indicate an increase in the mobility of domain boundaries.

Polarization reversal of the annealed samples by the above-described technique shows that samples are polarized more uniformly in this case. This is confirmed by the rectangular shape of the pyroelectric response observed at frequencies down to 0.1 Hz (at this frequency, the penetration depth of thermal waves in the crystal is 0.78 mm; the samples under study range in thickness from 1 to 2 mm).

CONCLUSIONS

The investigation performed shows that the doping of SBN crystals with Cr and Ce impurities differently affects the polarization state of the surface layers of these crystals. The fact that an ac electric field and annealing differently affect pure SBN crystals and SBN:Cr and SBN:Ce crystals can be related to the presence of impurities and to differences in the positions of Cr and Ce ions in the SBN crystal structure, i.e., to the change in the conditions of nucleation and motion of domain walls. This suggestion is confirmed by the neutron-activation data [8, 9], according to which Ce^{3+} and Cr^{3+} ions substitute, respectively, Sr/Ba and Nb sites in the SBN lattice.

The difference in the sample polarization before and after annealing may be related to the fact that annealing leads to the redistribution of Sr and Ba ions in the structure of these crystals.

ACKNOWLEDGMENTS

We are grateful to professors S. Kapphan and R. Pankrath (Osnabrük University, Germany) for supplying the crystals for investigation.

REFERENCES

1. Yu. S. Kuz'minov, *Electro-optical and Nonlinear-optical Niobate Lithium Crystal* (Nauka, Moscow, 1987) [in Russian].
2. V. M. Fridkin, *Photoferroelectrics* (Nauka, Moscow, 1976; Springer-Verlag, Berlin, 1979).
3. D. V. Isakov, T. R. Volk, L. I. Ivleva, *et al.*, JETP Lett. **80** (4), 258 (2004).
4. O. V. Malyshkina, I. L. Kislova, B. B. Ped'ko, *et al.*, in *Proceedigns of the Research and Application Conference "Piezoelectric Technique 2003," Moscow, 2003* (Mosk. Inst. Radiotekh. Élektr. Avtom., Moscow, 2003), p. 57.
5. O. V. Malyshkina, A. A. Bogomolov, and M. M. Major, Ferroelectrics **182**, 11 (1996).
6. Yu. N. Zakharov, S. G. Gakh, V. Z. Borodin, *et al.*, in *Semiconductor Ferroelectrics* (Izd. RGU, Rostov-on-Don, 1973), p. 133 [in Russian].
7. A. S. Sonin and B. A. Strukov, *Introduction to Ferroelectricity* (Vysshaya Shkola, Moscow, 1970) [in Russian].
8. Th. Woike, G. Weckwerth, Y. Palme, *et al.*, Solid State Commun. **102** (10), 743 (1997).
9. Th. Woike, U. Dofler, L. Tsankov, *et al.*, Appl. Phys. B: Lasers Opt. **72** (6), 661 (2001).

Translated by Yu. Sin'kov

Crystallography Reports, Vol. 50, Suppl. 1, 2005, pp. S32–S36.

PHYSICAL PROPERTIES OF CRYSTALS

Synthesis and Properties of a High-Frequency Dielectric in the $BaO–Pr_2O_3–TiO_2$ and $BaO–Pr_2O_3–TiO_2–Ta_2O_5$ Systems

N. A. Shishonok, V. V. Petrashko, L. E. Soshnikov, A. A. Leusenko, and Yu. V. Radyush

Institute of Solid State Physics and Semiconductors, National Academy of Sciences of Belarus, ul. Brovki 17, Minsk, 220072 Belarus

e-mail: soshnikov@ifttp.bas-net.by

Received February 8, 2005

Abstract—The $(Ba_{1-a}Pb_a)_4(Pr_{1-y-z}Bi_ySm_z)_{9+1/3}Ti_{18}O_{54}$ compound in the ternary $BaO–Pr_2O_3–TiO_2$ system and the $Ba_2Pr_4Ti_6Ta_4O_{30}$, $Ba_3Pr_3Ti_5Ta_5O_{30}$, $Ba_4Pr_2Ti_4Ta_6O_{30}$, and $Ba_5Pr_1Ti_3Ta_7O_{30}$ compounds in the quaternary $BaO–Pr_2O_3–TiO_2–Ta_2O_5$ system are obtained by solid-phase synthesis under high (up to 7 GPa) pressure. The influence of the synthesis conditions and the partial substitution of Pb ions for Ba and Bi (or Bi/Sm) ions for Pr on the composition of the phases synthesized and their structure and dielectric properties is studied. The dielectric properties of the compounds synthesized are studied at the frequencies 10^2, 10^3, 10^4, and 10^6 Hz in the temperature range from 20 to 100°C. The synthesis modes and the Pb, Bi, Sm, and Bi/Sm concentrations necessary for the synthesis of materials with improved dielectric properties and an almost zero temperature coefficient of the resonance frequency are determined. In the ternary system of solid solutions of, the compounds with permittivity $\varepsilon \cong 100–110$ and dielectric-loss angle $\tan\delta \simeq 0.0015–0.003$ are synthesized. In the quaternary system, the compounds with $\varepsilon \simeq 100–150$ and $\tan\delta \simeq 0.0015–0.003$ are obtained. © *2005 Pleiades Publishing, Inc.*

INTRODUCTION

The intense development of telecommunication and other communication facilities in the microwave range (satellite and mobile communication) has stimulated the elaboration of new technologies for the synthesis of dielectric materials with high permittivity ε and small dielectric-loss angles $\tan\delta$, as well as the study of their properties. These materials should possess high ε_r values in order to reduce the resonator dimensions, as well as low dielectric losses and an almost zero temperature coefficient of the resonant frequency τ_f in order to maintain a stable resonance frequency [1]. The search for such materials requires the study of a large number of dielectric systems. However, only a few of these systems are of practical interest. Among them, the $BaO–R_2O_3–TiO_3$ (R = La–Gd) systems are of special interest. Rare earth ions (from La to Gd) in these systems form a series of solid solutions that is described by the general formula $Ba_{6-3x}R_{8+2x}Ti_{18}O_{54}$ and that possesses high ε_r values and low $\tan\delta$ values, with the parameter τ_f varying over a large interval: from positive values for La–Nd to negative values for Sm, Eu, and Gd [1]. The functional properties of these materials are strongly dependent on a number of parameters, such as the purity of the starting materials, the content of rare earth element, the Ba/Ti ratio in the starting materials, the synthesis conditions, crystal lattice and phase ratio of the final product, its density, etc. With R varying from La to Gd, the region of solid solutions becomes narrower, whereas the ε_r and τ_f values decrease. The microwave dielectric properties of these materials are considerably improved by combining various rare earth oxides and using the partial substitution of other alkali earth elements (Ca, Sr) for barium. The materials with such compositions usually satisfy high requirements with respect to $\tan\delta$ and ε_r but the parameter τ_f considerably varies and should be additionally controlled by the introduction of special additives, usually, Bi_2O_3 and PbO oxides or titanates.

At present, promising studies are being performed in two directions: first, the search for new dielectric materials with better dielectric characteristics and, second, the improvement of dielectric properties of already known compounds. Of all the $Ba_{6-3x}R_{8+2x}Ti_{18}O_{54}$ compounds, the materials with R = Nd are widely used in electronics. At the same time, attempts are made to improve their dielectric properties. Studies show [2–6] that the dielectric characteristics (and, especially, the parameter τ_f) may be considerably improved by the introduction of Bi and Pb additions in combination with other rare earth elements (Sm, Gd). However, the properties are in fact improved only if the concentration of these additives does not exceed the solubility limit; otherwise, new additional phases are formed, which considerably deteriorate the dielectric properties of the materials synthesized (increase in $\tan\delta$ and τ_f and a slight decrease in ε_r). In the process of material synthesis, Bi and Pb are partly evaporated, and therefore, to avoid the formation of impurity phases at this stage, one has to maintain the stoichiometry and high density of the final product. Also, the known data on the structure, composition, and properties of these materials are often

1063-7745/05/5001-S0032$26.00

inconsistent. The optimum synthesis modes and composition of the materials with highly reproducible high microwave dielectric properties have not been established as yet. Therefore, it is necessary to perform additional systematic studies in order to elaborate new technologies for the synthesis of materials with high ε_r and Q values and an almost zero coefficient of resonance frequency τ_f.

In the $BaO–Pr_2O_3–TiO_2$ system [7, 8], there exists the region of the solid solutions described by the general formula $Ba_{6-3x}R_{8+2x}Ti_{18}O_{54}$ ($0 < x < 0.75$). The dielectric materials formed in this region have high permittivity and low dielectric losses and are very attractive for application in microwave electronics. With an increase in the concentration x of a rare earth element, the permittivity and the resonance-frequency coefficient decrease so that τ_f attains its minimum value ~125 ppg/K at $x = 0.75$, although the quality factor Q attains its maximum value at $x = 0.74$. The resonance-frequency coefficient of the materials is rather high and should be reduced by modifying the chemical composition.

Ternary compounds of the $Ba_{6-3x}R_{8+2x}Ti_{18}O_{54}$ type with the structure of tungsten bronze have rather high dielectric characteristics (permittivity $\varepsilon \cong 60–80$) and dielectric losses ($\tan\delta \cong 0.001$) and, therefore, are used in dielectric resonators in various communication facilities. The quaternary compounds in the $BaO–R_2O_3–TiO_2–Ta_2O_5$ systems (R = Nd, Sm) have better dielectric characteristics, $\varepsilon \cong 70–174$ and $\tan\delta \cong 0.0001$, and, therefore, are widely used in the systems of mobile communication facilities. The dielectric properties and temperature stability of these materials are strongly dependent on the synthesis conditions and partial substitution of structure-forming elements.

SAMPLES AND EXPERIMENTAL METHODS

The ceramic $(Ba_{1-a}Pb_a)_4(Pr_{1-y-z}Bi_ySm_z)_{9+1/3}Ti_{18}O_{54}$ (with $a = 0–0.4$, $y = 0–0.24$, $z = 0–0.06$) compounds formed in the $BaO–Pr_2O_3–TiO_2$ system and the ceramic $Ba_2Pr_4Ti_6Ta_4O_{30}$, $Ba_3Pr_3Ti_5Ta_5O_{30}$, $Ba_4Pr_2Ti_4Ta_6O_{30}$, and $Ba_5Pr_1Ti_3Ta_7O_{30}$ compounds in the $BaO–Pr_2O_3–TiO_2–Ta_2O_5$ system were obtained by solid-phase synthesis under high pressures (up to 7 GPa). The samples were prepared from the $BaCO_3$, Pr_2O_3, Bi_2O_3, TiO_2, Sm_2O_3, and PbO powders by the methods of solid reactions in air. The powder mixtures were subjected to (2–6)-h-annealing at 1000–1170°C. The annealed powders of the corresponding compositions were ground and pressed into tablets, which then were synthesized in different modes. Some samples were synthesized directly in the temperature range 1230–1350°C. The synthesis time ranged from 1 to 4 h. Some other materials were synthesized under the simultaneous action of high temperatures and pressures and then were annealed at 1160–1250°C.

The phase compositions of the dielectrics obtained were studied on a DRON-3 diffractometer (Cu_{K_α}-radiation). The samples for dielectric measurements were polished disks 8–10 mm in diameter and 0.3–1.0 mm in thickness. After the study of their microstructure, silver electrodes were applied to their surfaces. The dielectric properties were measured in the mode of slow (0.5–1.0 K/min) heating by E7-12 and E7-14 LCR meters at the frequencies 10^2, 10^3, 10^4, and 10^6 Hz in the temperature range from 20 to 100°C.

The temperature coefficient of the resonance frequency τ_f was calculated as $\tau_1 = -\tau_\varepsilon/2 - \alpha$, where τ_ε is the temperature coefficient of permittivity measured at the frequency 1 MHz and α is the thermal expansion coefficient ($\approx 10^{-5}$ K^{-1}).

RESULTS AND DISCUSSION

Dielectric Properties of Bi-Doped $Ba_4Pr_{9+1/3}Ti_{18}O_{54}$ Solid Solutions

X-ray phase analysis of $Ba_4(Pr_{1-y}Bi_y)_{9+1/3}Ti_{18}O_{54}$ samples (with $y = 0$, 0.03, 0.06, 0.18, and 0.24) synthesized for 2 h at the temperature 1350°C showed that all the samples consisted of only one phase with the structure of tungsten bronze (Fig. 1). The dielectric properties of the materials depend on the bismuth content in $Ba_4(Pr_{1-y}Bi_y)_{9+1/3}Ti_{18}O_{54}$ (Table 1). The study of the

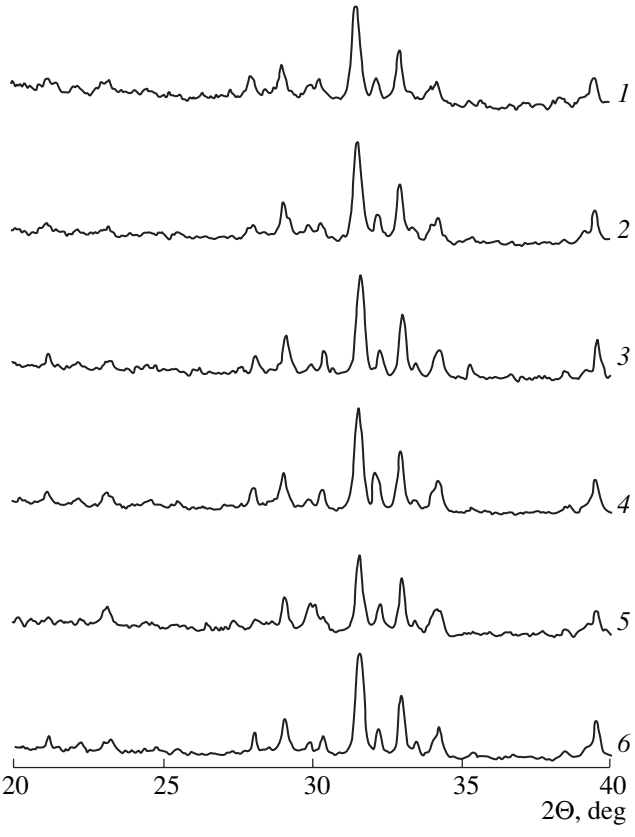

Fig. 1. X-ray phase analysis of $Ba_4(Pr_{1-y}Bi_y)_{9+1/3}Ti_{18}O_{54}$ samples synthesized at 1350°C for 2 h at different y values: (*1*) 0, (*2*) 0.03, (*3*) 0.06, (*4*) 0.15, (*5*) 0.18, (*6*) 0.24.

Table 1. Lattice parameters, dielectric properties, and temperature coefficients of the resonance frequency τ_f and permittivity τ_ε of $Ba_4(Pr_{1-y}Bi_y)_{9+1/3}Ti_{18}O_{54}$ samples synthesized for 2 h at 1350°C at different Bi concentration (y). Dielectric properties were measured at frequency 1 MHz

y	a, nm	b, nm	c, nm	ε	$\tan\delta$	τ_f, ppm/K	τ_ε
0	122.6	223.33	38.41	95.4	0.0029	12.4	–44.8
0.03	122.68	223.44	38.36	99.0	0.0028	1.0	–22.0
0.06	122.79	223.63	38.36	96.8	0.0023	29.9	–79.8
0.15	122.08	221.94	38.63	110.8	0.0020	0.28	–20.0
0.18	122.07	221.7	38.67	106.1	0.0021	6.8	–33.0
0.24	122.26	221.92	38.56	106.6	0.0015	–37.6	55.2

dielectric properties in the temperature range 20–100°C showed only a weak dependence of the dielectric characteristics on temperature.

With an increase in the bismuth concentration in the samples, the permittivity increases and attains its maximum value ($\varepsilon = 110.8$) at $y = 0.15$. At this y value, the coefficient of resonance frequency has the minimum value ($\tau_f \sim 0.28$ ppm/K). With a further increase in the bismuth content, the permittivity ε decreases and τ_f deteriorates, which may be explained by the formation of small amounts of impurity phases not detectable from the X-ray patterns (Fig. 1). A similar situation was observed on $Ba_4(Pr_{1-y}Bi_y)_{9+1/3}Ti_{18}O_{54}$ samples [3]. At $y = 0.06$, the sample surface had some microcracks, which could cause the deterioration of the dielectric properties.

Partial substitution of Bi for Pr in the $Ba_4(Pr_{1-y}Bi_y)_{9+1/3}Ti_{18}O_{54}$ samples leads to dielectric materials with better dielectric properties and to a weak temperature dependence of the permittivity. The best dielectric properties at the frequency 1 MHz belong to the samples of the composition $Ba_4(Pr_{0.85}Bi_{0.15})_{9+1/3}Ti_{18}O_{54}$ ($\varepsilon = 108$, $\tan\delta = 0.002$, and $\tau_f = 0.28$ ppm/K).

DIELECTRIC PROPERTIES OF $Ba_4(Pr_{1-y}Bi_y)_{9+1/3}Ti_{18}O_{54}$ SAMPLES SYNTHESIZED UNDER HIGH PRESSURE

The mixtures of the starting oxide and carbonate powders corresponding to the compositions $Ba_4(Pr_{1-y}Bi_y)_{9+1/3}Ti_{18}O_{54}$ ($y = 0$, 0.03, 0.06, 0.15, 0.18, and 0.24) were annealed for 3 h at 1180°C. After grinding, the mixtures were pressed into tablets and subjected to the simultaneous action of high hydrostatic pressure (up to 7 GPa) and high temperature (910–940°C) and subsequent 4-h-annealing at 1200°C. The properties of the samples thus obtained are indicated in Table 2.

Synthesis under high hydrostatic pressures but at lower temperatures gave dielectric materials with high ε and low dielectric losses. However, the dielectric properties depended on the duration and temperature of annealing of the samples synthesized. Immediately after synthesis, the materials showed semiconductor-type conductivity. They were transformed into dielectrics only after additional annealing until sample saturation with oxygen.

Effect of the Temperature of High-Pressure Synthesis (5 GPa) of $Ba_4(Pr_{0.85}Bi_{0.15})_{9+1/3}Ti_{18}O_{54}$ Samples on Their Dielectric Properties

The values of permittivity and dielectric losses of ceramic $Ba_4(Pr_{0.85}Bi_{0.15})_{9+1/3}Ti_{18}O_{54}$ samples at different temperatures of their synthesis under a quasihydrostatic pressure (5 GPa) and subsequent annealing at the temperatures 1170–1206°C and the corresponding measurement frequencies are indicated in Table 3. Permittivity of materials ε only weakly depends on temperature.

Ten-minute synthesis of $Ba_4(Pr_{0.85}Bi_{0.15})_{9+1/3}Ti_{18}O_{54}$ samples under high pressure (5 GPa) in the temperature range 380–1400°C for 10 min yields dielectric materials with high permittivity and low dielectric losses. The dielectric properties (ε and $\tan\delta$) only weakly depend on the frequency and temperature in the temperature range from 20 to 100°C. Synthesis at higher temperatures (1500°C) leads to sample fracture, whereas synthesis at lower temperature, to degradation of their dielectric properties.

Table 2. Dielectric properties of $Ba_4(Pr_{1-y}Bi_y)_{9+1/3}Ti_{18}O_{54}$ samples synthesized under high pressure (frequency 1 MHz)

y	ρ, 10^3 kg/m^3	ε	$\tan\delta$
0	4.23	94.7	0.006
0.03	4.66	88.5	0.003
0.06	4.89	88.1	0.002
0.15	4.84	93.9	0.003
0.18	4.83	90.5	0.003
0.24	4.89	101.3	0.003

Table 3. Dielectric properties of ceramic $Ba_4(Pr_{0.85}Bi_{0.15})_{9+1/3}Ti_{18}O_{54}$ samples synthesized for 10 min under the quasihydrostatic pressure 5 GPa

Synthesis temperature, °C	f = 100 Hz		f = 1 kHz		f = 10 kHz		f = 1 MHz	
	ε	tanδ	ε	tanδ	ε	tanδ	ε	tanδ
300	86.0	0.0020	85.9	0.0014	85.9	0.0014	86.4	0.0022
380	92.3	0.0021	92.1	0.0019	92.1	0.0015	92.6	0.0023
730	92.7	0.0015	92.4	0.0013	92.4	0.0012	92.7	0.0020
1200	90.7	0.0024	90.4	0.0025	90.3	0.0021	90.6	0.0024
1400	92.6	0.0020	92.3	0.0015	92.2	0.0015	93.0	0.0032

Table 4. Dielectric properties of $Ba_4(Pr_{0.85-z}Sm_zBi_{0.15})_{9+1/3}Ti_{18}O_{54}$ samples at different Sm concentrations (z) measured at the frequency f = 1 MHz

z	ε	tanδ	Synthesis temperature, °C	Pressure, GPa	Synthesis duration, min
0	92.7	0.002	630	5	10
0.05	97.8	0.003	630	5	10
0.10	84.9	0.009	630	5	10
0.12	74.9	0.008	630	5	10
0.15	85.2	0.003	630	5	10
0.20	66.3	0.004	630	5	10
0.40	92.2	0.004	630	5	10
0.60	82.9	0.012	630	5	10

Dielectric Properties of $Ba_4(Pr_{0.85-z}Sm_zBi_{0.15})_{9+1/3}Ti_{18}O_{54}$ Samples Synthesized under High Pressure

Table 4 indicates dielectric properties of ceramic $Ba_4(Pr_{0.85-z}Sm_zBi_{0.15})_{9+1/3}Ti_{18}O_{54}$ samples synthesized for 10 min under a quasihydrostatic pressure of 5 GPa at 630°C with subsequent 2-h-annealing in the temperature range 1218–1236°C. The best dielectric properties belong to samarium-doped samples (z = 0.05). Higher samarium content in the samples results in degradation of their dielectric properties.

The samples of the composition $Ba_4(Pr_{0.7}Sm_{0.15}Bi_{0.15})_{9+1/3}Ti_{18}O_{54}$ synthesized for 3 min under a quasihydrostatic pressure of 7 GPa at two temperatures, 1220 and 1560°C, with subsequent 4-h-annealing at 1169–1204°C had the following dielectric properties: ε = 74.4, tanδ = 0.002 and ε = 73.8, tanδ = 0.006, respectively. In other words, faster synthesis performed at higher pressures and temperatures does not improve the dielectric properties of the materials.

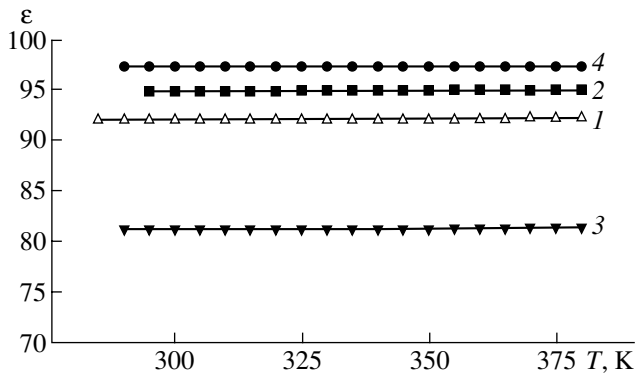

Fig. 2. Temperature dependences of permittivity of $(Ba_{1-a}Pb_a)_4(Pr_{0.8}Bi_{0.15}Sm_{0.05})_{9+1/3}Ti_{18}O_{54}$ samples at different a: (*1*) 0.4, (*2*) 0.3, (*3*) 0.1, (*4*) 0.2.

Our studies showed that the use of a high quasihydrostatic pressure at relatively low synthesis temperatures allows one to obtain samples of the $Ba_4(Pr_{0.85-z}Sm_zBi_{0.15})_{9+1/3}Ti_{18}O_{54}$ composition with a higher permittivity and lower dielectric losses.

Influence of Lead on Dielectric Properties of $(Ba_{1-a}Pb_a)_4(Pr_{0.8}Bi_{0.15}Sm_{0.05})_{9+1/3}Ti_{18}O_{54}$ Ceramics

The dielectric properties of the ceramic samples of the composition $(Ba_{1-a}Pb_a)_4(Pr_{0.8}Bi_{0.15}Sm_{0.05})_{9+1/3}Ti_{18}O_{54}$ synthesized for four hours at 1234–1245°C are indicated in Table 5. The typical temperature dependence of sample permittivity, ε(T), is shown in Fig. 2. With an increase in the lead content in the samples, their permittivity increases, attains the maximum value at A = 0.2, and then decreases. The dependence of dielectric losses on the lead content in the samples is of a more complicated character. Partial substitution of lead for barium results in a synthesis of dielectric ceramic materials with high and stable permittivity (with values in respect to temperature) and low dielectric losses.

Table 5. Dielectric properties of $Ba_4(Ba_{1-a}Pb_a)_4(Pr_{0.8}Bi_{0.15}Sm_{0.05})_{9+1/3}Ti_{18}O_{54}$ ceramics synthesized for 4 h at 1234–1245°C at different Pb concentrations (a) measured at the frequency f = 1 MHz

a	ε	tanδ
0	86.6	0.004
0.1	94.3	0.006
0.2	101.4	0.004
0.3	93.5	0.003
0.4	84.2	0.003

Dielectric Properties of Materials Synthesized in the $BaO–Pr_2O_3–Ti_2O_3–Ta_2O_5$ and $Ag(Nb,Ta)O_3$ Systems

In the process of searching for new dielectric materials with permittivity exceeding 100 and low values of dielectric losses, we studied a number of compounds in the $BaO–Pr_2O_3–Ti_2O_3–Ta_2O_5$ (I) and $Ag(Nb,Ta)O_3$ (II) systems. We obtained new dielectric materials with high dielectric properties at the frequency 1 MHz: ε = 109–154 and tanδ = 0.0015–0.009 in system I and ε = 239 and tanδ = 0.009 in system (II). The temperature dependences of permittivity for the samples with the compositions $Ba_2Pr_4Ti_6Ta_4O_{30}$, $Ba_3Pr_3Ti_5Ta_5O_{30}$, $Ba_4Pr_2Ti_4Ta_6O_{30}$, and $Ba_5Pr_1Ti_3Ta_7O_{30}$ synthesized in the quaternary $BaO–Pr_2O_3–TiO_2–Ta_2O_5$ are shown in Fig. 3. The use of a certain dopant allows one to considerably decrease the synthesis temperature without degradation of the dielectric properties of the samples, which is very important for the mass production of dielectrics.

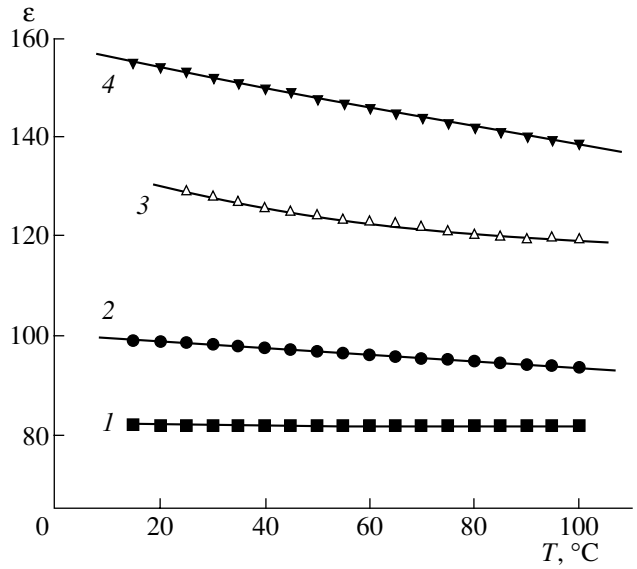

Fig. 3. Temperature dependences of the frequency of (*1*) $Ba_2Pr_4Ti_6Ta_4O_{30}$, (*2*) $Ba_3Pr_3Ti_5Ta_5O_{30}$, (*3*) $Ba_4Pr_2Ti_4Ta_6O_{30}$, and (*4*) $Ba_5Pr_1Ti_3Ta_7O_{30}$ samples synthesized in the quaternary $BaO–Pr_2O_3–TiO_2–Ta_2O_3$ system.

CONCLUSIONS

High-frequency ceramic materials in the $BaO–Pr_2O_3–TiO_2$ system are studied. New materials of the composition $(Ba_{1-a}Pb_a)_4(Pr_{1-y-z}Bi_ySm_z)_{9+1/3}Ti_{18}O_{54}$ are synthesized and their dielectric properties are studied at the frequencies f = 100 Hz–1 MHz. The influence of the partial substitution of Pb ions for Ba ions and of Bi and Bi/Sm ions for Pr ions and the synthesis conditions (including synthesis under a high (up to 7 GPa) quasi-hydrostatic pressure) on the structure, phase composition, and dielectric properties of the samples is studied at frequencies up to 1 MHz. The temperature dependences of permittivity and dielectric losses are studied in the temperature range from 20 to 100°C. The Pb, Bi, Sm, and Bi/Sm concentrations that ensure the synthesis of materials with better dielectric properties relative to those of the matrix composition are determined, as well as the modes of synthesis of ceramic samples with high permittivity, low dielectric losses, and almost zero temperature coefficient of the resonance frequency. The experimental samples are obtained with the following characteristics: ε = 100–110, tanδ = 0.0015–0.003, τ_f = 0.3–7.0 ppm/K at f = 1 MHz. A number of samples with different compositions are studied in the $BaO–Pr_2O_3–Ta_2O_3–Ta_2O_5$ (I) and $Ag(Nb,Ta)O_3$ (II) systems. Ceramic samples with high dielectric properties are synthesized in system I (ε = 154, tanδ = 0.0015) and in system II (ε = 239, tanδ = 0.009). The studies performed show that it is possible to synthesize new materials with high dielectric parameters, elaborate a new technology on their basis, and obtain new dielectrics with high permittivity, low dielectric losses, and an almost zero temperature coefficient of the resonance frequency.

REFERENCES

1. D. Suvorov, M. Valant, and D. Kolar, J. Mater. Sci. **32**, 6483 (1997).
2. M. Valant, D. Suvorov, and D. Kolar, J. Mater. Res. **11** (4), 928 (1996).
3. T. Okawa, M. Imaeda, and H. Ohsata, Jpn. J. Appl. Phys. **39**, 5645 (2000).
4. M. Podlipnik, D. Suvorov, M. Valant, and D. Kolar, J. Mater. Res. **15** (8), 1735 (2000).
5. Yong Jun Wu and Xiang Ming Chen, J. Am. Ceram. Soc. **83**, 1837 (2000).
6. M. Valant, D. Suvorov, and D. Kolar, Jpn. J. Appl. Phys. **35**, 144 (1996).
7. M. V. Varfolomeev and A. S. Mironov, Zh. Neorg. Khim. **33**, 1070 (1988).
8. K. Fukuda, R. Kitch, and I. Awai, J. Mater. Res. **10**, 312 (1995).
9. L. S. Kim, Ch. Cheon, *et al.*, J. Mater. Sci. **35**, 1487 (2000).

Translated by L. Man

Crystallography Reports, Vol. 50, Suppl. 1, 2005, pp. S37–S45.

PHYSICAL PROPERTIES OF CRYSTALS

Elastic and Dielectric Properties of $A^{II}B^{V}_2$ (A = Cd or Zn, B = P or As) Single Crystals

L. E. Soshnikov*, V. M. Trukhan*, T. V. Golyakevich*, and H. L. Soshnikova**

** Institute of Solid-State and Semiconductor Physics, National Academy of Sciences of Belarus, ul. Brovki 17, Minsk, 220072 Belarus*

*** Belarussian State University, ul. Leningradskaya 14, Minsk, 220080 Belarus*

e-mail: Soshnikov@ifttp.bas-net.bu

Received February 7, 2005

Abstract—Elastic and dielectric properties of CdP_2, ZnP_2, and $ZnAs_2$ single crystals are investigated at frequencies of 10^2, 10^3, 10^4, 10^6, and 10^7 Hz in the [00*l*], [*h*00], and [*hk*0] directions in the temperature range 78–400 K. The elastic constants, the Gruneisen parameters, and the force constants of the crystals are calculated from the measured ultrasonic velocities. The elastic constants C_{ij} decrease with an increase in temperature and anomalously change in narrow (ΔT = 10–20 K) temperature ranges. The permittivity sharply increases from $\varepsilon \approx 7$–14 at 78–150 K to $\varepsilon \approx 10^2$–10^3 in the temperature range 175–225 K without any signs of a structural phase transition. The behavior of the temperature–frequency dependences of the complex permittivity $\varepsilon^*(f, T)$ is typical of relaxation processes. The dielectric relaxation in $A^{II}B^{V}_2$ is considered on the basis of the model of isolated defects. The conductivity σ of the single crystals under study is a sum of the frequency-dependent (hopping) conductivity σ_h and the conductivity σ_s that is typical of semiconductors. The hopping conductivity increases with an increase in frequency according to the law $\sigma_h \sim f^{\alpha}$, where $\alpha < 1$ at low temperatures and $\alpha > 1$ at high temperatures. © *2005 Pleiades Publishing, Inc.*

INTRODUCTION

Compounds of the $A^{II}B^{V}$ group are promising for use in optical, electronic, and thermal sensors; photovoltaic detectors; solar cells; and IR detectors. At the same time, $A^{II}B^{V}$ compounds are characterized by complex phase diagrams, polymorphism (for a number of compounds), the existence of metastable and amorphous phases, wide homogeneity ranges, and structural distortions with corresponding structural rearrangements [1].

$A^{II}B^{V}_2$ semiconductors have attracted the attention of researchers owing to such phenomena as incommensurate phases, polytypism, and the devil's staircase, which were observed in two representatives of this family: CdP_2 and ZnP_2 [2–6]. $A^{II}B^{V}_2$ compounds are crystallized as single crystals with a tetrahedral coordination of atoms, layered structure, and zigzag chains of anions, passing through a crystal.

Interest in the properties and structural transformations in $A^{II}B^{V}_2$ crystals is occasioned by the specific features of their crystal structure. Crystals are tetrahedrally coordinated to off-center covalent bonds and a fraction of an ionic bond. Tetrahedra forming a continuous chain are significantly distorted, which leads to lattice instability with respect to structural transformations and to the formation of superstructures of different types [1–6]. One might expect the presence of strong nonlinear effects and anharmonic instability in crystals of $A^{II}B^{V}_2$ compounds [7]. Although the structural distortions and related characteristic reconstructions belong to specific features of $A^{II}B^{V}$ compounds [1], the mechanisms of lattice distortions and structural transformations in the crystals are still obscure. The electron and defect subsystems also significantly affect the properties of semiconductor crystals. The interaction between the phonon and electron subsystems may give rise to such phenomena as thermal memory and metastable states with phase transitions [8].

According to the formula $A^{II}B^{V}_2$, in the Zn–P, Cd–P, and Zn–As systems, the following structures are crystallized: two modifications of CdP_2: orthorhombic α-CdP_2 and tetragonal β-CdP_2, two modifications of ZnP_2: tetragonal α-ZnP_2 and monoclinic β-ZnP_2, and monoclinic $ZnAs_2$. In the structure of these crystals, each atom of a metal M ($M \equiv$ Cd, Zn) is surrounded by four anion A atoms ($A \equiv$ As, P) and each A atom is surrounded by two M atoms and two A atoms. The radius of an A atom is about 0.1 nm. Since the A–A distance is about 0.21 nm, the anion bond is sufficiently strong. Atoms of a metal M, being located at the center of a deformed tetrahedron, link chains of anion atoms into a three-dimensional (3D) structure. A complex character

Table 1. Elastic constants C_{ij} and the Debye temperature Θ_D of β-CdP_2, α-ZnP_2, and $ZnAs_2$ single crystals at room temperature T_r = 300 K

C_{ij}, GPa / Compound	C_{11}	C_{22}	C_{33}	C_{44}	C_{66}	C_{12}	C'	C''	Θ_D, K
β-CdP_2	78.7		99.5	26.25	30.45	42.79	91.21	32.73	198.2
α-ZnP_2	102.1		115.7	42.85	52.08	30.76	118.5	27.13	280.2
$ZnAs_2$		86.4							

of chemical bond is observed in the compounds under consideration: the anion–anion bond is covalent and the metal–anion bond is partially (by different estimates, from 16 to 54%) ionic [9]. The bond lengths in the compounds are different (the difference is on average as high as 10%); thus, to form a continuous spatial network, the bond angles vary in wide limits, which leads to distortion of tetrahedra and a change in the bond lengths [10, 11].

It is the structure and optical properties of $A^{II}B_2^V$ single crystals that have mainly been studied [10–14]. A recent X-ray diffraction study gave refined data on the bond lengths and angles [11]. The elastic properties of the crystals were measured mainly at room temperature [14–16]. Temperature investigations are scarce and far from being complete [17, 18]. Study of the dielectric properties and the conductivity of $A^{II}B_2^V$ crystals showed fairly unusual temperature behavior of the noted characteristics and gave rise to a discussion in press concerning the existence of superionic conductivity in these crystals [19, 20]. It is of interest to investigate in detail the elastic and electrical properties of crystals of $A^{II}B_2^V$ compounds and to establish the mechanisms of anomalous behavior of these properties and structural distortions in the crystals.

In this work, we investigated the elastic and dielectric characteristics of $A^{II}B_2^V$ (A = Cd, Zn; B = P, As) single crystals in the temperature range 78–400 K and, on the basis of the data obtained, calculated the anisotropy, Gruneisen parameters, effective Sigetti charge, and force constants of these crystals. The purpose was to reveal the nature of the chemical bond and the anisotropy and anharmonicity of $A^{II}B_2^V$ (A = Cd, Zn; B = P, As) single crystals on the basis of data on the elastic and dielectric properties of these crystals at different frequencies and in a wide temperature range.

EXPERIMENTAL TECHNIQUE AND RESULTS

Single crystals of the β-CdP_2, α-ZnP_2, β-ZnP_2, and $ZnAs_2$ phases were grown by chemical vapor deposition. Samples for study were oriented and cut in the (001), (100), (010), and (110) planes. The working surfaces of the samples were ground and polished.

To investigate the elastic properties of the crystals grown, we measured the ultrasonic velocities by the pulse echo method at a frequency of 10 MHz. The samples for ultrasonic experiments were cut in the form of parallelepipeds with plane-parallel polished faces. The velocities of longitudinal and shear elastic waves were measured in the crystallographic directions *a* and *c* in β-CdP_2 and α-ZnP_2 and in the *b* direction in β-ZnP_2. In $ZnAs_2$, the velocities of longitudinal elastic waves were measured in the *a*, *b*, and *c* directions.

The dielectric properties of β-CdP_2 (permittivity ε, loss tangent tanδ, and conductivity σ) were investigated using E7-12 and E7-14 LCR meters at frequencies of 10^2, 10^3, 10^4, and 10^6 Hz. The sample in the form of a thin plate with thin (~0.1 mm) graphite layers deposited on grinded opposite faces was placed between polished brass electrodes. Measurements were performed in the [001] and [200] directions.

Ultrasonic and dielectric measurements were carried out in the temperature range 78–400 K upon slow heating/cooling at a rate of 1–2 K/min. The error of the dielectric measurements and the relative measurements of the ultrasonic velocity did not exceed 0.1%. Temperature was measured accurate to 0.1–0.2 K.

Elastic Properties of β-CdP_2, α-ZnP_2, β-ZnP_2, and $ZnAs_2$ Single Crystals

On the basis of the measured ultrasonic velocities, we calculated the elastic constants C_{ij} by the formula $C = \rho V^2$, where ρ is the crystal density: 4.18×10^3, 3.51×10^3, and 5.245×10^3 kg/m^3 for β-CdP_2, α-ZnP_2, and $ZnAs_2$, respectively (Table 1). The elastic constants were used to calculate the elastic compliances S_{ij}, the Young modulus E, the shear modulus G, the bulk compression modulus K, and the Poisson ratio ν. Table 2 contains the experimental results and the data of [16] for the elastic constant C_{13} of tetragonal β-CdP_2.

Figure 1 shows the typical temperature dependences of the elastic constants C_{ij} of β-CdP_2 and α-ZnP_2 single crystals. The temperature dependences of the elastic constants C_{11}, C_{33}, C_{44}, and C_{66}, as well as $C' = (1/2)(C_{11} + C_{12} + 2C_{66})$ and $C'' = (1/2)(C_{11} - C_{12})$, for the tetragonal modifications of CdP_2 and ZnP_2 were obtained by calculation using the measured velocities

of longitudinal and shear elastic waves in the [001], [010], and [110] directions. The temperature dependences of the velocities of longitudinal ultrasonic waves in monoclinic zinc diarsenide $ZnAs_2$ and zinc diphosphide β-ZnP_2 (Fig. 2) were measured, respectively, in the [001], [010], and [100] directions and in the [001] direction. The temperature dependences of the elastic constants $C_{ij}(T)$ are, on the whole, fairly monotonic and linear. They are described by the simple equation $C_{ij}(T) = C_{ij}^0 + A_{ij}T$. However, at certain temperatures, the linear dependences are violated by the presence of regions with anomalous changes in the elastic constants and the slope of the curves with respect to the temperature axis. In the temperature range 78–410 K, the elastic constants exhibit anomalous changes in the form of small minima (about 0.1–0.4% in magnitude). The anomalies evolve with a change in temperature as follows. At low temperatures, the region of anomalous changes contains three minima, the intermediate minimum being located approximately in the middle of the interval. With an increase in temperature, the intermediate minimum shifts to the low-temperature minimum to collapse with it. At high temperatures, the region of anomalous changes contains two minima, spaced at a distance approximately from 5 to 20 K. Large portions between the temperature ranges with anomalous changes are characterized by monotonic, often close to linear, change in the elastic constants and different slopes with respect to the temperature axis. The temperatures corresponding to the minima somewhat differ in different measurements and depend on the rate of temperature change and the sample history. The best reproducibility was obtained when the measurement unit with a sample was kept at initial temperatures for several (4–8) h and subsequent measurements were carried out at the rates of temperature change from 0.05 to 0.1 K/min.

Dielectric Properties and Conductivity

The temperature dependences of the permittivity $\varepsilon(T)$ (Fig. 3), the loss tangent $\tan\delta(T)$, and the conductivity $\sigma(T)$ were measured in the [001] and [*h*00] directions of β-CdP_2 single crystals at frequencies 10^2, 10^3, 10^4, and 10^6 Hz in the temperature range 78–400 K. At low temperatures (78–150 K), the permittivity changes little: $\varepsilon \approx 7$–14. With an increase in temperature, the permittivity ε sharply increases to ≈300–400 with subsequent increase to $\approx 10^3$ at high temperatures. With an increase in the measuring frequency, the permittivity decreases and the temperature–frequency dependences $\varepsilon(\omega, T)$ shift to higher temperatures.

The temperature dependences of the loss tangent show characteristic peaks located in the region where the permittivity sharply increases. At liquid-nitrogen temperature and up to 130 K, $\tan\delta$ is close to zero. With an increase in temperature to 150 K, a sharp increase in the loss tangent is observed to the values $\tan\delta_{max}$. Then, the loss tangent sharply decreases to zero in the temperature range ΔT = 200–250 K. The peak values $\tan\delta_{max}$ increase with an increase in the measuring frequency and obey the dependence $\tan\delta_{max} = 0.332 + 0.144\log f$. At temperatures above 350 K, $\tan\delta$ increases owing to the dc conductivity.

Table 2. Elastic compliances S_{ij}, the Young modulus E, the shear modulus G, the bulk modulus K, and the Poisson ratio ν measured in the main crystallographic directions in β-CdP_2 and α-ZnP_2 single crystals at room temperature T = 300 K

Elastic characteristics	β-CdP_2	α-ZnP_2
S_{11}, 10^{-11} m^2/N	2.327	1.25
S_{33}, 10^{-11} m^2/N	2.288	1.264
S_{44}, 10^{-11} m^2/N	3.81	2.334
S_{66}, 10^{-11} m^2/N	3.295	1.92
S_{12}, 10^{-11} m^2/N	–0.504	–0.15
S_{13}, 10^{-11} m^2/N	–1.096	–0.469
$E_{100} = 1/S_{11}$, GPa	42.97	79.95
$E_{101} = 1/S_{33}$, GPa	43.71	79.14
$G = (C_{11} - C_{12})/2$, GPa	17.97	35.7
$\nu_{12} = -E_{100} \times S_{12}$	0.217	0.12
$\nu_{13} = -E_{001} \times S_{13}$	0.479	0.371
K, GPa	64.5	62.91

Figure 3 shows the experimental temperature dependences of the conductivity measured at frequencies $f = 10^2$, 10^3, 10^4, and 10^6 Hz (curves *1*, *2*, *3*, and *4*, respectively). The conductivity, being the sum of the contributions of the conventional and hopping conductivities, is characterized by a pronounced frequency dependence.

RESULTS AND DISCUSSION

Elastic Properties of the Crystals

In tetragonal crystals, the elastic constants C_{11}, C_{12}, and C_{66} characterize the bonding forces in a layer (intralayer constants), whereas the elastic constants C_{33}, C_{13}, and C_{44} characterize to a large extent the bonding forces between layers (interlayer constants). Measurements in the directions along and across layers showed a difference between the elastic, structural, and electrical characteristics. The anisotropy of the elastic properties of the crystals studied is characterized by the anisotropy coefficient $A = 2C_{44}/(C_{11} - C_{12})$ and the deviations from the Cauchy relations $G_{kk} = C_{ij} - C_{9-i-j, 9-i-j}$ (where $i \neq j \neq k$; $i, j, k = 1, 2, 3$), which are caused by the off-center character of the interaction between atoms (Table 3).

The elastic anisotropy in β-CdP_2 is higher than in α-ZnP_2. Apparently, the reason for this fact is that the ionic radius of Cd exceeds that of Zn and distortions of tetrahedra in β-CdP_2 are larger than in α-ZnP_2 [1]. Deviations from the Cauchy relations indicate that the

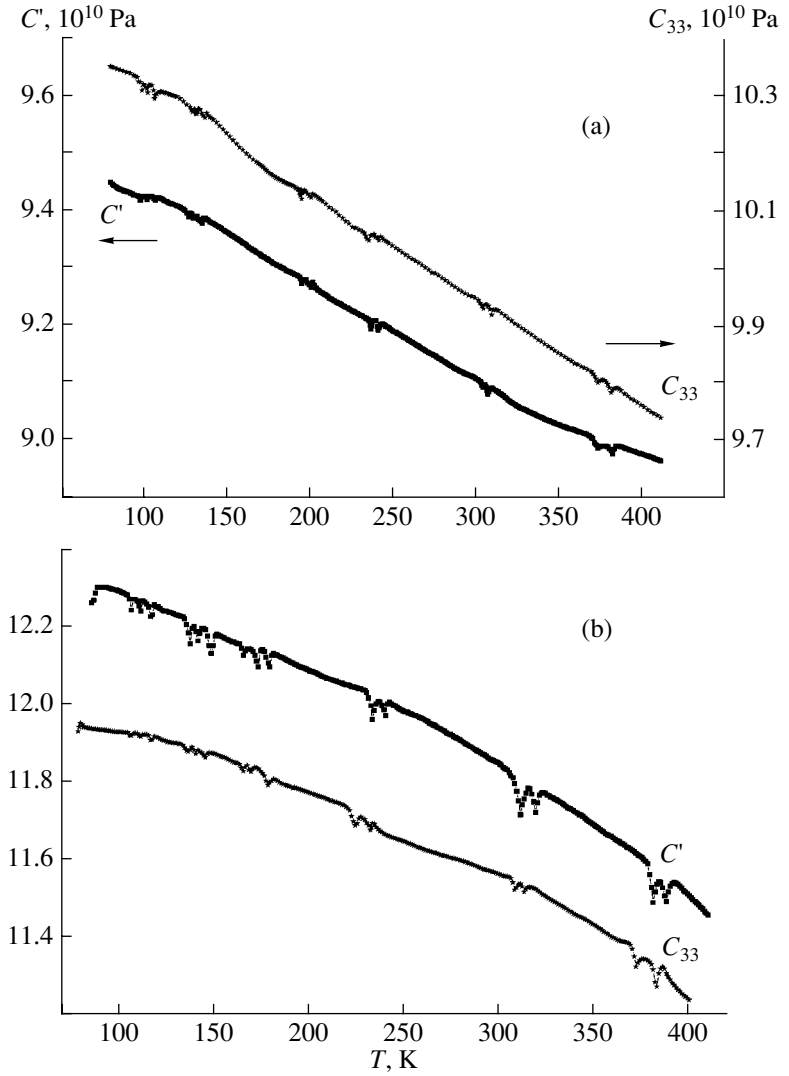

Fig. 1. Temperature dependences of the elastic constants C_{ij} of (a) β-CdP_2 and (b) α-ZnP_2 single crystals.

model of central forces is not valid for crystals of diphosphides.

The Gruneisen parameters characterize nonlinear (anharmonic) properties of crystals. The Gruneisen constant $\gamma_{ij} = \frac{M}{\rho c_p}\alpha_{kl}c^s_{ijkl}$, where M is the molecular weight, ρ is the density, α is the coefficient of thermal expansion, c_p is the specific heat, and c^s_{ijkl} are the adiabatic elastic constants, characterizes the anharmonicity of thermal vibrations. For tetragonal crystals, this parameter has two components with different directions: along the fourfold symmetry axis and perpendicular to it:

$$\gamma_{\parallel} = \frac{(C^s_{33}\alpha_{\parallel} + 2C^s_{13}\alpha_{\perp})M}{\rho c_p},$$

$$\gamma_{\perp} = \frac{[(C^s_{11} + C^s_{12})\alpha_{\perp} + C^s_{13}\alpha_{\parallel}]M}{\rho c_p},$$

where $\alpha_{\parallel}$ and $\alpha_{\perp}$ are, respectively, the coefficients of thermal expansion along and perpendicular to the fourfold symmetry axis (Table 4).

Table 3. Elastic-anisotropy parameter A and deviations from the Cauchy relations, G and δ, for β-CdP_2 and α-ZnP_2 single crystals at room temperature

Anisotropy	α-ZnP_2	β-CdP_2
$A = 2C_{44}/C_{11}$	1.2	1.46
$\delta = (C_{44} - C_{12})/C_{11}$	0.12	–0.21
$G_{11} = C_{23} - C_{44}$	6.5	32
$G_{33} = C_{12} - C_{66}$	–21.4	12.4
C_{11}/C_{33}	0.88	0.79
C_{11}/C_{44}	2.4	3
C_{66}/C_{44}	1.22	1.16

It can be seen from Table 4 that the Gruneisen parameters and, accordingly, the anharmonicity of α-ZnP_2 exceed those of β-CdP_2. The anharmonicity of thermal atomic vibrations in the lattices of diphosphides of tetragonal modification is higher in the plane of layers than along the fourfold symmetry axis.

Deviations from the Cauchy relations suggest that a transverse component arises in the bonding forces. In tetrahedrally coordinated crystals, the structure is stabilized by the bonds of off-center (shear or transverse) type. The forces corresponding to the transverse bonds are typically high, since they correspond to the off-center forces of covalent bonds. Actually, a force constant of a crystal is the force acting on an ion in the lattice site *A* in the *i*th direction if the ion in the site *B* shifts by a length unit in the *j*th direction.

In the Born model of crystals, in which the nearest neighbors are bound by central and off-center forces [21], the force constants α' and β' are related to the elastic constants by the expressions $C_{11} = (\alpha' + \beta')/4a$, $C_{12} = (\alpha' - 2\beta')/4a$, and $C_{44} = [3\beta'(\alpha' + \beta'/4)/[4a(\alpha' + \beta')]$, where *a* is the lattice parameter.

In tetrahedrally coordinated compounds with the sp^3-type of bonding, the crystal structure is stabilized by bond-bending forces. In the valence-force field (VFF) model, bonds are interpreted as bond-stretching and bond-bending ones [22]. Keating extended the VFF model to homopolar crystals with diamond-like structure, in which the second-order elastic constants are described by longitudinal (bond-stretching) and shear (bond-bending) force constants (α and β, respectively) [21, 23]: $C_{11} = (\alpha + 3\beta)/4a$, $C_{12} = (\alpha - \beta)/4a$, and $C_{44} = \alpha\beta/a(\alpha + \beta)$, where *a* is the lattice parameter. This model was extended by Martin [24] to heteropolar crystals with a zinc blende structure by including into consideration long-range Coulomb interactions. The longitudinal α and transverse β components correspond to the diagonal and off-diagonal elements of the force-constant matrix. The off-diagonal elements are additionally separated into symmetric and antisymmetric components [25]. In terms of α and β, the second-order elastic constants have the form

$$C_{11} = \frac{(\alpha + 3\beta)}{a} - 4.053\frac{Z^2e^2}{4\pi\varepsilon_0 a^4},$$

$$C_{12} = \frac{(\alpha - \beta)}{a} - 5.538\frac{Z^2e^2}{4\pi\varepsilon_0 a^4},$$

$$C_{44} = \frac{(\alpha + \beta)}{a} - 5.538\frac{Z^2e^2}{4\pi\varepsilon_0 a^4} - \left(\frac{(\alpha + \beta)}{a} - 4.189\frac{Z^2e^2}{4\pi\varepsilon_0 a^4}\right)\xi^2,$$

where *a* is the lattice parameter, *e* is the elementary charge, *Z* is the effective charge, and ε_0 is the permittivity of free space

$$\xi = \left[\frac{(\alpha - \beta)}{a} - 10.058\frac{Z^2e^2}{4\pi\varepsilon_0 a^4}\right] \times \left[\frac{(\alpha - \beta)}{a} - 4.189\frac{Z^2e^2}{4\pi\varepsilon_0 a^4}\right]^{-1}.$$

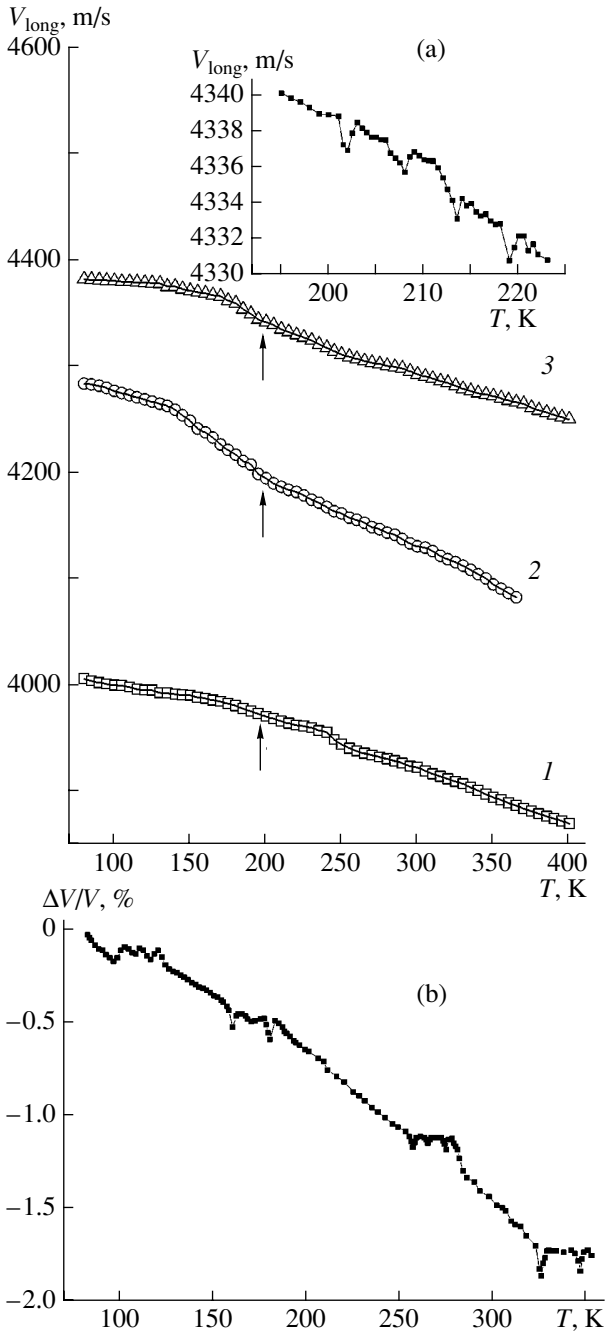

Fig. 2. Temperature dependences of (a) the longitudinal ultrasonic velocities $V_{long}(T)$ in $ZnAs_2$ single crystals in the (*1*) [001], (*2*) [010], and (*3*) [100] directions and (b) the relative longitudinal ultrasonic velocity in β-ZnP_2 single crystals in the [001] direction.

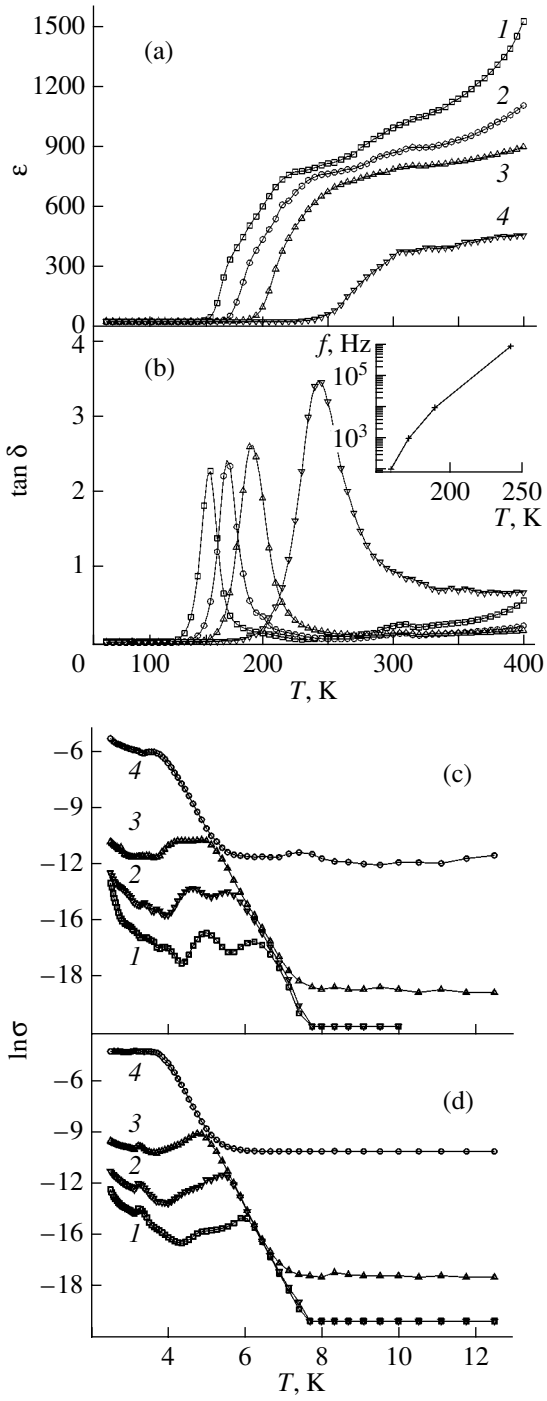

Fig. 3. Temperature dependences of the characteristics of β-CdP_2 single crystals: (a) permittivity and (b) loss tangent measured in the [200] direction and conductivity measured in the (c) [001] and (d) [200] directions at measuring frequencies f = (*1*) 100 Hz, (*2*) 1 kHz, (*3*) 10 kHz, and (*4*) 1 MHz.

The model contains three parameters: the longitudinal α and transverse β force constants and the fitting parameter ξ. A characteristic feature of the model is that it takes into account the polarization (arising due to the overlap of the electron shells of ions), which is introduced into the calculation formulas through the effective charge Z.

The ratio β/α is the measure of the covalent bonding. When a crystal becomes more ionic, the transverse forces tend to decrease. In the ionic limit, $\beta/\alpha \longrightarrow 0$ since $\beta \longrightarrow 0$ and the closed shells of the ions form a structure with predominantly central Coulomb forces. Vice versa, more covalent compounds have large values of β, and large force constants provide a more stable tetrahedrally coordinated structure [23].

Within the Keating model, the values of longitudinal force constants α for the bonds of the *A*–*B*, *A*–*A*, and *B*–*B* types in binary semiconductors with tetrahedral atomic coordination were obtained by Neumann using the expression $\alpha = \alpha_0 \exp(-bd)$, where d is the bond length, $b = (1.13 \pm 0.02) \times 10^{10}$ m^{-1}, and the constant α_0 is equal to 704 or, more rarely, 766 N/m [26].

Different models yield different values of the force constants (Table 5). Calculations in terms of the Keating model were performed using the values of the effective charge Z obtained from optical measurements [9]. As a result, averaged values for the force constants were found. According to the experimental data on the elastic constants, the value of the covalent contribution to the bonding, β/α, for α-ZnP_2 exceeds that for β-CdP_2 by a factor of about two (Table 6).

An increase in the cation size increases the ionicity of the structure (i.e., the effective charge) and the elastic anisotropy and decreases the covalent contribution to the chemical bonding. This effect indicates a smaller stability of the tetrahedrally coordinated lattice of β-CdP_2 as compared to the lattice of isomorphic α-ZnP_2.

In cadmium diphosphide, the covalent contribution to the bonding is smaller than in zinc diphosphide. Accordingly, the lattice of CdP_2 is less stable. In the ideal case of an ionic crystal, where overlap of electron clouds is absent, $e^*/e = 1$. However, electron shells in real crystals overlap, which leads to the deformation of the electron cloud. Effective charge is the measure of the polarization caused by this overlap. In highly ionic crystals, the effective charge e^* is smaller than e by 10–20%. The reason for the deviation of the ratio e^*/e from unity is that the interaction between electron clouds of neighboring ions modifies the electrical dipole moment, and the thermal motion of ions affects the overlap of electron shells. The increase in anharmonic interactions with an increase in temperature leads to additional distortion of electron clouds and decreases the effective charge [27].

The values of e^*/e calculated for β-CdP_2 from experimental data, using the values of permittivity measured at low temperatures [27], are $e_c^*/e = 0.197$ and $e_a^*/e = 0.089$. These values are consistent with the concept of predominantly covalent bonding in crystals of diphosphides with a fraction of ionic bonding [1]. However, such a value of the effective charge suggests high

Table 4. Debye temperatures Θ, average ultrasonic velocities V_m, the bulk (K) and shear (G) moduli, and the Gruneisen constants γ

Parameter / Compound	Θ, K	V_m, m/s	K, GPa	G, GPa	$\gamma_\parallel$	$\gamma_\perp$	$\gamma_\perp/\gamma_\parallel$
α-ZnP_2	280.2	3708.1	63.6	39.3	0.632	0.723	1.144
β-CdP_2	198.2	2603.3	64.2	22.1	0.449	0.46	1.024

Table 5. Force constants of diphosphides, calculated within the Born model of central and off-center forces and the Keating model

Model	Born model			Keating model				
				Neumann's data		Martin's data		
Force constant, N/m	α'	β'	β/α	$\alpha_{(M-P)}$	$\alpha_{(P-P)}$	α	β	β/α
α-ZnP_2	152.38	46.28	0.3	47.61	60.61	27.95	8.84	0.32
β-CdP_2	136.24	24.45	0.18	38.47	60.61	30.28	4.54	0.15

Table 6. Elastic constants C_{ij} (in 10^{10} N/m^2); the force constants α and β; measure of the covalent contribution, β/α; and the effective charge $S \sim (\omega_1^2 - \omega_t^2)$, obtained from the optical splitting of frequencies in crystals with tetrahedral coordination of atoms [10, 16]

Characteristic / Compound	C_{11}, GPa	C_{44}, GPa	C_{12}, GPa	α, N/m	β, N/m	β/α	S
α-ZnP_2	102.12	42.85	30.76	27.95	8.84	0.32	0.39
β-CdP_2	78.73	26.25	42.79	30.28	4.54	0.15	0.66

polarization and the presence of dipoles in the crystal lattice.

Dielectric Properties and Conductivity

Zinc diarsenide and cadmium diphosphide are wide-gap semiconductors. The band-gap width E_g is ≅2.03 and ≅(2.05–2.22) eV in tetragonal β-CdP_2 and α-ZnP_2, respectively, and ≅(1.44–1.602) and ≅0.89 eV in monoclinic β-ZnP_2 and $ZnAs_2$, respectively [28–30].

Typical temperature–frequency dependences of the permittivity ε(ω, T) and the loss tangent tanδ(ω, T) are shown in Fig. 5. Such large values of the permittivity are typical of ferroelectric and wave-charge density materials [31]. However, there are no experimental data allowing us to speak with confidence about a phase transition to the ferroelectric or wave-charge density state in single crystals of $A^{II}B_2^V$ compounds in the temperature range under consideration. Similar temperature–frequency dependences of ε and tanδ are more characteristic of orientational dielectric relaxation [32]. Apparently, the obtained values of permittivity are related to the mechanisms of dielectric relaxation.

One of the possible mechanisms describing strong dielectric relaxation in semiconducting ceramic samples is the Maxwell–Wagner relaxation [33]. The samples under study are almost perfect single crystals with a small concentration of defects. These samples contain no separate regions that could serve as grains. The single crystal itself can be regarded as grain. Then, the Maxwell–Wagner relaxation may be caused by the capacitance of the air gap between an electrode and the crystal surface. To avoid this effect, a semi-insulating graphite interlayer between the ground sample surface and the electrodes was used. In this case, the Maxwell–Wagner relaxation is unlikely to occur.

To explain the thermally activated increase in the permittivity of ternary semiconductor compounds $Cd_{1-x}Mn_xTe$ ($0 \le x \le 0.7$), a model of hopping charge exchange was proposed [24]. According to this model, hopping charge exchange in multiply charged defects (which introduce deep levels into the band gap) in an external electric field should lead to an increase in the permittivity. However, this mechanism is unlikely in the case under consideration. Indeed, to increase the permittivity to ε ≈ 200, the defect concentration should be about 10^{19}–10^{20} cm^{-3}. In other words, the sample should be strongly imperfect, whereas the single crystals we used were much more perfect: the concentration of point defects in them did not exceed 10^{13}–10^{17} cm^{-3} [28].

The model proposed by Ramirez [34, 35] to explain the high permittivity of $CaCu_3Ti_4O_{12}$ gives the most

Table 7. Activation energies ΔE_a (eV) in the [001] direction in β-CdP_2 single crystals at different temperatures and different frequencies of the measuring field

Frequency, Hz / ΔT, K	10^2	10^3	10^4	10^6
80–130	–	–	0.01	0.003
130–260	0.6546	0.7305	0.5916	0.5889
260–350	0.04	0.0016	0.001	0.12
350–400	1.2	0.38	–	–

likely description of the processes occurring in cadmium diphosphide β-CdP_2. Phosphorous vacancies V_P, which deteriorate the quality on the initial crystal structure, can play the role of isolated defects in this case.

Under the action of an external ac electric field, the defect regions undergo distortions and relax between alternative equivalent configurations, retaining on average the crystal structure. This model is in good agreement with the results obtained here.

The temperature dependences of the specific conductivity $\ln\sigma_{sp}(1/T)$ are characteristic of semiconductors: they are broken curves, with separate portions corresponding to different types of conductivity. The slope of the curve $\ln\sigma_{sp}(1/T)$ can be used to calculate the activation energy of carriers at a given frequency from the formula for the conductivity of semiconductors: $\sigma = \sigma\exp(-\Delta E_a/2kT)$. The calculated values are listed in Table 7.

In the temperature range $\Delta T \approx$ 130–260 K, the dependence becomes linear: $\ln\sigma_{sp}$ = (10–3500)(1/T), which suggests the impurity character of conductivity. Furthermore, the carrier concentration does not change, the impurity levels are depleted, and the conductivity is determined by the carrier mobility $\mu(T)$ and the hopping conductivity with the activation energy $\Delta E_a \approx$ 0.01–0.1 eV. The linear portion at temperatures above 350 K corresponds to either impurity or intrinsic conductivity of the material.

The values of the activation energy are different at different frequencies, which is related to the frequency dependence characteristic of hopping conductivity. The conductivity exhibits a pronounced frequency dependence, which is due to the superposition of the conventional and hopping conductivities. At low temperatures, $\sigma(f) \sim f^{\alpha}$ ($\alpha \approx 0.75$–0.85); at high temperatures, $\sigma(f) \sim f^{\beta}$ ($\beta > 1$).

CONCLUSIONS

The elastic and dielectric properties of β-CdP_2, α-ZnP_2, β-ZnP_2, and $ZnAs_2$ single crystals are investigated in the temperature range 78–400 K. The elastic-anisotropy parameters, the Debye temperature, the Gruneisen parameters, and the force constants of the crystals are calculated. Anomalies related to complex structural transformations are revealed in the temperature dependences of the elastic constants and the ultrasonic velocity. Dielectric relaxation is observed in the crystals, which can be described by the model of isolated defects with a low concentration (presumably, anion vacancies). The conductivity of the crystals investigated is the sum of the conventional (typical of conductors) and hopping conductivities.

REFERENCES

1. V. B. Lasarev, V. Ya. Shevchenko, Ya. Kh. Grinberg, and V. V. Sobolev, *Semiconductor Compounds of II–V Group* (Nauka, Moscow, 1978) [in Russian].
2. C. Manolikas, J. van Tendeloo, and S. Amelinckx, Phys. Status Solidi A **97** (1), 87 (1986).
3. A. U. Sheleg and V. V. Zaretskiĭ, Fiz. Tverd. Tela (Leningrad) **25** (10), 3174 (1983).
4. A. U. Sheleg and V. V. Zaretskiĭ, Pis'ma Zh. Éksp. Teor. Fiz. **39** (4), 166 (1984) [JETP Lett. **39** (4), 196 (1984)].
5. L. E. Soshnikov and A. U. Sheleg, Phys. Status Solidi A **111** (2), 485 (1989).
6. V. V. Zaretskiĭ, L. E. Soshnikov, S. S. Khasanov, and V. Sh. Shekhtman, Fiz. Tverd. Tela (Leningrad) **30** (4), 952 (1988) [Sov. Phys. Solid State **30** (4), 553 (1988)].
7. J. A. Krumhansl and R. J. Gooding, Phys. Rev. B **39** (5), 3047 (1989).
8. R. F. Mamin, Kristallografiya **38** (1), 140 (1993) [Crystallogr. Rep. **38** (1), 74 (1993)].
9. N. N. Syrbu and V. É. L'vin, Fiz. Tekh. Poluprovodn. (St. Petersburg) **25** (10), 1136 (1991) [Sov. Phys. Semicond. **25** (10), 1062 (1991)].
10. J. G. White, Acta Crystallogr. **18** (2), 217 (1965).
11. K. B. Aleĭnikova, A. I. Kozlov, S. G. Kozlova, and V. V. Sobolev, Fiz. Tverd. Tela (St. Petersburg) **44** (7), 1206 (2002) [Phys. Solid State **44** (7), 1257 (2002)].
12. A. P. Krokhmal', V. A. Gubanov, and Z. Z. Yanchuk, Fiz. Tverd. Tela (St. Petersburg) **45** (7), 1177 (2003) [Phys. Solid State **45** (7), 1233 (2003)].
13. A. I. Kozlov, S. G. Kozlova, A. V. Matveev, and V. V. Sobolev, Fiz. Tekh. Poluprovodn. (St. Petersburg) **36** (7), 809 (2002) [Semiconductors **36** (7), 755 (2002)].
14. Yu. V. Ilisavskiĭ, L. A. Kulakova, A. B. Pevtsov, *et al.*, Fiz. Tverd. Tela (Leningrad) **23** (6), 1816 (1981) [Sov. Phys. Solid State **23** (6), 1059 (1981)].
15. E. Karajamaki, R. Laiho, T. Levola, and A. U. Sheleg, Semicond. Insul. **5**, 153 (1980).
16. V. Ya. Kuryachiĭ, V. P. Mikhal'chenko, N. V. Stuchinskaya, and I. I. Tychina, Ukr. Fiz. Zh. **30** (2), 248 (1985).
17. A. U. Sheleg, É. M. Smolyarenko, N. P. Tekhanovich, *et al.*, Neorg. Mater. **16** (2), 347 (1980).
18. K. S. Dubrova, V. S. Koval', V. Ya. Kuryachiĭ, and N. V. Stuchinskaya, Ukr. Fiz. Zh. **33** (8), 1259 (1988).
19. V. P. Novikov, A. U. Sheleg, and V. A. Filimonov, Fiz. Tverd. Tela (Leningrad) **30** (1), 289 (1988) [Sov. Phys. Solid State **30** (1), 166 (1988)].
20. Z. V. Silyavichyus, Z. V. Yanushkevichyus, A. P. Kezhenis, and A. S. Orlyukas, Fiz. Tverd. Tela (Leningrad) **27** (10), 3159 (1985) [Sov. Phys. Solid State **27** (10), 1902 (1985)].

21. P. N. Keating, Phys. Rev. **145** (2), 637 (1966).
22. M. J. F. Musgrave and J. A. Pople, Proc. R. Soc. London **268** (1335), 474 (1962).
23. P. N. Keating, Phys. Rev. **152** (2), 774 (1966).
24. R. M. Martin, Phys. Rev. B **1** (10), 4005 (1970).
25. H. Rakel, C. Falter, and W. Ludwig, Z. Phys. B: Condens. Matter **75** (2), 179 (1989).
26. H. Neumann, Cryst. Res. Technol. **24** (6), 619 (1989).
27. J. K. Vassiliou, J. Appl. Phys. **59** (4), 1125 (1986).
28. V. V. Sobolev, A. I. Kozlov, Yu. I. Polygalov, *et al.*, Phys. Status Solidi B **154** (1), 377 (1989).
29. R. S. Berg and P. Y. Yu, Solid State Commun. **46** (2), 101 (1983).
30. V. A. Morozova, S. F. Marenkin, and O. G. Koshelev, Neorg. Mater. **38** (4), 409 (2002) [Inorg. Mater. **38** (4), 325 (2002)].
31. A. P. Ramirez, M. A. Subramanian, M. Gardel, *et al.*, Solid State Commun. **115**, 217 (2000).
32. B. M. Tareev, *Physics of Dielectric Materials* (Énergoizdat, Moscow, 1982) [in Russian].
33. V. V. Lemanov, A. V. Sotnikov, E. P. Smirnova, and M. Weihnacht, Fiz. Tverd. Tela (St. Petersburg) **44** (11), 1948 (2002) [Phys. Solid State **44** (11), 2039 (2002)].
34. P. V. Zhukovskiĭ, A. Rodzik, and Yu. A. Shostak, Fiz. Tekh. Poluprovodn. (St. Petersburg) **31** (6), 714 (1997) [Semiconductors **31** (6), 610 (1997)].
35. A. P. Ramirez, G. Lawes, V. Butko, *et al.*, cond-mat/0209498.

Translated by Yu. Sin'kov

Crystallography Reports, Vol. 50, Suppl. 1, 2005, pp. S46–S52.

PHYSICAL PROPERTIES OF CRYSTALS

Methods for Measuring Light Scattering in Germanium and Paratellurite Crystals

I. A. Kaplunov*, A. I. Kolesnikov*, and S. L. Shaĭovich**

** Tver State University, Sadovyĭ per. 35, Tver, 170002 Russia*

*** All-Russia Research Center Vavilov State Optical Institute, Birzhevaya liniya 12, St. Petersburg, 199034 Russia*

Received February 8, 2005

Abstract—Methods for studying the scattered light in germanium and paratellurite (α-TeO_2) crystals are considered. Investigations of the light scattering in Ge crystals were performed in the infrared wavelength range by the photometric-sphere method (in the range 2–3 μm) and by measuring the line-scattering functions (at 10.6 μm). In the visible range, the paratellurite single crystals were investigated by recording and analyzing images of laser beams transmitted through the samples. It is shown that small-angle Mie scattering is characteristic of both materials. Some conclusions about the sizes and the physical nature of scattering inhomogeneities are drawn. The effect of high-temperature annealing on the scattering intensity is studied. © *2005 Pleiades Publishing, Inc.*

INTRODUCTION

With the development of the techniques used to grow crystals for optics, optoelectronics, and acoustooptics, the materials obtained have reached some level of structural quality. In particular, the concentration of the largest defects, which mainly determine light loss and light wavefront distortions in the crystals, has decreased. For optical germanium, light loss is caused by the absorption by charge carriers. For paratellurite, light loss is related to the presence of gas bubbles, impurity clusters, and optical inhomogeneities (striations). At a certain stage in the development of growth techniques, the problem of decreasing the light loss caused by scattering (which is obscured by absorption in imperfect crystals) becomes urgent. The problem of decreasing light scattering is urgent for devices based on both germanium and paratellurite, especially for Ge-based infrared imaging devices and devices of laser (in particular, force) optics and paratellurite acousto-optic filters and deflectors.

The light scattering in germanium crystals has been studied insufficiently. There are few experimental studies [1–3], in which complex systems were applied for direct measurement of scattered fluxes using CO_2 lasers (only at a wavelength of 10.6 μm). The light scattering in paratellurite single crystals has not been investigated at all. It was mentioned only in view of the manifestation of gyrotropy [4] and has not been considered quantitatively. The optical quality of paratellurite crystals with respect to light scattering has been estimated in Russia and abroad fairly subjectively [5]. Crystals are arbitrarily divided into three groups (*A*, *B*, *C*) in ascending order with respect to the intensity of scattered laser light in the visible range. In crystals of group *A*, laser beams are not visualized, whereas, in crystals of groups *B* and *C*, the light scattering is pronounced. In crystals of group *C*, the scattering manifests itself in the form of subfilamentous inclusions, whose nature has not been established.

The up-to-date certificates for optical germanium classify materials only in the attenuation factor [6, 7]. This photometric parameter is determined by measuring the transmission of optical germanium samples on spectrophotometers with subsequent calculation of the attenuation. However, spectrophotometers of all models measure mixed transmission including both the directed and scattered components, especially at small scattering angles.

The spectrophotometric method proposed in [8] can be used to study the light scattering in germanium and paratellurite. This method, characterized by a simple instrumentation and measurement scheme, makes it possible to record scattering spectra and estimate the sizes of scattering centers. The drawbacks of this method are its relatively low sensitivity and difficulties in quantitative estimation of the scattering.

In this paper, we report the method for monitoring optical samples using the photometric-sphere method and the method for measuring line-scattering functions, which ensure a sufficiently exact and efficient determination of the magnitude of scattering and input monitoring of the materials used to prepare parts of optical systems. For paratellurite single crystals, we will consider a method that uses visible laser light by recording and analyzing images of the cross sections of laser beams transmitted through samples. We believe that it is useful to combine in one study the data on the light scattering in germanium and paratellurite crystals

1063-7745/05/5001-S0046$26.00 © 2005 Pleiades Publishing, Inc.

(which are significantly different in structure and physical properties). This approach makes it possible to reveal general problems related to the methods for measuring scattered light and provides an impetus to carry out similar investigations of other optical crystals.

CRYSTAL GROWTH

Paratellurite crystals were grown by the Czochralski method in air using platinum crucibles. The seed crystals were oriented in the [110], [001], [111], and [$1\bar{1}0$] directions. The best results were obtained for the [110] growth direction, which is related to the implementation of the tangential mechanism of the growth of the particular singular face (110) of paratellurite crystals. Powder tellurium dioxide of 7–4 high-purity analytical grade was used as a starting raw material. The total impurity concentration in the raw material was about 5×10^{-5} and the average effective impurity-distribution coefficient K varied in the range $0.1 \le K \le 1$ during the crystal growth.

Germanium crystals were grown by the Czochralski method in vacuum in a carbon heating unit. The single crystals were oriented in the [111] direction. Polycrystalline germanium had a grain size of 0.5–3.0 mm. Zone-purified polycrystalline germanium (GPZ grade) was used as a starting raw material. Pure and doped Ge crystals were grown, in which the density and distribution of dislocations were determined.

METHODS FOR STUDY

Photometric-Sphere Method

The scattering coefficients of the optical elements were measured on an FM-115 system, whose schematic is shown in Fig. 1.

The photometric-sphere method is based on the comparison of the illuminance of the image of the blackbody *1*, located against the uniform bright background in the photometric sphere *3*, and the illuminance of the image of the sample *7* formed by the auxiliary objective *5*. The illuminance in the photometric sphere *3* was formed by the radiation source *2* fed by the power supply *8*. The radiation detector in the measurement unit *9* is a noncooled PbS photoresistor, whose spectral characteristic allows for measuring signals in the spectral range 2–3 μm.

This method makes it possible to measure the fraction of scattered light as a ratio of the illuminance of the image of a blackbody (i.e., a nonemitting and nonreflecting object) to the illuminance of a bright background image. The blackbody size (diameter) can be varied in order to change the convergence angle of scattered light.

The magnitude of scattering was determined by measuring the illuminance of the blackbody image formed by the luminous flux transmitted through the sample. The illuminance of the background image was measured after a segment was installed in the entrance aperture of the sphere. The fraction of light S scattered from the sample under study was determined by the formula

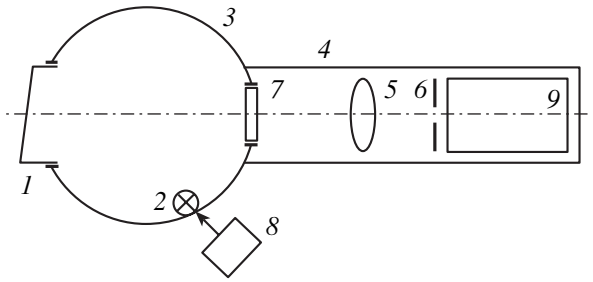

Fig. 1. Schematic of the method for measuring scattering by the photometric-sphere method.

$$S = I_{bg}/I_{bb}, \quad (1)$$

where I_{bg} is the illuminance of the background image and I_{bb} is the illuminance of the blackbody image.

Method for Measuring Line-Scattering Functions

The most important criteria for the estimation of the quality of germanium samples include the shape and the half-width of the indicatrix, which characterizes changes in the propagation direction and the spatial distribution of the intensity of a parallel light beam transmitted through a sample. Changes in the propagation direction are caused by the light scattering in the bulk of a germanium sample and by the nonuniform distribution of the refractive index in the samples. The presence of scattering and inhomogeneity in the refractive index leads to image diffusion and decreases the quality of images obtained by objectives made of these samples.

The measurements of the scattering indicatrix by this method are based on the comparison of the quality of the images of a reference objective obtained in a parallel light beam with a sample installed before the objective and without a sample. This approach makes it possible to estimate the total effect of the scattering in samples and their inhomogeneity in refractive index on the quality of the reference-objective image.

The quality of Ge samples was estimated by measuring the line-scattering functions and the modulation-transfer coefficients at the center of the view field of the reference objective for the spatial frequencies N in the range from 10 to 20 lines/mm. In this case, we compared the half-width of the line-scattering function (width at half-maximum) and the modulation-transfer coefficients of the reference objective obtained with a germanium sample before the objective and without a sample.

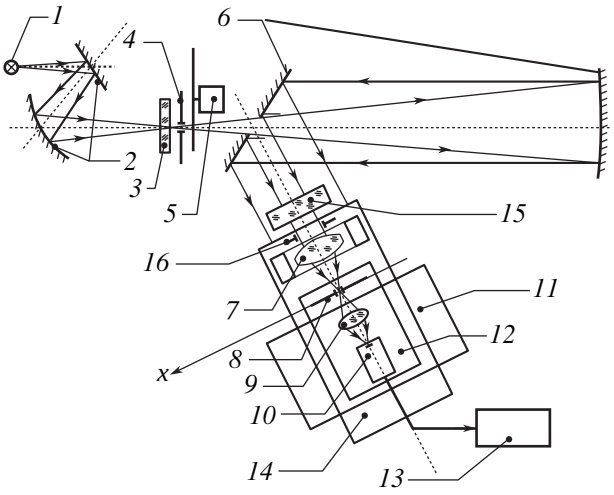

Fig. 2. Schematic of the method for measuring the line-scattering functions.

On the basis of the measurement results, we calculated the quality-loss coefficient using the relation

$$K_{ql} = (T_r(N) - T_{r+s}(N))/T_r(N), \quad (2)$$

where $T_r(N)$ and $T_{r+s}(N)$ are the modulation-transfer coefficients of the reference objective without and with a sample before it.

The method for determining the modulation-transfer coefficient of the reference objective consists in measuring the line-scattering function, i.e., the distribution of the relative illuminance in the image of an infinitely narrow luminous line, formed by the sample tested, with subsequent numerical Fourier transformation of the measured line-scattering function on a computer. The set of values of the modulation-transfer coefficient for different spatial frequencies *N* form the modulation-transfer function.

The line-scattering function is measured by scanning the image of an illuminated slit diaphragm (simulator of the luminous line), formed by the reference objective, by a measuring slit diaphragm mounted before the sensitive layer of a one-area photodetector.

The shape and the half-width of the function characterizing the inhomogeneity and the scattering indicatrix of the samples were determined as follows: on the basis of the measured line-scattering function, the modulation-transfer functions of the reference objective with and without a sample before it ($T(N)_{r+s}$ and $T(N)_r$, respectively) were calculated; the modulation-transfer function ($T(N)_s$), characterizing the quality of a sample studied, was calculated from the relation

$$T(N)_s = T(N)_{r+s}/T(N)_r; \quad (3)$$

and the values of the line-scattering function (which is the scattering indicatrix in the angular measure), characterizing the quality of the sample studied, were calculated by reverse numerical Fourier transformation of the function $\Phi(N)_s$.

The schematic of this method is shown in Fig. 2. The measurement equipment includes a laser *1* with a wavelength of 10.6 μm, a condenser *2*, a test object *4* (a round diaphragm 0.15 mm in diameter), a modulator *5*, a mirror collimator *6*, a scanning slit diaphragm *8* with a width of 0.004 mm, a photodetector *10*, a measuring system *13*, a reference objective, an aperture diaphragm 30 mm in diameter, and a sample *15*. An NP35 single-lens Ge objective with the focal length $F = 50$ mm was used as a reference objective.

Method for Recording and Analyzing Images of Laser Light Beams

The light scattering in paratellurite single crystals in the visible range was investigated using laser radiation with wavelengths of 0.63 μm (a He–Ne laser) and 0.53 μm (a double-frequency YAG laser). The lasers were generated in the transverse mode TEM_{oo}; the laser-beam cross section was in the form of a circle with the Gaussian radial intensity distribution. The beam width *w* (at a level of e^{-2}) was 2.9 and 2.4 mm for the YAG and He–Ne lasers, respectively.

The intensity distribution in the laser beams was studied in a completely darkened room, either directly, on a screen located at a distance of 3.5 m from the samples (by a digital camera), or using a cooled CCD array installed at the same distance coaxially with the beam. Both transmitted through the crystals (and partially scattered) light beams and the beams propagating by the crystals were studied. The images of the beams propagating by the crystals were subtracted from the images of the beams transmitted through the crystals in order to reveal only scattered light.

In the first stage of studying the light scattering, we recorded the image of the laser beam passing by the crystal. The corresponding intensity distribution was calculated using a specially developed computer program by averaging the beam intensity over the coaxial rings around the beam center.

In the second stage, we investigated the images obtained under illumination of a distant screen by laser beams transmitted through the paratellurite single crystals. To cut off central (brightest) regions of the beams, formed by directly transmitted or scattered light, an aperture with a radius of 1 cm was cut in the screen. In the absence of the aperture, the strong illumination from the spot center impedes the measurement of scattered light.

The paratellurite crystals under study were rectangular parallelepipeds with polished faces. Their sizes were 60, 25, and 25 mm in the [110], [001], and $[\bar{1}10]$ directions, respectively. According to the accepted classification of paratellurite quality in terms of scattering intensity, the samples studied belonged to groups *A*, *B*, and *C* (in order of decreasing quality). The average dis-

location density in the samples varied from 7×10^2 to 2×10^5 cm^{-2}. The samples contained no bubbles, cracks, or visual inclusions.

RESULTS

Optical investigation of the cylindrical germanium single crystals grown by the Czochralski method showed the presence of infrared-radiation scattering in them with a characteristic distribution over ingots. The scattering has a pronounced small-angle character: the scattered flux is mainly concentrated in a cone with an opening angle smaller than 2°. Such scattering indicatrices are characteristic of Mie scattering, which occurs when the light wavelength is close to the sizes of scattering inhomogeneities. The dependences of the fraction of scattered light S on the height of cylindrical single-crystal and polycrystalline germanium ingots 50–55 mm in diameter are shown in Fig. 3. The characteristic feature of the scattering distribution for the single crystals (curve *1*) is the presence of enhanced scattering in the initial and final parts of the ingots. The scattering distribution for the polycrystals (curve *2*) is more complex and the magnitude of scattering in the polycrystals exceeds that in the single crystals.

Paratellurite and germanium crystals were subjected to a long-term high-temperature annealing. Annealing of germanium crystals at 790–880°C for 14–28 h led to significant changes in the scattering intensity (table). The scattering data for five single-crystal samples (*1–5*) and two polycrystalline samples (*6*, *7*) are obtained by the integral photometric-sphere method in the spectral range 2–3 μm. The diaphragms S_{20} and S_{40}, used in this method, correspond to blackbody diameters of 20 and 40 mm, respectively (Fig. 1), and provide the required convergence angle of scattered light.

As can be seen from the table, the scattering in some single-crystal samples decreases by a factor of 7–8 (with the diaphragm S_{20}) and by a factor of 15 (with the diaphragm S_{40}). The reflection of light from grain boundaries in polycrystals makes a contribution to the scattering, which, as a result, exceeds several times the scattering in single crystals. However, after annealing, the scattering in polycrystals also significantly decreases. In addition, a decrease in the average dislocation density N_d in single crystals was observed after annealing.

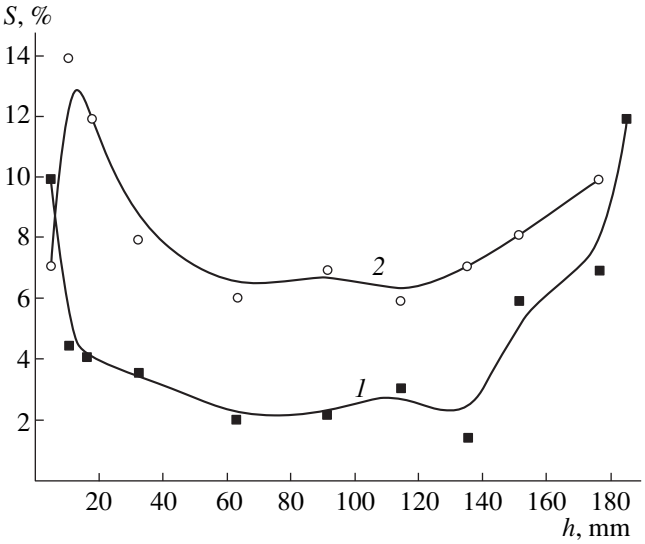

Fig. 3. Distribution of the fraction of scattered light S over the length h of (*1*) a Ge single crystal and (*2*) a Ge polycrystal.

It follows from the Rayleigh scattering theory that, if the total amount (concentration) of inhomogeneities in a material does not change, the scattering coefficient α_s, which enters the exponential Bouguer–Lambert law as a term in the extinction coefficient $\alpha_e = \alpha_a + \alpha_s$, is related to the average radius r of an inhomogeneity and the impurity concentration c by the expression:

$$\alpha_s = \frac{1}{r}\left[\frac{4\pi}{3c}\right]^{-\frac{1}{3}} \ln\left[\left[\frac{4\pi}{3c}\right]^{\frac{2}{3}} \Big/ \left[\left[\frac{4\pi}{3c}\right]^{\frac{2}{3}} - \pi\right]\right]. \quad (4)$$

Light scattering from Ge samples

Sample no.		1	2	3	4	5	6*	7*
Before annealing								
Scattering, %	S_{20}	6	10.2	14	10	13	6	14.5
	S_{40}	1.3	2.2	7	4.2	3	15	20.5
$N_d \times 10^{-4}$, cm^{-2}		0.5	0.57	0.78	7.2	1.25		
After annealing								
Annealing temperature, °C		790	880	790	790	880	790	880
Annealing time, h		14	21	14	21	21	14	21
Scattering, %	S_{20}	1.4	1.4	1.3	1.4	1.5	1.9	6
	S_{40}	0.3	0.7	0.7	0.7	0.8	1.0	2.5
$N_d \times 10^{-4}$, cm^{-2}		0.5	0.4	0.8	3.6	0.75		

* Polycrystalline Ge.

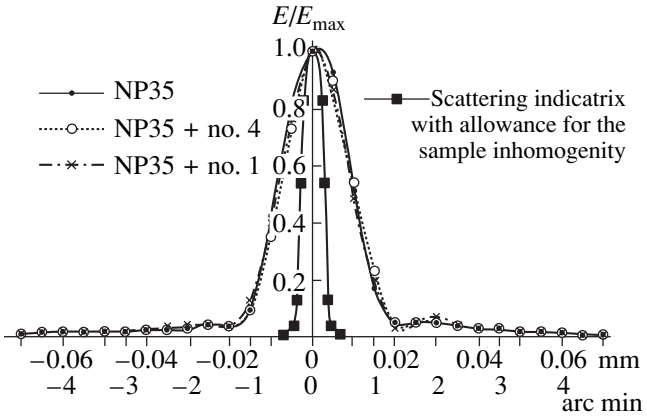

Fig. 4. The line-scattering functions and the scattering indicatrix for the reference objective NP35 with Ge samples *1* and *4*.

According to (4), a decrease in the scattering coefficient at a constant impurity concentration should be observed at annealing-induced enlargement of inhomogeneities.

Two germanium single-crystal samples (*1*, *4*) were investigated by measuring their line-scattering functions. The fraction of scattered light in these samples was measured by the photometric-sphere method. The scattering-line functions of the reference objective NP35 with and without samples before it are shown in Fig. 4. The horizontal coordinate axis in Fig. 4 is digitized both in linear (transverse displacement (in mm) in the objective focal plane) and angular measures. The calculated scattering indicatrix (line-scattering function), characterizing the quality of optical samples, determined by the scattering and the refractive-index inhomogeneity, is also shown in Fig. 4.

The half-width of the indicatrix of the test samples, calculated by the above-described technique, is smaller than 0.003 mm (15 s in the angular measure). When a sample under study is installed before the objective, we have the so-called convolution of the line-scattering function with the scattering indicatrix of the sample rather than summation of these parameters. Therefore, the half-width of the total line-scattering function is smaller than the sum of the half-widths of separate functions. Measurement of the modulation-transfer coefficients at spatial frequencies up to 20 lines/mm yielded a value of the quality-loss coefficient of 0.03. This estimation shows that the samples tested (*1*, *4*) have the best quality in optical homogeneity and scattering indicatrix in the spectral range 8–12 μm, in accordance with the requirements for the quality of germanium used for optical elements. However, the measurements of the scattering magnitude by the photometric-sphere method (see table) showed the presence of scattered light in these samples: 6 and 10% for samples *1* and *4*, respectively. The measurement of the line-scattering functions did not reveal any scattering in these limits or a difference between the samples studied.

Experimental investigation of the visible-light scattering in the paratellurite single crystals made it possible to reveal a number of regularities and to determine the main scattering mechanism. Figures 5 and 6 show the images obtained under illumination of a distant screen by polarized and unpolarized laser beams (λ = 0.53 and 0.63 μm, respectively) transmitted in the [001] direction through a 10-mm-thick paratellurite single-crystal sample, belonging to the quality group *A* with respect to scattering. According to the measurement technique, the central aperture with a radius of 1 cm for cutting off the central regions of the light beams is present in the images.

The results of the computer processing of the images obtained are shown as plots in Fig. 7. The top (*2*) and bottom (*1*) dependences correspond to the beams of red unpolarized and green polarized light, respectively. Both plots and figures demonstrate ring-shaped angular maxima and minima, as predicted by

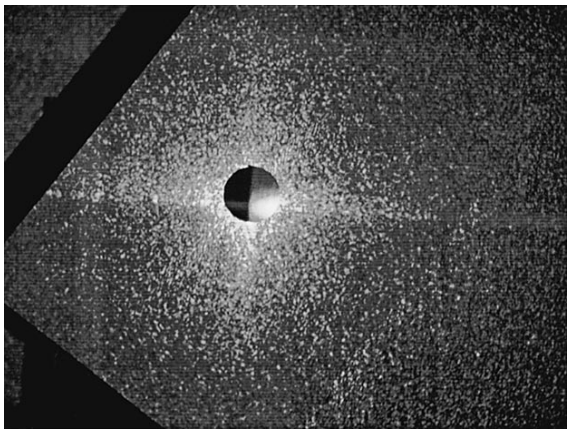

Fig. 5. Scattering of a polarized laser beam (λ = 0.53 μm) by the paratellurite single crystal (observation on a distant screen).

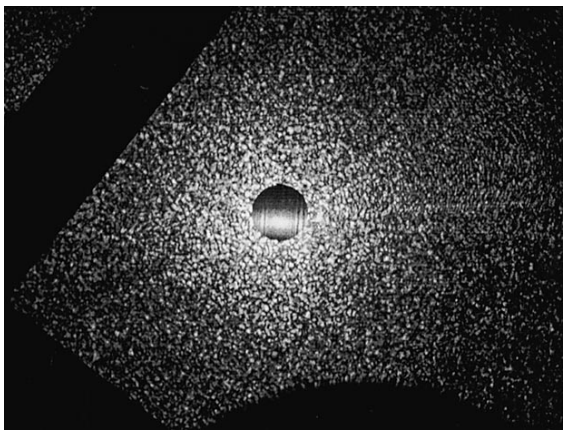

Fig. 6. Scattering of an unpolarized laser beam (λ = 0.63 μm) by the paratellurite single crystal (observation on a distant screen).

the theory of small-angle Mie scattering. The intensity of scattered light at the edge of the screen aperture is lower than the intensity in the first-order, closely located, maximum. The scattering intensity decreases in radius almost linearly by 60–70% for the scattering in the crystal scattering at angles as small as 20′–30′. There are also pronounced second-order maxima. The difference in the positions of the maxima in curves *1* and *2* is consistent with the difference in the light wavelengths.

As follows from the Mie scattering theory, the average distances between scattering inhomogeneities can be estimated with high accuracy using the formulas for Bragg diffraction by a bulk periodic structure. Thus, the average distance $\bar{a}$ between inhomogeneities can be found from the relation

$$\bar{a} = \frac{nm\lambda}{2\sin[\arctan(r/L)]}, \quad (5)$$

where n is the refractive index of the crystal, m is the order of the maximum, λ is the light wavelength, L is the distance from the crystal to the screen, and r is the distance from beam axis to the diffraction maximum. Calculations by formula (5) give the value of 180 μm for $\bar{a}$. It should be noted that this distance corresponds to the average distance between dislocations at an average dislocation density of 3×10^3 cm^{-2}. Specifically, this value was obtained by selective chemical etching for the sample under consideration. The average size of inhomogeneities is ~1–2 μm. These values approximately correspond to the sizes of impurity clouds and dislocation loops. In all paratellurite single crystals under study, the values of scattered-light intensity are in agreement with the values of the impurity concentration and dislocation density.

The effect of high-temperature annealing on the light scattering in the paratellurite single crystals was investigated experimentally in the temperature range 600–700°C. The upper limit of this range is only 33 K below the melting temperature. The annealing time was varied from 24 to 60 h. No changes in the scattering intensity were observed in the samples in comparison with the initial state. Thus, neither decay of inhomogeneities nor their enlargement occurred. We believe that this fact is related to the high impurity concentration in the paratellurite crystals (about 10^{18} cm^{-3}). By way of comparison, the typical dopant concentrations in optical germanium are in the range 10^{13}–10^{14} cm^{-3}.

CONCLUSIONS

The methods for measuring the light scattering in paratellurite and germanium single crystals in the wavelength range 0.35–3 μm and at 10.6 μm, respectively, revealed a number of general regularities for both materials.

At the noted light wavelengths, small-angle Mie scattering occurs, at which up to 99% of light rays scattered in crystals make angles with the primary-beam axis that do not exceed 2°. The sizes of scattering inhomogeneities are close to the light wavelengths. The paratellurite scattering indicatrices show maxima and minima, different from 0°, 90°, and 180°. These extrema were used to determine the average distance between inhomogeneities, which was found to be tens to hundreds of micrometers. These values are consistent with the average distance between dislocations when the dislocation density in the crystals ranges from 10^2 to 10^5 cm^{-2}. In the crystals of both types, when the sample thickness amounts to 1 cm, the total scattering-induced light loss may range from 0.5 to 20%, depending on the presence of structural defects: dislocations, low-angle boundaries, slip lines, and impurities.

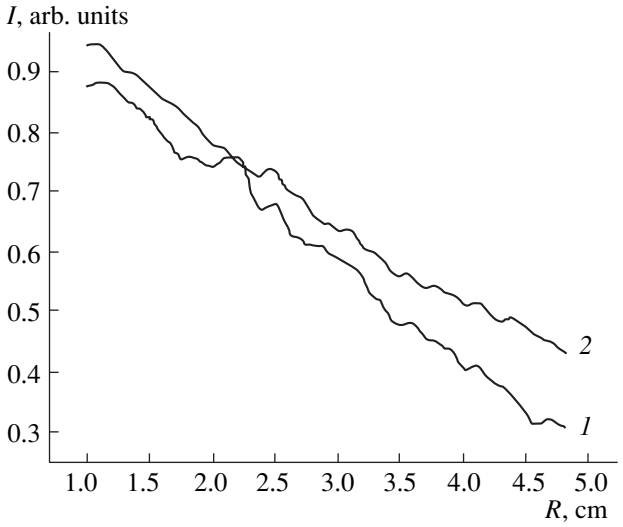

Fig. 7. Dependences of the average intensity of light scattered by the paratellurite single crystal on the distance from the beam center: (*1*) polarized light with λ_g = 0.53 μm and (*2*) unpolarized light with λ_r = 0.63 μm.

The loss-related scattering coefficients α_s, entering the light extinction coefficients, are comparable in many cases with the extinction coefficients themselves. This circumstance should be taken into account when interpreting the results of measurements of the extinction coefficients, especially in germanium crystals, since the loss assigned to the absorption by electrically active impurities can in fact be related to the light scattering by inhomogeneities of another physical nature.

The occurrence of small-angle light scattering in germanium and paratellurite crystals is caused by the presence of structural defects in these crystals. These defects and the related thermoelastic stresses lead to local changes in the permeability, resulting in light scattering (the photoelasticity effect). On the whole, impurity clouds, dislocations, and dislocation loops decorated by impurities should be considered as scattering inhomogeneities.

The annealing of Ge crystals at 790–880°C for 14–28 h leads to a decrease in the scattered-light intensity

by several times. This fact indicates that inhomogeneities change in size and shape and, possibly, decay. The annealing of the paratellurite single crystals even at temperatures close to the melting temperature (733°C) does not lead to a significant decrease in scattering.

The results obtained point to different possible methods for decreasing light loss caused by scattering. These methods include long-term high-temperature annealing, the use of initial raw materials of ultrahigh purity, and primarily, the improvement of techniques for the growth of germanium and paratellurite single crystals by the Czochralski method. Specifically, conditions should be created that would provide for the maximum possible structural homogeneity of the materials as a result of decreasing temperature gradients and melt-temperature fluctuations and using extremely high growth rates for paratellurite and germanium single crystals.

ACKNOWLEDGMENTS

We are grateful to A.V. Glazyrin (Vavilov State Optical Institute, St. Petersburg) and V.Ya. Molchanov (RTC Acoustooptics, MISIS) for supplying the equipment, the help in experiments, and helpful participation in the discussion of the results.

REFERENCES

1. V. P. Kalinushkin, Tr. Inst. Obshch. Fiz., Ross. Akad. Nauk **4**, 3 (1986).
2. V. V. Voronkov, G. I. Voronkova, B. V. Zubov, *et al.*, Fiz. Tverd. Tela (Leningrad) **23** (1), 117 (1981) [Sov. Phys. Solid State **23** (1), 65 (1981)].
3. V. V. Voronkov, G. I. Voronkova, B. V. Zubov, *et al.*, Fiz. Tverd. Tela (Leningrad) **19** (6), 1784 (1977) [Sov. Phys. Solid State **19** (6), 1040 (1977)].
4. V. A. Kizel' and V. I. Burkov, *Gyrotrophy of Crystals* (Nauka, Moscow, 1980) [in Russian].
5. A. I. Kolesnikov, R. M. Grechishkin, I. A. Terent'ev, *et al.*, in *Physics of Crystallisation* (Tversk. Gos. Univ., Tver, 2002), p. 18 [in Russian].
6. *Optical Germanium Crystals*, TU 48-4-522-89.
7. *Optical Crystal Materials* (Gos. Opt. Inst., Leningrad, 1991) [in Russian].
8. I. A. Kaplunov and A. I. Kolesnikov, Poverkhnost, No. 2, 14 (2002).

Translated by Yu. Sin'kov

Crystallography Reports, Vol. 50, Suppl. 1, 2005, pp. S53–S57.

PHYSICAL PROPERTIES OF CRYSTALS

Polarization Distribution in DTGS Crystals under Nonequilibrium Thermal Conditions

A. A. Bogomolov and A. V. Solnyshkin

Tver State University, Sadovyĭ per. 35, Tver, 170002 Russia

e-mail: a.solnyshkin@mail.ru

Received December 28, 2004

Abstract—The polarization distribution in crystals of deuterated triglycine sulphate in a constant temperature gradient is investigated on the basis of the dynamic method for studying the pyroelectric effect. It is shown that, under equilibrium thermal conditions, the polarization distribution is uniform except for the surface layer ~20-μm-thick. The nonuniform polarization distribution in this layer may indicate its multidomain state. In a steady-state temperature gradient, the layer thickens and its domains grow into the sample bulk. © *2005 Pleiades Publishing, Inc.*

The dielectric properties of ferroelectric crystals under nonequilibrium conditions have been investigated in detail [1–3]. At the same time, the pyroelectric properties of crystals under nonequilibrium thermal conditions (in the presence of a temperature gradient) have been studied much less thoroughly, although they are of interest both from the scientific point of view [4] and as possible applications related to measurements of high-intensity heat fluxes by radiation detectors. It was established previously that irradiation by high-intensity heat fluxes results in the depolarization of the surface regions of ferroelectric crystals. In this context, it is important to determine at what depth and to what extent the polarization changes near the sample surface and to estimate the stability of the single-domain state and the pyroelectric characteristics throughout the crystal volume.

To study the pyroelectric properties of crystals by the dynamic method, we used single-crystal samples of deuterated triglycine sulphate (DTGS), which belongs to the group of triglycine sulphate (TGS). The crystals were grown at the Institute of Crystallography of the Russian Academy of Sciences.

Triglycine sulphate $(H_2CH_2COOH)_3H_2SO_4$ is a uniaxial ferroelectric of the order–disorder type, which may undergo a second-order phase transition. Below the Curie point, crystals of the TGS group belong to the symmetry class 2. In the paraelectric phase, they are described by the point-symmetry group 2/*m*. TGS crystals have a monoclinic lattice. The phase-transition temperatures are ~49 and ~60°C for TGS and DTGS crystals, respectively.

The samples of naturally unipolar DTGS crystals were prepared in the form of 1-mm-thick plane-parallel plates in the *Y* cut with an area of 5×5 mm^2 and 0.7–1-mm-thick disks 17–20 mm in diameter. Silver electrodes were formed on the polar faces of the samples by vacuum deposition (gold electrodes were formed on the plane-parallel plates of DTGS crystals) and silver black was deposited on the surface facing the source of thermal radiation.

The schematic of the setup for studying the effect of steady-state temperature gradient on the pyroelectric characteristics of ferroelectrics is shown in Fig. 1.

A sample *1* was placed in the thermostatic chamber *2* on a massive brass substrate, which served as a heatsink for the sample rear. To form a temperature gradient, radiation of the incandescent lamp of the OI-24 illuminator *3* was focused on the blackened sample surface. The heat-flux density could be changed from 15 mW cm^{-2} to 1 W cm^{-2}. In this case, the temperature

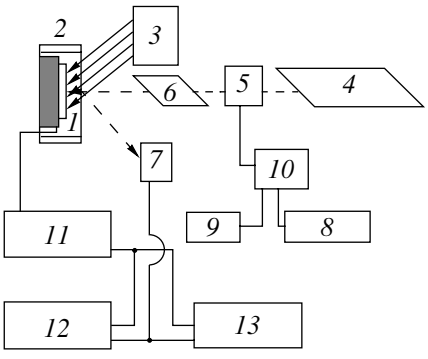

Fig. 1. Schematic of the setup for studying the effect of a steady-state temperature gradient on the pyroelectric properties of DTGS crystals: (*1*) sample, (*2*) thermostatic chamber, (*3*) illuminator, (*4*) laser, (*5*) electrooptic modulator, (*6*) Nicol's prism, (*7*) photocell, (*8*) power supply, (*9*) oscillator, (*10*) isolation scheme, (*11*) selective amplifier, (*12*) double-beam oscilloscope, and (*13*) phase-difference meter.

1063-7745/05/5001-S0053$26.00

distribution in a ferroelectric plate is linear:

$$\theta(y) = \frac{\beta_0 W_0}{k}(d - y), \quad (1)$$

where β_0 is the absorption coefficient of the black, W_0 is the heat-flux density, k is the thermal-conductivity coefficient, d is the sample thickness, and y is a current coordinate. The temperature gradient $\partial\theta/\partial y$ is constant over depth in this case. The pyroelectric properties of DTGS crystals were investigated using sinusoidally modulated radiation of the LG-126 laser *4* with a power of ~1 mW. Modulation was performed using the ML-5 electrooptic modulator *5* and the Nicol's prism *6*. To apply simultaneously a bias and an ac electric field to the modulator, we used the B5-50 power supply *8* and the GZ-33 oscillator *9*, respectively (voltages were applied to the modulator through the isolation scheme *10*, including a capacitance C = 1000 pF and a resistance R = 1 MΩ). A pyroelectric response was measured by the U2-8 selective amplifier *11*. The signal from the amplifier output arrived at one of the inputs of the C1-55 oscilloscope *12* and at the first input of the F2-34 phasemeter *13*. The phase of the modulated heat flux was monitored by the photocell *7*, whose signal arrived at the other input of the oscilloscope *12* and at the second input of the phasemeter *13*. Thus, the phase shift between a pyroelectric signal and a modulated heat flux could be monitored both visually (on the oscilloscope screen) and numerically (from phasemeter readings).

The experimental results, including the frequency dependences of the amplitude value of the pyroelectric current and the phase shift between the modulated heat flux and the pyroelectric response, were processed to obtain the spatial distribution of the pyroelectric coefficient in the samples near the illuminated surface.

To reconstruct the spatial distribution of the pyroelectric coefficient, we used the method proposed in [5]. On the basis of the frequency dependences of the real ($\mathrm{Re}I_0(\omega)$) and imaginary ($\mathrm{Im}I_0(\omega)$) components of the pyroelectric current, which is caused by the action of the probe laser radiation on the sample, we calculated the pyroelectric coefficient by the formula

$$\gamma_a(y_{pen}) = \frac{c\rho d}{\beta_0 W_0 A}[\mathrm{Re}I_0(\omega) - \mathrm{Im}I_0(\omega)], \quad (2)$$

where c and ρ are the specific heat and the density of the crystalline sample, respectively; A is the illuminated surface area; y_{pen} is the penetration depth of a thermal wave in the sample,

$$y_{pen} = \sqrt{\frac{2\alpha}{\omega}}; \quad (3)$$

and α is the thermal diffusivity. It was shown in [5] that the approximating function $\gamma_a(y)$ fairly exactly describes the distribution of the pyroelectric coefficient $\gamma(y)$ in the surface region of the samples under consideration.

Investigation of the pyroelectric properties of DTGS single crystals in a steady-state temperature gradient were performed in a wide temperature range, including the phase-transition region.

Figure 2 shows the distribution of the pyroelectric coefficient $\gamma(y)$ in a ~60-μm-thick surface layer at room temperature. Curve *1* corresponds to the distribution $\gamma(y)$ in the absence of heat fluxes and curves *2*, *3*, and *4* show the distributions in temperature gradients of 4, 9, and 13 K mm^{-1}, respectively. The behavior of the curves shows that the distribution of the pyroelectric coefficient over the sample thickness, $\gamma(y)$, is uniform under equilibrium thermal conditions, except for the surface layer with a thickness of ~20 μm. In this layer, the pyroelectric coefficient monotonically decreases almost to zero. This fact may indicate the existence of a multidomain surface layer [6, 7]. The effect of the temperature gradient leads to the following. In a layer with a uniform polarization distribution (in the absence of a temperature gradient), the pyroelectric coefficient linearly depends on the coordinate, whereas, in the surface layer with a thickness of ~20 μm, the effect of the temperature gradient on γ is not so significant.

With an increase in temperature, in both the absence and presence of a temperature gradient, no significant changes in the polarization distribution occur, up to a temperature of ~46°C, which corresponds to the peak in the dependence $\gamma(T)$ obtained in the presence of a temperature gradient of about 13 K mm^{-1} in the sample. The distribution of the pyroelectric coefficient at a temperature of 46°C is shown in Fig. 2b. It should be noted that the thickness of the layer with a nonuniform distribution of γ remains constant under equilibrium thermal conditions. Temperature gradients of 4 and 9 K mm^{-1} similarly affect the distribution $\gamma(y)$ at this temperature, as at 20°C. However, the behavior of the pyroelectric coefficient at grad$T$ = 13 K mm^{-1} turns out to be different: the temperature gradient leads to a decrease in the thickness of the multidomain surface layer, as evidenced by an almost uniform distribution of γ over the layer thickness up to 10 μm, but then γ significantly decreases and, near the surface (at a depth of 5 μm), a layer arises with a negative pyroelectric coefficient (in comparison with the value of γ for the main sample volume).

In the absence of a temperature gradient, a further increase in the crystal temperature almost does not affect the distribution of the pyroelectric coefficient up to the phase-transition point. At the same time, the presence of a temperature gradient in the sample increases the thickness of the layer with negative γ (Fig. 2c).

The coordinate dependence of the pyroelectric coefficient at the phase-transition point for DTGS crystals (59°C) is shown in Fig. 2d. Curve *1* (grad$T$ = 0) shows that a layer with inverse polarization arises in the surface layer with a thickness of ~5 μm, as evidenced by

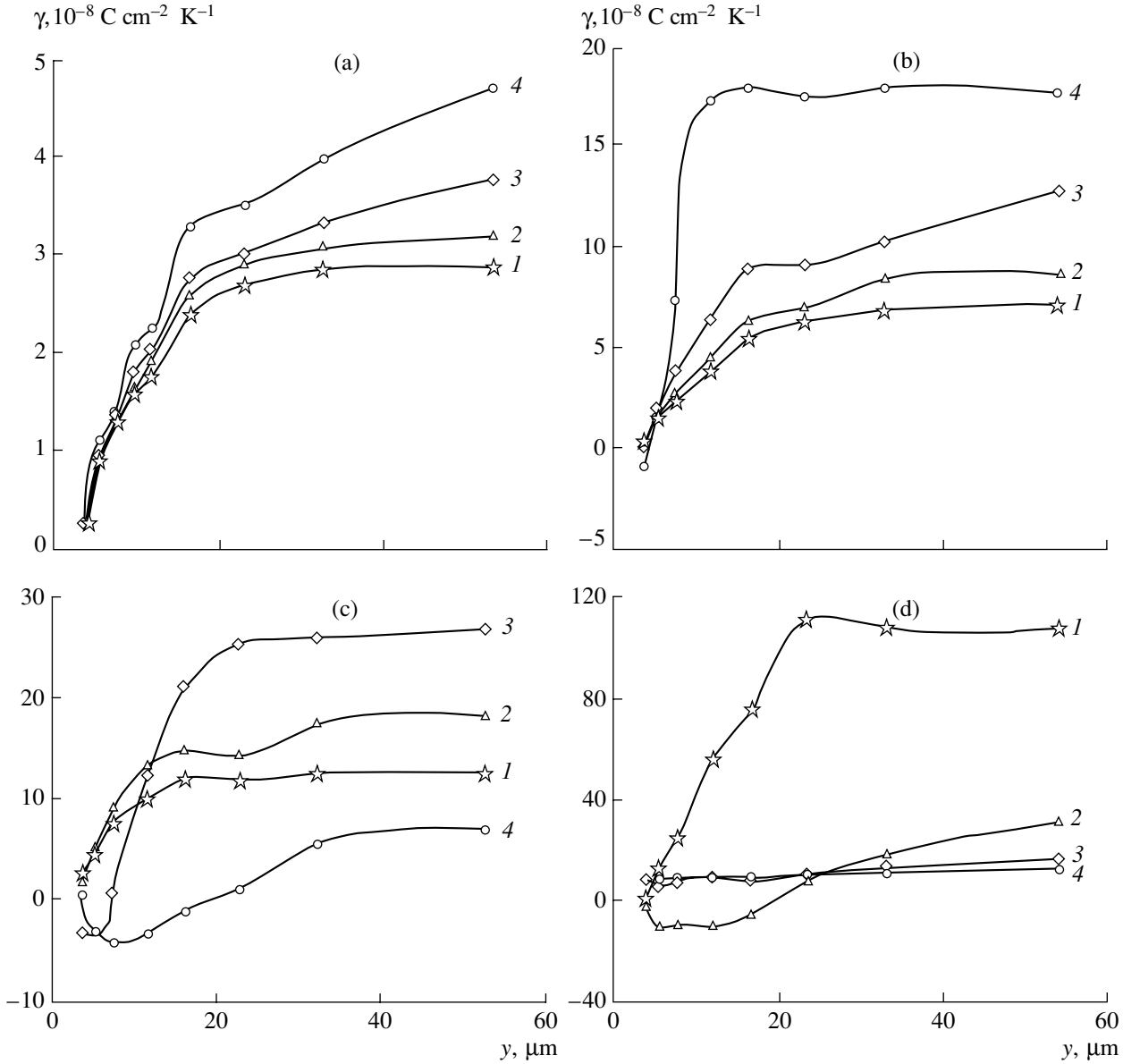

Fig. 2. Distributions of the pyroelectric coefficient in a DTGS single-crystal sample (a) at room temperature and (b) at temperatures of the rear sample surface of (b) 46, (c) 52, and (d) 59°C; $d\theta/dy$ = (*1*) 0, (*2*) 4, (*3*) 9, and (*4*) 13 K mm^{-1}.

the change in the sign of the pyroelectric coefficient. Temperature gradients of 4 and 9 K mm^{-1} lead to an increase in the thickness of this layer to 25 and 35 μm, respectively. At grad$T$ = 13 K mm^{-1}, the region with inverse polarization becomes comparable in thickness with the layer probed. Note that the pyroelectric coefficient is almost coordinate-independent and has small values: ~0.4×10^{-8} C cm^{-2} K^{-1}. It should also be noted that at the above-mentioned temperature gradients the layer probed is in the paraelectric phase.

The temperature dependence of the spontaneous polarization of TGS crystals, according to the phenomenological theory of phase transitions, obeys the law

$$P_s = \pm\sqrt{\frac{\alpha_0}{\beta}}(T_C - T)^{\frac{1}{2}}, \quad (4)$$

where α_0 and β are the coefficients of series expansion of the free energy in polarization. The expression for the pyroelectric coefficient, which characterizes the rate of change in the spontaneous polarization with temperature, has the form

$$\gamma = \frac{\partial P_s}{\partial T} = \pm\frac{1}{2}\sqrt{\frac{\alpha_0}{\beta}}(T_C - T)^{-\frac{1}{2}}. \quad (5)$$

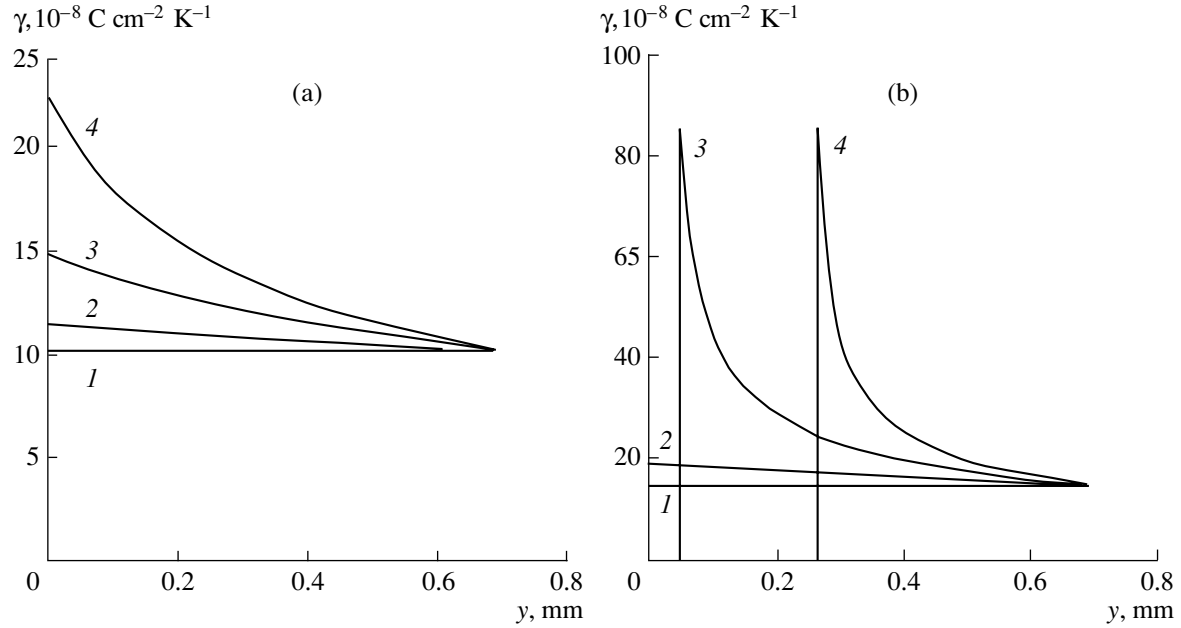

Fig. 3. Calculated distributions of the pyroelectric coefficient in a DTGS single-crystal sample at temperatures of the rear sample surface of (a) 46 and (b) 52°C; temperature gradient $d\theta/dy$ = (*1*) 0, (*2*) 4, (*3*) 9, and (*4*) 13 K mm^{-1}.

According to the generally accepted representations, under equilibrium thermal conditions, the spontaneous polarization and the pyroelectric coefficient of crystalline insulators with ferroelectric properties are constant throughout a crystal when the latter is in the single-domain state. In other words, the polarization distribution is uniform. However, the effect of heat fluxes may lead to a nonuniform temperature distribution in the crystal volume, i.e., to the occurrence of temperature gradients. Since the values of P_s and γ depend on temperature, the presence of a temperature gradient in a crystal leads to a nonuniform distribution of the polarization and the pyroelectric coefficient in the crystal.

Let us consider a DTGS single-crystal sample with a thickness d, cut in a polar plane. We assume that a constant heat flux is incident on the front sample surface ($y = 0$) and the rear sample side contacts a massive substrate that serves as a heatsink (the specific heat of the substrate is assumed to be infinitely high). In the first-order approximation, we can assume that the temperature gradient is constant over the sample thickness ($d\theta/dy$) = const. In this case, the temperature distribution in a ferroelectric plate is linear:

$$T = T_0 + (d - y)\frac{d\theta}{dy}, \qquad (6)$$

where T_0 is the temperature of the rear sample surface. Thus, when the dependences $P_s(T)$, $\gamma(T)$, and $T(y)$ are known, one can find the distributions $P_s(y)$ and $\gamma(y)$.

In studying the pyroelectric properties of ferroelectric crystals by quasi-static and dynamic methods, the pyroelectric coefficient is determined experimentally. Furthermore, we will consider the distribution $\gamma(y)$. When necessary, this distribution can be used to find the polarization distribution over the sample thickness.

For numerical calculations of the spatial distribution of the pyroelectric coefficient, the sample was divided into 1-μm-thick layers. The value of the pyroelectric coefficient within a layer was assumed to be constant. The coefficient $\frac{1}{2}\sqrt{\frac{\alpha_0}{\beta}}$, entering Eq. (5), was found from the experimental temperature dependence of the pyroelectric coefficient: 3.7×10^{-7} C cm^{-2} K$^{-1/2}$. According to the thermodynamic theory of phase transitions, at temperatures $T > T_C$, $P_s = 0$; hence, the pyroelectric coefficient is zero for $T > T_C$. At $T = T_C$, the pyroelectric coefficient was limited by the value $\gamma = 9 \times 10^{-7}$ C cm^{-2} K^{-1}.

Figure 3a shows the results of the numerical calculation of the distribution of the pyroelectric coefficient in a DTGS crystal in the absence of a temperature gradient (curve *1*, uniform distribution) and in steady-state temperature gradients of 4, 9, and 13 K mm^{-1} (curves *2*, *3*, and *4*, respectively). The temperature of the rear surface of the DTGS plate was assumed to be 46°C. As can be seen in Fig. 3a, the distribution of the pyroelectric coefficient becomes more nonuniform with an increase in the temperature gradient. Near the luminated surface, the deviation of γ from the corresponding value observed in the absence of a temperature gradient is maximum.

At temperatures $T > 48.5$°C, in a sample with a temperature gradient, a region of the paraelectric phase arises (Fig. 3b, $T = 52$°C). As a result, the distribution

of the pyroelectric coefficient in the crystal bulk becomes highly nonuniform, which may affect significantly the results of pyroelectric measurements. In this case, the thickness l_{pe} of the paraelectric layer in a temperature gradient of 9 K mm^{-1} is 50 μm. At grad$T$ = 13 K mm^{-1}, l_{pe} = 270 μm. At the points y_1 = 50 μm and y_2 = 270 μm, the curve describing the distribution $\gamma(y)$ pass through the maximum.

Comparing the spatial distributions of the pyroelectric coefficient obtained by numerical analysis (Figs. 3a, 3b) and calculated on the basis of the experimental data (Figs. 2b, 2c), we can conclude that the inconsistency in the behavior of the curves is due to the nonuniform distribution $\gamma(y)$ near the surface in actual samples, which is related to the existence of a multidomain surface layer [6, 7]. The multidomain state of this layer is evidenced by step polarization reversal during the formation of a temperature gradient (at the initial instant of time), as a result of which the thickness of the multidomain surface layer increases. Provided the surface layer in the ferroelectric phase with a nonuniform polarization distribution had another (different from ferroelectric) nature, the above-mentioned phenomenon would be absent.

REFERENCES

1. B. A. Strukov, A. V. Davtyan, and E. L. Sorokin, Fiz. Tverd. Tela (Leningrad) **25** (4), 1089 (1983) [Sov. Phys. Solid State **25** (4), 627 (1983)].
2. B. A. Strukov, A. V. Davtyan, E. L. Sorokin, and K. A. Minaeva, Izv. Akad. Nauk SSSR, Ser. Fiz. **49** (2), 276 (1985).
3. B. A. Strukov, A. V. Davtyan, E. L. Sorokin, and V. T. Kalinnikov, Vestn. Mosk. Univ., Ser. 3: Fiz., Astron. **26** (6), 81 (1985).
4. S. P. Alpay, Z.-G. Ban, and J. V. Mantese, Appl. Phys. Lett. **82**, 1269 (2003).
5. B. Ploss, R. Emmerich, and S. Bauer, J. Appl. Phys. **72**, 5363 (1992).
6. O. V. Malyshkina, in *Ferroelectrics and Piezoelectrics* (Izd-vo TvGU, Tver, 1993), p. 132 [in Russian].
7. A. A. Bogomolov and O. V. Malyshkina, Izv. Ross. Akad. Nauk, Ser. Fiz. **57** (3), 199 (1993).

Translated by Yu. Sin'kov

Crystallography Reports, Vol. 50, Suppl. 1, 2005, pp. S58–S61.

PHYSICAL PROPERTIES OF CRYSTALS

Flow of Space-Charge-Limited Currents in Cubic Boron Nitride

N. A. Shishonok, G. V. Gatal'skiĭ, and A. Yu. Erosh

Institute of Solid State Physics and Semiconductors, National Academy of Sciences of Belarus, ul. Brovki 17, Minsk, 220072 Belarus

e-mail: soshnikov@ifttp.bas-net.by

Received February 7, 2005

Abstract—Current–voltage characteristics of polycrystal cubic nitride samples are studied at various temperatures. The samples were undoped crystals obtained by the method of direct phase transformation of pyrolytic graphite-like boron nitride and crystals doped with sulfur to obtain *n*-type conductivity. The current–voltage characteristics consist of three different parts: linear and quadratic segments and the region of dramatic increase in the current, which indicates the existence of space-charge-limited currents. The activation energy, E_t, and concentration of the trapping centers, N_t, are determined. The experimental data obtained allowed us to calculate, for the first time, the mobility and concentration of free carrier in the conduction band. Possible mechanisms giving rise to a dramatic increase in are made the current on the current–voltage characteristics are discussed.

INTRODUCTION

High energy-gap semiconductor materials possess a number of considerable advantages over traditional materials, which allows one to use these materials in devices operating in wide temperature ranges, light sources operating in the visible and ultraviolet spectrum ranges and having high values of the critical breakdown field and high radiation and chemical stability. Cubic boron nitride (cBN) occupies a special position among intensely studied nitrides of A^3 elements. In its crystallochemical class, cubic boron nitride is the material with the strongest interatomic bonds, which determines the maximum value of its elasticity modulus, band gap, hardness, thermal conductivity, and other basic semiconductor parameters. Therefore, it is natural to expect that the practical use of cBN would allow one to attain record parameters in various devices for solid state electronics. However, the electrophysical properties of cubic boron nitride have been studied insufficiently, which hinders the practical use of this material. Below, we make an attempt to establish some characteristic features of charge transfer in polycrystal cBN samples.

SAMPLE PREPARATION

We studied polycrystal cubic boron nitride samples obtained as a result of direct phase transformation and phase transformation in the presence of a catalyst (extra pure ACD-4 metallic aluminum). The Al content in the charge ranged from 0.5 to 4.0 wt %. The study of aluminum-doped samples is of great interest because aluminum is an isovalent dopant and, therefore, will not change the electrical properties of the material.

The starting material was high-purity graphite-like pyrolytic boron nitride and additionally purified carbothermic boron nitride.

In order to obtain the material with *n* type conductivity, the charge was also doped with sulfur (elemental OS-4 sulfur powder with the total impurity content not exceeding 10^{-5}–10^{-3} wt %). We used sulfur because it is the lightest element of group 6 (except for oxygen), which should be easily incorporated into the cBN crystals' lattice.

Samples were synthesized in a DO-138A pressing setup. The parameters of the synthesis of polycrystal samples were the following: pressure 7.7–8.0 GPa and temperature 2200°C for samples obtained in the presence of the catalyst and 2500°C for the direct phase transformation.

The samples thus synthesized were shaped to rectangular parallelepipeds. One of the faces was polished for microstructural analysis on an optical MMP-4 microscope at a magnification ranging from 480 to 760. Analysis showed that the samples thus prepared had a homogeneous microgranular one-phase structure.

X-ray phase analysis of the samples on a DRON-3 diffractometer confirmed their sphalerite structure; no traces of a graphite-like phase were revealed.

The electrophysical properties of cBN were studied on three groups of samples with different compositions: (1) undoped ones; (2) sulfur-doped ones with the S concentrations 0.5, 1.0, and 2.5 wt %; and (3) aluminum-doped ones with Al concentrations 2.0, 3.0, and 4.0 wt %.

1063-7745/05/5001-S0058$26.00

The electrical parameters were measured with the use of three types of contacts: those based on silver paste, tantalum contacts, and Cu–Ni–Ti-based solder. The results obtained on all the contacts were similar; however, silver contacts had higher resistivity and were less stable, especially in high-temperature measurements.

EXPERIMENTAL RESULTS AND DISCUSSION

The study of the electrical conductivity of all three groups of samples showed that doping with sulfur results in the formation of *n*-type conductivity and decreases the resistivity by two to four orders of magnitude depending on the sulfur concentration. The presence of aluminum decreases resistivity by an order of magnitude irrespective of its concentration and ensures the electron-type conductivity.

The study of the current–voltage characteristics of undoped samples at room temperature showed that they are all of a nonlinear character. These curves may satisfactorily be described by the expression $j \sim E^2$ (curve *1* in Fig. 1). Repeated (including multiple) measurements gave the same results. The electrical conductivity at room temperature remains constant over a wide range of field strength.

Then, we also measured the density of the current flowing through the sample as a function of the electric-field strength at elevated temperatures (373–673 K). It is seen (curves *2* and *3* in Fig. 1) that, at relatively low temperatures (374–473 K), the curves have the same slope as at room temperature and are described by a quadratic law.

Upon the attainment in the sample of the field strength 120 V/cm, the current–voltage curves demonstrated a dramatic increase in the current (by two to four orders of magnitude) at the temperature 573 K (curve *4* in Fig. 1). With a further increase in the field strength, the dependence is once again described by a quadratic law.

The current–voltage characteristics of aluminum-doped cBN samples at room temperature are described by expressions that are intermediate between $j \sim E$ and $j \sim E^2$. Similar to the case of undoped samples, the current–voltage characteristics at high temperatures had a region of dramatic increase in current. The current density at the transition to the low-ohmic state has close values for all the samples with the same composition.

The current–voltage characteristics of sulfur-doped samples at room temperature are shown in Fig. 2. It is seen that they are close to linear dependences. An increase in the temperature also results in the formation of a region of drastic increase in current, which, as earlier, acquires a quadratic character in stronger fields. Some sulfur-containing samples showed breakdown at room temperature (Fig. 3).

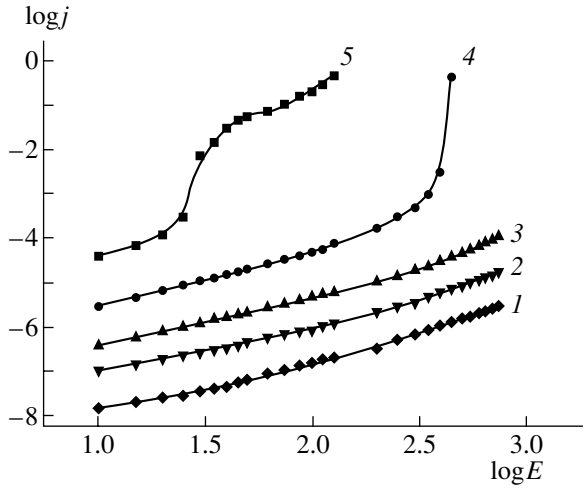

Fig. 1. Current–voltage characteristics of undoped cBN sample at different temperatures *T*: (*1*) 283, (*2*) 373, (*3*) 473, (*4*) 573, and (*5*) 673 K.

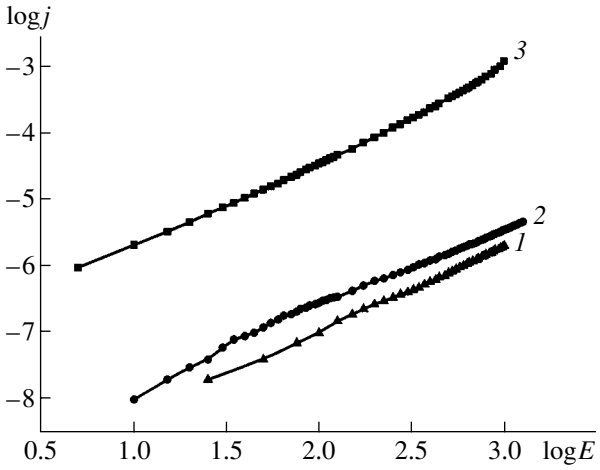

Fig. 2. Current–voltage characteristics of sulfur-doped cBN samples. Sulfur concentration: (*1*) 0.5, (*2*) 1.0, and (*3*) 2.5 wt %.

The studies of the current–voltage characteristics are summarized for all the groups of samples in the table. The vertical arrow indicates the region of dramatic increase in the current.

One of the important features of the current–voltage characteristics is the current hysteresis formed with a lowering of the voltage and observed for the samples of all compositions. Regular measurements of the current–voltage characteristics of all samples showed a regular decrease in the voltage and the temperature of transition to the low-ohmic state. The current–voltage characteristics of the samples measured after different time intervals are shown in Fig. 4.

Thus, the current–voltage characteristics of all samples studied irrespective of their compositions had three characteristic portions (Fig. 3). The first one, located in the region of weak fields, is described by dependences

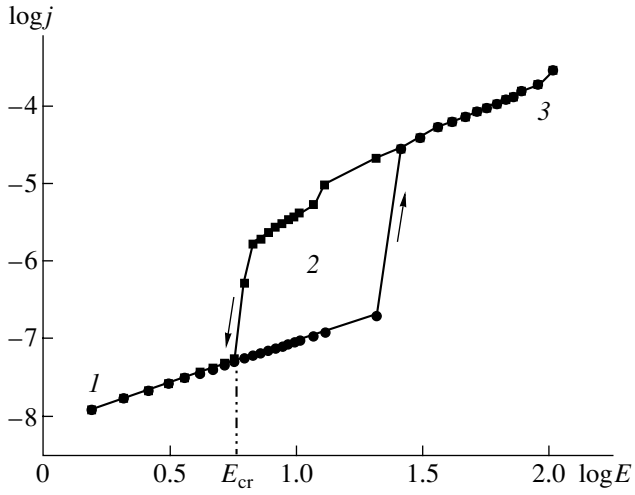

Fig. 3. Current–voltage characteristics of the cBN sample with 0.5 wt % S at 283 K: (*1*) ohmic portion, (*2*) region of dramatic increase in current, and (*3*) region described by a quadratic law corresponding to the absence of trapping centers.

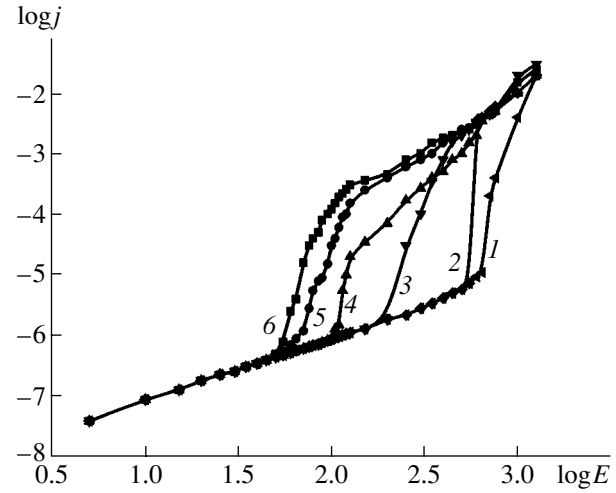

Fig. 4. Current–voltage characteristics of undoped cBN samples measured after different time intervals: (*1*) 1 month, (*2*) one week, (*3*) 24 h, (*4*) 1 h, (*5*) 10 min, (*6*) 1 min.

that are intermediate between $j \sim E$ and $j \sim E^2$. The second portion is characterized by a drastic increase in the current at a certain critical field strength. The third portion of all the current–voltage characteristics is characterized by the quadratic law, $j \sim E^2$.

As is well known, the existence of a region of intense increase in the current on the current–voltage characteristics of high-resistance materials is the most characteristic feature of the space-charge-limited currents [1]. Therefore, analysis of the results obtained should be performed within the framework of the theory of space-charge-limited currents. The linear dependence of current density on the field strength in the region of low fields (portion *1* in Fig. 3) can be explained by the fact that the concentration of the carriers injected from the cathode into the given region is lower than their equilibrium concentration [2]. Ignoring the diffuse component of the current density, the current at this portion can be written as

$$j = q\mu n_0 E, \tag{1}$$

where q is the absolute value of the electron charge, μ is the mobility of electrons in the conduction band, n_0 is the equilibrium electron concentration, and E is the electric-field strength.

For some samples, there is no ohmic branch and the current–voltage characteristics even at low field strengths are described by the quadratic dependence. This portion corresponds to the presence of monoenergetic traps with the energy E_t in the band gap and is described by the equation

$$j = \theta\varepsilon\mu\left(\frac{E^2}{a}\right), \tag{2}$$

where $\theta = (N_c/N_t)\exp(-E_t/kT)$; ε and a are the dielectric constant and sample thickness, respectively; N_c is the effective density of quantum states in the conduction band; N_t is the trap density; and E_t is the distance from the energy level of traps to the conduction-band bottom.

It is well known from the theory of space-charge-limited currents that shallow traps located in the vicinity of the conduction band do not affect the flow of space-charge-limited currents irrespective of the trap concentration. Assuming the existence in the band gap of deep local centers (traps), which can trap the charge carriers and, thus, generate an electric field decelerating the injection of free carriers, we determined the activation energy E_t and concentration N_t of such trapping centers. The concentration was calculated using the well-known formula for the critical voltage of the current–voltage characteristic in the theory of space-charge-limited currents [3]

$$V_{cr} = \frac{qa^2N_t}{2\varepsilon}. \tag{3}$$

Thus, the calculation yielded $N_t = (1.5\text{–}1.8) \times 10^{11}$ cm^{-3}.

The activation energy E_t was determined by a method that is independent of the method of space-charge-limited currents: it was determined from the shape of the peak of thermally stimulated conductivity [4]:

$$E_t = 1.51\frac{kT_1T_m}{T_m - T_1}, \tag{4}$$

where k is the Boltzmann constant, T_1 is the temperature corresponding to half-intensity of the peak from the low-temperature side, and T_m is the temperature of the maximum. The value obtained ranges within E_t = 1.2–1.4 eV.

We used the same method (characteristics of the thermally stimulated conductivity curve) to evaluate the concentration of the trapping centers by the formula [4]

$$N_t = \frac{ekT_m^2 n_{cm}}{E_t \tau_r b}, \quad (5)$$

where e is the exponent, k is the Boltzmann constant, T_m is the temperature of the maximum, n_{cm} is the concentration of nonequilibrium charge carriers in the conduction band, E_t is the activation energy, τ_r is the time of nonequilibrium-carrier recombination, and b is the rate of the temperature increase. The concentration calculated by this method, $N_t = 1.2 \times 10^{11}$ cm^{-3}, satisfactorily agrees with the result obtained by the first method.

The region of dramatic increase in the current is usually interpreted under two different assumptions: (1) an increase in the current is associated with filling of the traps and (2) on the contrary, an increase in the current is associated with the field ionization by free carriers of those traps which have already managed to trap the current carriers.

Keeping of the samples under voltage gradually reduced the current. This may be interpreted as the formation of the spatial charge during the capture of carriers by traps. Then, a dramatic increase in the current may be explained by an emptying of the traps due to the field. This is also confirmed by the criterion of the mechanism manifestation suggested in [5]. According to this criterion, if

$$N_t < 2\varepsilon E_{cr}/aq \quad (6)$$

(where E_{cr} is the critical field strength), then the region of a dramatic decrease in resistivity is associated with filling of all the traps and *vice versa*. In our case, $N_t > 10^{11}$ cm^{-3} are the values calculated on the basis of this criterion.

Our assumption is also favored by the current–voltage characteristics measured at elevated temperatures (Fig. 1). It is seen that the threshold electric-field strength necessary for the start of trapping-center emptying decreases with an increase in temperature. Thus, the region of dramatic increase in the current is most probably associated with thermal emptying of traps.

Portion *3* of the current–voltage characteristics in Fig. 3 corresponds to the "trap-free" quadratic portion of the curves and is described by the well known 3/2 law in the metal–semiconductor–metal system:

$$j = \theta\varepsilon\mu\left(\frac{E^2}{a}\right). \quad (7)$$

Using the above equation, we calculated electron mobility, $\mu = 100$ cm^2/(V s). Once this value is determined, we may calculate the current density from the classical formula

$$j = q\mu n_c E \quad (8)$$

and evaluate the concentration free-charge carriers in the conduction band, n_c. In the range of field strengths and temperatures studied, the n_c varied from 10^{10} to 5×10^{12} cm^{-3}.

Current-voltage characteristics of cBN samples of different compositions

Sample group/Curve portion	*1*	*2*	*3*
Undoped	$j \sim E^2$	↑	$j \sim E^2$
Sulfur-doped	$j \sim E$	↑	$j \sim E^2$
Aluminum-doped	$j \sim E^{1-2}$	↑	$j \sim E^2$

CONCLUSIONS

The current–voltage characteristics of undoped and doped (with isovalent and donor impurities) polycrystal cubic boron nitride samples are studied. It is shown that doping with donor impurity (sulfur) results in the formation of a material with the electron-type conductivity and higher conductivity.

It is established that the current–voltage characteristics of the samples studied have three characteristic portions irrespective of their compositions. The first portion in the region of weak fields is described by dependences that are intermediate between $j \sim E$ and $j \sim E^2$. The second portion is characterized by a dramatic increase in the current at a certain critical value of the field strength. The third portion is described by the quadratic law $j \sim E^2$.

On the basis of the current–voltage characteristics of the samples, we analyzed the results obtained within the theory of space-charge-limited currents. The mobility and concentration of charge carriers are evaluated as well as the depth of location and concentration of trap levels.

REFERENCES

1. B. L. Timman and V. M. Fesenko, Fiz. Tekh. Poluprovodn. (St. Petersburg) **7** (3), 441 (1973) [Sov. Phys. Semicond. **7** (3), 385 (1973)].
2. P. T. Oreshkin, *Physics of Semiconductors and Dielectrics* (Vysshaya Shkola, Moscow, 1977) [in Russian].
3. M. Lampert, Phys. Rev. **103**, 1648 (1956).
4. L. I. Grossweiner, J. Appl. Phys. **24**, 1306 (1953).
5. Yu. S. Ryabinkin, Fiz. Tverd. Tela (Leningrad) **6** (10), 2989 (1964) [Sov. Phys. Solid State **6** (10), 2382 (1964)].

Translated by L. Man

Crystallography Reports, Vol. 50, Suppl. 1, 2005, pp. S62–S67.

CRYSTAL GROWTH

A Thermal Model of Periodic Crystallization

O. N. Shablovsky

Gomel State Technical University, Gomel, 246746 Belarus

e-mail: shabl@gstu.gomel.by

Received February 7, 2005

Abstract—A model of periodic crystallization is constructed on the basis of the wave equation of heat transfer with two energy sources exponentially dependent on temperature. In the problem of metal crystallization in a mold, these sources are competing. In the problem of explosive crystallization of amorphous films, the sources have the same sign. Both problems are analytically solved using the generalized separation of variables and the construction of finite-mode Galerkin approximations. The amplitude and period of oscillations of the phase boundary velocity are analyzed. Spatially periodic structures of the one- and two-dimensional thermal fields are constructed. It is found that the isotherm chains are arranged in a staggered manner. Other important regularities are revealed. © *2005 Pleiades Publishing, Inc.*

INTRODUCTION

The crystallization periodicity most clearly manifests itself in two phenomena: (i) crystallization of a steel ingot [1] and (ii) explosive crystallization of amorphous films [2]. Different physical and physicochemical factors can be responsible for the formation of periodic inhomogeneities. The purpose of this study is to offer a clear explanation of the conditions favorable for the development of a periodic structure during crystallization in the framework of thermal physics.

THEORETICAL ANALYSIS

1. The hyperbolic heat conduction equation allowing for the finite velocity $w = (\lambda/c\gamma)^{1/2}$ of thermal perturbations is derived using the variational principles [3, 4]; that is,

$$c\left(\frac{\partial T}{\partial t} + \gamma\frac{\partial^2 T}{\partial t^2}\right) = \lambda\nabla^2 T + q_v(T); \quad \lambda, c, \gamma = \text{const}. \quad (1)$$

Here, ∇^2 is the Laplacian, γ is the time of thermal relaxation, λ is the thermal conductivity coefficient, c is the heat capacity per unit volume, and q_v is the power of internal heat sources (sinks).

The physical aspects of justification of Eq. (1) were described in [5]. Let us assume that the wave mechanism dominates over the diffusion mechanism: $\gamma\partial/\partial t \gg 1$. Then, in the two-dimensional case, Eq. (1) takes the form

$$\frac{\partial^2 T}{\partial t^2} = w^2\left(\frac{\partial^2 T}{\partial x^2} + \frac{\partial^2 T}{\partial y^2}\right) + k_v(T), \quad (2)$$

where x and y are the Cartesian coordinates and $k_v = q_v/(c\gamma)$. For a one-dimensional process, we assume that $\partial T/\partial y \equiv 0$. For liquid (amorphous) and crystalline phases, it is assumed that $\lambda_l = \lambda_s$ and $(c\gamma)_l = (c\gamma)_s$. Equation (2) can be applied to describe qualitatively thermal processes during periodic crystallization. The source functions can be written in the following form:

$$k_v(T) = k_v^{(1)}(T) + k_v^{(2)}(T); \quad (3)$$

$$k_v^{(1)}(T) = a_1\exp(T - T_c) = b_1\exp T, \quad b_1 = a_1\exp(-T_c); \quad (4)$$

$$k_v^{(2)}(T) = a_2\exp[-2(T - T_a)] = b_2\exp(-2T), \quad b_2 = a_2\exp(2T_a); \quad (5)$$

$$b_1, b_2 = \text{const}; \quad T_a, T_c = \text{const}.$$

These relationships are similar to those used in an elliptic problem [6] for the dependence of the vorticity on the current function when studying two-dimensional steady-state flow of an inviscid fluid. The mathematical results obtained in [6] will be used for our purposes. In order to transform the equations into the dimensionless form, we take the quantity scales (designated by the subscript b) that provide the invariance of the dimensional and dimensionless forms: $\lambda_b t_b = x_b^2 c_b$, $\lambda_b T_b = x_b^2 (q_v)_b$, etc. We will consider two physical phenomena.

I. Periodic crystallization of a metal melt in a mold. In this case, the following two thermal processes are dominant: (1) heat release at the solidification front and (2) heat transfer to the mold wall. The situation can be simulated using two competing energy sources. The positive source $k_v^{(1)}(T) > 0$ is located in the vicinity of the isotherm $T = T_c$, which is associated with the phase boundary (here, T_c is the equilibrium crystallization temperature). The energy sink $k_v^{(2)}(T) < 0$ is located in the vicinity of the isotherm $T = T_a$, which is associated

with the cold wall. The thermal field in the formed solid phase is studied between two isotherms: $T \in [T_a, T_c]$. For definiteness, the dependences of the coefficients a_1 and a_2 in relationships (4) and (5) on the main parameters of the process are represented as follows: $a_1 = LN/(c\gamma a^0)$ and $a_2 = q/(c\gamma a^0)$, where N and $|q|$ are the characteristic (for example, maximum) velocity of the phase boundary and the magnitude of the heat flux to the mold wall, respectively; L is the heat of phase transition per unit volume of a material; and the quantity a^0 has the length dimension.

II. Explosive crystallization of amorphous films. The characteristic features of this process are a high velocity and periodicity of propagation of the crystallization front. According to [7], the process is predominantly affected by the crystal nuclei distributed in the amorphous phase region: crystallization with the participation of a large number of "embedded" nuclei is accompanied by an increase in the phase boundary velocity, and growing nuclei "shield" the heat of crystallization. Such processes can be simulated by two positive energy sources. The parabolic problem regarding the velocity of a crystallization autowave in an amorphous material with distributed crystal nuclei was solved in [8]. A number of thermal aspects of the problem concerning high-rate crystallization were described in [9].

For problem **II**, the source functions are also represented by relationships (3)–(5). As in problem **I**, the source $k_v^{(1)}(T) > 0$ is associated with the crystallization phase boundary. The source $k_v^{(2)}(T) > 0$ is located in the vicinity of the isotherm $T = T_a < T_c$ characteristic of the amorphous phase. By analogy with the formula for the power of a heat release source in the growth zone of crystal nuclei [8], the coefficient a_2 in relationship (5) can be written in the following form:

$$a_2 = LN_1 l^2 [c\gamma l_0^3 |1 - (N/w)|^3]^{-1}, \quad (6)$$

where l is the characteristic linear crystal size in the amorphous phase, N_1 is the characteristic linear crystal growth velocity, and l_0 is the minimum distance between nuclei. The thermal field is studied in the region ahead of the phase boundary: $T \in [T_a, T_c]$.

2. For problem **I**, we consider a self-similar process in which the temperature depends on two arguments of the traveling wave type: $\alpha = x + at$ and $\beta = y + bt$, where a and b are constants. The wave equation (2) of heat transfer takes the form

$$(a^2 - w^2)\frac{\partial^2 T}{\partial \alpha^2} + 2ab\frac{\partial^2 T}{\partial \alpha \partial \beta} + (b^2 - w^2)\frac{\partial^2 T}{\partial \beta^2} = k_v(T). \quad (7)$$

The source term is defined by formulas (3)–(5) in which $b_1 > 0$ and $b_2 < 0$. A thermal analogue of the gas-dynamic Mach number is given by the expression $M^2 = (a^2 + b^2)/w^2$. The subsonic process when $M^2 < 1$ and Eq. (7) has an elliptical form is of prime interest. By using the characteristic variables $\xi = \beta - k_1\alpha$ and $\eta = -k_2\alpha$, Eq. (7) is rewritten in the canonical form

$$\frac{\partial^2 T}{\partial \xi^2} + \frac{\partial^2 T}{\partial \eta^2} = h_1 \exp T + h_2 \exp(-2T), \quad (8)$$

$$h_1 = b_1/[(a^2 - w^2)k_2^2] < 0,$$

$$h_2 = b_2/[(a^2 - w^2)k_2^2] > 0,$$

$$k_1 = ab/(a^2 - w^2),$$

$$k_2 = w(w^2 - a^2 - b^2)^{1/2}/(a^2 - w^2).$$

Therefore, in the subsonic process ($a^2 < w^2$), the energy source $k_v(T)$ reverses sign. Equation (8) is a mathematical analogue of a steady-state equation for the flow function in the case of inviscid flow. The solution is constructed and analyzed according to the algorithm described in [6]; that is,

$$E \equiv \exp T = f(\eta) + g(\xi) > 0; \quad (9)$$

$$(f')^2 = H_1(f), \quad H_1 = 2h_1 f^3 - \mu f^2 + 2h_0 f + a_0; \quad (10)$$

$$(\dot{g})^2 = H_2(g),$$
$$H_2 = 2h_1 g^3 + \mu g^2 + 2h_0 g - h_2 - a_0, \quad (11)$$

The prime and dot on function symbols mean differentiation with respect to the arguments η and ξ, respectively. Here, a_0, h_0, and μ are arbitrary constants. A qualitative analysis of Eqs. (10) and (11) leads to the following results.

If the algebraic equation $H_1(f) = 0$ has three real different roots f_1, f_2, and f_3 such that $f_1 < f_2 < f_3$, the equation $\tilde{H}_2(g) \equiv h_2 + H_2(g) = 0$ possesses the roots $\tilde{g}_1 = -f_1$, $\tilde{g}_2 = -f_2$, and $\tilde{g}_3 = -f_3$. The graph of the function $H_2(g)$ is obtained from the graph of the function $\tilde{H}_2(g)$ by downward parallel translation along the ordinate axis. For our purposes, it is sufficient to take $h_0 = 0$. For two roots f_2 and f_3, we have formulas $\mu/(2h_1) = (f_2^2 + f_2 f_3 + f_3^2)/(f_2 + f_3)$ and $a_0/(2h_1) = f_2^2 f_3^2/(f_2 + f_3)$. Initially, we assume that $a_0 < 0$ and $\mu < 0$ and the roots of the equation $H_1(f) = 0$ satisfy the inequalities $f_1 < 0 < f_2 < f_3$. Then, the function $H_1(f)$ exhibits two extrema, namely, a minimum at $f_* = 0$ and a maximum at $f_{**} = \mu/(3h_1)$. Consequently, the function $f(\eta)$ is periodic in the range of values $f \in [f_2, f_3]$. At $a_0 + h_2 < 0$, the examination of the behavior of the dependence $H_2(f)$ leads to the inequalities $g_3 < g_2 < 0 < g_1$. This means that the function $g(\xi)$ is periodic at $g \in [g_2, g_1]$. It is clear that, in this case, the condition $E > 0$ is fulfilled. Now, we assume that $a_0 > 0$ and $\mu > 0$ and the roots of the equation $H_1(f) = 0$ satisfy the inequalities $f_1 < f_2 < 0 < f_3$. Then,

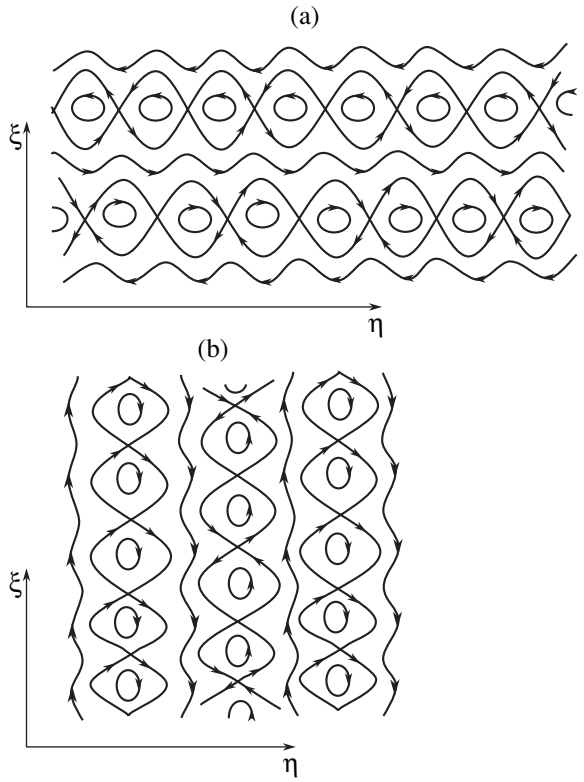

Fig. 1. A staggered arrangement of the isotherm chains for the "metal melt–mold" system at temperatures (a) $T_3 < T_2$ and (b) $T_3 > T_2$.

$\tilde{g}_3 < 0 < \tilde{g}_2 < \tilde{g}_1$ and the roots of the equation $H_2(g) = 0$ correspond to the inequalities $g_3 < 0 < g_2 < g_1$. The function $f(\eta)$ is periodic in the range of values $f \in [f_2, f_3]$. The function $g(\xi)$ is also periodic in the range of values $g \in [g_2, g_1]$. Since the inequality $f_2 + g_2 > 0$ is fulfilled, we have $E > 0$. Therefore, there are two variants of the roots f_1, f_2, and f_3 when there exist solutions periodic in each argument, ξ and η. In these cases, we have $f > 0$ and $g > 0$ in their own ranges of values.

Let us discuss the behavior of the isotherms $T(\xi, \eta) = T_i = \text{const}$. From the formula $E(T_i) \equiv E_i = f(\eta) + g(\xi)$, we have the equation for the isotherm; that is, $d\eta/\dot{g}(\xi) = d\xi/[-f'(\eta)] = d\alpha^1$, where α^1 is a parameter. The corresponding dynamic system takes the following form:

$$d\xi/d\alpha^1 = -f'(\eta), \quad d\eta/d\alpha^1 = \dot{g}(\xi). \qquad (12)$$

After the shift transformation with respect to arguments ξ and η in Eqs. (10) and (11), we find that the functions $f(\eta)$ and $g(\xi)$ exhibit maxima at zero. As a result, we have $f = f_{\max}$ at $\eta = M\tau_f$ and $f = f_{\min}$ at $\eta = [M + (1/2)]\tau_f$, where τ_f is the period of the function $f(\eta)$ and M is an arbitrary integer number. In turn, we obtain $g = g_{\max}$ at $\xi = M\tau_g$ and $g = g_{\min}$ at $\xi = [M + (1/2)]\tau_g$, where τ_g is the period of the function $g(\xi)$. The extrema of the functions $f(\eta)$ and $g(\xi)$ are the stationary points of the dynamic system (12). The characteristic roots r obey the equation $r^2 + \ddot{g}(\xi)f''(\eta) = 0$. Consequently, the points in the plane (η, ξ) at which the functions $f(\eta)$ and $g(\xi)$ have extrema of the same type (maxima or minima, i.e., $\ddot{g}f'' > 0$) are singular points of the "center" type for the dynamic system (12). The points at $\ddot{g}f'' < 0$ correspond to saddle points. A point (ξ_0, η_0) is considered critical when the equality $[f'(\eta_0)]^2 + [\dot{g}(\xi_0)]^2 = 0$ is satisfied. The corresponding critical temperature is $T_0 = T(\xi_0, \eta_0)$, i.e., $E_0 = E(T_0)$. Therefore, in the class of solutions (9)–(11), there are four critical solutions $E(T_1) = f_3 + g_1$, $E(T_2) = f_2 + g_1$, $E(T_3) = f_3 + g_2$, and $E(T_4) = f_2 + g_2$. The isotherms T_1 and T_4 correspond to stable equilibrium states of the center type, and the isotherms T_2 and T_3 correspond to unstable saddle singularities. The phase portrait of the dynamic system (12) illustrates qualitative properties of the isotherm field (Fig. 1). The lines $T = T_2$ and $T = T_3$ are separatrices of the dynamic system (12) and pass from one saddle point to another saddle point. Figure 1a depicts the arrangement of isotherms at $T_3 < T_2$. The saddle points fall in the lines $\xi = \tau_g M/2$. The parallel chains of the isotherms are arranged in a staggered manner. The right-hand side of Eq. (8) can be represented in the form $(a^2 - w^2)k_v/[w^2(w^2 - a^2 - b^2)]$. This relationship for a particular chain has a specific sign, which becomes opposite for the neighboring chain. The inversion is associated with the competing effect of the volume energy sources $k_v^{(1)}$ and $k_v^{(2)}$. Figure 1b shows the arrangement of isotherms at $T_2 < T_3$. The saddle points fall in the lines $\eta = \tau_f M/2$. For both variants in Fig. 1, there are isotherms located between chains. At $T_2 = T_3$, such isotherms are absent; i.e., the neighboring chains share boundaries.

In the physical plane (x, y), the process under consideration can be described as follows. The lines $\eta = \text{const}$ move along the OX axis at the velocity $(-a)$. The lines $\xi = \text{const}$ move at the subsonic velocity $N_\xi = w^2 b/[(a^2 - w^2)^2 + a^2 b^2]^{1/2}$. At each fixed instant, the temperature is a periodic function of the arguments $y - k_1 x$ and $-k_2 x$. At each fixed point (x, y), the function $E(T)$ is a superposition of two periodic functions of the arguments $(b - k_1 a)t$ and $-k_2 at$. The oscillation periods in time t for these functions are $\tau_g/(b - k_1 a)$ and $\tau_f/(-k_2 a)$. For each isotherm $T_i \in [T_a, T_c]$ at $\beta = \beta_i(\alpha)$, the velocity of the line $E_i \equiv \exp T_i = f(\eta) + g(\xi)$ can be written in the form

$$N_E = \frac{a(d\beta_i/d\alpha) - b}{(d\beta_i/d\alpha)^2 + 1} = \frac{a[k_1 - k_2(d\xi/d\eta)] - b}{\{[k_1 - k_2(d\xi/d\eta)]^2 + 1\}^{1/2}}.$$

At the points of the isotherm at which $f = f_2$ or $f = f_3$, we have $d\xi/d\eta = 0$ and, hence, $N_E^2 = (ak_1 - b)^2/(1 + k_1^2) = N_\xi^2$, which corresponds to the velocity of the ξ line. At the points of the isotherm at which $g = g_1$ or $g = g_2$, we

have $d\xi/d\eta \longrightarrow \infty$ and, hence, $N_E^2 = a^2$, which corresponds to the velocity of the η line. This clarifies the physical meaning of the parameters a and b: these parameters characterize the subsonic velocities of isotherms at the points corresponding to $f = f_2$ and $f = f_3$ for $g \in (g_2, g_1)$ or $g = g_1$ and $g = g_2$ for $f \in (f_2, f_3)$.

3. Problem **II** (explosive crystallization) will be solved using the one-dimensional variant of Eq. (2). The variables x and t are separated in a way similar to that for the solution to the elliptic problem; that is,

$$E \equiv \exp T = f(x) + g(t) > 0; \tag{13}$$

$$w^2(f')^2 = F(f), \quad F = -2b_1 f^3 + \mu f^2 - 2b_0 f - a_0; \quad f' = df(x)/dx, \tag{14}$$

$$(\dot{g})^2 = G(g), \quad G = 2b_1 g^3 + \mu g^2 + 2b_0 g - a_0 - b_2, \quad \dot{g} = dg(t)/dt. \tag{15}$$

Here, a_0, b_0, and μ are arbitrary constants; $b_1 > 0$; and $b_2 > 0$. Now, we perform the qualitative analysis of these equations. For this purpose, we examine the behavior of the real roots of the equations $F(f) = 0$ and $G(g) = 0$. To three real different roots f_1, f_2, and f_3 ($f_1 < f_2 < f_3$) of the equation $F(f) = 0$ there correspond three roots $\tilde{g}_1 = -f_3$, $\tilde{g}_2 = -f_2$, and $\tilde{g}_3 = -f_1$ of the equation $\tilde{G} \equiv b_2 + G(g) = 0$. The equation $G(g) = 0$ has the roots g_1, g_2, and g_3 such that $g_1 < g_2 < g_3$. Let us discuss the conditions under which the solution $g(t)$ to Eq. (15) is a periodic function. The function $G(g)$ exhibits two extrema, namely, a maximum at $g = g_* = (-\mu - D^{1/2})/(6b_1)$ and a minimum at $g = g_{**} = (-\mu + D^{1/2})/(6b_1)$, where $D = \mu^2 - 12b_0b_1 > 0$, $\mu < 0$, and $0 < g_* < g_{**}$. We consider three positive roots of the equation $G(g) = 0$: $0 < g_1 < g_2 < g_3$. Then, we find that $g_1g_2 + g_2g_3 + g_1g_3 = b_0/b_1 > 0$, $g_1 + g_2 + g_3 = -\mu/(2b_1)$, and $g_1g_2g_3 = (a_0 + b_2)/(2b_1) > 0$. The function $g(t) > 0$ is periodic in the argument t at $g \in [g_1, g_2]$. The equation $\tilde{F} \equiv F(f) - b_2 = 0$ possesses the negative roots $\tilde{f}_1 = -g_1$, $\tilde{f}_2 = -g_2$, and $\tilde{f}_3 = -g_3$ such that $\tilde{f}_3 < \tilde{f}_2 < \tilde{f}_1 < 0$. The graph of the function $F(f)$ is obtained from the graph of the function $\tilde{F}(f)$ by upward parallel translation along the ordinate axis. Consequently, at $b_2 > 0$, we obtain the root $f_1 < 0$ [$F(f_1) = 0$] such that $f_1 + g_1 > 0$. The condition $E > 0$ in relationship (13) is fulfilled at $f \in [f_0, f_1)$ when the initial value f_0 satisfies the inequalities $(-g_1) < f_0 < f_1$. The constant a_0 satisfies the condition $a_0 + b_2 \geq 0$. From expression (14), we find

$$w(df/dx) = [F(f)]^{1/2} > 0, \quad x \in [0; \infty);$$
$$x = 0, \quad f(0) = f_0; \quad x \longrightarrow \infty, \quad f \longrightarrow f_1.$$

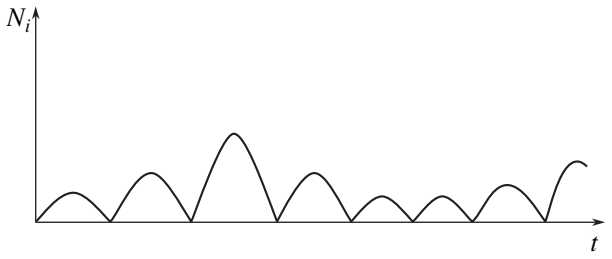

Fig. 2. Oscillations of the velocity of the phase boundary of the explosive crystallization.

At $x \in (-\infty, 0)$, the formulas are similar. For the isotherm going to the right ($dx > 0$), we have $df/dx > 0$. For the isotherm going to the left ($dx < 0$), we have $df/dx < 0$; i.e., as before, $df > 0$. In both cases, the inequality $dF/df < 0$ is satisfied. Therefore, the temperature varies in the half-open interval $E \in [g_1 + f_0, g_2 + f_1)$. Let us analyze the behavior of the isotherm $T = T_i \equiv$ const with the equation of motion $x = x_i(t)$. It is evident that the function $f[x_i(t)] = E_i - g(t)$ is periodic in time t and is limited from above by the value $E_i - g_1$ and from below by the value $E_i - g_2$, where $E_i = \exp T_i$. Any isotherm in the range $E_i \in [g_1 + f_0, g_2 + f_1)$ moves at a finite velocity N_i given by the formula $N_i^2/w^2 = G(g)/F[f(x_i)]$. This formula holds true on any finite interval x. The function $N_i(t)$ vanishes periodically. The total amplitude of oscillations of the velocity N_i is also periodic function of the time (Fig. 2). This oscillation process is represented by specific beats. It is clear that this inference is also valid for the isotherms $T = T_a$ and $T = T_c$ bounding the temperature range under investigation. It will be demonstrated below that there exists a two-dimensional solution with similar properties. This behavior of the phase boundary velocity explains the experimentally observed characteristic "lobed" and "scaly" structures formed upon explosive crystallization in films [2, p. 147; 7]. The constant a_0 characterizes the initial (at $t = 0$) thermal field $T(x, 0)$ in the amorphous phase. The thermal process is periodic in time when the parameters a_0 and $b_2 > 0$ (the energy source parameter in the zone of nucleus growth) satisfy the inequalities $(-a_0^*) < (-a_0) < b_2$ (the formula for $a_0^* > 0$ is not given).

4. The solution to the differential equation (15) can be represented in the form of the finite-mode Galerkin approximation

$$g(t) = n_0 + n_1 \sin kt + n_2 \cos kt + n_3 \sin 2kt + n_4 \cos 2kt + \ldots. \tag{16}$$

Approximations of this type turned out to be efficient in the study of a nonlinear behavior of distributed kinetic systems with an aperiodic instability [10]. Substituting formula (16) into Eq. (15) and omitting harmonics higher than the second harmonic, we obtain

$n_2 = 0$ and $n_3 = 0$. The frequency k and three coefficients n_0, n_1, and n_4 are related to each other by three algebraic equations (not given). The approximate solution $g(t) \cong n_0 + n_1 \sin kt + n_4 \cos 2kt$ possesses the following properties: the quantity $n_0 + n_4 = g(0)$ characterizes the initial temperature at a fixed point x, $(n_0 - n_4)$ is the "mean" value about which oscillations occur, and $2n_1$ is the total oscillation amplitude. The convergence of the formal series (16), which is the quasi-harmonic solution to Eq. (15), can be proved using the method described in [11]. Numerical calculations indicate that the obtained quasi-harmonic approximation is characterized by a good practical convergence at $|n_0| > |n_1| > |n_4| > |n_5|$, etc.; $n_4 < 0$; and $|4n_4/n_1| < 1$. For example, at $n_0 = 5$, $n_1 = 1$, $n_4 = -0.1$, and $k^2 = 1$, we find $b_1 = 1$ and $(a_0 + b_2)/b_1 \cong 280.12$.

The properties of the analytical relationships representing the approximate solution $g(t)$ are as follows. The constants a_0, b_0, and μ are calculated from the coefficients n_0, n_1, and n_4. It is significant that the constants μ and b_0 depend linearly on either of the source parameters b_1 and b_2 or, equivalently, on b_1 and k^2. When the parameters of temperature oscillations (the total oscillation amplitude, the initial and mean values) are specified, the oscillation frequency is determined from the formula

$$k^2 = 2\left(2b_1 n_4 - 3b_1 n_0 - \frac{\mu}{2}\right) + 2n_4(6b_1 n_0^2 + 2\mu n_0 + b_1 n_4^2) n_1^{-2}.$$

Note the following important relationship

$$a_0 + b_2 = A^1 k^2 + A^0 b_1, \quad A^1 > 0, \tag{17}$$

where the quantities A^0 and A^1 are calculated from the coefficients n_0, n_1, and n_4 (the corresponding formulas are not presented). Therefore, we obtain the inequality $d(a_0 + b_2)/d(k^2) > 0$. Consequently, the larger the parameter $b_2 > 0$ (i.e., the more pronounced the conditions providing the acceleration of the phase boundary), the higher the circular frequency squared. According to expression (6), we have $b_2 \sim a_2 \sim l_0^{-3}$. Therefore, the periodicity of propagation of the explosive-crystallization front depends substantially on the concentration of crystal nuclei.

RESULTS AND DISCUSSION

For the problems under consideration, the necessary conditions for the formation of a spatial and temporal periodicity of the temperature field are (1) the wave mechanism of heat transfer and (2) the presence of two energy sources corresponding to two different isotherms. These sources are competing in problem **I** associated with metal crystallization in the mold and have the same sign in problem **II** concerning explosive crystallization of amorphous films.

For definiteness, we assume that $l_0 = (g_1 + g_2)/2$ in problem **II**. Then, we find that the total oscillation amplitude is directly proportional to the circular frequency squared: $(g_2 - g_1) \sim k^2/b_1$, where, according to relationship (17), $k^2 \sim b_2 \sim l_0^{-3}$. There is a finite range of values l_0 such that a decrease in the minimum distance l_0 between frozen-in crystal nuclei leads to a decrease in the period of temperature oscillations and an increase in their total amplitude. Periodic stops of the isotherm $T = T_c$ suggest drastic changes in the velocity of the crystallization phase boundary (Fig. 2). Let us study the specific features of solutions in the following cases: (1) a two-dimensional self-similar process and (2) a supersonic mode ($M^2 > 1$) of the field evolution. Equation (7) is written in the canonical form

$$\frac{\partial^2 T}{\partial \xi^2} - \frac{\partial^2 T}{\partial \zeta^2} = \frac{(a^2 - w^2)k_v}{w^2(w^2 - a^2 - b^2)} \equiv k_v^1, \tag{18}$$

$$\xi = \beta - k_1 \alpha, \quad \zeta = -k_3 \alpha,$$

$$k_1 = ab/(a^2 - w^2), \quad k_3 = w(a^2 + b^2 - w^2)^{1/2}/(a^2 - w^2).$$

By convention, the direction along the OX axis will be referred to as the principal direction in the two-dimensional problem. If the process in the principal direction is supersonic ($a^2 > w^2$), we have the hyperbolic equation (18), in which the sign of the energy source $k_v^{(1)}$ is opposite to the sign of the energy source k_v irrespective of the value of b. In this supersonic process, the energy source reverses sign. When the velocity in the principal direction is subsonic but the process, on the whole, is hyperbolic, i.e.,

$$a^2 < w^2 < a^2 + b^2, \tag{19}$$

the sign inversion is absent. Equation (18) is analyzed using the solution in the form of relationships (13)–(15). The necessary replacements are obvious: $x \longleftrightarrow \zeta$, $t \longleftrightarrow \xi$, and $k_v \longleftrightarrow k_v^{(1)}$.

In this case, the main variant corresponds to conditions (19), i.e., to the supersonic process without inversion. It turns out that the data obtained in Section **3** on the oscillation of the phase boundary velocity in time can be generalized to the two-dimensional self-similar problem. For the isotherm $T_i = T(\alpha, \beta_i(\alpha)) = \text{const}$ [$\beta = \beta_i(\alpha)$], the condition for the stop of the phase boundary $N_i = 0$ is described by the equation

$$G(g) = a_*^2 F(f), \quad a_*^2 = a^2(a^2 + b^2 - w^2)/(b^2 w^2) < 1; \tag{20}$$
$$E(T_i) = f(\zeta) + g(\xi), \quad f \in [f_0, f_1), \quad g \in [g_1, g_2].$$

Here, $f(\zeta)$ is a monotonic function. To each value of f there corresponds the sole value of g at which Eq. (20) is satisfied. Since the function $g(\xi)$ is periodic in the argument $\xi = y - k_1 x + t(b - ak_1)$, the isotherm $y_i + bt = \beta_i(x + at)$ is characterized by the velocity N_i periodic in

the argument $x + at$. Consequently, at each fixed coordinate x, the velocity N_i vanishes periodically (it is this result that was obtained in solving the one-dimensional problem). Moreover, at each instant of time t, the isotherm $T = T_i$ involves points $[x, y_i(x, t)]$ at which the isotherm velocity is equal to zero. These stationary points are arranged periodically in the coordinate x. This arrangement has a pronounced two-dimensional character. The substantial spatial and temporal temperature inhomogeneities obtained are periodic and responsible for the formation of lobed and scaly structures in films. Note also that the studied classes of solutions to problem **II** with the use of Eqs. (18) and (8) indicate the physical impossibility of explosive crystallization for two self-similar variants, namely, in the cases of (1) a supersonic process ($M^2 > 1$) with inversion of the source sign and (2) a subsonic evolution of the temperature field. For a more general class of solutions, this question remains open.

Now, we examine the "metal melt–mold" thermal system in a supersonic mode. The one-dimensional and self-similar two-dimensional solutions do not contain fundamental quantitative differences. In the one-dimensional case, the analysis of the class of solutions (13)–(15) to the hyperbolic equation (2) demonstrates that, at $b_1 > 0$ and $b_2 < 0$, there are no processes periodic in time t. The function $E(x, t) = f(x) + g(t)$ is periodic in the coordinate x and relaxes with time from the initial state $E(x, 0)$ to the state $E_\infty(x)$ at $t \longrightarrow \infty$. In the relaxed state, the highest achievable temperature decreases with an increase in the parameter $(-b_2)$, which characterizes energy transfer to the mold wall.

Let us consider the two-dimensional variants. (1) In the supersonic case with inversion of the sign of the energy source k_v, there is a process periodic in the argument ξ, i.e., along the line whose slope relative to the principal direction is equal to k_1, and the solution relaxes with respect to the argument ζ. (2) When the inversion is absent [see conditions (19)], the process is periodic in the argument ζ, i.e., along the principal subsonic direction, and the solution relaxes with respect to the argument ξ. The distinctive feature of these supersonic processes is that the isotherms are open in the (x, y) plane. These results and also two variants of isotherm chains in Fig. 1 are in qualitative agreement with the experimental data obtained in [12]. In [12], the authors investigated the arrangement of pores and the presence of other defects in profiled sapphire crystals as a function of growth conditions. It was revealed that a molybdenum crucible used for growing crystals affects the growth process and that the crystal structure involves periodically arranged chains composed of individual small-sized pores. It is significant that chains are aligned parallel, perpendicular, or at an angle to the growth direction with a specific period [12, p. 1493]. In the subsonic case, a staggered arrangement of isotherm chains (Fig. 1) is governed by the competition of the energy sources. This effect has two hydrodynamic analogues, such as (1) a two-dimensional vortex flow of an ideal fluid [6] and (2) a two-dimensional periodic flow of a viscous fluid due to the spatial periodic force in a finite-sized channel [13].

CONCLUSIONS

The wave heat transfer in a "medium–two nonlinear energy sources" system is responsible for the formation of a spatial and temporal periodicity during crystallization. The nonlinear dynamic properties of the process depend substantially on whether the evolution of the temperature field occurs in a subsonic or supersonic mode.

REFERENCES

1. A. S. Él'darkhanov, *Processes of Crystallization in the Field of Elastic Waves* (Metallurgiya, Moscow, 1996) [in Russian].
2. L. N. Aleksandrov, *Kinetics of Crystallization and Recrystallization of Semiconductors Films* (Nauka, Novosibirsk, 1985) [in Russian].
3. Yu. T. Glazunov, Inzh.-Fiz. Zh. **40** (1), 134 (1981).
4. N. I. Yavorskiĭ, Izv. Akad. Nauk SSSR, Mekh. Zhidk. Gasa, No. 3, 3 (1986).
5. N. I. Nikitenko, Inzh.-Fiz. Zh. **73** (4), 851 (2000).
6. O. V. Kaptsov, Prikl. Mekh. Tekh. Fiz., No. 1, 109 (1989).
7. N. M. Bogdanov, V. P. Koverda, V. N. Skokov, *et al.*, Dokl. Akad. Nauk SSSR **293** (3), 595 (1987) [Sov. Phys. Dokl. **32** (3), 221 (1987)].
8. V. P. Koverda, Zh. Tekh. Fiz. **64** (3), 62 (1994) [Tech. Phys. **39** (3), 255 (1994)].
9. O. N. Shablovskiĭ, *Relaxation Heat Transfer in Nonlinear Media* (Gomel. Gos. Tekh. Univ., Gomel, 2003) [in Russian].
10. B. A. Malomed and M. I. Tribel'skiĭ, Dokl. Akad. Nauk SSSR **275** (6), 1363 (1984) [Sov. Phys. Dokl. **29** (4), 294 (1984)].
11. A. D. Bryuno, *Local Method of Nonlinear Analysis of Differential Equations* (Nauka, Moscow, 1979) [in Russian].
12. G. A. Satunkin, V. A. Tatarchenko, E. M. Tseĭtlin, and T. N. Yalovets, Izv. Akad. Nauk SSSR, Ser. Fiz. **40** (7), 1492 (1976).
13. E. B. Gledzer, F. V. Dolzhanskiĭ, and A. M. Obukhov, *Hydrodynamic Systems and Their Applications* (Nauka, Moscow, 1981) [in Russian].

Translated by O. Borovik-Romanova

Crystallography Reports, Vol. 50, Suppl. 1, 2005, pp. S68–S73.

CRYSTAL GROWTH

Concept of Specific Supersaturation (Specific Supercooling) and Practical Aspects of Its Application

B. G. Ivanov

Federal State Unitary Enterprise "Vavilov State Optical Institute, All-Russia Research Center," Birzhevaya liniya 12, St. Petersburg, 199034 Russia

e-mail: bimgvfa@hotmail.ru

Received February 3, 2005

Abstract—It is demonstrated that the normal growth rate of crystals from solutions and melts depends on the area of the crystallization front. New growth parameters, namely, the specific supersaturation and the specific supercooling, are introduced, and the quantitative dependence of the normal growth rate on these parameters is determined. It is noted that the normal growth rate affects the formation of defects. The criteria and the range of the possible use of the specific supersaturation (specific supercooling) for optimizing the conditions of crystal growth from solutions and melts are revealed. © *2005 Pleiades Publishing, Inc.*

INTRODUCTION

The regularities of the formation (ontogeny) of crystals, including the formation of particular growth defects, in a broad sense, are the only reliable criterion for evaluating both growth conditions and qualitative characteristics of the crystals. The internal structure of crystals is formed as a result of a combined effect of many growth conditions. However, eventually, the specific features of the crystal formation are directly related to the normal growth rate A, i.e., the rate of crystal growth in the direction perpendicular to the crystallization front [1].

CONCEPT OF SPECIFIC SUPERSATURATION (SPECIFIC SUPERCOOLING)

Investigation into the factors responsible for the normal growth rates is one of the basic problems of the crystallization kinetics. It is universally accepted that the dependence of the normal growth rate on the supersaturation (for solutions) or the supercooling (for melts) without regard for other factors is described by the power function

$$\partial R/\partial t \approx \Delta C^n. \quad (1)$$

Here, R is the radius or another characteristic crystal size, t is the time, ΔC is the supersaturation, and the exponent n varies from 1 to 3. At $n = 1$, this dependence exhibits an almost linear behavior [2–5]. However, even in special experiments, similar dependences have been evaluated accurate to within an order of magnitude and could be used only for analyzing qualitative tendencies in processes. These estimates are quite insufficient for revealing quantitative regularities and cannot be applied to any calculations of conditions for practical growth methods. In our opinion, this situation is associated with a number of crucial circumstances. Although the notions of the supersaturation and supercooling are well known and have a clear physical meaning, the problem associated with the establishment of the dependence of the normal growth rate on the supersaturation and supercooling lies in the inadequate use of these notions.

On the one hand, the above dependence of the normal growth rate should hold only for supersaturations or supercoolings that occur directly at the crystallization front and are true driving forces (energy potentials) of crystallization. However, these quantities in general are not constant both on a macroscale (for example, within the same face in the case of faceted growth) and on a microscale. Moreover, the measurement of these quantities in the vicinity of the crystallization front or their calculation from indirect data involve considerable difficulties or are impossible at all for real crystal growth processes.

On the other hand, real crystals of specific types, sizes, and masses grow in particular growth media (zones of growth) with spatiotemporal boundaries. As a rule, the supersaturations or supercoolings are specified or estimated for these particular growth media and specific time intervals. It is these quantities (in this sense) that are used in reference to the definitions of the type "supersaturation in a solution" or "supercooling in a melt" in view of their quantitative meaning. These quantities have real values only in the absence of growth processes in specific media. During the crystal growth, a combined effect of convection and diffusion processes and kinetic factors of growth leads to the for-

1063-7745/05/5001-S0068$26.00

mation of temperature–concentration fields of complex configurations with different gradients of concentrations for solutions or temperatures for melts in growth media. The supersaturations (supercoolings) at the crystallization front are intermediate between the supersaturation (supercooling) in the growth medium and the equilibrium concentration (melting temperature) [5].

It is evident that the supersaturation (supercooling) at the crystallization front and in the growth medium differs radically. However, the dependence of the normal growth rate on the supersaturation (supercooling) [see relationship (1)] is very frequently considered without regard for the above differences. Since these quantities have a particular effect on the normal growth rate, they are used for approximate calculations and then the normal growth rate is optimized in an experimental way (as a rule, for a long time) for specific conditions. It is believed that other factors that govern specific features of the internal structure of crystals and their qualitative characteristics, such as the sizes and (or) the number of growing crystals, etc., are of secondary importance and can be ignored in the majority of cases.

The necessity of preparing high-quality crystals with maximum sizes determines the tendency to the growth of a small number of crystals (in the limit, one crystal) from a growth medium. It is a widespread belief (associated with the practice of growth of large single crystals) that the smaller the number of crystals, the higher the crystal quality, all other factors being the same [6, 7]. The practice of large-scale growth of crystals from solutions demonstrates that, under identical growth conditions, in particular, at constant supersaturations in growth media, the quality of crystals grown in the case of a small number of large-sized crystals appears to be substantially worse than the quality of crystals grown in the case of a large number of small-sized crystals. Investigations into regularities of the formation of mother-solution inclusions as an indicator of normal growth rate during the growth of yttrium aluminum garnet crystals from solutions in melts showed that there is a one-to-one correspondence between the formation of these inclusions and the normal growth rate: the larger the number (the higher the quality) of growing crystals, the lower the normal growth rate, and vice versa [8].

Analysis of the mass transfer balance equation for crystallization from solutions in specific growth media shows that the normal growth rate, which is the first derivative of the radial crystal size R with respect to the time t ($A = \partial R/\partial t$, cm/s), depends not only on the supersaturation and can be represented by the relationship

$$\begin{aligned}\partial R/\partial t &= -0.01M(\partial C/\partial T)(\partial T/\partial t)/3NR^2\rho k \\ &= -0.01C'(t)M/3NR^2\rho k \\ &= -(0.01M/3k\rho)[C'(t)/NR^2].\end{aligned} \quad (2)$$

Here, M is the mass (g) of the growth medium, C is the solubility (wt %) of the crystallized material, N is the number of growing crystals, k is the coefficient determined by the crystal shape, ρ is the crystal density (g/cm^3), and T is the solution temperature (K).

According to relationship (2), the normal growth rate depends on two independent variables; i.e., it is proportional to the rate of change in the mass of the crystallized material in the solution {this rate determines the supersaturation [at $n = 1$ in expression (1), A is directly proportional to the saturation] and inversely proportional to the product NR^2. The product NR^2 is proportional to the crystallization front area, and, hence, the normal growth rate is inversely proportional to this area. At a constant supersaturation in the growth medium, the normal growth rate is not constant in the course of growth, as should follow from expression (1). Depending on the variation in the crystallization front area, the normal growth rate regularly and often substantially varies, in particular, with a change in the number of growing crystals (Fig. 1). The factors N and R^2 are functions of the number of growing crystals to different powers: the larger the number of growing crystals N, the larger the crystallization front area for crystals with identical masses, the lower the normal growth rate, and the higher the crystal quality. These regularities are consistent with the aforementioned experimental data [8].

The dependence of the normal growth rate on the crystallization front area is affected not only by the number of growing crystals but also by other characteristics of crystal growth, such as crystal size, the presence of shapers, etc. Therefore, it is necessary to allow for any change in the crystallization front area, including the case of growth of individual crystals. In the general case, upon change in both independent variables, namely, supersaturation in the growth medium and the crystallization front area, the effect of the latter quantity, as a rule, is considerably stronger than that of the former quantity. This is additional evidence for the necessity of accounting for the crystallization front area.

The analysis of the growth of yttrium aluminum garnet, corundum, and fluoride crystals by the melt methods demonstrates that similar regularities are observed in the course of crystal growth from melts. For the most part, the methods for growing crystals from melts have been developed for the preparation of individual single crystals. Crystals grow when the crystallization isotherm moves in the growth medium due to the supercooling provided by removal of the thermal energy from the crystallization front. The normal growth rate in these methods is two or three orders of magnitude higher than that in methods for growing crystals from solutions. The shape of the crystallization front is governed by the shape of the crystallization isotherm with

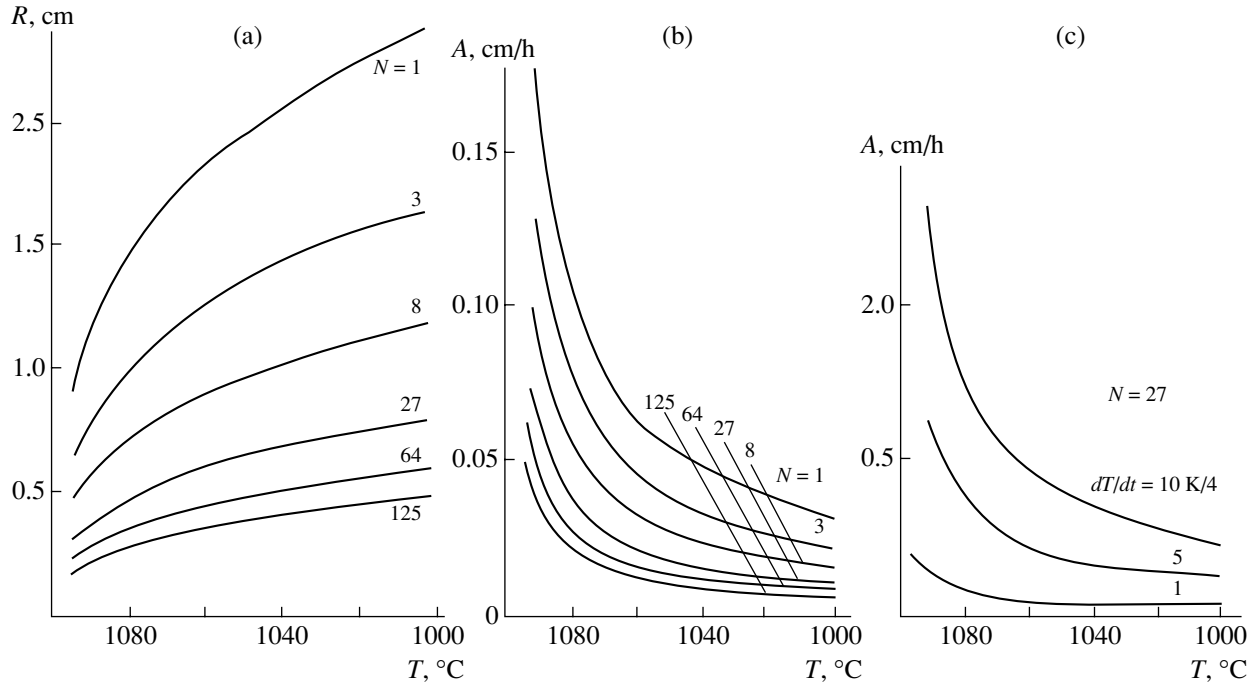

Fig. 1. Temperature dependences of (a) the crystal size R at different numbers N of growing crystals and (b, c) the normal growth rate A under different conditions of growth of yttrium aluminum garnet crystals from the solution in the melt for (b) dT/dt = 5 K/h and different values of N [8] and (c) N = 27 and different values of dT/dt.

allowance made for temperature gradients in different front regions.

The assumption that the volume of the crystallized material is proportional to the change in the power delivered to the growth medium $\Delta W = K\Delta V$ (where W is the power, V is the crystal volume, K is the proportionality factor) is valid virtually for all melt methods [9]. Then, the normal growth rate can be written in the form

$$\partial h/\partial t = (\partial W/\partial t)/KS(h), \qquad (3)$$

where h is the change in the crystal size in the growth direction perpendicular to the crystallization front (along the growth axis) or, in the general case, in the direction of removal of the thermal energy from the crystallization front; t is the time; and $S(h)$ is the change in the crystallization front area. Since the change in the quantity $\partial W/\partial t$ corresponds to the conditions of supercooling in the growth medium, the normal growth rate during the growth from melts, like during the growth from solutions, is also determined by two independent parameters: the normal growth rate is proportional to the rate of change in the supercooling of the growth medium and inversely proportional to the crystallization front area. Consequently, the normal growth rate in the case of growth from melts should be estimated with due regard for the crystallization front area and its change. However, there are radical differences between the estimations of the normal growth rates in the methods for growing from solutions and melts. In the melt methods, the thermal energy is predominantly removed from the growth medium in a particular direction. In this case, the important aspect of the estimation of the normal growth rate is the inclusion not only the area but also the shape (curvature) of the crystallization front. The front curvature determines the angle between the vector of the temperature gradient governing the direction of the isotherm motion in each specific region (point) of the crystallization front and the heat removal direction (growth axis) according to the cosine law $V_\alpha = V_{vert}\cos\alpha$ (Fig. 2) [9]. As follows from this law, the normal growth rate varies along the crystallization front surface from the maximum rate at the growth axis (the dominant heat removal direction) to the rate close to zero at the lateral surface of the crystal. Different normal growth rates are observed at the crystallization front depending on defect and impurity distributions, morphology, etc. In particular, it is characteristic that defects are primarily formed in central crystal regions along the growth axis, i.e., in regions with maximum normal growth rates.

In different methods for growing crystals from melts, their specific features and efficiency can depend on the shape and curvature of the crystallization front. It is believed that, except for special cases, a planar crystallization front is most optimum for a number of important applications of crystals, such as doping, etc. However, the area of the planar crystallization front is minimal compared to those of any other shapes. The planar crystallization front is characterized by the max-

imum normal growth rates, which lead to an increase in the probability of forming particular growth defects. Therefore, the small area of the crystallization front is not optimum in many methods used, for example, for growing fluoride and corundum crystals.

The variation in the normal growth rates (described by the cosine law) at the crystallization front in melt methods substantially affects the morphological features of crystals, in particular, specific features of faceted growth [10]. Crystals grow from melts via the atomically rough mechanism with the formation of curved (irrational) surfaces that involve an insignificant number of faceted regions at the crystallization front (face effect). Evaluation of the morphological significance of different faceted forms indicates that the type of faceted forms grown on the crystal surface depends on the normal growth rate. In yttrium aluminum garnet crystals, the {211} faces are formed in central regions of the crystallization front at maximum normal growth rates, whereas the {110} faces occur at lower normal growth rates in regions closer to the lateral surface and at its boundary. Therefore, faceted forms of an yttrium aluminum garnet habit change regularly with variation in the normal growth rate. More than ten faceted forms of the *F* and *S* types can be observed on the lateral surfaces of yttrium aluminum garnet crystals at normal growth rates close to zero. In corundum crystals grown by the method devised at the State Optical Institute (St. Petersburg, Russia), no faces occur at the crystallization front, but the lateral surface contains large (0001) faces. It is known that the (0001) face is characterized by an extremely high morphological stability and these crystals do not grow hardly at all along the [0001] direction. However, this face is formed at $A \approx 0$. It should be noted that the genesis of faces on the lateral surface of crystals exhibits specific features. The faces are formed via tangential growth along the line of contact between the melt mirror and the crystal, and the crystal does not grow in the direction perpendicular to the face surface. Consequently, growth pyramids are absent. However, analysis of this genesis confirms the inference that the morphological stability of faces depends on the normal growth rate.

Therefore, the aforementioned regularities theoretically revealed from relationships (2) and (3) suggest that the normal growth rate depends on the crystallization front area. The analysis of the supersaturation or supercooling of growth media (zones of growth) shows that the normal growth rate depends on two independent parameters for any growth mechanism (growth method) of crystals. Despite qualitative differences, the dependence of the normal growth rate eventually leads to identical results, which are confirmed by observations of crystal growth from solutions and melts. Investigations into the specific features of the growth of yttrium aluminum garnet crystals from solutions in melts [8] and special model experiments on the growth of alum from aqueous solutions made it possible to combine these parameters by introducing a qualitatively new parameter, namely, the specific supersaturation defined as the supersaturation of a growth medium according to growth conditions per unit area of the crystallization front [8]. Since similar dependences are observed for the melt methods, it is possible to introduce a new growth parameter, i.e., the specific supercooling defined as the supercooling of a growth medium per unit area of the crystallization front. Then, from relationships (2) and (3), we obtain an important dependence: the normal growth rate of crystals is directly proportional to the specific supersaturation (specific supercooling), all other growth factors being the same.

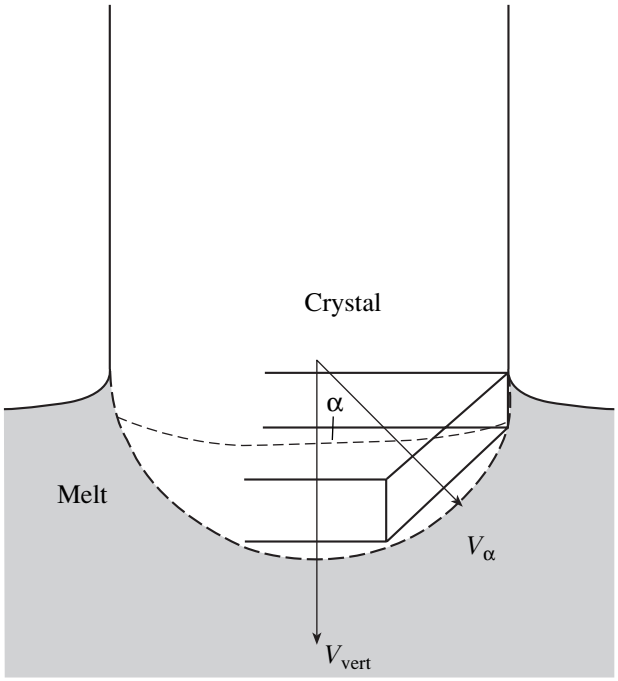

Fig. 2. Schematic diagram illustrating the cosine law. $V_\alpha = V_{vert}/\cos\alpha$ [9].

The introduced parameters and the corresponding dependences suggest the necessity and importance of the inclusion of the geometric factor, i.e., the crystallization front area and its change over the course of crystal growth. It is known that, in practice, the supersaturation (supercooling) for the vast majority of grown crystals varies insignificantly in the growth medium and is often maintained at a constant level. The change in the crystallization front area in the general case is considerably larger than that of the supersaturation (supercooling) and depends on specific growth conditions. When the solubility as a function of the temperature (or the cooling rate as a function of the delivered power) and the shape of grown crystals are known, the above dependences can be calculated with a high accuracy.

In essence, the proposed growth parameters and the obtained dependences are statistical and disregard all numerous real features of crystal formation, such as the growth rate anisotropy; fluctuations of crystal, temperature gradient, concentration, and impurity distributions; convection in growth media; interaction of diffusion and kinetic growth factors; etc. However, these parameters appear to be convenient and have definite physical meaning, because they enable one to perform direct quantitative estimations of real phenomena and growth of natural and synthetic crystals, such as dendritic and faceted growth, defect formation, morphological features, etc. The main criteria for the use of the specific supersaturation and the specific supercooling are the possibility of determining the normal growth rates when analyzing the growth of specific crystals in different growth media. Despite their averaged and statistical character, the specific supersaturation and the specific supercooling permit one to reliably reveal the quantitative criteria for the conditions necessary for manifestation of specific qualitative characteristics of crystals with the use of the dependences of the normal growth rate on these parameters by estimating the limiting normal growth rates of the formation of particular growth defects. Therefore, these parameters can and should find practical application in calculating optimum growth conditions for different methods (from the crystal growth from aqueous solutions to high-temperature variants of the Czochralski, Stockbarger, Schtober, Kyropoulos, and other methods that are used for growing crystals from melts).

The optimization of the conditions of the crystal growth from cooled solutions, as a rule, requires experimental correction, because the main criterion for the evaluation of the conditions is the formation of defects determining the crystal quality. Therefore, the growth conditions should be calculated by determining the limiting conditions of the defect formation, whose main characteristics are represented by the normal growth rate and its dependence on the specific supersaturation [8], with the inclusion of other important factors, for example, the diffusion control [11].

The cooling rate of the growth medium at different stages of the process depends on a number of factors. The main factors are the change in the crystallization front of crystals and the retardation of transfer with a decrease in the temperature. At the initial stages when the crystal (seed) sizes are small, the solution should be cooled at minimum rates, even though the permissible normal growth rates are highest. With an increase in the crystallization front area, which leads a decrease in the permissible normal growth rates, it is possible to increase the cooling rate. Subsequently, the rate of increase in the crystallization front area is retarded, this increase does not compensate for the decrease in the permissible normal growth rates, and it is necessary to decrease the cooling rate of the solution.

In the case of crystal growth from melts, the growth conditions providing the normal growth rates at which high-quality crystals are grown can be optimized using simple mathematical models that adequately describe the processes responsible for the formation of stable temperature fields in the growth zone [9]. The conditions under which the normal growth rate and the corresponding specific supercooling ensure the required crystal quality at each point of the crystallization front can be treated as optimum. The crystallization front area, which in the general case depends on the shapes of the crystallization front and crystals, can change considerably (decrease, increase) during the growth process and lead to a corresponding change in the specific supercooling and the normal growth rate. The optimum conditions should provide the maintenance of the optimum normal growth rate at a constant level or its decrease with due regard for impurities that retard the growth of crystals [9]. By assuming that the volume of the crystallized material is proportional to the power delivered to the growth medium and using relationship (3), the rate of change in the heater power can be represented in the form

$$\partial W/\partial t = KS(h)\partial h/\partial t. \quad (4)$$

Then, the growth conditions are calculated depending on the form of the function $S(h)$.

CONCLUSIONS

Thus, the problems associated with the fields of crystal growth investigations that are believed to have been thoroughly studied and universally accepted were analyzed in this work. Without pretending to the revision of the universally accepted concepts, the author called attention to a number of regularities that in his opinion deserve more consideration. New parameters, namely, the specific supersaturation and the specific supercooling, were introduced. The dependences of the normal growth rate on these parameters make it possible to gain a deeper insight into different aspects of real crystal growth processes, on the one hand, and can be used for evaluating the conditions of crystal formation and developing practical technological processes of crystal growth, on the other.

REFERENCES

1. Yu. K. Vorob'ev, *Regularities of the Growth and Evolution of Crystals of Minerals* (Nauka, Moscow, 1990) [in Russian].
2. A. A. Chernov, in *Modern Crystallography*, Vol. 3: *Crystal Growth*, Ed. by B. K. Vainshtein, A. A. Chernov, and L. A. Shuvalov (Nauka, Moscow, 1980; Springer, Berlin, 1984).

3. T. G. Petrov, E. B. Treivus, and A. P. Kasatkin, *Growing Crystals from Solution* (Nedra, Leningrad, 1967; Consultants Bureau, New York, 1969).
4. E. B. Treĭvus, *Kinetics of Growth and Dissolution of Crystals* (Leningr. Gos. Univ., Leningrad, 1979) [in Russian].
5. R. F. Strickland-Constable, *Kinetics and Mechanism of Crystallization* (Academic, London, 1968).
6. B. Ya. Lyubov, *Theory of Crystallization in Large Volumes* (Nauka, Moscow, 1975) [in Russian].
7. E. V. Khamskii, *Crystallization from Solutions* (Nauka, Leningrad, 1967; Consultants Bureau, New York, 1969).
8. B. G. Ivanov, Zap. Leningr. Gorn. Inst. im. G. V. Plekhanova **LXXIV** (2), 104 (1977).
9. B. G. Ivanov, V. N. Nikolaev, A. Turkbaev, and Yu. P. Gudkov, in *Advanced Materials and Technologies* (GUP TsNII KM Prometeĭ, St. Petersburg, 1999), p. 105 [in Russian].
10. B. G. Ivanov and A. Turkbaev, in *Problems of Materials Science* (GUP TsNII KM Prometeĭ, St. Petersburg, 1999), p. 81 [in Russian].
11. B. G. Ivanov, Tr. Gos. Opt. Inst. **54** (188), 45 (1983).

Translated by O. Borovik-Romanova

Crystallography Reports, Vol. 50, Suppl. 1, 2005, pp. S74–S77.

CRYSTAL GROWTH

Model Calculation of Experimentally Observed Eutectic Structures

A. P. Gus'kov and A. D. Orlov

Institute of Solid State Physics, Russian Academy of Sciences, Chernogolovka, Moscow oblast, 142432 Russia

e-mail: guskov@issp.ac.ru

Received February 3, 2005

Abstract—A model of directed crystallization is developed that considers the stability of the phase boundary to periodic (temporal and spatial) temperature and concentration perturbations. In the case of instability, i.e., increase in the amplitude of perturbations with time, the dependence of the eutectic structure period on the crystallization rate is determined from the model. A possible shape of the crystallization front and the structure of the solid phase formed are considered qualitatively. The corresponding model calculation of experimentally observed eutectic structures is presented. © *2005 Pleiades Publishing, Inc.*

INTRODUCTION

Most modern studies devoted to the directed crystallization of eutectic alloys are based on the classical study of Jackson and Hunt [1]. For example, Ginibre *et al.* [2] compared their experimental data on eutectic structures with the calculations [3, 4]. In these studies, the Jackson–Hunt theory was used to analyze the reasons for the formation of eutectic structures of different types.

In [5, 6], eutectic structures of different types were obtained by the superposition of periodic temporal oscillations on the three-phase equilibrium point. The Jackson–Hunt theory was used to relate the crystallization rate, the structure period, and the temporal oscillation frequency. The calculation of experimentally observed structures in [7] is based on the phase field theory [8]. In this case, comparison with the theory [1] was also performed and the structures experimentally observed in [2, 3] were simulated.

In this study, using the solutions derived in [9], we calculated the type of structure that was experimentally obtained in [2]. The model of directed crystallization was developed in [9] on the basis of the perturbation theory. The problem considers the stability of the phase boundary to periodic (temporal and spatial) perturbations of temperature and concentration. Transformation of the solutions obtained in [9] from a curvilinear to a rectangular coordinate system makes it possible to use these solutions for model calculation of the crystallization front shape and the structure of the solid phase formed.

THEORETICAL ANALYSIS

Solutions for the temperature and concentration distributions in the liquid phase and the temperature distribution in the solid phase were found in [9]. Within the proposed theory of directed crystallization, a dispersion equation was obtained by joint solution of the diffusion and heat-conduction equations for small perturbations. Numerical analysis of the dispersion equation made it possible to find the expression for the period of temperature and concentration perturbations corresponding to the maximum growth increment. The calculated and experimental dependences of the structure period on the crystallization rate were compared in [9]. In this study, we attempted to simulate numerically not only the period of the structure but also its shape, i.e., the structure of eutectic fibers formed during the directed crystallization, taking into account both spatial and temporal perturbation frequencies.

Furthermore, we carry out calculations on the basis of the solutions to the directed crystallization problem found in [9].

Schematically, the complex solutions in a curvilinear coordinate system have the form [9]

$$T(z, y, \tau) = T_S(z) + T_m(z) + \exp(Ky + \omega\tau), \quad (1)$$

$$C(z, y, \tau) = C_S(z) + C_m(z)\exp(Ky + \omega\tau), \quad (2)$$

where $K = K_1 + iK_2$, $\omega = \omega_1 + i\omega_2$, and $T_m(z)$ and $C_m(z)$ are complex quantities. $T_S(z)$ and $C_S(z)$ form a solution to the steady-state problem and $T_m(z)$ and $C_m(z)$ form a solution to the problem of small perturbations.

To obtain the actual distribution pattern, we will separate the real part of the solution and transform the solutions from the curvilinear to the rectangular coordinate system. Then, we record all quantities in the real form. After these transformations, the solution to the heat-conduction equation has the form (bars denote the rectangular coordinate system at rest and caps denote

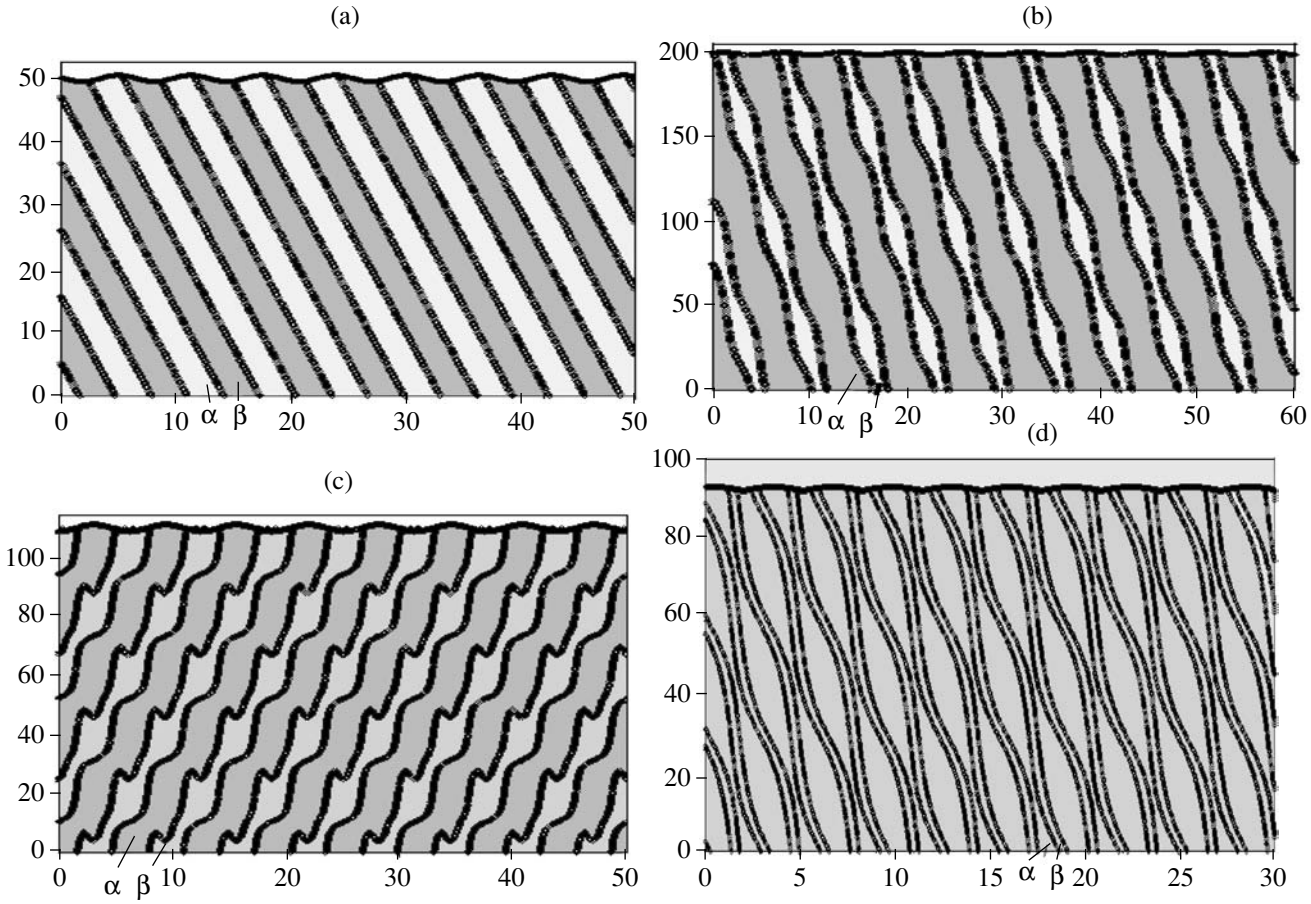

Fig. 1. Calculated eutectic structures obtained for different values of the calculation parameters: distributions of the component concentration at the crystallization front and the crystallization front shape.

the moving rectangular coordinate system)

$$\bar{T}(\hat{z}, \bar{y}, \bar{\tau}) = T(\hat{z})_S + T(\hat{z})_{m1} - \left(\frac{\partial T(\hat{z})_S}{\partial z} + \frac{\partial T(\hat{z})_{m1}}{\partial z}\right)\hat{z}_b, \quad (3)$$

where

$$T(\hat{z})_{m1} = b_T \exp(K_1 y + \omega_1 \tau + a_T z) \times \cos(\rho_T + a_T^i \hat{z} + K_2 y + \omega_2 \tau).$$

The solution to the diffusion equation has the form

$$\bar{C}(\hat{z}, \bar{y}, \bar{\tau}) = C(\hat{z})_S + C(\hat{z})_{m1} - \left(\frac{\partial C(\hat{z})_S}{\partial z} + \frac{\partial C(\hat{z})_{m1}}{\partial z}\right)\hat{z}_b, \quad (4)$$

where

$$C(\hat{z})_{m1} = b_C \exp(K_1 y + \omega_1 \tau + a_C z) \times \cos(\rho_C + a_C^i \hat{z} + K_2 y + \omega_2 \tau).$$

Here, ρ_T, ρ_C, a_T, a_C, a_T^i, a_C^i, b_T, and b_C are the coefficients found from the solutions to the problem. The small quantity $\hat{z}_b$ characterizes the crystallization front shape and is found from the implicit equation

$$\hat{z}_b = \frac{f(\hat{z}_b, \bar{y}, \bar{\tau})}{1 + \xi}. \quad (5)$$

Here,

$$\xi = \left.\frac{\partial f(\hat{z}_b, \bar{y}, \bar{\tau})}{\partial \hat{z}}\right|_{z = \hat{z}_b}, \quad (6)$$

$$\sum_1^5 U_n \exp(S_n \hat{z}_b + K_1 y + \omega_1 \tau) \times \cos(W_n \hat{z}_b + L_n + K_2 y + \omega_2 \tau) = f(\hat{z}_b, \bar{y}, \bar{\tau}). \quad (7)$$

The quantities U_n, S_n, W_n, and L_n are constants. The function $f(\hat{z}_b, \bar{y}, \bar{\tau})$ is in essence a linear combination of the solutions to the heat-conduction and diffusion equations. Solution (4) is summed with the same solution containing the negative wave number (a similar procedure is also carried out with solution (3)). This operation is permissible because $K = K_1 + iK_2$ enters the equations of the directed crystallization problem only

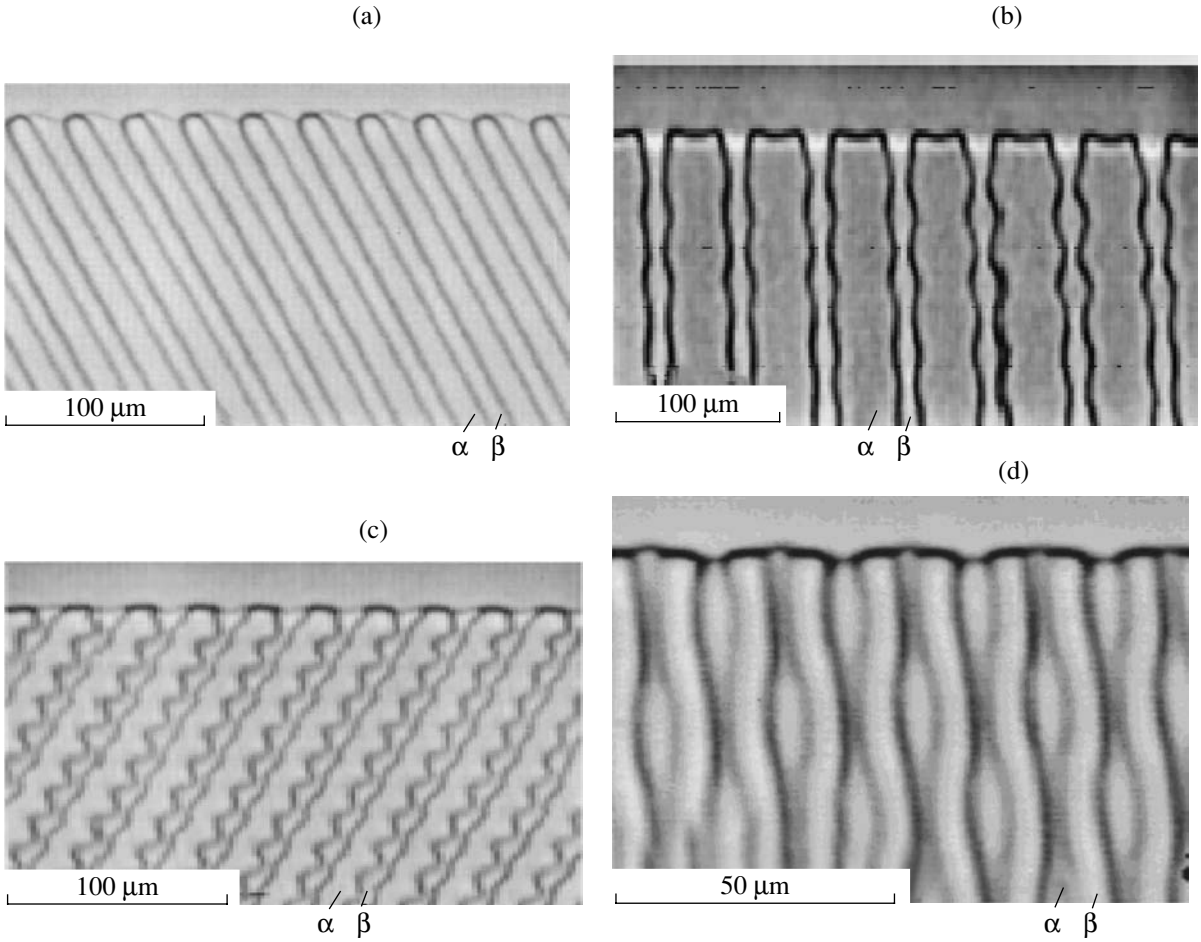

Fig. 2. Experimentally observed structures corresponding to the calculated structures in Fig. 1.

in the quadratic form. Solution (4) is valid for both positive and negative K_2; the sum of the solutions is also a solution to the problem. As a result, we have the solution in the form

$$\begin{aligned}\bar{C}(\hat{z}, \bar{y}, \bar{\tau}) &= C(\hat{z}_b)_S + \left.\frac{\partial C(\hat{z})_S}{\partial z}\right|_{z = z_b} \hat{z}_b \\ &+ h_1\left[C(\hat{z}_b)_{m1} - \left.\frac{\partial C(\hat{z})_{m1}}{\partial z}\right|_{z = z_b} \hat{z}_b\right] \\ &+ h_2\left[C(\hat{z}_b)_{m1} - \left.\frac{\partial C(\hat{z})_{m1}}{\partial z}\right|_{z = z_b} \hat{z}_b\right].\end{aligned} \quad (8)$$

Here, h_1 and h_2 are arbitrary constants. The terms in the first and second square brackets are the solutions with positive and negative values of K_2, respectively. Expression (8) makes it possible to calculate the concentration at the boundary and thus to determine a possible structure of the solid phase. The term $\hat{z}_b$ in expression (8) has the form

$$\hat{z}_b = \frac{h_1 \bar{f}^+}{1 + h_1 \xi^+} + \frac{h_2 \bar{f}^-}{1 + h_2 \xi^-}, \quad (9)$$

$\bar{f}^+$ and ξ^+ are described by Eqs. (6) and (7), respectively, with positive K_2, and $\bar{f}^-$ and ξ^- are described by the same equations but with negative K_2.

We should note the following. (i) Since we consider the problem to be infinite in the y direction, we obtain for large values of y ($y \longrightarrow \infty$) at any K_1 an infinitely large amplitude in solutions (3) and (4). Therefore, on the basis of physical considerations (temperature and concentration cannot be infinitely large), we equate K_1 to zero. (ii) The value of the temporal frequency (growth increment) ω_1 allows us to determine whether the imposed perturbations will increase or decrease with time [10]. However, in the model calculations we assume that the perturbation amplitude is determined (or limited) by real physicochemical processes. Hence, we equate ω_1 to zero.

RESULTS AND DISCUSSION

On the basis of the correspondence with experiment for the dependence of the eutectic structure period (i.e., the wave number K_2) on the crystallization rate, found previously in [9, 11, 12], we assume that the frequen-

cies of temporal and spatial perturbations do not change during the transition from initial small perturbations to the developed steady-state process of eutectic crystallization. Expression (8), with due regard for (9), gives the model structures shown in Fig. 1. The corresponding experimental structures are shown in Fig. 2.

The structure in Fig. 1a was calculated with the following model parameters: $C(z_b) = 0.2\cos(y + 0.3\tau)$ is the distribution of the component concentration at the crystallization front and $z_b = 0.5\cos(y + 0.3\tau)$ is the calculated shape of the crystallization front. Figure 1b corresponds to the model equations

$$C(z_b) = \sin(z_b + y + 0.05\tau) + 0.3\sin(z_b - y + 0.05\tau),$$
$$z_b = -\cos(y + 0.05\tau) - 0.3\cos(y - 0.05\tau);$$

Fig. 1c corresponds to the equations

$$C(z_b) = -15\cos(z_b + y - 0.15\tau) - 9\cos(z_b - y - 0.15\tau),$$
$$z_b = 0.7\cos(y - 0.15\tau) + 0.42\cos(y + 0.15\tau);$$

and Fig. 1d corresponds to the equations

$$C(z_b) = |\exp(2z_b)\sin(y + 0.05\tau) + 0.1\exp(2z_b)\sin(-y + 0.05\tau)|,$$
$$z_b = |\cos(y + 0.05\tau) + 0.1\cos(-y + 0.05\tau)|$$

(the modulus in the latter expressions takes into account the change in the sign of the slope of the liquidus line when it passes through the area of eutectic concentration, on the assumption of the symmetric equilibrium diagram [11]).

CONCLUSIONS

We have shown that the solutions to the directed crystallization problem obtained here and previously [9–12] make it possible to model experimentally observed eutectic structures. In this context, we suggest that the reason for the formation of the structures under consideration, as well as the classical (normal) eutectic structures, is the instability of the phase boundary to temperature and concentration perturbations.

REFERENCES

1. K. A. Jackson and J. D. Hunt, Trans. Metall. Soc. AIME **236**, 1129 (1966).
2. M. Ginibre, S. Akamatsu, and G. Faivre, Phys. Rev. E **56**, 780 (1997).
3. A. Karma and A. Sarkissian, Metall. Mater. Trans. A **27A**, 635 (1996).
4. K. Kassner and C. Misbah, Phys. Rev. A **44**, 6533 (1991).
5. V. Datye and J. S. Langer, Phys. Rev. B **24**, 4155 (1981).
6. B. A. Wolfe Diesslin and W. T. Grayhack, Phys. Rev. B **50**, 9111 (1994).
7. S. G. Kim, W. T. Kim, T. Suzuki, *et al.*, J. Cryst. Growth **261**, 135 (2004).
8. I. Steinbach and F. Pezzola, Physica D (Amsterdam) **134**, 385 (1999).
9. A. P. Gus'kov, Zh. Tekh. Fiz. **73** (5), 46 (2003) [Tech. Phys. **48** (5), 569 (2003)].
10. A. P. Gus'kov, Izv. Ross. Akad. Nauk, Ser. Fiz. **63** (9), 1772 (1999).
11. A. P. Gus'kov and A. D. Orlov, Materialovedenie, No. 3, 150 (2004).
12. A. P. Gus'kov, Pis'ma Zh. Tekh. Fiz. **27** (11), 86 (2001) [Tech. Phys. Lett. **27** (6), 480 (2001)].

Translated by Yu. Sin'kov

Crystallography Reports, Vol. 50, Suppl. 1, 2005, pp. S78–S81.

CRYSTAL GROWTH

Non-Kossel Crystals: Calcium and Magnesium Oxalates

L. N. Rashkovich*, E. V. Petrova*, T. G. Chernevich*, O. A. Shustin*, and A. A. Chernov**

** Faculty of Physics, Moscow State University, Leninskie gory, Moscow, 119992 Russia*

e-mail: rashk@polly.phys.msu.ru

*** NASA, Huntsville, USA*

e-mail: alex.chernov@msfc.nasa.gov

Received February 7, 2005

Abstract—The rate of movement of elementary growth layers at faces of $CaC_2O_4 \cdot H_2O$ and $MgC_2O_4 \cdot 2H_2O$ crystals is measured in situ by atomic force microscopy under kinetic growth conditions at a constant supersaturation with a varying excess of cations or anions in the solution. It is shown that, as the deviation of the $Ca^{2+}/C_2O_4^{2-}$ (or $Mg^{2+}/C_2O_4^{2-}$) ratio from unity increases, the rate of movement of the growth layers decreases abruptly and nonlinearly. A model describing this effect is discussed. © *2005 Pleiades Publishing, Inc.*

INTRODUCTION

This paper describes a model of growth of a crystal built up of particles *A* and *B* (building units) formed upon dissociation of the compound *AB* and reports on the results of the experimental verification of the proposed model. It is assumed that the density of kinks at the steps bounding the elementary growth layers is relatively low, which is typical of poorly soluble crystals. Experimental investigations into the influence of the composition of the solution (the deviation of the amount of *A* and *B* from the stoichiometric composition) on the crystallization kinetics are few in number, and their results have not made it possible to reveal any regularities. Studies pertinent to the problem are reviewed in [1, 2].

THEORY

The normal growth rate of crystal faces with a low density of kinks is determined by the rate of movement of steps *V,* which depends on the rate of movement v and on the density ρ of the kinks. Arrival of a kink to a particular point of a step means that it has moved forward at a distance of *b* equal to the distance between the rows of the building units. Therefore, we can write

$$V = b\rho v. \quad (1)$$

For a Kossel crystal ($A \equiv B$), the rate of movement of a kink has the form

$$v = a(\omega_+ - \omega_-), \quad (2)$$

where ω_+ and ω_- are the frequencies of attachment of the particles to the kink and their detachment from it, respectively, and *a* is the distance between the building units in the step. The supersaturation of a solution is defined as $s = \omega_+/\omega_- - 1$. Hence, we can write $v = a\omega_- s$ and $\omega_+/\omega_- = C/C_0$, where *C* and C_0 are the actual and equilibrium concentrations of the solution, respectively.

The expression for the rate of movement of the kinks, which alternatively include particles *A* and *B*, was derived independently by different authors within different approaches [1–6]:

$$v = 2fa\frac{\omega_{+A}\omega_{+B} - \omega_{-A}\omega_{-B}}{\omega_{+A} + \omega_{+B} + \omega_{-A} + \omega_{-B}}. \quad (3)$$

Let us now change over from the frequencies to the activities of the components in the solution. From the expression $\omega_{+A} = \nu\exp(\mu_{LA} + E_{+A})/kT$ (where $\mu_{LA} = kT\ln a_A + \varphi$ is the chemical potential of particle *A* in the solution, a_A is the activity of particle *A* in the solution, φ is a function independent of the concentration, and ν is the characteristic frequency of attempts to overcome the potential barrier E_A), we can easily obtain $\omega_{+A} = f_A a_A$ (where f_A is a constant). A similar expression can be derived for the frequency of attachment ω_{+B} for particle *B*. The frequencies of detachment can be expressed by the formulas $\omega_{-A} = f_A a_{Ae}$ and $\omega_{-B} = f_B a_{Be}$, where a_{Ae} and a_{Be} are the activities of particles *A* and *B* in the saturated solution, respectively. As a first approximation, we can assume that $f_A = f_B = f$. Then, expression (3) takes the form

$$v = 2fa\frac{a_A a_B - a_{Ae}a_{Be}}{a_A + a_B + a_{Ae} + a_{Be}}. \quad (4)$$

The product of the activities $K = a_{Ae}a_{Be}$ is a constant. Let us introduce the designation $\Pi = a_A a_B$. Then, the supersaturation can be represented as

$$s = (\Pi/K)^{1/2} - 1. \quad (5)$$

The isotherm of solubility of the *AB* compound is schematically shown in Fig. 1. Let a_A and a_B be the coordinates of the composition of the supersaturated

solution. In the course of crystallization from this solution, the composition of the liquid changes along the straight line forming an angle of 45° with the axes of coordinates and connecting the point corresponding to the initial composition of the solution and the point a_s characterizing the composition of the solution at a given instant of crystallization, i.e., at an excess (relative to stoichiometric) content of component *A* in water. It is seen from Fig. 1 that $a_s = a_A - a_B = a_{Ae} - a_{Be}$. Therefore, we can write the relationship

$$a_A + a_{Be} = a_{Ae} + a_B. \quad (6)$$

Then, the expression for the rate of movement of the kinks takes the form

$$v = af\frac{\Pi - K}{a_A + a_{Be}}. \quad (7)$$

Designating $\varepsilon_1 = a_A/a_B$ and $\varepsilon_2 = a_{Ae}/a_{Be}$, we obtain

$$\begin{aligned} a_A &= (\Pi\varepsilon_1)^{1/2}, \quad a_B = (\Pi/\varepsilon_1)^{1/2}, \\ a_{Ae} &= (K\varepsilon_2)^{1/2}, \quad a_{Be} = (\Pi/\varepsilon_2)^{1/2}. \end{aligned} \quad (8)$$

Taking into account relationship (5), expression (7) can be rewritten as

$$v = af(K)^{1/2}\frac{s(s+2)}{(s+1)\sqrt{\varepsilon_1} + \sqrt{\varepsilon_2^{-1}}}. \quad (9)$$

Using relationship (6) and the specified values of *s* and ε_1, we obtain ε_2:

$$\sqrt{\varepsilon_2} = 1/2(s+1)(\sqrt{\varepsilon_1} - \sqrt{\varepsilon_1^{-1}}) \times\left[\sqrt{1 + \frac{4}{(s+1)^2(\sqrt{\varepsilon_1} - \sqrt{\varepsilon_1^{-1}})^2}} + 1\right]. \quad (10)$$

For a solution of the stoichiometric composition (i.e., the solution containing *A* and *B* in stoichiometric amounts), we have $\varepsilon_1 = \varepsilon_2 = 1$. Then, from expression (9), we obtain formula (2); that is, $v = af(K)^{1/2}s = afa_{Ae}s = a\omega_s = a(\omega_+ - \omega_-)$. Note also that, although expressions (9) and (6) are derived by assuming that $a_A > a_B$, they remain unchanged in the reverse case when $\varepsilon_1 = a_B/a_A > 1$. To put it differently, the dependence $v(\varepsilon_1)$ is symmetric with respect to the deviation of the composition of the solution from stoichiometry in both directions and, hence, there is a special point on the curve at $\varepsilon_1 = 1$.

Thus, at a constant supersaturation, the rate of movement of the kinks should proportionally decrease as the composition of the solution deviates from stoichiometry. Moreover, the quantity $1/v$ should be a linear function of the denominator in expression (9). These two inferences can be verified experimentally by measuring the rate of movement of the steps *V* [see relationship (1)] under the assumption that the density of kinks weakly depends on the stoichiometry of the solution.

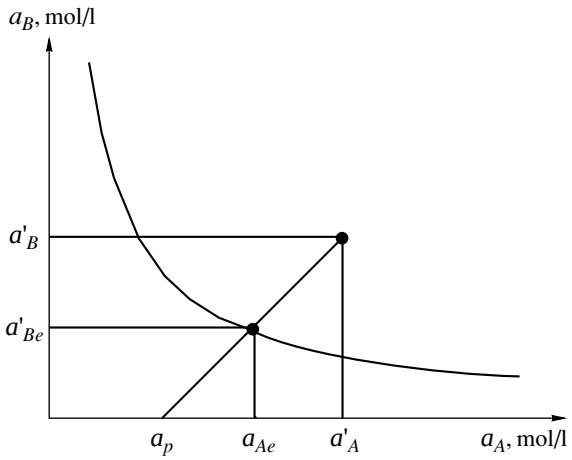

Fig. 1. Schematic isotherm of solubility of the *AB* compound. The curve $K = a_{Ae}a_{Be}$ is shown.

EXPERIMENTAL TECHNIQUE

The experiments were performed on crystal faces of calcium oxalate monohydrate $CaC_2O_4 \cdot H_2O$ (COM) and magnesium oxalate dihydrate $MgC_2O_4 \cdot 2H_2O$ (MOD). Samples in the form of 10- to 30-μm crystals were prepared according to a procedure similar to that described in [7]. The products of the activities K_{COM} and K_{MOD} were 2.0×10^{-9} and 4.83×10^{-6} $(mol/l)^2$, respectively. The quantity ε was taken equal to the ratio of the cation activity to the anion activity. The activity coefficient γ calculated from the standard Debye–Hückel formula for diluted solutions was equal to 0.33. The rate of movement of steps *V* was measured in situ under kinetic growth conditions provided by pumping a supersaturated solution along the studied face (the quantity *V* did not depend on the flow rate). The measurements were performed using a Nanoscope 3 atomic-force microscope. The shape of the dislocation growth hillocks is seen in the AFM images displayed in Fig. 2.

The rate of movement of steps *V* as a function of the nonstoichiometry of the solution at a constant supersaturation is presented in Fig. 3. It is seen that the points corresponding to $\varepsilon > 1$ and $\varepsilon < 1$ fall on the same curve. Similar dependences were obtained for different faces and directions of movement of the steps.

Figure 4 shows the dependences depicted in Fig. 3 after their linearization according to formula (9). It can be seen that the experimental points are in good agreement with theory.

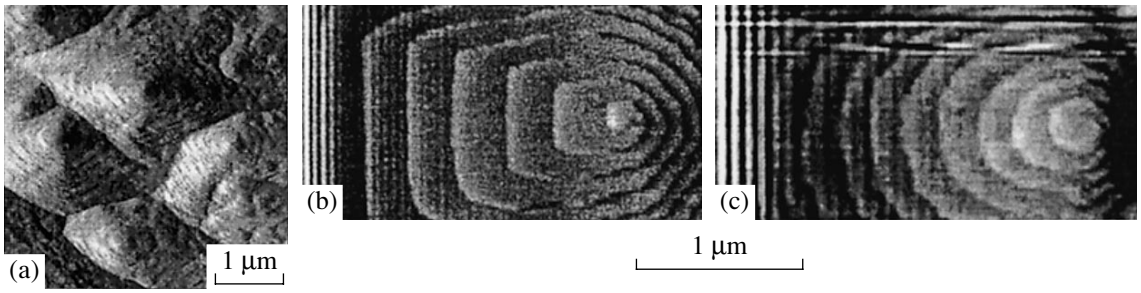

Fig. 2. (a) The (010) face of $CaC_2O_4 \cdot H_2O$. The step height is equal to one-half the lattice parameter (0.73 nm). (b) The (010) face of $MgC_2O_4 \cdot 2H_2O$. The step height is equal to the lattice parameter (0.54 nm). Conditions: $s = 2$, [Mg]/[Ox] = (b) 1 and (c) 5.

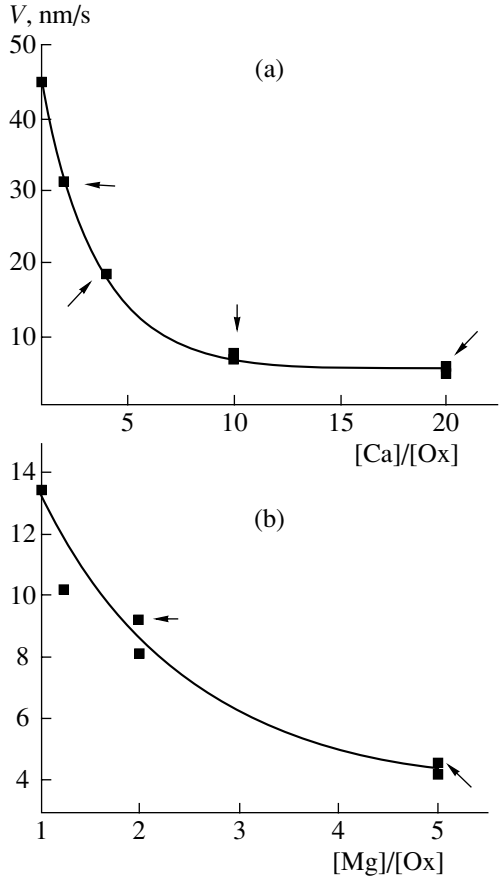

Fig. 3. Influence of the nonstoichiometry of the solution on the rate of movement of steps for (a) $CaC_2O_4 \cdot H_2O$ crystals at $s = 5.633$ ($\Pi/K = 44$) and (b) $MgC_2O_4 \cdot 2H_2O$ crystals at $s = 2.0$ ($\Pi/K = 9$). Arrows indicate points for which the values plotted along the abscissa axis are equal to the ratio of the anion activity to the cation activity.

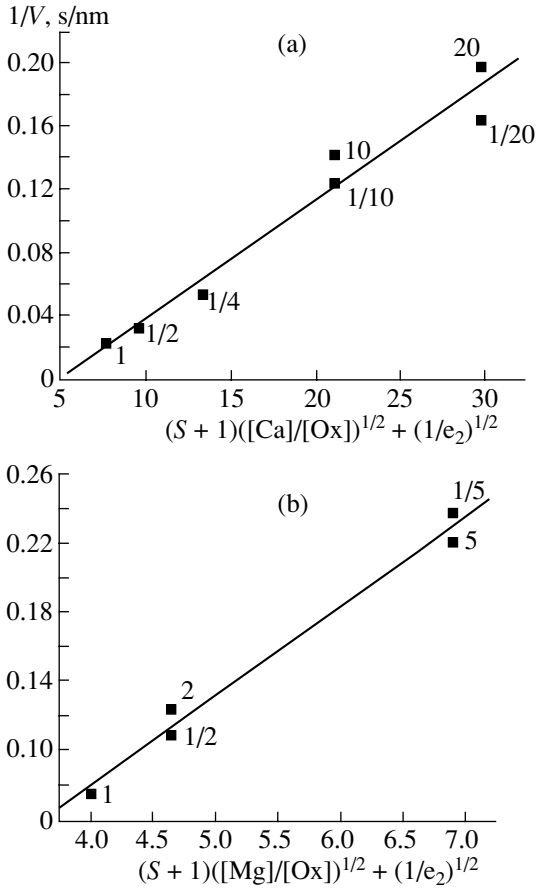

Fig. 4. The data presented in Fig. 3 after their linearization according to formula (9). The values of ε_2 were calculated from formula (10) for (a) $CaC_2O_4 \cdot H_2O$ crystals at $s = 5.633$ and (b) $MgC_2O_4 \cdot 2H_2O$ at $s = 2$. The numerals near the experimental points indicate the activity ratio of the components in the solution.

DISCUSSION

This study is not faultless. Below, we note the shortcomings of the experiment and the limitations of the model.

Experiment. The supersaturation was calculated under the assumption that the compounds are completely dissociated. This is obviously not the case: there can exist dissolved complexes that involve a large number of ions of the oxalate, calcium, or magnesium. Unfortunately, we have not found thermodynamic data necessary for the appropriate calculations. Therefore, we cannot be sure in the constancy of the supersaturation s as the stoichiometry of the solution changes.

Model. In an ideal solution, the frequencies of detachment ω_- depend only on the temperature. The consequences following from this fact were described in [6]. A question arises as to whether the frequencies of detachment ω_- in our case can be considered to be dependent on the ratio of the components in the solution. We have no answer to this question.

Another question arises as to whether the density of kinks depends on the composition of the solution. As the concentration of the oxalate ions (the point a_p in Fig. 1) increases, the solubility of the salts decreases, which should lead to an increase in the surface free energy of the step rises [8] and to a decrease in the density of kinks ρ. This effect is actually observed (Fig. 2): as the nonstoichiometry increases, the steps become less rough and more polygonized. A similar phenomenon is observed with decreasing supersaturation s. So far, we have failed to measure the density of kinks and to take into account the above effect.

The unit cell of $CaC_2O_4 \cdot H_2O$ contains two crystallographically independent oxalate anions and calcium cations. Therefore, the crystal cannot be built of two types of particles. In this case, we should take into account that particles A_1 and A_2, as well as particles B_1 and B_2, are not equivalent to each other. An appropriate model has not been developed yet.

ACKNOWLEDGMENTS

This study was supported by the Russian Foundation for Basic Research, project no. 03-02-16113.

REFERENCES

1. J. Zhang and G. H. Nancollas, J. Colloid Interface Sci. **200**, 131 (1998).
2. A. V. Nardov and S. V. Moshkin, in *Crystallography and Crystal Chemistry* (Leningrad State University, Leningrad, 1982), No. 4, pp. 42–46 [in Russian].
3. A. A. Chernov, Usp. Fiz. Nauk **100**, 277 (1970) [Sov. Phys. Usp. **13** (1), 101 (1970)].
4. A. E. Nielsen, Pure Appl. Chem. **53**, 2025 (1981).
5. A. A. Chernov, J. Mater. Sci.: Mater. Electron. **12**, 437 (2001).
6. A. A. Chernov, L. N. Rashkovich, and P. G. Vekilov, J. Cryst. Growth **275**, 1 (2005).
7. N. V. Gvozdev, E. V. Pertova, T. G. Chernevich, *et al.*, J. Cryst. Growth **261**, 539 (2004).
8. O. Sohnel, J. Cryst. Growth **57**, 101 (1982).

Translated by I. Polyakova

Crystallography Reports, Vol. 50, Suppl. 1, 2005, pp. S82–S87.

CRYSTAL GROWTH

Effect of Impurity Adsorption on the Growth of Rochelle Salt Crystals

D. A. Vorontsov, V. N. Portnov, and E. V. Chuprunov

Nizhni Novgorod State University, pr. Gagarina 23, Nizhni Novgorod, 603950 Russia

e-mail: vorontsovda@mail.ru

Received February 3, 2005

Abstract—The influence of impurities of copper compounds on the growth of Rochelle salt crystals of the composition $KNaC_4H_4O_4 \cdot 4H_2O$ is studied. The growth rates of the faces of various simple forms experimentally measured as functions of the $CuCO_3$ concentration in solution at a constant supersaturation and temperature are compared with the theoretical models of impurity adsorption on the faces of a growing crystal. Deceleration of the growth of various faces of a Rochelle salt crystal is satisfactorily described by the Bliznakov equation with the use of the Langmuir, Frumkin–Fowler, and de Boor adsorption isotherms for all the faces except for {010}. However, such a comparison does not allow one to reveal the cause of adsorption or its type on different faces. Photometric scanning of Rochelle salt solutions with copper-compound impurity showed that a small addition of alkali (0.06–0.4 g/l) to the solution results in the appearance in the absorption spectra of both the solution and the crystal grown from it of a maximum at the wavelength 660–670 nm. The intensity of this maximum increases with an increase in the copper concentration. The EPR data, the absorption spectra of the solution and the crystal, and the modified crystal shape showed that the addition of alkali to the solution results in the formation of new copper complexes that more actively decelerate the growth of Rochelle salt faces. © *2005 Pleiades Publishing, Inc.*

INTRODUCTION

The influence of impurities on crystal growth has been studied for a long time. First, one observed the changes in crystal shape caused by the presence of impurities in the solutions [1]. Then, the growth rates of various crystal faces were measured [2], which allowed one to compare the theoretical and experimental data [3, 4].

The effect of impurity adsorption manifests itself at low concentrations without noticeable changes in the solution state. The impurity adsorption is characterized by selectivity, fall of the growth-rate curves dependent on impurity concentration, and the reduction of this effect with an increase in temperature.

High selectivity of the effect is observed for various dyes. Thus a direct light-blue dye strongly decelerates growth only of the {100} faces of a cube in potassium alum, the {101} faces of a bipyramid in potassium dihydrogen phosphate (KDP) crystals, and the {010} faces of the pinacoid in Rochelle salt crystals $KNaC_4H_4O_6 \cdot 4H_2O$. A decrease in the growth rate of these faces is accompanied by the dye capture by the corresponding growth sectors [5, 6].

In many instances, the impurity compounds introduced into the solution become the basis for the formation of new active impurities, with their composition and activity varying with the concentration of the main substance, solution pH, etc. [7, 8]. It has repeatedly been indicated that knowledge of the solution state and the structure of impurity particles is necessary for determining the mechanism of impurity effect on crystal growth [9].

It has been indicated [1] that the most pronounced changes in the shape of Rochelle salt crystals observed in the presence of Cu^{2+} ions are explained by a decrease in the growth rate of the {001} and {210} faces. As a result, in the [001] zone, the {210} faces prevail and, thus, the grown crystal is rather short along the *c* axis. Irrespective of which of the Cu^{2+}-containing salts is used to introduce the Cu^{2+} ions into the solution, the effect observed is always associated with these ions [10]. The addition to the solution of copper carbonate, $CuCO_3$, decelerates the growth of {001} faces and gives rise to the formation of a platelike habit. The ⟨001⟩ growth sectors acquire a blue color, which indicates the incorporation of copper ions into the crystal. An analogous effect is also produced by copper vitriol, $CuSO_4 \cdot 5H_2O$, and copper hydroxide, $Cu(OH)_2$.

The effect of the impurities mentioned above may be multiply increased by an additional introduction into the solution of NaOH or KOH alkali. The addition to the solution of a small amount of $CuCO_3$ (2 g/l) reduces the crystal dimension along the *c* axis by a factor of about 2. The same effect may also be achieved at a considerably lower $CuCO_3$ concentration by adding to the solution a small amount of alkali. On the contrary, the effect of $CaCO_3$ is weakened by adding to the solution a small amount of the H_2SO_4 acid. The influence of the alkali addition manifests itself especially pronouncedly

1063-7745/05/5001-S0082$26.00

in the case of the $CuSO_4 \cdot 5H_2O$ impurity. To reduce the crystal length along the *c* axis by a factor of 2, one has to add to the solution either 20 g/l of $CuSO_4 \cdot 5H_2O$ or only 0.2 g/l of $CuSO_4 \cdot 5H_2O$ in the presence in the solution also of 2 g/l NaOH. It is assumed [10] that this effect is explained by an increase in the adsorbing power of crystal faces because of an increase in solution pH.

The present study was undertaken to measure the growth rates of different faces of a Rochelle salt crystal in the presence of Cu^{2+} ions and to compare the results obtained with the theoretical data. We also studied the changes of impurities in the solution.

MEASUREMENTS OF GROWTH RATES OF CRYSTAL FACES

To obtain quantitative data on the influence of copper ions on growth rate, we measured the growth rates of the faces of Rochelle salt spheres in the case where the solution contained the $CuCO_3$ addition. Figure 1 shows the shape of a Rochelle salt crystal grown from pure solution. Figure 2 shows the stereographic projection of this crystal with the indication of the faces whose growth rates were measured.

The measurements were performed at the absolute supersaturation 20 g/l and for a planetary rotation of spheres with a frequency 60 rev/min at the temperature 20°C. The growth rates of different faces thus measured are indicated in Fig. 3. The accuracy of the determination was $\Delta R = \pm 0.1$ mm/h. The growth rates of the faces as functions of impurity content in the solution rapidly decrease and tend to a certain constant value. Only the curve for the {010} face turned out to be nonmonotonic. The impurity acts selectively: the most pronounced influence of impurity is observed on the {001} and {210} faces.

It is seen from Fig. 3 that at low $CuCO_3$ concentrations (up to 0.4 g/l), the grown crystals have a platelike habit, because the {001} faces have relatively low growth rates. In this case, the {210} faces of the rhombic prism and the {010} faces of the pinacoid are the most pronounced. At a higher impurity content, the crystal becomes faceted mainly with the {001} and {$\bar{2}$10} faces. Our growth experiments confirm these conclusions.

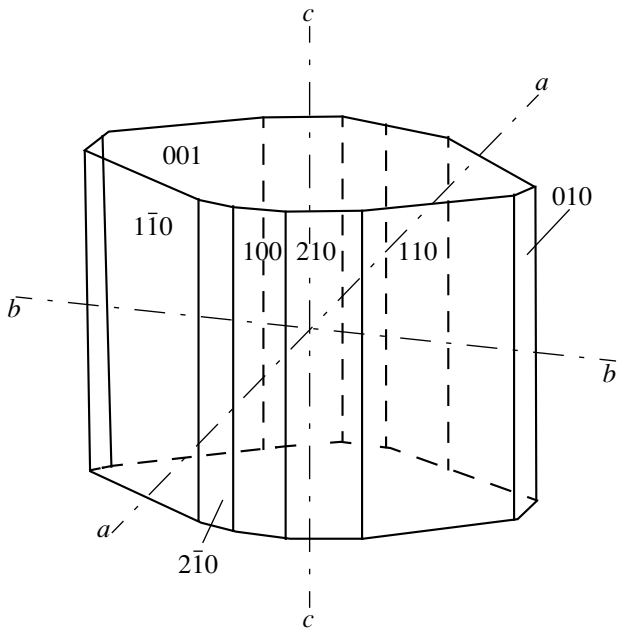

Fig. 1. Shape of a Rochelle salt crystal grown from pure solution.

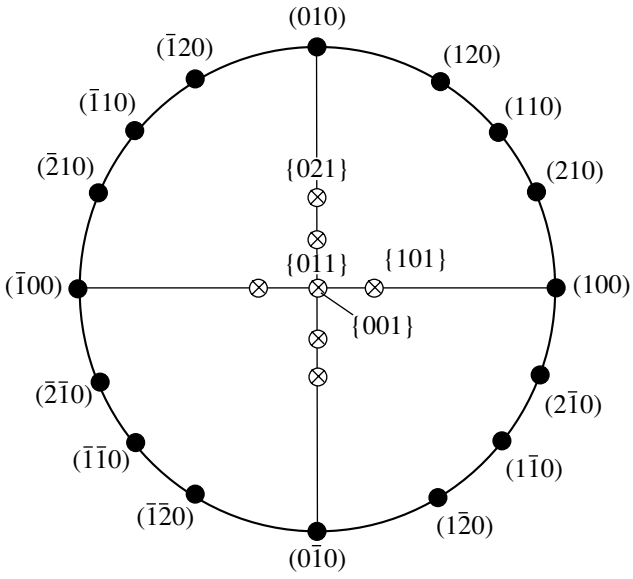

Fig. 2. Stereographic projection of a Rochelle salt crystal.

BLIZNAKOV EQUATION AND ADSORPTION ISOTHERMS

To describe the growth rates of the faces, *R*, as functions of impurity concentration in the solution and impurity adsorption one usually invokes the Bliznakov equation [3, 11]

$$R = R_0(1 - \alpha\theta), \quad (1)$$

where R_0 is the growth rate of a face in the absence of impurity, $\alpha = \dfrac{R_0 - R_\infty}{R_0}$, R_∞ is the steady-state growth rate at high impurity content, and θ is the occupancy of the growth sites with impurity particles. The quantity α characterizes the efficiency of the impurity effect.

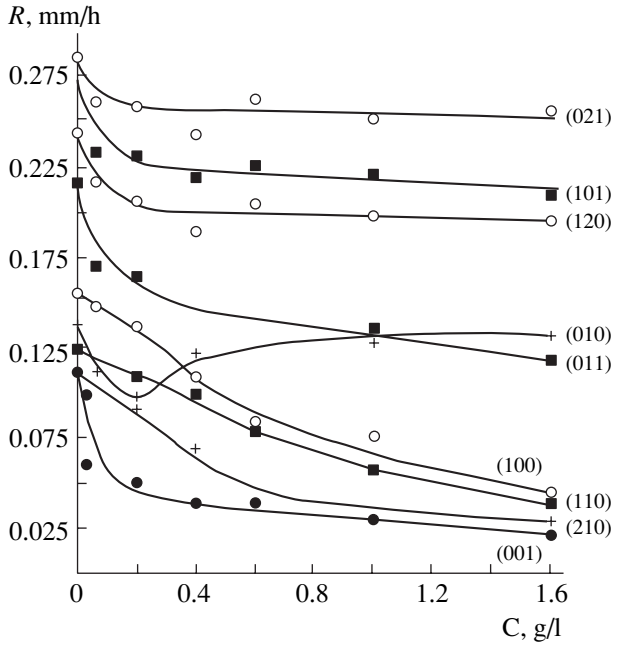

Fig. 3. Change in the growth rates of different faces of a Rochelle salt crystal depending on the $CuCO_3$ concentration in the solution.

If the surface is covered with adsorbed two-dimensional islands of impurity, the quantity θ signifies the fraction of the surface covered with the impurity film.

The degree of adsorption is described by the adsorption isotherms. One such isotherm is the Langmuir adsorption isotherm

$$\theta = \frac{C}{k + C}, \tag{2}$$

where C is the impurity concentration in the medium and k is the adsorption constant equal to

$$k = k_0 \exp\left(-\frac{\varphi_{AB}}{kT}\right),$$

where φ_{AB} is the adsorption energy. The use of Eqs. (1) and (2) allows one to interpret the curves of the growth rate of the faces of $MgSO_4 \cdot 7H_2O$ in the presence of borax and $NaClO_3$ in the presence of Na_2SO_4 [11]. It was assumed that in this case adsorption occurs at kinks.

Another isotherm taking into account the mutual attraction of impurity molecules in the adsorbed state and the surface diffusion was suggested by de Boor

$$C = k_1 \frac{\theta}{1-\theta} \exp\left(\frac{\theta}{1-\theta} - k_2\theta\right), \tag{3}$$

where k_1 is the adsorption constant and k_2 is the coefficient taking into account the interaction between the impurity molecules. In this case, adsorption of impurity molecules may be accompanied by the formation of groups and islands. The critical k_2 value of the beginning of two-dimensional impurity condensation equals 6.75.

There is another type of adsorption accompanied by the formation of two-dimensional coatings without surface migration of impurity molecules. The corresponding isotherm was obtained by Frumkin and Fowler [13]

$$C = k_1' \frac{\theta}{1-\theta} \exp(-k_2'\theta), \tag{4}$$

where k_1' is the coefficient of adsorption strength and k_2' is the quantity taking into account interactions of impurity molecules in the adsorbed state. Here, the critical value of k_2' equals 4. Obviously, one has to use the above isotherms with certain precautions, because, sometimes, the data obtained from these isotherms are inconsistent with the experimentally measured ones.

COMPARISON OF THEORETICALLY CALCULATED AND MEASURED DATA

The experimental curves of growth-rates of different faces (Fig. 3) may be represented by the equation obtained by substituting Eq. (2) into Eq. (1) and linearized to the form

$$\frac{R_0}{R_0 - R} = \frac{k}{\alpha}\frac{1}{C} + \frac{1}{\alpha}. \tag{5}$$

The experimental points allow one to determine k and α values. The errors in their determination are within 15–20%.

The above equation satisfactorily describes the experimental growth-rate curves for the {001}, {101}, {011}, {120}, and {021} faces. However, Eq. (5) is inapplicable to the {100}, {110}, and {210} faces because the growth-rate curves of these faces have inflection points.

It follows from Eq. (2) and table that, with an increase in the impurity concentration in the solution, coverage θ attains its saturation the faster, the lower the k value, i.e., the higher the adsorption energy of the impurity. It seems that, with an increase in the adsorption energy, the efficiency of the impurity influence α should have also increased. However, in our case, it is not so. Thus, for the {021} face, the k value is minimal and, at the same time, the α value is also minimal. The smallness of α may be explained under the assumption that the growth sites on the face may be divided into several groups. Then Eq. (1) takes the form

$$R = R_0\left(1 - \sum_{i=1}^{\nu} n_i\theta_i\right), \tag{6}$$

where ν is the number of the groups, n_i is the fraction of the sites of the ith group, and θ is coverage. In this case $\sum_{i=1}^{\nu} n_i = 1$.

To illustrate the situation, assume that there are only two groups of growth sites on the face. Then Eq. (6) is modified to the form

$$R = R_0(1 - n_1\theta_1 - n_2\theta_2).$$

Under the condition that the sites of the second group do not adsorb impurities at all, we obtain

$$R = R_0(1 - n_1\theta_1).$$

Obviously, the n_1 value can be much less than unity.

The growth-rate curves of all the faces (except for the {010} face) may be described using Eqs. (1) and (3). All the curves have the same value of k_2, which depends only on the adsorbate properties. In this case, the α value was taken to be unity.

For the main simple forms of a Rochelle salt crystal at $k_2 = 4$, we obtained the following k_1 values: 0.13 g/l for the {001} faces, 2.5 g/l for the {110} faces, 1.9 g/l for the {100} faces, and 1.3 g/l for the {210} faces. The curves calculated with the use of these values are close to the experimental ones.

The de Boor adsorption isotherm can be used in the presence of surface diffusion of impurity particles; however, this diffusion plays an important role only on smooth *F* faces. For a Rochelle salt crystal, such faces seem to be the {001}, {210}, {110}, and {100} faces.

Finally, Eqs. (1) and (4) allow one to explain the shapes of some experimental curves.

The above formal comparison of the theoretical equations with the experimental data does not allow one to answer the question as to the cause of adsorption and type of adsorption at different faces of a Rochelle salt crystal. To answer these questions one has to perform an additional detailed study of the composition and the structure of impurity particles in solutions.

STUDY OF SOLUTIONS

To observe the changes in Rochelle salt solutions caused by adding to it impurities (copper compounds) or alkali, we performed photometric scanning of solutions on an FM-56 photometer. Figure 4 shows the optical-density curves of Rochelle salt solutions with different $CuCO_3$ content. Similar optical-density curves were obtained when to the Rochelle salt solutions were added small amount of copper tartrate $CuC_4H_4O_6 \cdot 3H_2O$.

The Bouguer–Lambert–Beer law is fulfilled for both $CuCO_3$ and $CuC_4H_4O_6 \cdot 3H_2O$. In other words, irrespective of the wavelength, the optical density linearly depends on impurity concentration.

The additional introduction of 0.2 g/l NaOH to the $CuCO_3$-containing solution transforms the absorption spectrum of the solution (curve *4* in Fig. 4). The spectrum shows the absorption band with the maximum at 660–670 nm gradually formed with the introduction of new NaOH portions into the solution. The appearance of this maximum is recorded after the introduction of 0.06 g/l NaOH.

k and α for different simple forms of a Rochelle salt crystal

{*hkl*}	{021}	{001}	{101}	{011}	{120}
α	0.1	0.8	0.2	0.4	0.2
k, g/l	0.01	0.02	0.02	0.04	0.05

We also performed photometric scanning of Rochelle salt solutions under the constant addition of new portions of NaOH (0.1 g/l) and introduction of various quantities of $CuCO_3$ (Fig. 5). In this case as well, we observed the formation of the optical-density maximum in the range 660–670 nm. With an increase of the $CuCO_3$ concentration, the height of this maximum increases proportionally to the amount of the added impurity. It is possible to assume that the formation of the maxima is associated with the action of the impurity.

The EPR spectra of the Rochelle salt solutions with copper tartrate also showed the formation in the solution of a new compound upon the addition of alkali. The solution containing 2 g/l of copper tartrate at room temperature yields an EPR spectrum with a broad line with the *g* factor ranging within 2.05–2.32. This diffuse line is associated with the copper tartrate complexes having random orientations in the solution. The introduction of NaOH (2 g/l) gives rise to the formation in the EPR spectrum of one more narrow line with $g = 2.06$. This indicates the presence in the solution of a new copper complex. It should be indicated that a small

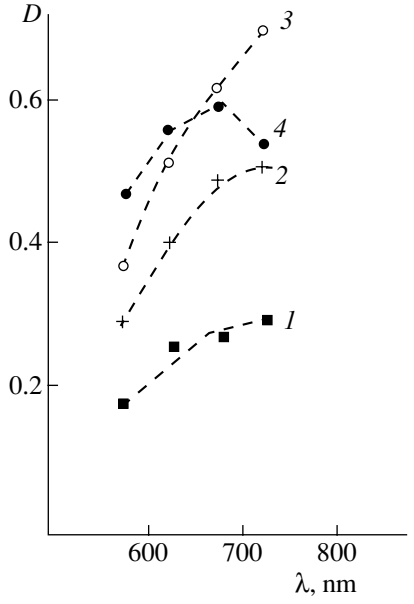

Fig. 4. Absorption spectrum of Rochelle salt solutions with different amounts of $CuCO_3$ impurity: (*1*) 0.2, (*2*) 0.4, and (*3*) 0.6 g/l. Curve *4* corresponds to the addition to the solution of 0.6 g/l of $CuCO_3$ and 0.2 g/l of NaOH.

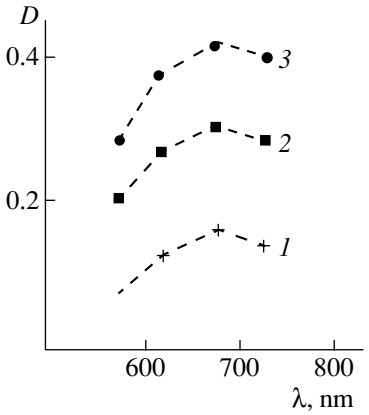

Fig. 5. Absorption spectrum of Rochelle salt solutions with different amounts of $CuCO_3$ impurity at a constant NaOH concentration: (*1*) 0.1, (*2*) 0.23, and (*3*) 0.40 g/l.

number of these complexes is also contained in the solution without NaOH because of the high pH characteristic of the Rochelle salt solution, pH 8.2.

The latter conclusion is confirmed by the growth experiments on $KNaC_4H_4O_6 \cdot 4H_2O$ single crystals. Single crystals obtained from the solutions with 0.1 and 0.3 g/l $CuCO_3$ change their shape in such a way that the *c*/*b* ratio becomes equal to 0.9 and 0.6, respectively. For crystals grown from pure solution, this ratio equals unity. The addition to these solutions of a small amount of alkali (2 g/l) considerably enhances the impurity activity. The *c*/*b* ratios become equal to 0.6 and 0.3, respectively.

Similar changes in the shape of Rochelle salt crystals were also observed with the introduction into the solution of copper tartrate. Moreover, the optical-density curves measured for crystals grown from the solutions containing copper carbonate and copper tartrate, either with or without the addition of alkali, had the same shape. The absorption bands of crystals and the corresponding solutions also coincided (660–670 nm).

CONCLUSIONS

The measurements of the growth rates of different faces and observation of the growth form of the crystal faces of Rochelle salt crystals of the composition $KNaC_4H_4O_6 \cdot 4H_2O$ indicate the adsorption mechanism of impurity action. The growth-rate curves of different faces of a Rochelle salt crystal obtained at different impurity concentrations are approximately described by the Bliznakov equation with the use of different adsorption isotherms.

At the same time, the establishment of the mechanism of impurity action requires a knowledge of the structure of impurity particles in the solution.

The growth of crystals, absorption spectra of the solutions and crystals, and also their EPR spectra provide evidence that the introduction into solution of alkali results in the formation of Cu^{2+} new complexes. Thus, the assumption about an increase in the adsorptive capacity of the faces a Rochelle salt crystal with the addition to the solution of alkali [10] is not confirmed by our experiments.

It is highly probable that the addition of alkali to the solution results in the formation of hydroxy complexes of the $Cu(OH)_n(H_2O)_{6-n}$ type [14]. These complexes are also present in the solution without alkali because of the high pH of a Rochelle salt solution. The addition of alkali to the solution increases the amount of this impurity, which is adsorbed by the faces and, thus, decelerates crystal growth. Possibly, some kinks are poisoned with certain complexes or form coatings of impurity groups or islands.

The similar absorption spectra of solutions and crystals grown from these solutions show that copper complexes, which are active impurities, from the solution are incorporated into the crystal structure with a somewhat changed arrangement of surrounding Cu^{2+} ions.

The EPR spectra of a Rochelle salt crystal $KNaC_4H_4O_6 \cdot 4H_2O$ doped with Cu^{2+} ions show that these ions occupy the sites of Na^+ ions in the structure [15] and are coordinated with two oxygen ions, one hydroxyl ion, and three water molecules. Therefore the role of the active complex in a Rochelle salt solution may be played by the complex of the composition $[Cu(OH)(H_2O)_5]^{1+}$. Perhaps tartrate copper complexes of two different types are also active complexes in the solutions.

Thus, the structure of impurities in the solution may readily be changed. This, in turn, changes the quantitative ratio between active and inactive impurity molecules. The change in the main-component concentration, pH, and temperature as well as the introduction into the solution of other compounds displace the chemical equilibrium in the solution. Our study illustrates once again the complex nature of the impurity effect on crystal growth from solutions.

REFERENCES

1. H. Buckley, *Crystal Growth* (Wiley, New York, 1951; Inostrannaya Literatura, 1954).
2. V. A. Mokievskiĭ and I. A. Mokievskaya, Zap. Vses. Mineral. O–va **39** (1), 15 (1956).
3. G. M. Bliznakov, Kristallografiya **4** (3), 150 (1959) [Sov. Phys. Crystallogr. **4** (3), 134 (1959)].
4. N. Cabrera and D. A. Vermilyea, *Growth and Perfection of Crystalls* (Plenum, New York, 1958), p. 393.
5. V. N. Portnov, Kristallografiya **11** (6), 916 (1966) [Sov. Phys. Crystallogr. **11** (6), 774 (1966)].
6. V. N. Portnov, A. V. Rykhlyuk, and A. V. Belyustin, Kristallografiya **14** (6), 1093 (1969) [Sov. Phys. Crystallogr. **14** (6), 954 (1969)].

7. T. G. Petrov, E. B. Treivus, and A. P. Kasatkin, *Growing Crystals from Solution* (Nedra, Leningrad, 1967; Consultants Bureau, New York, 1969).
8. V. N. Portnov and A. V. Belyustin, Kristallografiya **10** (3), 362 (1965) [Sov. Phys. Crystallogr. **10** (3), 231 (1965)].
9. A. A. Chernov, L. N. Rashkovich, I. L. Smol'skiĭ, *et al.*, in *Crystal Growth* (Nauka, Moscow, 1986), Vol. 15, p. 43 [in Russian].
10. A. V. Belyustin, in *Crystal Growth* (Nauka, Moscow, 1964), Vol. 4, p. 10 [in Russian].
11. G. M. Bliznakov, Coll. Int. Cancer Res. (Paris), No. 152, 291 (1965).
12. J. H. de Boer, *The Dynamical Character of Adsorption* (Clarendon Press, Oxford, 1953; Inostrannaya Literatura, Moscow, 1962).
13. R. Kern, in *Crystal Growth* (Nauka, Moscow, 1968), Vol. 8, p. 5 [in Russian].
14. E. A. Buketov, M. Z. Ugorets, and K. M. Akhmetov, *Dehydration of Metal Hydrates in Alkaline Solutions* (Nauka Kazakhskoĭ SSR, Alma-Ata, 1971) [in Russian].
15. G. Volkel and W. Windsch, Phys. Status Solidi **17** (1), 75 (1966).

Translated by L. Man

Crystallography Reports, Vol. 50, Suppl. 1, 2005, pp. S88–S91.

CRYSTAL GROWTH

Growth of Single Crystals of $Li_6Y_{1-x}Eu_x(BO_3)_3$ (x = 0–1) Solid Solutions by the Czochralski Method

R. P. Yavetskiĭ, E. F. Dolzhenkova, M. F. Dubovik, T. I. Korshikova, and A. V. Tolmachev

Institute for Single Crystals, National Academy of Sciences of Ukraine, pr. Lenina 60, Kharkov, 61001 Ukraine

e-mail: yavetskiy@isc.kharkov.ua

Received February 8, 2005

Abstract—The mutual solubility in the $Li_6Y(BO_3)_3$–$Li_6Eu(BO_3)_3$ system was investigated by differential thermal analysis and X-ray phase analysis. Single crystals of the $Li_6Y_{1-x}Eu_x(BO_3)_3$ solid solutions more than 1 cm^3 in volume were grown by the Czochralski method. The photoluminescence and thermoluminescence properties of the crystals grown are studied. *© 2005 Pleiades Publishing, Inc.*

INTRODUCTION

In view of the intense development of neutron-based techniques, the problem of measuring neutron fluxes is fairly urgent. This problem can be solved by both the scintillation method and solid-state dosimetry [1]. In this context, one of the intensively developed scintillation materials is cerium-activated lithium–gadolinium borate $Li_6Gd(BO_3)_3$: Ce (LGBO : Ce), which contains Gd, B, and Li—elements with high selective sensitivity to thermal neutrons [2–6]. Variation in the isotopic composition of this compound makes it possible to reach a high theoretical light yield: S = 59600 photons/neutron [2]. A drawback of LGBO is the large effective atomic number (Z = 46), which is responsible for the sensitivity of this material to gamma radiation and impedes its application in mixed n/γ fields. The use of the isostructural lithium–yttrium borate $Li_6Y(BO_3)_3$: Ce (LYBO : Ce) makes it possible to decrease the sensitivity to gamma background (Z = 26), although this leads to some decrease in the thermal-neutron capture cross section [3]. It was shown in [7, 8] that LGBO:Ce and LYBO:Ce cannot be used in solid-state dosimetry because of their low thermally-stimulated luminescence (TSL) yield. Doping of LGBO:Ce with sodium or magnesium increases the TSL yield by more than an order of magnitude [9]. However, it is insufficient for the practical application of this material.

In [9, 10], we reported for the first time about the presence of intense TSL in $Li_6Gd_{1-x}Eu_x(BO_3)_3$ single crystals, which was attributed to the decay of hole O^- centers. An O^- center is a hole localized at the oxygen p orbital near a stabilizing negative defect. It was shown that this material is promising for application in solid-state dosimetry of thermal neutrons. It was suggested that, owing to the ionization, some portion of Eu ions in the lattice of a $Li_6Gd_{1-x}Eu_x(BO_3)_3$ crystal passes to the divalent charge state: $Eu^{3+} \longrightarrow Eu^{2+}$. Simultaneously, O^- centers are formed, being localized at bridge oxygen atoms, which link Gd atoms into chains. Thermal decay of a $Eu^{2+}_{Gd^{3+}} + O^-$ center leads to the radiative relaxation of the trivalent Eu ion. To decrease the sensitivity to gamma background, we propose to use the lithium–yttrium orthoborate $Li_6Y_{1-x}Eu_x(BO_3)_3$. There are data in the literature on the growth of europium-activated $Li_6Y(BO_3)_3$ single crystals by the Czochralski method [11]. However, the concentration limit for $Li_6Y_{1-x}Eu_x(BO_3)_3$ solid solutions has not been established. This information is not only of scientific interest but also has practical importance for optimization of the growth of single crystals of specified composition. $Li_6Y_{1-x}Eu_x(BO_3)_3$ single crystals of different composition in a wide concentration range are necessary to establish types of radiation defects and study the concentration dependence of the TSL yield. The purpose of this work is to investigate the possibility of growing single crystals of $Li_6Y_{1-x}Eu_x(BO_3)_3$ solid solutions by the Czochralski method in the concentration range x = 0–1 and to determine their photo- and thermoluminescence characteristics.

EXPERIMENTAL

The $Li_6Y_{1-x}Eu_x(BO_3)_3$ compounds were synthesized by the solid-phase method. The phase composition of the samples was determined on a Siemens D500 powder diffractometer (CuK_α radiation). The liquidus temperatures were determined by differential thermal analysis (DTA) with an error of ±5 K, using the technique described in [12]. DTA was performed on a *Q*-1500*D* derivatograph in the dynamic mode, with a heating rate of 5 K/min and using an α-Al_2O_3 reference. The Eu concentration in the crystals grown was deter-

1063-7745/05/5001-S0088$26.00

mined by atomic emission spectroscopy with arc excitation. A DFS-8 spectrometer was used. Optical measurements were carried out on plane-parallel polished plates $7 \times 7 \times 2$ mm^3 in size, cut perpendicular to the growth direction. The absorption spectra were measured on a Specord M40 UV-VIS spectrophotometer. The photoluminescence spectra of the crystals were measured on an SDL-2 automatic complex (LOMO). The TSL curves were measured on an experimental setup using an FÉU-79 photomultiplier at a heating rate of ~5 K/min in the temperature range 300–650 K. The samples were irradiated by β particles at room temperature using a $^{90}Sr/^{90}Y$ radioactive source with an activity of 7.4×10^{10} Bq.

RESULTS AND DISCUSSION

The $Li_6Y_{1-x}Eu_x(BO_3)_3$ compounds were synthesized by the solid-phase reaction

$$3Li_2CO_3 + \left(\frac{1-x}{2}\right)Y_2O_3 + \left(\frac{x}{2}\right)Eu_2O_3 + 3H_2BO_3 = Li_6Y_{1-x}Eu_x(BO_3)_3 + 4.5H_2O + 3CO_2.$$

As the initial components, we used H_3BO_3 (reagent grade), Li_2CO_3 (high-purity grade), Gd_2O_3 (ItO-B grade), and Eu_2O_3 (EvO-Zh grade). Analysis of the heating curves of the initial mixtures used for the formation of the $Li_6Y(BO_3)_3$, $Li_6Eu(BO_3)_3$, and $Li_6Gd(BO_3)_3$ compounds (Fig. 1), as well as the $Li_6Y_{1-x}Eu_x(BO_3)_3$ solid solutions, showed that similar processes occur in all the systems studied upon solid-phase interaction. Taking into account the specific features of the phase formation in the Li_2O–B_2O_3–Gd_2O_3 system [13], we can conclude that the synthesis of these compounds has a step character. In the initial stage, intermediate compounds are formed: lithium borates ($2Li_2O \cdot B_2O_3$, $3Li_2O \cdot 2B_2O_3$, etc.), which, with an increase in temperature to 660–750°C, interact with Y_2O_3 and Eu_2O_3 with the formation of $Li_6Y_{1-x}Eu_x(BO_3)_3$ solid solutions.

To establish the solubility limits for the $Li_6Y(BO_3)_3$–$Li_6Eu(BO_3)_3$ system, the $Li_6Y_{1-x}Eu_x(BO_3)_3$ compounds were synthesized with a step in x of 0.1. The samples were annealed in air in two stages: at temperatures 560–600 and 700–750°C. As can be seen in Fig. 2, the $Li_6Y(BO_3)_3$–$Li_6Eu(BO_3)_3$ system is characterized by unlimited mutual solubility, which makes it possible to grow single crystals of specified composition in the entire concentration range by the Czochralski method. $Li_6Y_{1-x}Eu_x(BO_3)_3$ melts demonstrate wide temperature ranges of supercooling (up to 200°C). An increase in the Eu concentration is accompanied by a decrease in the melting temperature of the $Li_6Y_{1-x}Eu_x(BO_3)_3$ compound, which is consistent with the increase in the unit-cell volume of this compound (Fig. 2).

$Li_6Y_{1-x}Eu_x(BO_3)_3$ single crystals were grown by the Czochralski method from an oriented seed. When seeds

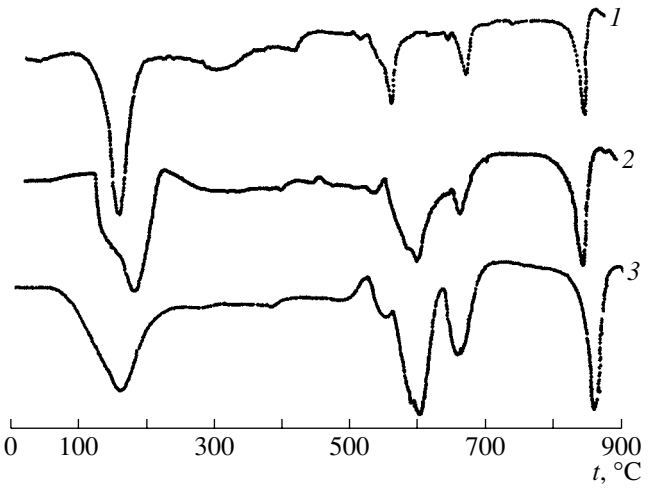

Fig. 1. DTA curves for the initial stoichiometric mixtures used to form (*1*) $Li_6Gd(BO_3)_3$, (*2*) $Li_6Eu(BO_3)_3$, and (*3*) $Li_6Y(BO_3)_3$ compounds.

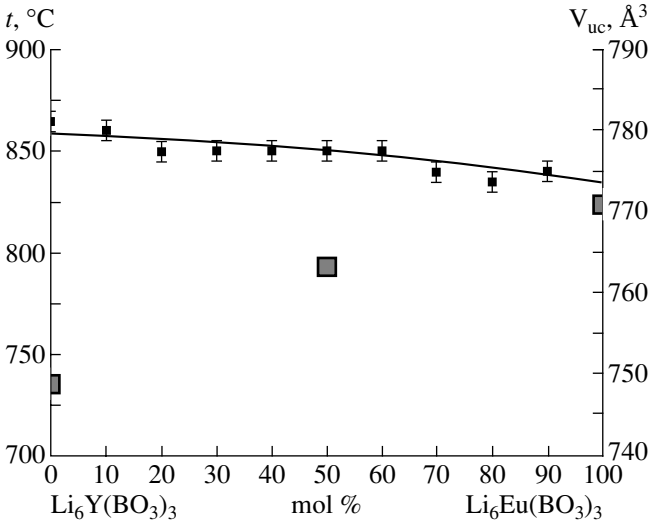

Fig. 2. Liquidus temperatures and the unit-cell volume (■) of crystals in the $Li_6Y(BO_3)_3$– $Li_6Eu(BO_3)_3$ system.

of arbitrary orientation were used, the crystals grown showed a tendency to cracking upon cooling or mechanical treatment. In some cases, helical growth of boules occurred (observed also) at low axial temperature gradients in [11]. The use of a single-crystal seed oriented in the $[4\bar{3}2]$ direction, which corresponds to the intersection of the $(10\bar{2})$ and (121) planes, allowed us to grow transparent crystals without cracks, inclusions, or pores. Single crystals more than 1 cm^3 in volume were obtained with the following unit cell parameters: sp. gr. $P2_1/c$, a = 7.157(5) Å, b = 16.378(4) Å, c = 6.623(4) Å, β = 105.32(5)°, and V = 748.74(2) Å^3 ($Li_6Y(BO_3)_3$); sp. gr. $P2_1/c$, a = 7.2070(7) Å, b = 16.467(2) Å, c = 6.6681(6) Å, β = 105.32(5)°, and V =

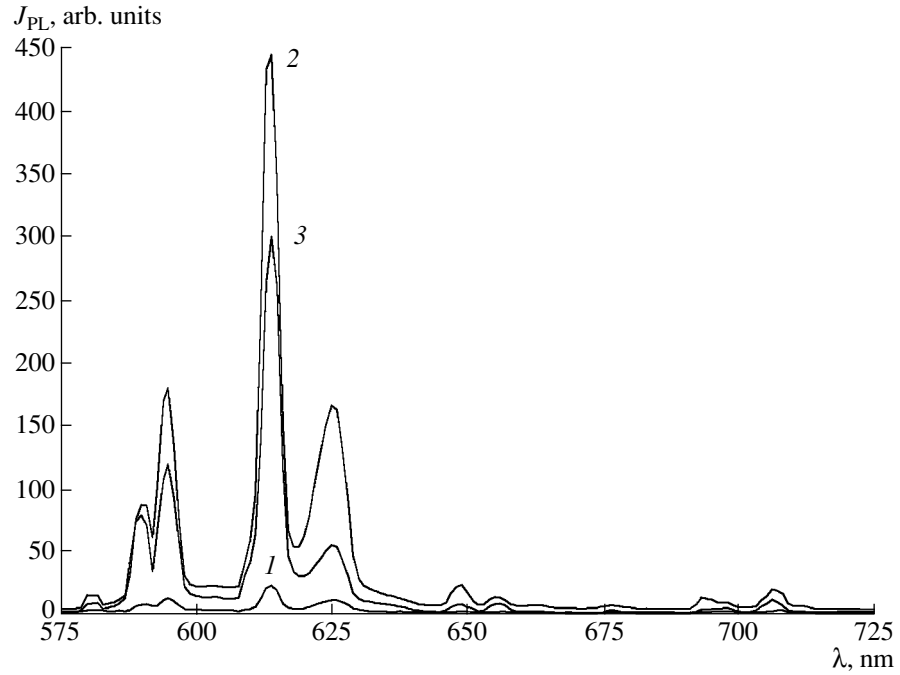

Fig. 3. Photoluminescence spectra of the $Li_6Y_{1-x}Eu_x(BO_3)_3$ samples (λ_{exc} = 395 nm) with x = (*1*) 0.03, (*2*) 0.5, and (*3*) 1.0; the composition is indicated for the charge.

763.19(2) Å^3 ($Li_6Y_{0.5}Eu_{0.5}(BO_3)_3$); and sp. gr. $P2_1/c$, a = 7.232(10) Å, b = 16.507(3) Å, c = 6.697(10) Å, β = 105.37(2)°, and V = 770.9(2) Å^3 ($Li_6Eu(BO_3)_3$). The effective Eu-distribution coefficient, determined by chemical analysis, is k_{eff} = 0.2 at activator concentrations $x \le 0.05$ in the initial charge. The value obtained is in agreement with the phase diagram (introduction of europium leads to a decrease in the melting temperature of this compound) and is consistent with the values of the ionic radii of the elements at a coordination number of 6:

$$r_{Y^{3+}}(6) = 1.04 \text{ Å}, \quad r_{Eu^{3+}}(6) = 1.09 \text{ Å}.$$

$Li_6Y(BO_3)_3$ crystals are transparent in the spectral range λ = 200–900 nm. Activation by europium leads to the formation of a wide charge-transfer band in the UV region, peaked at λ = 249 nm. This band corresponds to the transition of an electron from the 2*p* oxygen orbital to the unfilled 4*f* orbital of the Eu ion. The charge states of Eu and O ions change as follows: $Eu^{3+} + O^{2-} \longleftrightarrow Eu^{2+} + O^-$ [14]. The luminescence spectrum of the $Li_6Y_{1-x}Eu_x(BO_3)_3$ crystals contains groups of lines in the range between 575 and 725 nm, which correspond to the transitions from the first excited state $^5D_0$ of the Eu^{3+} ion to the ^7F_J (J = 0–4) levels [14–16]. Figure 3 shows the photoluminescence spectra of the $Li_6Y_{1-x}Eu_x(BO_3)_3$ single crystals. The highest photoluminescence intensity is observed for the $Li_6Y_{0.5}Eu_{0.5}(BO_3)_3$ single crystal (Fig. 3; curve *2*), which is in agreement with the data of [15] for the corresponding powders. Weak concentration luminescence quenching is caused by the weak interaction of Eu ions with the crystal-lattice field and is related to the anisotropy of the crystalline structure of this compound [14, 16]. After irradiation, the photoluminescence intensity of $Li_6Y_{0.97}Eu_{0.03}(BO_3)_3$ crystals decreases, which is indicative of the transition of some part of Eu ions to the stable divalent state ($Eu^{3+} \longrightarrow Eu^{2+}$) with the formation of $Eu^{2+}_{Gd^{3+}} + O^-$ centers.

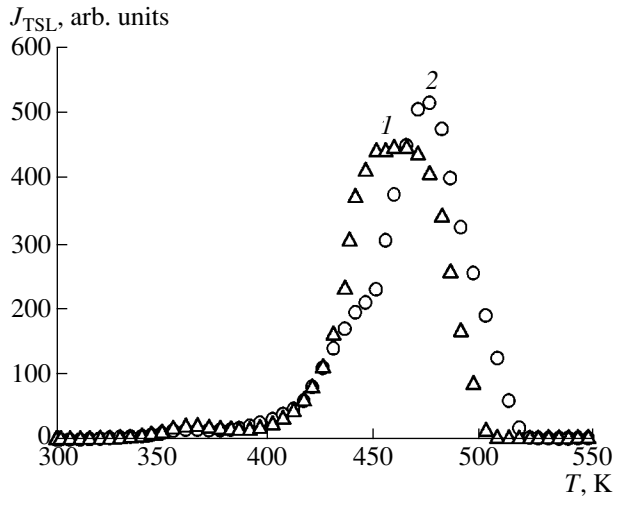

Fig. 4. TSL curves of the β-irradiated crystals (dose 10^6 rad): (*1*) $Li_6Y_{0.97}Eu_{0.03}(BO_3)_3$ and (*2*) $Li_6Gd_{0.97}Eu_{0.03}(BO_3)_3$; the composition is indicated for the charge.

$Li_6Y_{0.5}Eu_{0.5}(BO_3)_3$ and $Li_6Eu(BO_3)_3$ crystals, as well as $Li_6Gd(BO_3)_3$ pure crystals [7], show no TSL. The presence of weak TSL peaks in $Li_6Y(BO_3)_3$ crystals is apparently related to the presence of rare-earth elements in very small amounts (according to the chemical-analysis data, their total concentration is 10^{-3} wt %). In Fig. 4, the TSL curves for the $Li_6Y_{0.97}Eu_{0.03}(BO_3)_3$ crystals are compared with the corresponding curves for the $Li_6Gd_{0.97}Eu_{0.03}(BO_3)_3$ crystals. It can be seen that the curves are almost identical. Both contain a doublet in the temperature range t = 450–480°C with similar activation energies (E_a ~ 1.2 eV). The similarity of the TSL curves is also characteristic for other isostructural oxide crystals, for example, M_2SiO_5 : Ce (M = Lu, Y, Yb, or Er) [17]. Therefore, we can suggest that the TSL of the $Li_6Y_{0.97}Eu_{0.03}(BO_3)_3$ crystals is also related to the decay of O^- hole centers (high-temperature hole centers are known to exist in borate glasses [18]). A hole, released as a result of thermal activation, is captured by an Eu^{2+} ion. As a result, radiative relaxation occurs according to the equation $Eu^{2+} + e^+ \longrightarrow (Eu^{3+})^* \longrightarrow Eu^{3+} + h\nu$, where $(Eu^{3+})^*$ is the excitation state of the Eu^{3+} ion. After annealing, the photoluminescence intensity of the $Li_6Y_{0.97}Eu_{0.03}(BO_3)_3$ crystals takes its initial value. Measurements of the TSL using light filters confirm the mechanism proposed: the emission spectrum is located in the wavelength range $\lambda \geq 600$ nm, which is in good agreement with the experimentally observed emission spectrum of Eu^{3+}.

CONCLUSIONS

It is shown that the $Li_6Y(BO_3)_3$–$Li_6Eu(BO_3)_3$ system is characterized by unlimited mutual solubility. It is ascertained that single crystals of $Li_6Y_{1-x}Eu_x(BO_3)_3$ solid solutions can be grown by the Czochralski method in the entire range of values of x. Thermally stimulated luminescence of $Li_6Y_{1-x}Eu_x(BO_3)_3$ crystals was studied for the first time. The TSL of these crystals, as well as that of $Li_6Gd_{1-x}Eu_x(BO_3)_3$ crystals, is related to the decay of O^- centers with subsequent radiative relaxation of Eu^{3+} ions.

ACKNOWLEDGMENTS

We are grateful to V.N. Baumer for supplying the X-ray diffraction data and Z.V. Shtitel'man for help in the chemical analysis of samples.

REFERENCES

1. C. W. E. van Eijk, Radiat. Prot. Dosim. **110**, 5 (2004).
2. J. B. Czirr, G. M. MacGillivray, R. R. MacGillivray, and P. J. Seddon, Nucl. Instrum. Methods Phys. Res. A **424**, 15 (1999).
3. J. P. Chaminade, O. Viraphong, F. Guillen, *et al.*, IEEE Trans. Nucl. Sci. **48**, 1158 (2001).
4. V. V. Chernikov, M. F. Dubovik, V. P. Gavrilyuk, *et al.*, Nucl. Instrum. Methods Phys. Res. A **498**, 424 (2003).
5. J. B. Czirr, D. B. Merrill, D. Buehler, *et al.*, Nucl. Instrum. Methods Phys. Res. A **476**, 309 (2002).
6. A. M. Williams, P. A. Beeley, and N. M. Spyrou, Radiat. Prot. Dosim. **110**, 497 (2004).
7. V. N. Baumer, M. F. Dubovik, B. V. Grinyov, *et al.*, Radiat. Meas. **38**, 359 (2004).
8. M. J. Knitel, P. Dorenbos, C. W. E. van Eijk, *et al*., Nucl. Instrum. Methods Phys. Res. A **443**, 364 (2000).
9. R. Yavetskiy, A. Tolmachev, and B. Grinyov, in *Proceedings of the 3rd International Workshop "Physical Aspects of the Luminescence of Complex Oxide Dielectrics" (LOD-2004), Kharkiv, Ukraine, 2004* (Kharkiv, 2004), p. 27.
10. M. F. Dubovik, V. A. Tarasov, A. V. Tolmachev, and R. P. Yavetskiy, in *Proceedings of the 15th International Conference on Defects in Isulating Materials (ICDIM-2004), Riga, Latvia, 2004* (Riga, 2004), p. 92.
11. J. P. Chaminade, O. Viraphong, and S. Miyazawa, J. Cryst. Growth **237–239**, 864 (2002).
12. P. P. Fedorov and L. V. Medvedeva, Zh. Neorg. Khim. **34**, 2674 (1989).
13. T. I. Korshikova, R. P. Yavetskiy, and A. V. Tolmachev, Funct. Mater. **10** (3), 407 (2003).
14. V. Jubera, J. P. Chaminade, A. Garcia, *et al.*, J. Lumin. **101**, 1 (2003).
15. M. Leskelá and J. Hölsá, Eur. J. Solid State Inorg. Chem. **28**, 151 (1991).
16. J. Hölsá and M. Leskelá, J. Lumin. **48-49**, 497 (1991).
17. D. W. Cooke, B. L. Bennett, K. J. McClellan, *et al.*, J. Lumin. **92**, 83 (2001).
18. D. L. Griscom, J. Non-Cryst. Solids **13** (2), 251 (1974).

Translated by Yu. Sin'kov

Crystallography Reports, Vol. 50, Suppl. 1, 2005, pp. S92–S96.

CRYSTAL GROWTH

Effect of the Growth Rate on Thermal Conditions During the Growth of Single Crystals with Melt Feeding

N. N. Timoshenko, V. I. Goriletskiĭ, B. V. Grinev, V. I. Sumin, and O. V. Sizov

Institute for Scintillation Materials, National Academy of Sciences of Ukraine, pr. Lenina 60, Kharkov, 61001 Ukraine

e-mail: tymoshenko@isma.kharkov.ua

Received February 8, 2005

Abstract—An attempt is made to establish a correlation between the radial and axial growth rates and the change in the conditions of heat transfer from a growing crystal to the atmosphere of the water-cooled vacuum furnace for the growth of large alkali halide single crystals. It is found experimentally that an increase in the growth rate leads to an increase in the automatic compensation of the melt temperature by the main heater. In this case, the thickness of the layer of melt condensate on the end face and the lateral surface of the crystal decreases. It is revealed that the possibility of growing infinitely long ingots in the presence of intense melt evaporation is restricted by the possibilities of the heat transport through the boundary between the furnace atmosphere and the cooled furnace walls, onto which melt condensate deposits. © *2005 Pleiades Publishing, Inc.*

INTRODUCTION

The growth of crystals represents a certain sequence of physico-chemical processes occurring in a certain. Naturally, the longest-term processes attract more attention and have been studied in more detail. One such process is that of natural melt evaporation. Evaporation, which is a fundamental property of melts, is determined by the vapor elasticity tension, pressure, temperature, and the free melt surface. The optimal pressure in the growth furnace changes during the growth in a narrow range (from 1–5 Torr during the melting of the initial charge in the crucible to 15–30 Torr during all subsequent growth stages). The pressure increases to such values from vacuum (~10^{-1} Torr) by supplying such gases as He, Ar, N_2, CO_2, and their mixtures. After this, the melt evaporation decreases step-wise (and significantly). Quantitative estimates for different gases are absent, but rough estimation shows that the evaporation rate changes by several orders of magnitude. With a further increase in the partial gas pressure, the furnace atmosphere loses transparency and the process, which should be controlled visually, cannot be continued. Helium is an exception, since it retains transparency even at an excess pressure. However, due to strong convective fluxes in the melt, growth under such conditions also turned out to be impossible. No detailed investigations of the dependence of the evaporation rate of iodides of alkali metals on pressure in systems of this type have been performed. However, according to rough estimations, in the pressure range 15–30 Torr, the melt-evaporation rate does not change significantly for any of the above-mentioned gases. The purpose of this study is to establish the dependence of the intensity of heat transfer from the surface of a growing crystal to the environment at different growth rates.

EXPERIMENTAL TECHNIQUE

Investigations were performed on ROST vacuum compression systems [1] of the first and second generation. CsI(Na) and NaI(Tl) single crystals (up to 320 and 540 mm in diameter, respectively) were grown with an automatic control through the feedback with the temperature of the bottom heater using current data on the position of the melt level in the crucible [2]. It is the bottom heater that is chosen for automated control of the growth process in ROST systems. The contribution of this element to the melt heating is decisive. Therefore, the recorded change in the temperature t_{bot} of the bottom heater reflects to a large extent the change in the conditions of heat removal from a growing crystal.

The schematic of the ROST system is shown in Fig. 1. To maintain a constant level of melt in the crucible *1* during the growth of a crystal *2*, the system is equipped with an annular reservoir *3*, into which an initial charge is supplied from the feeder *4* through the transport tube *5*. Being melted by the lateral heater *6*, the charge flows through the aperture *7* into the gap between the crucible walls and the shield *8* and then is mixed with the melt *9*, whose level is measured by the probe of the melt-level meter *10*.

The growth of large CsI(Na), CsI(Tl), and NaI(Tl) single crystals in ROST systems occurs as follows. The initial salt is supplied to the charge-preparation unit, where it is subjected to additional dehydration at different temperatures and under continuous evacuation (the temperature regimes are different for the CsI and NaI

1063-7745/05/5001-S0092$26.00

salts). During the dehydration, the salt acquires flowability, which is necessary for the optimal operation of the vibration dispenser of the melt-feeding system. From the charge-preparation unit, the salt is transferred to the growth zone in evacuated quartz cells. If necessary, the salt is mixed with an activator in the growth zone. When CsI(Na) single crystals are grown, this procedure is omitted: an activator in the form of the NaI salt is loaded into the crucible only once immediately before the growth. Then, the salt is supplied from removable bins to maintain a constant melt level in the crucible throughout the experiment.

After loading the crucible with the initial charge, the growth furnace is degassed and the heater temperatures are increased at a certain rate to the melting temperature of the initial charge in the crucible under continuous evacuation. At the first signs of charge melting, the above-mentioned gases are fed into the furnace with an increase in pressure up to 15–30 Torr. Then, the charge in the crucible melts, after which the crystal growth begins.

The crystal growth is performed by seed pulling at a certain rate with simultaneous initial-charge feeding to the melt. During the growth, the single crystal and the crucible are uniformly rotated in the same direction but at different rates, which makes the temperature field symmetric and provides for the necessary melt stirring in the crucible. The crystal holder and the furnace walls are cooled by water to form the axial temperature gradient required for the crystal growth.

EXPERIMENTAL RESULTS

The melt temperature above the melting point is obtained when the salt melts in the crucible. The time during which the salt melts away depends on temperature: at a low superheating of the salt above the melting point, the melting process elongates; at a high superheating, we have enhanced evaporation. Such a parameter as the area of evaporation of the melt and its components (S_L) appears to be most important in the growth of large crystals, which require crucibles with large cross sections. Taking into account that the melt-level sensor should also be located on the melt surface, the diameter of the melt mirror should exceed the limiting crystal diameter. For this reason, there is an annular gap on the melt surface between the growing crystal and the crucible. It is this gap that determines the parameter S_L. In the stage of salt melting in the crucible, S_L is maximum; in the stage of radial crystal growth to the final diameter, this area decreases; and, in the stage of axial growth, the value of S_L is stabilized to the specified minimum. It is in the latter stage that the volatile activator Tl is introduced into the feed composition (as a thallium iodide salt) during the growth of CsI(Tl) and NaI(Tl) scintillation single crystals. The axial-growth time is 14–20 and 34–50 h for crystals about 320 and 540 mm in diameter, respectively.

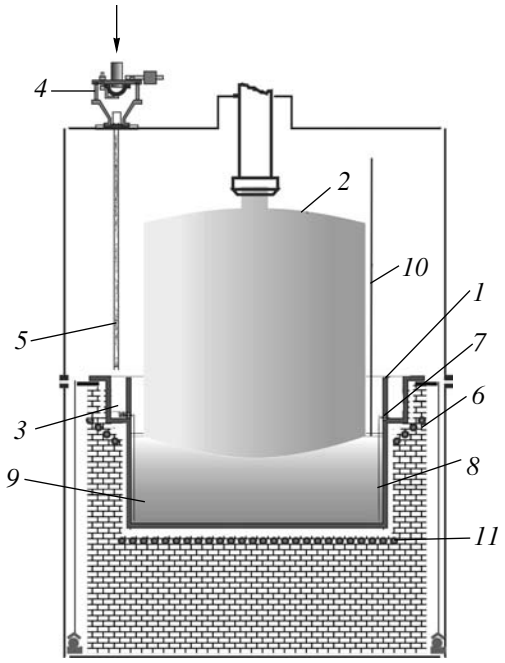

Fig. 1. Schematic of the ROST system: (*1*) crucible, (*2*) crystal, (*3*) annular peripheral reservoir, (*4*) feeder, (*5*) transport tube, (*6*) side heater, (*7*) apertures, (*8*) shield, (*9*) melt, (*10*) probe of the melt-level sensor, and (*11*) bottom heater.

The melt evaporation leads to the formation of a condensate on the crystal surface and the internal walls of the growth furnace. The deposition rate of the condensate and, therefore, its thickness depend on time and temperature for specific pressures in the furnace and sizes S_L. With an increase in the diameter, a radially growing crystal gradually reduces the melt surface, from which not only evaporation but also effective heat transfer to the environment occurs. The denser and thicker the condensate layer on the crystal, the smaller the amount of heat emerging from the crystal into the environment and the smaller the value of t_{bot}, which compensates for the heat transfer from the crystal to the environment by the automated system throughout the growth process and, especially, at the critical instant: when the crystal emerges outside the crucible. The main factor determining the temperature gradient in the atmosphere around the crystal is the transparency of the crystal surface for thermal radiation. In other words, the boundary condensate layer on the crystal is actually located between the heat source (heaters) and the environment in the growth furnace. Thus, the thermal conditions in the furnace volume are determined by the transparency of the condensate on the ingot surface.

The above considerations were verified experimentally. For example, when the time of the radial growth of a CsI(Na) crystal to the final size (310 mm) increased from 12 to 20 h, t_{bot} increased from 770 to 790°C by the end of this stage (Fig. 2). As was shown in [3] for dif-

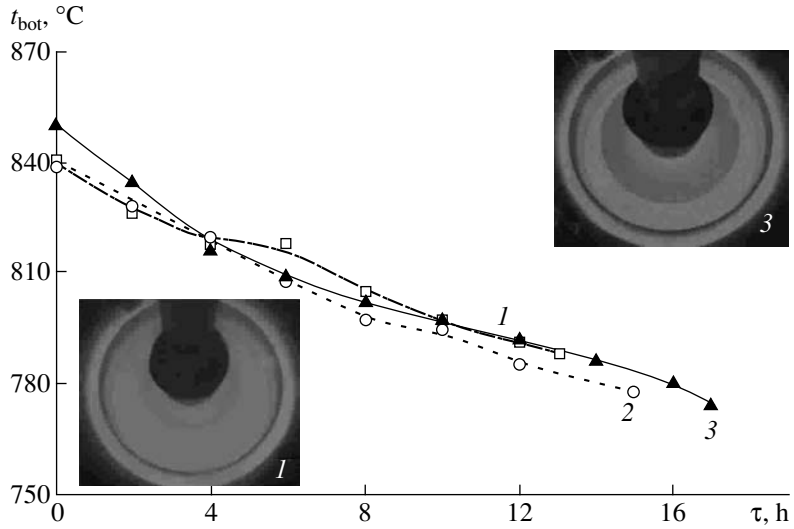

Fig. 2. Time dependences of the automatic correction of the bottom-heater temperature during the radial growth of 310-mm CsI(Na) single crystals at different growth rates: (*1*) 8.0, (*2*) 7.0, and (*3*) 6 mm/h. The numbers on the photographs correspond to the numbers of the curves.

ferent radial-growth rates, the condensate layer was thicker and denser specifically on the end face of the crystal that was grown for a longer time. In our opinion, this finding is confirmed by the photographs made without additional illumination, i.e., at natural temperature luminescence of the crucible, the melt, and the crystal (Fig. 2, bottom left and top right). These photographs can be considered as qualitative distribution patterns of the heat-insulating material (i.e., the layer of the melt condensate) over the radius of the growing ingot. A similar distribution is observed for the growth of other crystals, in particular, NaI(Tl) crystals up to 520 mm in diameter (Fig. 3). At high radial-growth rates, a large number of radial block boundaries may be formed. Therefore, we limited the radial-growth time to the minimum: 34 h (Fig. 3, curve *1*). In this case, the radial-growth rate was about 6 mm/h. It should be noted that scintillation crystals NaI(Tl) allow the presence of block boundaries leading to a lattice misorientation as high as several degrees. At radial-growth rates exceeding 6 mm/h, the growth edge of the crystal becomes discontinuous as a result of the additional melting at the block boundaries, and the process becomes unstable.

The time dependence of t_{bot} in this growth stage is characterized by a minimum. This minimum corresponds to the instant when the top face end of the crystal passes the level of the top rim of the crucible, after which the value of t_{bot} and, accordingly, the heat removal from the crystal begin to increase.

Thus, the investigations performed reveal a correlation between the radial-growth rate and the minimum value of t_{bot} (the latter directly depends on the properties and amount of the condensate on the crystal).

Concerning the probability of the defect formation in the volume of the growing crystal [4], the duration of the time interval from the onset of the salt melting in the crucible to the onset of axial growth becomes very important. An increase in the process duration is equivalent to a decrease in the axial temperature gradient. At the same time, the larger the axial-temperature gradient, the more stable is the growth and the lower is the probability of forming structural defects in the growing crystal, and vice versa.

The above considerations give grounds to conclude that the time from the onset of the salt melting in the crucible to the onset of the stationary phase (axial crystal growth) should be minimized.

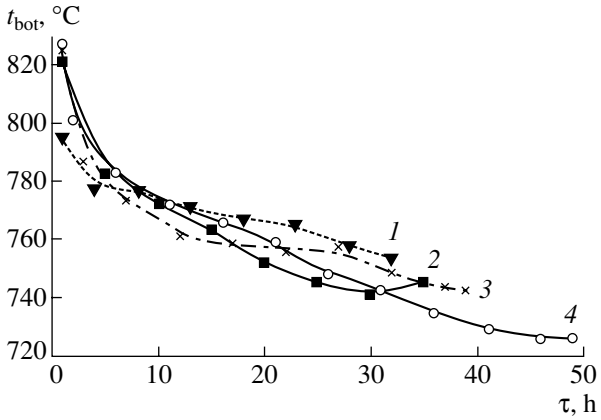

Fig. 3. Time dependences of the automatic correction of the bottom-heater temperature during the radial growth of 520-mm NaI(Tl) single crystals at different growth rates: (*1*) 5.8, (*2*) 5.4, (*3*) 5, and (*4*) 4 mm/h.

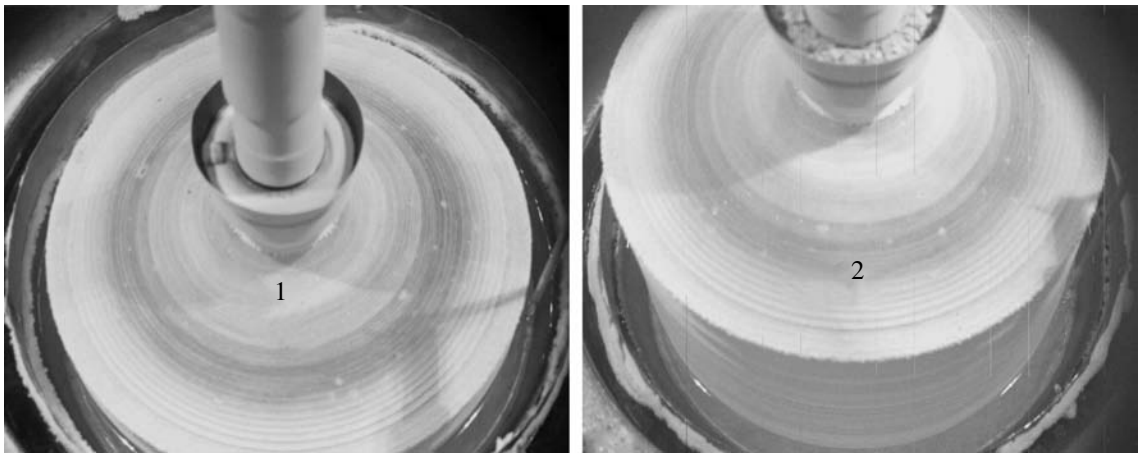

Fig. 4. Deposition of melt condensate on the top end faces of NaI(Tl) single crystals by the end of the radial growth to a diameter of 520 mm (crystal 1) and the stabilization of the condensate coating during the subsequent axial growth of the ingot after 100 h (crystal 2).

The presence of a condensate coating is an undesirable factor of the ingot growth. At the same time, this factor is favorable to a certain extent. Observations of the growth process show that the visual picture of the top face end of the crystal is nearly frozen at the instant when the growth changes from radial to axial. An example is the growth of NaI(Tl) single crystals up to 520 mm in diameter (Fig. 4): the time interval between the instances at which crystals 1 and 2 were photographed is about 100 h, but there is only a slight difference in the amount of condensate deposited by these instances. The reason for this phenomenon is not only the constancy of the parameter S_L and, respectively, the evaporation rate, but also that the mass evaporation rate is low in this stage and can be calculated for each specific case [5]. When the growth changes from radial to axial, a condensate layer begins to grow on the newly formed lateral surface, as evidenced by the stable picture observed on the end surface (Fig. 4). This observation suggests another conclusion: the area of the lateral crystal surface increases continuously and proportionally to the pulling rate. This increase is sufficient for the deposition of the entire amount of the evaporating condensate. Next, we can suggest that the magnitude of the current parameter t_{bot} in the axial-growth stage should depend on the rate of formation of the lateral crystal surface, i.e., on the axial-growth rate of the ingot.

This suggestion, which would seem to be inconsistent at first glance (from the general considerations, the increase in the crystal-growth rate should require a larger decrease in t_{bot} in comparison with lower growth rates), was confirmed by the results of our study. As can be seen in Fig. 5, which shows the actual dependences of the automatic compensation of the temperature of the main bottom heater on the crystal length at different growth rates, the slope of the curve $t_{bot}(H_{cr})$ increases after the minimum at higher growth rates. Such a situation is possible in only one case (all other factors being equal): when the phase boundary between the crystal surface and the surrounding furnace space becomes more transparent for the radiant heat transfer. Thus, a logical conclusion can be drawn: the condensate on such a surface should be thinner and more transparent

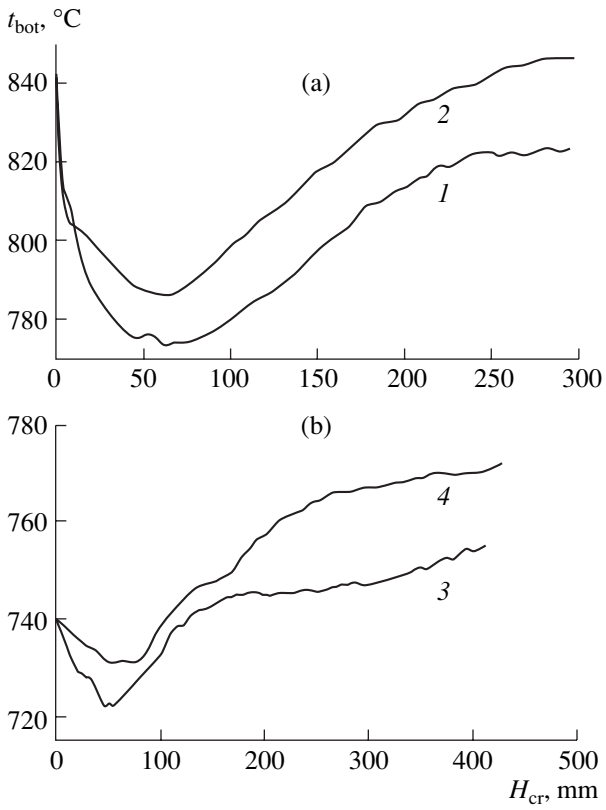

Fig. 5. Dependences of the automatic compensation for temperature by the bottom heater on the crystal length during the growth of (a) 310-mm CsI(Na) single crystals and (b) 540-mm NaI(Tl) single crystals at different growth rates: (*1*) 2.5, (*2*) 4.0, (*3*) 2.0, and (*4*) 3.7 mm/h.

for IR radiation at higher growth rates. Indeed, preliminary qualitative estimations of the amount of condensate on the surface of a grown crystal, made by measuring the condensate transparency to IR radiation, show a significant difference.

Since the condensate has a loose structure and high hygroscopicity, it is difficult to obtain quantitative data for it. However, there are plans to carry out such experiments.

In our opinion, another interesting result of this study is the evident possibility of controlling the axial temperature gradient in a growing crystal. Returning to the dependences $t_{bot}(H_{cr})$ in Fig. 5, we should note that the time compensation for t_{bot} is larger for crystals pulled at higher rates; in other words, the heat exchange between the crystal and the furnace atmosphere is more intense in this case, and, therefore, the temperature gradient in the crystal is higher.

On the basis of the results obtained, we can generalize the previous conclusion: not only the time interval from the onset of the salt melting in the crucible to the onset of the axial growth, but also the total time of the process (to the end of the crystal growth) should be minimized.

The above original result gives grounds to conclude that there is a significant resource in the further development of our physical understanding of the crystallization of alkali halides in the mode of automatic semicontinuous growth in ROST systems.

Considering the sequence of the dominant radiative heat transfer, we investigated only the phase boundary between the crystal and the furnace atmosphere. However, along with this boundary, other phase boundaries are known: crystal/melt; melt/furnace atmosphere; and the specific boundary between the furnace atmosphere and the water-cooled furnace walls, which is characteristic of only completely open nonconservative systems. Returning again to Fig. 5, note that the slope of the curves $t_{bot}(H_{cr})$ decreases when the crystal length reaches the value of approximately 250 mm at both growth rates for two types of crystals. In our opinion, this phenomenon confirms the existence of the thermophysical boundary between the furnace atmosphere and the water-cooled furnace walls. In the next heat-transfer sequence (after the heat transfer through the crystal/furnace boundary), the heat-transfer ability of the boundary between the furnace atmosphere and the furnace walls decreases as a result of the increase in the thickness of the condensate layer. In a narrow range of growth rates, the amount of condensate can be controlled by decreasing the process time. However, this method is invalid for the latter heat-transfer sequence. In essence, this experimental fact limits the length of ingots grown and indicates that a special technique should be developed to remove the condensate from the furnace. For alkali halide crystals, at least to date, this problem is not urgent.

Currently, we can draw some conclusions (based on the indirect experimental data) about the existence of some mental dependences. However, actual processes can be revealed only in direct experiments, which have already begun [6].

CONCLUSIONS

A correlation between the radial and axial crystal-growth rates and the change in the conditions of heat transfer from a growing crystal to the environment is established: with an increase in the growth rate, the heat exchange at the phase boundary between the crystal and the furnace atmosphere becomes more intense owing to the decrease in the thickness of the condensate layer deposited on the crystal surface. It is shown that the possibility of growing ingots of arbitrary length under conditions of intense melt evaporation is limited by the possibilities of the heat transfer through the boundary between the furnace atmosphere and the water-cooled furnace walls covered by a layer of melt condensate.

REFERENCES

1. L. G. Eidelman, V. I. Goriletsky, V. G. Protsenko, *et al.*, J. Cryst. Growth **128**, 1059 (1993).
2. S. K. Bondarenko, V. I. Goriletsky, and V. S. Suzdal, Funct. Mater. **6**, 380 (1999).
3. V. I. Goriletsky, S. K. Bondarenko, M. M. Smirnov, *et al.*, J. Korean Cryst. Growth Cryst. Technol. **13**, 5 (2003).
4. V. I. Goriletsky, B. V. Grinyov, V. S. Suzdal, *et al.*, in *Proceedings of the 14th International Conference on Crystal Growth, Grenoble, 2004* (Grenoble, 2004), p. 570.
5. V. I. Goriletsky and N. N. Smirnov, J. Cryst. Growth **218**, 125 (2000).
6. O. Ts. Sidletskii, V. I. Goriletskii, N. N. Timoshenko, *et al.*, in *Proceedings of the 11th National Conference on Crystal Growth, Moscow, Russia, 2004* (Moscow, 2004), p. 223.

Translated by Yu. Sin'kov

Crystallography Reports, Vol. 50, Suppl. 1, 2005, pp. S97–S99.

CRYSTAL GROWTH

Crystallization of Trigonal $(Tb,Er)(Fe,Ga)_3(BO_3)_4$ Phases with Hantite Structure in Bismuth Trimolybdate-Based Fluxes

L. N. Bezmaternykh*, V. L. Temerov*, I. A. Gudim*, and N. A. Stolbovaya**

** Kirenskiĭ Institute of Physics, Siberian Division, Russian Academy of Sciences, Akademgorodok, Krasnoyarsk, 660036 Russia*

e-mail: bezm@iph.krasn.ru

*** Krasnoyarsk State University, Krasnoyarsk, Russia*

Received February 3, 2005

Abstract—The stability regions of the trigonal $(Tb,Er)(Fe,Ga)_3(BO_3)_4$ phases are established in $(Bi_2Mo_3O_{12})$-based fluxes. The specific features of heterogeneous nucleation and the subsequent phase transformations during transition to the equilibrium are studied in the vicinity of the boundaries. The temperature modes of single crystal growth on seeds are suggested with due regard for the "nonequilibrium effect." *© 2005 Pleiades Publishing, Inc.*

INTRODUCTION

Single crystals of rare earth gallium ferroborates $R(Fe,Ga)_3(BO_3)_4$ with the hantite structure consist of linear chains of RO_6 trigonal prisms and helicoidal FeO_6 octahedra located along the threefold axis.

The quasi-one-dimensional structure of the rare earth and iron subsystems stimulated the study of the specific features of magnetism demonstrated by these compounds.

The widespread use of static magnetic measurements [1], methods of magnetic resonance [2], calorimetry [3, 4], linear and nonlinear optical spectroscopy [3, 5], and Mössbauer spectroscopy under high pressures [6] have allowed the most detailed studies of gadolinium ferroborate $GdFe_3(BO_3)_4$ single crystals.

In light of the study of magnetic ordering in the rare earth and iron subsystems and their interaction in this class of compounds, the experiments on single crystals of terbium and erbium ferrogalloborates, $Tb(Fe,Ga)_3(BO_3)_4$ and $Er(Fe,Ga)_3(BO_3)_4$, seem to be important.

The present study was undertaken to study the conditions of synthesis of the above single crystals from bismuth trimolybdate-based fluxes: $Bi_2Mo_3O_{12} + pB_2O_3 + q(Tb,Er)_2O_3 + r(Tb,Er)(Fe,Ga)_3(BO_3)_4$. Unlike the well-known Bi_2O_3-based fluxes [8], in bismuth trimolybdate-based fluxes, Bi_2O_3 is strongly bonded to MoO_3 [7], which should exclude any partial substitution of bismuth for rare earth elements during crystallization.

STABILITY REGIONS OF THE TRIGONAL $(Tb,Er)(Fe,Ga)_3(BO_3)_4$ PHASE

Fluxes with different *p*, *q*, and *r* values and weights up to 30 g were prepared in a 50-mm^3 platinum crucible by sequential melting together of the Bi_2O_3, MoO_3, B_2O_3, $(Fe,Ga)_2O_3$, and $(Tb,Er)_2O_3$ oxides at $t = 1000$°C. Homogenization processes, the spontaneous nucleation of crystals, and characteristics of the transition to the equilibrium states were studied only for fluxes with saturation temperatures not exceeding 1000°C. This limitation excluded any significant noncontrollable variations in the crystallization conditions even in long-durable experiments with an open crucible.

It was established that the trigonal phase of the $(Tb,Er)(Fe,Ga)_3(BO_3)_4$ compound is crystallized within a certain interval of the temperature range 1000–850°C only in the fluxes with nonstoichiometric amounts of the crystal-forming oxides ($p \neq 0$ and $q \neq 0$). The high-temperature phase that is stable in a large temperature range is formed only in the narrow region of the (*p*, *q*, *r*) parametric space. Examples of the fluxes of such compositions are indicated in the table (*1*, *2*, *4*, *5*).

ADJACENT PHASES. NONEQUILIBRIUM EFFECT

The stable high-temperature phase in the fluxes not containing Ga_2O_3 and with stoichiometric amounts of the crystal-forming oxides ($p = q = 0$) is the α-Fe_2O_3 phase (hematite). At a certain superstoichiometric amount of B_2O_3 ($p = p_1$ and $q = 0$), the hematite phase is transformed into the orthorhombic Fe_3BO_6 phase. Finally, in the fluxes with a considerable excess of boron oxides and rare earth element ($p > p_2$ and $q > q_2$), the stable high-temperature phase is the hexagonal $(Tb,Er)BO_3$ phase. In the (*p*, *q*, *r*) parametric space, the stability regions of the above phases are adjacent to the stability region of the trigonal $(Tb,Er)Fe_3(BO_3)_4$ phase.

It is established that the transition of supercooled flux *1* into the state equilibrium with respect to

Composition of bismuth trimolybdate-based fluxes

Flux	Fluxes composition					t_{sat}, °C	dt_{sat}/dn, °C/wt %	Competing nonequilibrium phases
	in moles				in quasibinary form			
	p	*q*	*r*	*s*				
1	1.5	0.3	0	0.88	70.9 wt % ($Bi_2Mo_3O_{12}$ + 1.5B_2O_3 + 0.3Tb_2O_3) + 29.1 wt % $TbFe_3(BO_3)_4$	950	5	α-Fe_2O_3
2	3	0.5	0	0.87	72.4 wt % ($Bi_2Mo_3O_{12}$ + 1.5B_2O_3 + 0.5Er_2O_3) + 27.6 wt % $ErFe_3(BO_3)_4$	945	5	α-Fe_2O_3, Fe_3BO_6, $ErBO_3$
3	4	0.5	0.5	0.99	65.1 wt % ($Bi_2Mo_3O_{12}$ + 4B_2O_3 + 0.3Tb_2O_3 + 0.5 Li_2MoO_4) + 24.9 wt % $TbFe_3(BO_3)_4$	940	4.5	α-Fe_2O_3
4	2	0.3	0	0.83	70 wt % ($Bi_2Mo_3O_{12}$ + 2B_2O_3 + 0.3Er_2O_3) + 30 wt % $ErGa_3(BO_3)_4$	930	5	β-Ga_2O_3
5	2.5	0.4	0	0.59	77 wt % ($Bi_2Mo_3O_{12}$ + 2.5B_2O_3 + 0.4Er_2O_3) + 23 wt % $ErGa_3(BO_3)_4$	940	4.5	–

$TbFe_3(BO_3)_4$ proceeds via the intense formation of hematite and its subsequent dissolution ("nonequilibrium effect"). Depending on *p*, *q*, and *r* values and the preset initial supercooling, this effect may manifest itself in the nucleation of another adjacent phase or of two adjacent phases simultaneously (Fig. 1a).

In fluxes not containing Fe_2O_3 (composition *4* in table) and containing stoichiometric amounts of the crystal-forming oxides ($p = q = 0$), the stable high-temperature phase is β-Ga_2O_3. However, the stability region of the trigonal phase in these fluxes is wider, so that it is possible to select *p*, *q*, and *r* such that the non-

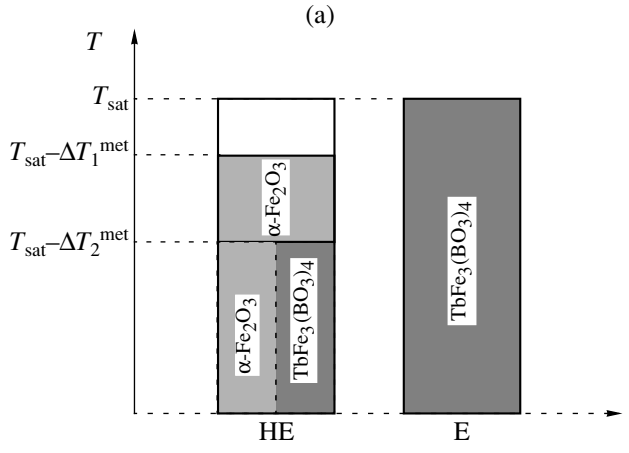

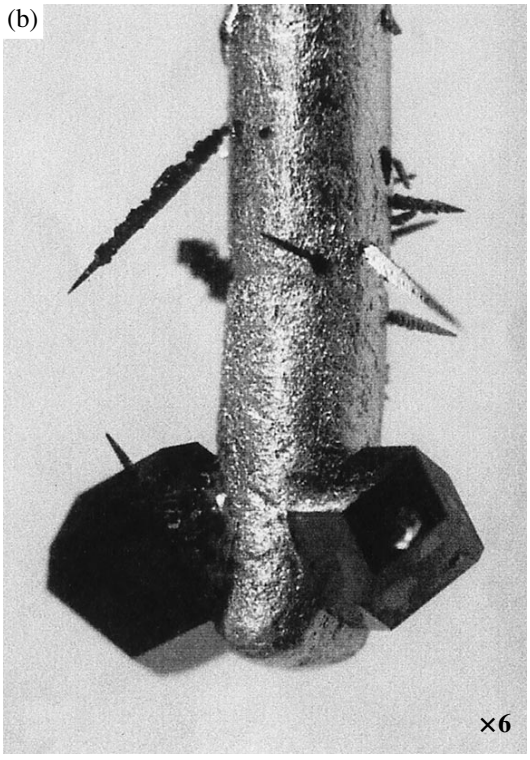

Fig. 1. (a) Nonequilibrium (NE) and equilibrium (E) temperature sequences for the phases crystallized in fluxes *3* (see table). For α-Fe_2O_3, the width of the metastable region is Δt_1^{met} = 7–10°C, for $TbFe_3(BO_3)_4$, Δt_2^{met} = 30–35°C. (b) Results of crystallization on a holder with two seeding $TbFe_3(BO_3)_4$ crystals in flux *3* at Δt_{in} = 12°C, τ = 24 h.

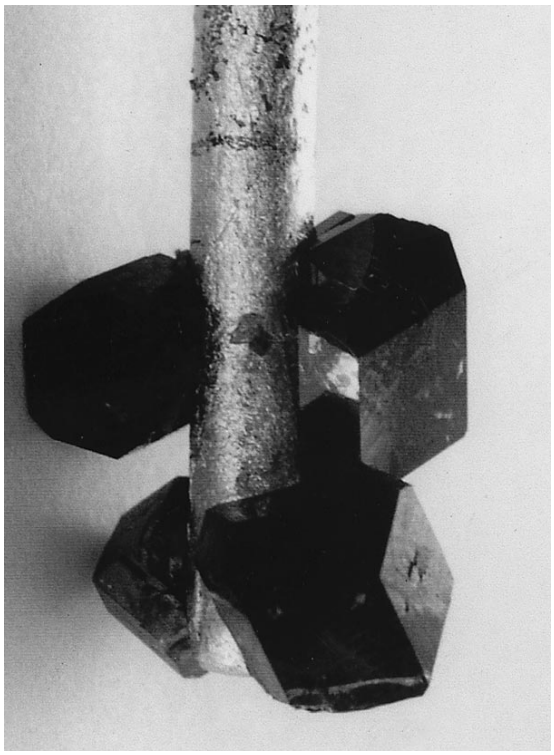

Fig. 2. $TbFe_3(BO_3)_4$ single crystals grown on seeds in flux *3* at Δt_{in} = 5°C, $dt/d\tau$ = (1–2)°C/day, τ = 4 days.

equilibrium effect will not manifest itself at all (composition *5* in table).

INFLUENCE OF FLUXES DILUTION BY LITHIUM MOLYBDATE

Addition of lithium molybdate to the above-mentioned bismuth trimolybdate-based fluxes decreases their viscosity and density in accordance with the reaction $Bi_2Mo_3O_{12} + pB_2O_3 + q(Tb,Er)_2O_3 + sLi_2MoO_4 + r(Tb,Er)Fe_3(BO_3)_4$. As a result, the danger of nucleation and growth of floating parasitic crystals on the fluxes surface kept by the forces of surface tension considerably decreases. With a decrease in viscosity, the probability of the formation of defects (fluxes inclusions) also decreases. At the same time, the stability region of the trigonal $(Tb,Er)Fe_3(BO_3)_4$ phase becomes narrower. A compromise between these two factors is achieved by the fluxes dilution with $s \le 0.5$ (composition *3* in table).

ALLOWANCE FOR NONEQUILIBRIUM EFFECT IN CRYSTALLIZATION ON SEEDS

If the nonequilibrium effect takes place, each of the phases is characterized by its own threshold supercooling Δt_{met} after the attainment of which nucleation takes place (Fig. 1a). In crystallization on $(Tb,Er)Fe_3(BO_3)_4$ seeds, the initial supersaturation and the rate of the subsequent gradual temperature decrease should be selected in such a way as to avoid the attainment of the threshold supercooling. Figure 1b shows the result of crystallization in the case where this condition was violated. Along with the $(Tb,Er)Fe_3(BO_3)_4$ seeds, "needle-like pyramids" consisting of small hematite rhombohedra also grew on the crystal holder. One such pyramid grew into the seed. The result of a growth experiment in the appropriate temperature mode is shown in Fig. 2.

CONCLUSIONS

The compositions of fluxes are found such that the trigonal $(Tb,Er)(Fe,Ga)_3(BO_3)_4$ phase is the high-temperature phase stable over a wide temperature range. These fluxes are much better than other known media for the growth of single crystals of this compound [8].

With due regard for the discovered nonequilibrium effect, the choice of the temperature modes of growth is substantiated. Trigonal single crystals of the composition $(Tb,Er)(Fe,Ga)_3(BO_3)_4$ are grown in order to study the specific characteristics of their magnetic properties related to the quasi-one-dimensional structure of the rare earth and iron subsystems.

REFERENCES

1. D. Balaev, L. N. Bezmaternykh, I. A. Gudin, *et al.*, J. Magn. Magn. Mater. **532**, 258 (2003).
2. A. I. Pankrats, G. A. Petrakovskiĭ, L. N. Bezmaternykh, *et al.*, Zh. Éksp. Teor. Fiz. **10**, 887 (2004) [JETP **99**, 766 (2004)].
3. R. Z. Levitin, E. A. Popova, and R. M. Chtsherbov, Pis'ma Zh. Éksp. Teor. Fiz. **79** (9), 531 (2004) [JETP Lett. **79** (9), 423 (2004)].
4. Yu. Hinatsu, Y. Doi, K. Ito, *et al.*, Solid State Chem. **172**, 438 (2003).
5. A. M. Kalashnikova, V. V. Pavlov, and R. V. Pisarev, Pis'ma Zh. Eksp. Teor. Fiz. **80** (5), 339 (2004) [JETP Lett. **80** (5), 293 (2004)].
6. L. N. Bezmaternykh, A. G. Gavriliuk, and S. A. Kharlamova, in *Abstract Book of EASTMAG* (Inst. Fiz. Sib. Otd., Krasnoyarsk, 2004), p. 148.
7. L. N. Bezmaternykh, S. A. Kharlamova, and V. L. Temerov, Kristallografiya **49** (4), 945 (2004) [Crystallogr. Rep. **49** (5), 855 (2004)].
8. N. I. Leonyuk, Prog. Cryst. Growth Charact. **31**, 279 (1995).

Translated by L. Man